Improved Model Predictive Control Design for Current-Source and Voltage-Source Motor Drives

by

Cheng Xue

A thesis submitted in partial fulfillment of the requirements for the degree of

Doctor of Philosophy

in

energy system

Department of Electrical and Computer Engineering

University of Alberta

Abstract

The linear control structure shows limited bandwidth for high-performance ac drive applications and also it is difficult to deal with complex systems with multi-objective optimization demand and nonlinear, high-order characteristics. With the development of more powerful digital platforms and the emergence of new switching devices, the control algorithm for industrial drives application is constantly evolving and significant research efforts have been carried out over the past several years. Particularly, model predictive control (MPC) emerges as an attractive solution to power converters and it has become a research hotspot recently. The time-domain modeling process makes MPC naturally suit the multiple-input multiple-output (MIMO) systems and it shows obvious advantages in the field of power electronics such as the intuitive concept, faster dynamic response, multi-variable control capability, nonlinear objective handling ability, etc. The research presented in this thesis thus exploits the benefits provided by MPC to address the prominent control challenges existing in industrial motors driven by current-source converters (CSCs) and voltage source converters (VSCs). Particularly, the medium voltage (MV) CSCs are applied with the megawatt power range such as in the wind tunnel drive system, fans and compressors, etc. While the VSCs can be more frequently seen in the relatively lower power occasion, such as electric vehicles, where the switching frequency can be higher to hundreds of kilohertz. The control scheme of both CSCs and VSCs should meet the increased demand and requirements imposed by industrial drive applications because these are directly related to

whether the motor can work normally, and also the system stability, reliability, efficiency, robustness, etc. Considering the limitation of the conventional linear approach and the lack of MPC design for the high-order system and back-to-back(BTB) drive-level optimization, the main work in this thesis can be divided into the following three aspects.

Firstly, the flexible cost-function design mode provided by MPC is exploited to coordinately control the BTB structure, achieving system-level optimization compared to the conventional linear approach. For the BTB CSCs-fed drives, the proposed cost function with direct multi-variable feedback is developed to solve the filter resonance with the second-order characteristic. Besides, the robustness is enhanced by incorporating the disturbance observer, and the long horizon prediction case with the benefits of only line current feedback is presented for such a second-order system. Furthermore, the selective harmonic magnitude penalization is included in the cost function to reject the grid-side harmonic. According to the operated speed region of the motor, the peak-to-peak value of the common mode voltage (CMV) and its third-order harmonic are respectively suppressed to address the common mode (CM) resonance for the transformerless operation. On the other hand, regarding the VSCs-fed drives for relatively low power applications, the nonlinear control objective in terms of intermediate dc-link capacitor current ripple reduction is developed in the BTB structure, which contributes to the lifetime extension or the size reduction of the dc-link capacitor.

Secondly, the potential of MPC is fully developed to control multiple state variables in the third-order LCL-filtered system, avoiding the nested multi-loop control structure in the linear approach. This benefit can be seen in both the LCL-filtered grid-connected application and the long cable-fed motor side with an output LC filter. The proposed MPC schemes show significant benefits in terms of the intuitive design concept, faster dynamic response, and simplified

tuning procedure compared to the conventional multi-loop approach.

Finally, when applying the MPC to the power converters with high switching frequency operation, the high sampling/interrupt frequency demand becomes a great challenge because of the big computational difficulty. Therefore, the multi-rate technique is designed into the MPC formulation, where the switching frequency can be significantly increased and a low sampling/interrupt frequency can be adopted. In this case, the quite long interrupt period allows the easy realization of the control algorithm and an abundant computational margin can remain in the digital platform. The proposed multi-rate MPC by enabling longer interrupt duration is more efficient than the conventional way focusing on how to reduce the execution time of the MPC algorithm itself. The multi-rate MPC also stands for a general formulation of MPC in the field of power electronics.

Preface

This thesis is structured into six chapters. The first chapter reviews the advantages and categories of model predictive control (MPC) applied to power converters. The dominant control challenges are introduced for the medium voltage current source converters (CSCs)-fed drives and the low-power voltage source converters (VSCs)-fed drives. The second chapter presents the predictive scheme to address the control challenges in the back-to-back (BTB) CSCs-fed drives, including resonance damping, harmonic rejection, common mode resonance, etc. The predictive control to reduce the intermediate dc-link capacitor current, which is an unsolved challenge for the BTB VSCs-fed drives, is included in the third chapter. Next, in the fourth chapter, by considering that the high-order filter is commonly used in the industrial drive system, the resonance problems in the LCL-filtered grid-connection application and the motor drive with the output LC filter are solved through the MPC scheme. In the fifth chapter, to solve the common computational challenge brought by high switching frequency power converters, a new tool is developed to facilitate the digital realization by building the multi-rate technique into the MPC framework. The last chapter summarizes the contribution of this thesis and gives insight into future work.

The journal articles related to each chapter are listed here.

Chapter 2

- C. Xue, L. Ding, Y. Li and N. R. Zargari, "Improved Model Predictive Control for High-Power Current-Source Rectifiers Under Normal and Distorted Grid Conditions," in IEEE Transactions on Power Electronics, vol. 35, no. 5, pp. 4588-4601, May 2020.

- C. Xue, L. Ding and Y. R. Li, "Model Predictive Control With Reduced Common-Mode Current for Transformerless Current-Source PMSM Drives," in IEEE Transactions on Power Electronics, vol. 36, no. 7, pp. 8114-8127, July 2021.

- C. Xue, L. Ding, X. Wu, Y. Li and W. Song, "Model Predictive Control for Grid-Connected Current-Source Converter With Enhanced Robustness and Grid-Current Feedback Only," in IEEE Journal of Emerging and Selected Topics in Power Electronics, vol. 10, no. 5, pp. 5591-5603, Oct. 2022.

Chapter 3

- C. Xue, L. Ding and Y.Li, "Improved Model Predictive Control With Reduced DC-Link Capacitor RMS Current for Back-to-Back Converter-fed PMSM Drives" in IEEE Transactions on Industrial Electronics, 2023 (Accepted).

Chapter 4

- C. Xue, D. Zhou and Y. Li, "Hybrid Model Predictive Current and Voltage Control for LCL-Filtered Grid-Connected Inverter," in IEEE Journal of Emerging and Selected Topics in Power Electronics, vol. 9, no. 5, pp. 5747-5760, Oct. 2021.

- C. Xue, D. Zhou and Y. Li, "Finite-Control-Set Model Predictive Control for Three-Level NPC Inverter-Fed PMSM Drives With LC Filter," in IEEE Transactions on Industrial Electronics, vol. 68, no. 12, pp. 11980-11991, Dec. 2021.

Chapter 5

- C. Xue, L. Ding, H. Tian and Y. Li, "Multirate Finite-Control-Set Model Predictive Control for High Switching Frequency Power Converters," in IEEE Transactions on Industrial Electronics, vol. 69, no. 4, pp. 3382-3392, April 2022.

- C. Xue, L. Ding, Z. Quan and Y. Li, " Multi-Rate Modeling and Predictive Control for WBG Device-Based High Switching Frequency Power Converters," in IEEE Transactions on Industrial Electronics, 2023 (Accepted).

Acknowledgements

I would like to express my deepest appreciation to my supervisor, professor Yunwei (Ryan) Li for his continuous support and encouragement during the Ph.D. journey. Being a world-renowned scholar, Dr. Li guided me with his broad academic horizon, great perceptiveness, and rigorous attitude towards research. His mastery of professional knowledge, passion for new things, and suggestions for my personal development would undoubtedly benefit my future career.

Thanks to Dr. John Salmon, Dr. Ali Khajehoddin, Dr. Hao Liang, and Dr. Carl Ngai Man Ho from the University of Manitoba for being part of my examination committee. They provided extremely valuable comments on the revision and improvement of the thesis work, especially in relation to the significance of my future research.

Thanks should also go to all of my peer colleagues and friends in the Electronic and Intelligent Grid Research lab group. Particular thanks to Dr. Li Ding, Dr. Dehong Zhou, Dr. Nie Hou, Dr. Yuzhuo Li, Dr. Jiangfeng Wang, Xuesong Wu, Mingzhe Wu, Han Zhang and Rui Liu. Their constructive advice and always timely support give me a smooth research process and colorful lab life.

I would also like to thank the Alberta Province's full-service innovation engine 'Alberta Innovates' for the graduate student scholarships program, which supports me financially during my Ph.D. study.

Last but most important, I would like to extend my sincere gratitude to my parents and my sister. Special thanks to my beloved girlfriend, Huiyu Chen. They give me the source of power to embrace the difficulty and also encourage me never to surrender no matter how bad or tough the challenge is.

Contents

List of Tables

List of Figures

List of Abbreviations

AD	Active damping
ADC	Analog to digital conversion
AFE	Active front end
AI	Artificial intelligence
ANN	Artificial neural network
AVR	Average voltage reduction
BTB	Back-to-back
CB-PWM	Carrier-based pulse-width modulator
CCS-MPC	Continuous-control-set model predictive control
CM	Common mode
CMV	Common mode voltage
CN	Control trigger
CPLD	Complex programmable logic device
CSCs	Current source converters
CSI	Current source inverter
CSR	Current source rectifier
DFT	Discrete Fourier transformation
DPC	Direct power control
DSPs	Digital signal processors
DTC	Direct torque control
EMI	Electromagnetic interference
EMPC	Explicit model predictive control
ESR	Equivalent series resistance
EV	Electric vehicle

FCS-MPC	Finite-control-set model predictive control
FFT	Fast Fourier transformation
FOC	Field-oriented control
FPGAs	Field-programmable gate arrays
GaN	Gallium nitride
GPC	Generalized predictive control
HEV	Hybrid electric vehicle
HPF	High-pass filter
HVDC	High-voltage direct current
INT	Interrupt trigger
IGBTs	Insulated-gate bipolar transistors
IGCTs	Integrated gate-commutated thyristors
kHz	Kilohertz
kW	Kilowatt
LPF	Low-pass filter
LQ	Linear quadratic
MIMO	Multiple-input multiple-output
ML-VSCs	Multilevel voltage source converters
MOSFETs	Metal-oxide-semiconductor field-effect transistor
MPC	Model predictive control
MRCCS-MPC	Multi-rate continuous-control-set model predictive control
MRFCS-MPC	Multi-rate finite-control-set model predictive control
MR-MPC	Multi-rate model predictive control
MV	Medium voltage
MSE	Mean square error
NPC	Neutral-point-clamped
OSV-MPC	Optimal switching vector model predictive control
OSS-MPC	Optimal switching sequence model predictive control
PI	Proportional-integral
PLL	Phase-locked loop

PMSM	Permanent-magnet synchronous motor
PR	Proportional-resonant
PTP	Peak-to-peak
PWM	Pulse-width modulator
QP	Quadratic programming
RHP	Receding horizon policy
RMS	Root-mean-square
SDFT	Sliding discrete Fourier transformation
SHC	Selective harmonic compensation
SHE	Selective harmonic elimination
SiC	Silicon carbide
S/I	Sampling/interrupt
SISO	Single-input single-output
SOGI	Second-order generalized integrator
SPWM	Sinusoidal pulse-width modulation
SRCCS-MPC	Single-rate continuous-control-set model predictive control
SRFCS-MPC	Single-rate finite-control-set model predictive control
SVPWM	Space vector pulse width modulation
SVM	Space vector modulator
THD	Total harmonic distortion
VOC	Voltage-oriented control
VSCs	Voltage source converters
VSD	Variable-speed drive
VSI	Voltage source inverter
VSR	Voltage source rectifier
WBG	Wide bandgap
ZOH	Zero-order hold

Chapter 1

Introduction

Power electronics is becoming a maturing technology recently with the offered flexibility, sustainability, improved production rates, and efficiency [1]–[3], where the widespread application could be found in the field of power systems [4]–[6] and variable-speed drive (VSD) systems [7]–[10]. During this process, power converters play an important role in energy conversion and management, and their control scheme is essential to meet the increased demand and requirements imposed by specific industrial application scenarios [11]–[13]. Especially, the VSD accounts for almost two-thirds of total industrial power demand and the sophisticated controller should be designed to ensure the system is operated with better power quality, efficiency, reliability, etc. On the other hand, the fast development of microprocessors enables more advanced control schemes that can be performed with an acceptable computational cost. This thesis thus aims at prominent control challenges existing in the typical industrial drives and develops advanced control strategies to improve the system performance.

1.1 MPC for Industrial Motor Drive Application

With the development of more powerful digital platforms and the emergence of new switching devices, the control algorithm for industrial drives application is constantly evolving and significant research efforts have been carried out over the past several years. Particularly, model predictive control (MPC) emerges

as an attractive solution to power converters and it has become a research hotspot recently [14]–[16]. Especially in the field of electrical and mechanical engineering, some outstanding mathematical models allow the prediction of system behavior with high accuracy. This section firstly reviews the classical controllers for industrial drives and then illustrates the advantages and motivations for adopting MPC and the new achievements that can be brought compared to classical control schemes. Finally, the operation principle and category of the MPC scheme for power converters will be introduced.

1.1.1 Classical Control Schemes

Several control schemes have been developed for industrial drives [15], [16], which typically include both the grid-side rectifier and the inverter-fed motor side. The hysteresis control considers the nonlinear nature of power converters and it exploits a pre-defined hysteresis width to directly selects the switching state such that the state variable can be controlled within the width. The hysteresis-based scheme includes several variants according to the type of control variables, such as direct torque control (DTC) for the inverter-fed motor side [17] and direct power control (DPC) for the grid side [18]. However, the hysteresis control requires a high sampling frequency operation and the ripple of the control variable is typically large due to the lack of an optimization mechanism. The selective harmonic elimination (SHE) has the lower harmonic distortion per switching frequency but the optimized switching angle is solved offline and its bandwidth is limited [15]. On the other hand, the typical cascaded control structure incorporated with the pulse-width modulator (PWM) are adopted for both the rectifier and inverter, which include the well-known voltage-oriented control (VOC) [19] and the field-oriented control (FOC) [20], [21] respectively. The state variables are regulated by the control loops and the voltage command is computed which will be synthesized by the PWM block, such as the carrier-based PWM (CB-PWM) and the space vector modulator (SVM). In this case, the linear control way can be used to generate such a command and the most common choice is the proportional-integral (PI) regulators. These linear control strategies have several practical limita-

Table 1.1: Summary of classical control schemes for industrial drives

Controller	Characteristic
FOC (motor side), VOC (grid side)	CB-PWM or SVM is used, Linear, Cascaded loops, Tedious tuning, Difficult to address nonlinear and multi-variable objectives
DTC (motor side), DPC (grid side)	Direct control, Hysteresis controller, Look-up table, Fast dynamic, Pronounced harmonic distortions
SHE	Low harmonic distortion per switching frequency, Offline, Low bandwidth

tions [22]. For example, to avoid interference between different loops, the outer loop should maintain approximately an order of magnitude smaller bandwidth compared to the inner one, resulting in a slow dynamic response. In addition, the controller cannot suit all of the operating points in practicality and its performance is also vulnerable to parameter variations and larger-signal external disturbances. Table 1.1 summarizes these classical controllers for industrial drives and their respective characteristics.

1.1.2 Advantages and Motivations of MPC for Industrial Drives

In the 1970s, MPC was introduced as an advanced control strategy in the process industry with the time-domain formulation [23]. The past decades have witnessed significant progress in the MPC schemes applied to the field of power electronics [14], [16], and it continuously attracted the interest of the research and academic communities. By exploiting the system modeling, MPC aims to forecast the future behavior of power converters within a moving horizon, and the online optimization process is performed to make the control decision. MPC shows obvious advantages over the conventional control approaches such as the intuitive concept, fast dynamic response, multivariable control capability, constraints, nonlinear objective handling ability, etc [15], [24]. The significant enhancement of the computational power of the digital platform enables the development and implementation of various kinds of MPC. In this case, the more stringent requirement that comes from the power converter side can be met and addressed. In general, the advantages of MPC

applied to power electronics can be summarized as follows.

1) MPC is formulated in the time domain rather than the frequency domain. Therefore, the MPC can address the system featuring nonlinear properties with a more intuitive concept and broad applicability;

2) The cost function-based evaluation procedure shows great flexibility and scalability to handle the nonlinear, complex, and even possibly conflicting control objective. It can also handle the hard constraints on the manipulated state and control variables;

3) The cascaded control loops in the conventional linear PI-based control can be replaced by the MPC, resulting in enhanced dynamic response and a simplified tuning procedure for the industrial drive application. Besides, the modulation stage can be eliminated;

4) The multivariable control property of MPC suits the multiple-input multiple-output (MIMO) systems, which can simplify the design, analysis, and tuning process compared to the way using multiple decoupled single-input single-output (SISO) loops.

Despite significant progress has been made in MPC research, some dominant control challenges that come from the industrial drives still remain unsolved. Therefore, in this thesis, it is expected to exploit the benefits provided by the MPC to address these control problems and the main achievement could be found through the following three aspects:

1) Linear control has a limited ability to handle nonlinear objectives. Fortunately, the multi-objective optimization for industrial drives can be achieved through the flexible cost function design in MPC, where the nonlinear objectives can be achieved along with the current/power control for both the grid and motor sides, such as selective grid-side harmonic suppression, common-mode (CM) resonance suppression and the dc-link filter size reduction in back-to-back (BTB) structure;

2) The high-order filters have been commonly used in industrial drive applications on both the grid side for harmonic attenuation and the motor side with a long cable. With more complex system modeling, the linear scheme requires more control loops, and the tuning complexity is increased. On the

other hand, although most of the existing MPC research was reported on the first-order L-filtered power converters, relatively little effort has been applied to the LC/CL/LCL-filtered cases. Particularly, the MIMO control property of MPC endows it with great flexibility and scalability to handle resonance problems in industrial drives with high-order filters. This thesis thus gives a distinctive insight into the resonance mechanism in the time domain along with the prediction process and the corresponding damping principle can be intuitively understood;

3) The existing approach to reducing the MPC algorithm's computational burden has limited potential. From another perspective, enabling long interrupt periods can be more computationally efficient than conventional methods. In this process, the system state-space modeling with slow-rate sampling information but a fast-rate control input can be built to facilitate the high switching frequency operation. In addition, the behavior of the power converter can be explicitly understood and well-controlled.

1.1.3 Operation Principle of MPC

The MPC predicts power converter behavior within a future time horizon, where the control input is taken as the unknown variable to be solved. In this case, discrete-domain state-space modeling is usually used to calculate the future state variable. Generally, the dynamic of the power converter system can be described by the linear time-invariant equation as follows [15].

$$\begin{aligned} \tfrac{d\boldsymbol{x}}{dt} &= \mathbf{A}\boldsymbol{x} + \mathbf{B}\boldsymbol{u} + \mathbf{E} \\ \boldsymbol{y} &= \mathbf{C}\boldsymbol{x} \end{aligned} \tag{1.1}$$

where, in general, the state vector $\boldsymbol{x} \in \mathcal{R}^n$, input vector $\boldsymbol{u} \in \mathcal{R}^p$, output vector $\boldsymbol{y} \in \mathcal{R}^q$ and the system matrix $\mathbf{A}$, input matrix $\mathbf{B}$, disturbance matrix $\mathbf{E}$, and output matrix $\mathbf{C}$ are of compatible dimensions, i.e., $\mathbf{A} \in \mathcal{R}^{n\times n}$, $\mathbf{B} \in \mathcal{R}^{n\times p}$, $\mathbf{E} \in \mathcal{R}^n$ and $\mathbf{C} \in \mathcal{R}^{q\times n}$. Typically, the state vector $\boldsymbol{x}$ includes the variable existing in power converters and motor drives, such as inductor current, capacitor voltage, motor torque, speed, flux, etc. The output vector $\boldsymbol{y}$ usually contains the measurable components. For the digital realization with constant sampling interval T_s (sampling frequency f_s equals $1/T_s$), the predictive equation

in the discrete domain can be expressed as

$$\begin{aligned} \boldsymbol{x}(k+1) &= \mathbf{A}_{\mathrm{d}}\boldsymbol{x}(k) + \mathbf{B}_{\mathrm{d}}\boldsymbol{u}(k) + \mathbf{E}_{\mathrm{d}} \\ \boldsymbol{y}(k) &= \mathbf{C}\boldsymbol{x}(k) \end{aligned} \tag{1.2}$$

where k represents the currently sampling step. According to the sampling interval T_s, the discrete matrices $\mathbf{A}_{\mathrm{d}}$, $\mathbf{B}_{\mathrm{d}}$ and $\mathbf{E}_{\mathrm{d}}$ can be calculated as follows.

$$\mathbf{A}_{\mathrm{d}} = e^{\mathbf{A}T_s}, \;\; \mathbf{B}_{\mathrm{d}} = \int_0^{T_s} e^{\mathbf{A}\tau}\mathbf{B}_{\mathrm{d}}\tau \;\; \text{and} \;\; \mathbf{E}_{\mathrm{d}} = \int_0^{T_s} e^{\mathbf{A}\tau}\mathbf{E}d\tau \tag{1.3}$$

where e denotes the matrix exponential. Based on the predictive equation (1.2), the state variable in the future time horizon N_p can also be calculated subsequently. Next, the optimization process can be performed to decide the optimized control input sequence within the time horizon N_p. Usually, the control objective of the power converter is reflected as a pre-defined cost function according to the MPC procedure, which maps the predictive variable, output, and manipulated control input into a scalar cost value. In this case, the evaluation of the control input can be done by comparing the corresponding cost value and the optimal one will be selected based on the minimized criteria. Generally, the cost function can be designed as follows [15].

$$J\left(\boldsymbol{x}(k), \boldsymbol{U}(k)\right) = \sum_{l=k}^{k+N_p-1} \Lambda\left(\boldsymbol{x}(l), \boldsymbol{U}(l)\right) \tag{1.4}$$

which contains the sum of all of the stage costs Λ within the predictive horizon N_p. The stage cost item can be flexibly designed to represent the comprehensive system performance, such as the penalization between the output variable and reference value, the switching frequency reduction, etc. Since the control is executed in each sampling interval, the manipulated control sequence in total number N_p can be aggregated in the vector

$$\boldsymbol{U}(k) = \left[\boldsymbol{u}^{\mathrm{T}}(k) \;\; \boldsymbol{u}^{\mathrm{T}}(k+1) \;\; \ldots \;\; \boldsymbol{u}^{\mathrm{T}}(k+N_p-1)\right]^{\mathrm{T}} \tag{1.5}$$

The control input $\boldsymbol{u}$ for each step can be directly the discrete switching state of the power converter or the reference continuous input that can be synthesized by the PWM stage. The future behavior of the power converter regarding the input $\boldsymbol{U}$(k) can be calculated and the performance is reflected by the cost

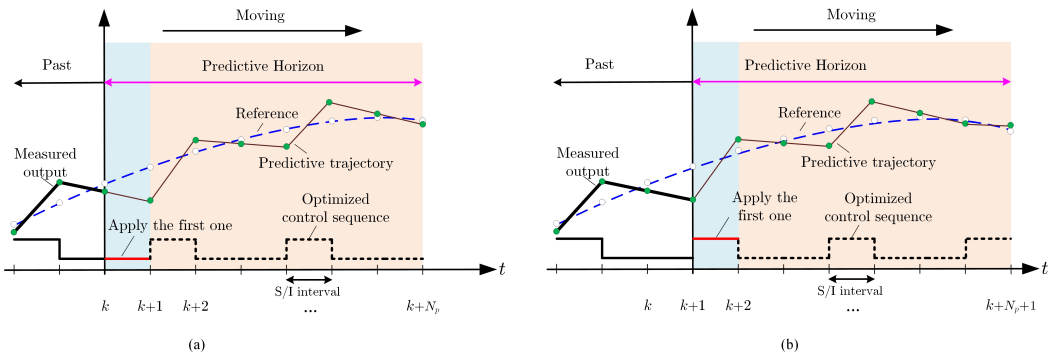

Figure 1.1: The operation principle of the MPC process. (a) The kth time step. (b) The $(k+1)th$ time step.

function (1.4). Therefore, the control problem turns to finding the optimal control sequence $\boldsymbol{U}_{\mathrm{op}}(\mathrm{k})$ in the available input set. As two typical ways of MPC, the solution of $\boldsymbol{U}_{\mathrm{op}}(k) = \left[\boldsymbol{u}_{\mathrm{op}}^{\mathrm{T}}(k) \;\; \boldsymbol{u}_{\mathrm{op}}^{\mathrm{T}}(k+1) \;\; \ldots \;\; \boldsymbol{u}_{\mathrm{op}}^{\mathrm{T}}(k+N_p-1)\right]^{\mathrm{T}}$ can be obtained by substituting each discrete switching state into the cost function to find the one with minimum cost value or can be solved through the differentiation of the cost function. The optimal solution $\boldsymbol{U}_{\mathrm{op}}(k)$ contains the control input for the future N_p sampling steps, i.e. from time step k to $k+$ N_p -1. However, only the first element in the optimal sequence, namely $\boldsymbol{u}_{\mathrm{op}}(k)$, is applied to the power converter. In the next sampling interval, the MPC procedure is repeated and the new optimal control input will be obtained based on the updated measurable variables. This way guarantees real-time feedback, which is referred to as the receding horizon policy (RHP). Fig. 1.1 shows the principle of the MPC scheme at the time step k. The predictive horizon with length N_p serves as a moving window, within which the future output information is calculated based on the kth step state variable and the control sequence. Only the first element in the optimal input sequence is applied. In the next sampling interval, the horizon window moves one step forward starting from the $(k+1)$th time step, and the same procedure will be repeated.

1.1.4 Categories of MPC for Power Converters

According to the type of the optimization problem, the MPC scheme can be mainly classified into the finite-control-set MPC (FCS-MPC) and continuous-control-set MPC (CCS-MPC) [14]. Each MPC category has its own advantages and can be combined with specific application scenarios. The FCS-MPC or direct MPC refers to that the available control input only contains the finite number of the switching state or pre-defined switching pulse provided by the power converter. In this case, the FCS-MPC transfers the optimization problem into the enumeration search stage, where each candidate control input is substituted into the cost function and the one with the minimum value will be selected by the sort algorithm. Therefore, the advantage of FCS-MPC is that it features an intuitive process and the flexible control objective can be designed into the cost function. Also, the dedicated modulator stage can be eliminated [16]. Based on the type of the control set, the FCS-MPC can be further classified into the optimal switching vector MPC (OSV-MPC) and optimal switching sequence MPC (OSS-MPC). The OSV-MPC represents the initial framework of FCS-MPC and the single switching state is applied during the whole sampling interval. Due to the absence of a modulator, the switching frequency is variable and the switching-to-sampling frequency ratio of OSV-MPV is low [25]. This specific type of FCS-MPC can handle multiple control objectives and it naturally suits the high power and relatively low switching frequency power converters [15]. The OSS-MPC can achieve the constant switching frequency since the pre-defined switching sequence contains multiple switching vectors within each sampling interval.

On the other hand, the CCS-MPC solves the optimization problem to find the explicit formulation of the control law which has the minimum cost function value within the feasible zone. In this case, the control input is the continuous signal and the modulator is utilized to generate the desired input for the power converter. As a result, the constant switching frequency can be achieved and the value can be conveniently set, hence, it is now more frequently seen in the application of VSCs with the requirement on the switching frequency. The

Table 1.2: Summary of the MPC schemes for power converters application

Indices	OSV-MPC	OSS-MPC	GPC	EMPC
Category	FCS-MPC	FCS-MPC	CCS-MPC	CCS-MPC
Modulator	Not required	Not required	Required	Required
Switching frequency	Variable	Fixed	Fixed	Fixed
Optimization	Online	Online	Online	Offline
Constraints	Yes	Yes	Increased computational burden	Yes
Long horizon prediction	Dedicated searching algorithm	Dedicated searching algorithm	Yes	Yes
Formulation	Very simple	Simple	Complex	Complex

CCS-MPC applied to the power converter mainly includes the generalized predictive control (GPC) and explicit MPC (EMPC). The GPC is initially developed based on the transfer-function model and further has been extended to the state-space model, where the unconstrained solution of the optimization problem is usually used. The EMPC enables the user to consider the system constraints, however, the explicit solution is solved offline and then stored in the controller. Table 1.2 gives the summary of the MPC categories and their respective characteristics. In this thesis, the developed FCS-MPC refers to the OSV-MPC type and the developed CCS-MPC refers to the GPC type in the following chapters.

1.2 Power Converters and Industrial Variable-Speed Drives

According to the report for the global industrial motors market [26], the revenue of motor applications is valued at 19.81 billion USD in 2020 and is expected to be 23.48 billion by 2026. High-power converters and medium voltage (MV) VSD systems have gained widespread applications such as large compressors, steel rolling mills, railway locomotive traction, pumped hydro storage systems, etc. [27]. They still present an ever-growing trend because of the energy-saving advantage and the potential productivity that offers for

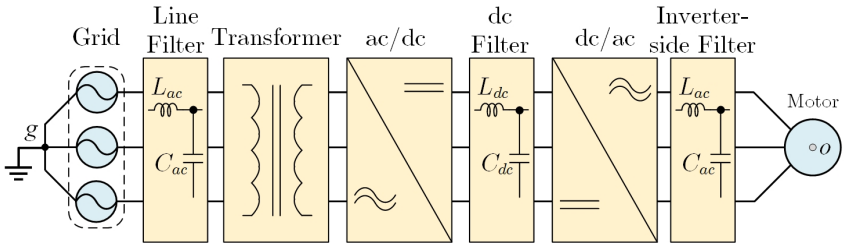

Figure 1.2: A typical configuration of the industrial VSD system.

industrial automation demands. Fig. 1.2 shows a general configuration of high-power VSD systems [27], [28]. The rectifier converts the ac electricity from the grid to dc quantities, and the rectifier could employ the diode bridge or active front end (AFE) power converters. The intermediate link severs the energy buffer and also stabilizes the system. The inverter transforms the dc energy into the ac voltage/current with variable frequency to drive the motor. In addition, the isolation transformer can block the voltage stress and the bearing current of the inverter-side as well as reduce grid current distortion. The ac filters can be optional based on the application requirements and converter topologies. On the other hand, the VSD with the typical lower power range from 2-500 kilowatt (kW) is increasingly applied in electric vehicle (EV) and hybrid electric vehicles (HEV) [29], [30]. The battery-powered inverter is the critical component in the EV system and higher efficiency, reduced size, lower cost, etc. are desired.

Power converters are a significant part of the industrial VSD system. Basically, power converters are composed of active switching devices, such as insulated-gate bipolar transistors (IGBTs), metal–oxide–semiconductor field-effect transistors (MOSFETs), integrated gate-commutated thyristors (IGCTs), gate turn-off thyristors, etc [31]. Besides, the passive filter elements are usually essential in the conversion process to filter the high-order switching harmonic and assist in the commutation of the switching device. Today, both the current source converters (CSCs) and voltage source converters (VSCs) have been the popular choice in the VSD scenes [29], [32]. Especially, VSCs receive great favor in relatively low power occasion, where the switching frequency ranges from a few thousand hertz to hundreds of kilohertz (kHz) [33]–[36], or high power

application with multilevel VSCs (ML-VSCs) topologies and lower switching frequency operation [37]. On the other hand, CSCs feature a simple converter configuration, low switching dv/dt, and reliable overcurrent protection capability, which has been commonly used in industries with the megawatt power range [38], such as in VSD-based wind energy conversion systems [39] and high-voltage direct current (HVDC) transmission [40]. Recently, the newly wide bandgap (WBG) material-based switching devices, such as silicon carbide (SiC) and gallium nitride (GaN), feature the advantageous property of higher breakdown field, faster-switching speed, lower on-state loss, etc [41], [42]. Therefore, they have become favorable in EV applications, where high switching frequency, efficiency, and density are desired [43]. In this case, the WBG power converter enables the VSD system to meet the demands, such as high-speed operation, low-inductance design, more compact and integrated requirements, etc. Table 1.3 shows a summary of VSD products from the major manufacturers in the world [27] and some WBG device-based drives found in the industrial product [43], with the type of adopted power converter and switching devices, as well as the voltage and power range. The CSCs are mainly developed in the MV VSD system application, and the VSCs can be frequently seen in the relatively low power occasion, especially with the integration of the SiC device.

The technical requirements and challenges appear in the power converter-fed VSD system and they must be well addressed to ensure the motor work normally, and also the system stability, reliability, efficiency, robustness, etc. The requirements and challenges mainly include the following several aspects [27]: the power quality requirements of the grid-side power converter, the challenges raised from the design of the motor-side power converter, the operational constraints of the switching devices, and the design constraints regarding the other components in the VSD system, such as the size of the dc-link. The design of the control scheme for CSCs and VSCs is directly related to these mentioned requirements and challenges [44]. This chapter will illustrate the control problems of the CSCs and VSCs-fed VSD system in the following contents, and then the research objectives, contributions, and structure of this

Table 1.3: Summary of the motor drive product marketed by manufacturers and companies

Inverter Configuration	Switching Device	Power Range	Voltage Range	Manufacturer/Company
CSCs	Symmetrical IGCT	0.2-20MVA	2.4-6.6kV	Rockwell Automation (PowerFlex 7000)
Two-level VSCs	IGBT	1.4-7.2MVA	-	Alstom (VDM5000)
Three-level	GCT	0.3-5MVA	2.4-4.16kV	ABB (ACS 1000)
neutral point	GCT	3-27MVA	3-3.3kV	ABB (ACS 6000)
clamped VSCs	IGBT	0.6-7.2MVA	2.4-4.16kV	Siemens (Simovert MV)
Two-level VSCs	SiC	1.6MVA	10kV	Calnetix
	SiC	200kVA	1.05kV	John Deere
	SiC	200kVA	1.2kV	Tesla Model 3 Inverter
	Integrated SiC module	60kVA	-	Mitsubishi

thesis will be presented.

1.3 Technical Requirements and Challenges of Medium-Voltage CSCs

ML-VSCs occupy the dominant market share for high-power drive systems [37]. However, with the increased number of switching devices, the control algorithm for ML-VSCs becomes more complicated. CSCs suit the high-power motor drive well and could be a good alternative to ML-VSCs [38]. Fig. 1.3 shows the typical configuration of the MV transformerless BTB CSCs-fed permanent-magnet synchronous motor (PMSM) drive system, which utilizes the IGCTs as the switching device. The current source rectifier (CSR) serves as the front-end converter of the system to provide dc-link current, where the ac grid supplies three-phase voltage through the parasitic resistance R_r and an input LC filter to the converter bridge. A large differential dc choke L_{diff} is connected with the output of the CSR bridge to smooth the dc-link current and the CM choke L_{cm} is for the CM current reduction. The filter capacitor at both the CSR and current-source inverter (CSI) sides helps to refine the current waveforms while supporting the commutation of switching devices. The capacitor can also reduce the dv/dt for the CSI-fed motor side. The switching frequency

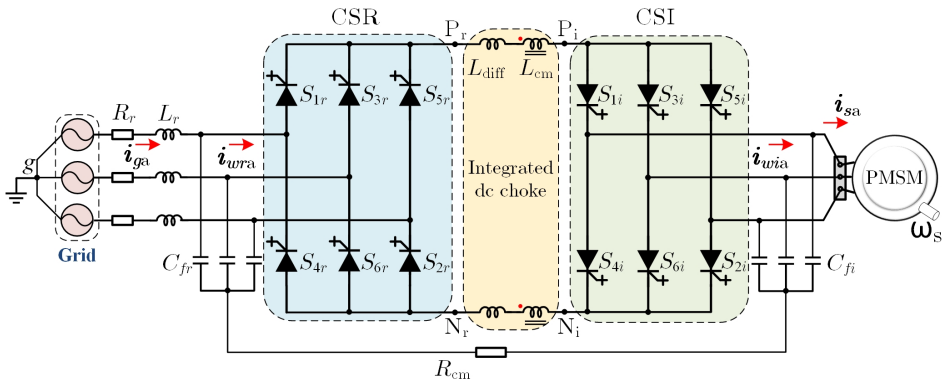

Figure 1.3: High-power MV transformerless CSCs-fed PMSM drive system.

for the IGCTs configurated CSCs are normally lower than 1kHz to reduce the switching losses. The CSCs-fed VSD system faces prominent control problems including filter resonance, grid-side harmonic pollution, and CM resonance in the transformerless operation.

1.3.1 Second-order Filter Resonance

Since the second-order LC/CL filter is configured in CSCs, the dynamic change trends regarding capacitor voltage and inductor current is a mutual interaction process when the control input, i.e., the current vector of CSCs is applied. Taking the CSR side modeling as an example, the transfer function between the grid current and rectifier current in the s-domain can be derived as follows.

$$\frac{i_g(s)}{i_{wr}(s)} = \frac{1}{s^2 L_r C_{fr} + s R_r C_{fr} + 1} \tag{1.6}$$

A similar transfer function can be derived between the stator current of PMSM and the converter current of CSI. Fig. 1.4 shows the bode diagram of the transfer function of (1.6) using the typical LC parameters in the MV CSR (L_r=4.588mH, C_{fr}=76.64μF, R_r=0.581Ω). It can be found that the resonance current peak will emerge at the frequency

$$f_{\text{LC\_res}} = \frac{1}{2\pi\sqrt{L_r C_{fr}}} \text{rad/s} \tag{1.7}$$

Besides, due to the small resistive impedance of the grid-side line and stator winding, significant harmonic distortion will be presented in the grid current

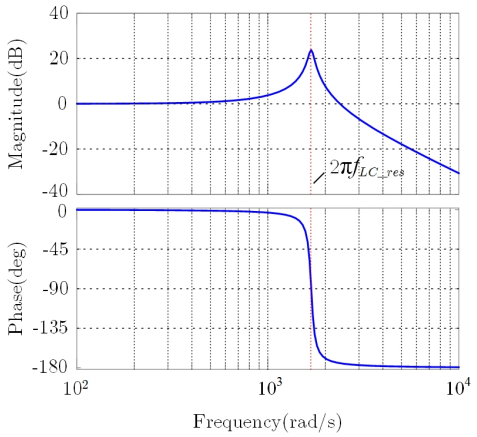

Figure 1.4: Bode diagram of the LC filter in CSR.

and stator current of the motor. Since the constant grid-side frequency (50Hz or 60 Hz), the LC filter in CSR will normally cause dominant 5^{th} and 7^{th} harmonic current distortion. The harmonic order of stator current caused by CL filter resonance will change with the motor speed.

The CSC features second-order characteristics and thus the typical challenge is to dampen the resonance caused by the ac side inductor and filter capacitor. Specifically, the modulated switching pulse of the converter bridge will induce the parallel resonance. The resonance causes large spikes and oscillations in the grid current at the CSR side, which leads to an unstable system and over-current protection. The physical resistor can dampen the resonance but with the increased power loss and cost. Therefore, the active damping (AD) method was proposed in [45] to suppress the resonance by emulating a virtual resistor in parallel with the filter capacitor. A high-pass filter (HPF) was used to extract the high-frequency component of capacitor voltage. In [46], another alternative AD scheme using inductor current feedback proved to be effective and simple. In [47], four groups of hybrid state variable feedback control methods are concluded and compared to dampen the filter resonance in CSR. However, the complex calculation of feedback gain value is based on the objective to only suppress the magnitude of the first dominant harmonic frequency in the grid current, which is inflexible. Likewise, the output capacitor, together with the stator inductor will cause the CL resonance in the motor

current, which needs to be suppressed as well. The virtual-impedance-based AD control has also been realized in the CSI-fed PMSM drive [48].

1.3.2 Grid-side Harmonic Rejection

In the grid-connected CSR application, the harmonic disturbance in the grid voltage will induce the series resonance issue in the LC filter loop when the supply grid contains background harmonics (mainly 5^{th} or 7^{th} harmonics). The series resonance will be excited and the performance of the above AD schemes for parallel resonance suppression will be compromised. In [47], the CSR system supplied with the ac grid containing 2% 5^{th} (resonant frequency) and 1% 7^{th} harmonic has been tested but no further improvement strategy is proposed to deal with the series resonance. In [49], conventional SHE with selective harmonic compensation (SHC) has been proposed for CSR working under distorted grid conditions. The principle is to make the capacitor voltage harmonic and grid background harmonic cancels each other out. The limitations of the SHC scheme include the complex derivation to calculate the switching angle and offline implementation.

1.3.3 Transformerless Operation in the BTB CSCs

Besides the filter resonance problem, common-mode voltage (CMV) accompanied by the switching action is another challenge for the CSCs-fed motor drive. The CMV raises the voltage stress of the motor shaft with respect to the ground and induces the bearing current, which seriously threatens the lifetime of the motor. In [50], the SVM scheme without using the zero-state vectors can reduce the peak-to-peak (PTP) value of CMV in CSC-fed motor drive, but comes at the expense of deteriorating the power quality and increased switching frequency. Furthermore, an improved SVM was proposed with the mechanism that selects the zero-state vector with the minimum CMV at each sampling interval [51]. This way can achieve better system performance and reduced CMV. To realize the transformerless operation of the CSC-fed motor drive system, the total CMV can be approximately clamped to zero by directly connecting the neutral point of the input and the output capacitor

[52], as shown in Fig. 1.3. To limit the CM current, the CM choke L_{cm} and the damped resistor R_{cm} are used to increase the impedance of the CM loop. Yet, the CM choke still represents a considerable size and weight of the system. Since the CM loop includes the inductive choke and two ac-side capacitors, the CM resonance will be excited by the CSI side CMV when the motor runs in the low-speed region [52]. As a result, a large CM current will be induced in the loop, which can cause the magnetic saturation of the CM choke. Therefore, it is still necessary to refine the waveform of the CMV although the transformerless operation is realized. Being different from previous work, the SVM scheme with the average value reduction (AVR) of the CSI side CMV was proposed in [53] to reduce the dominant third-order harmonic and thus alleviate the CM resonance. However, the filter resonance was not taken into account and the dynamic performance is limited through the multiloop control.

1.4 Technical Requirements and Challenges of VSCs for Low Power Application

The VSCs are the popular choice in relatively low-power occasions to connect the dc type source/load and the ac type load/source. The switching devices used in those VSCs are mainly IGBT or the newly emerging WBG device to cover the switching frequency ranging from several kHz to dozens of kHz. In the BTB VSCs-fed VSD system, the intermediate dc-link capacitor was reported to be a weak component in the whole system with a high failure rate [54]. Besides, with more requirements posed on the power density, cost, and system reliability, the design in terms of capacitors has more constraints, such as the smaller volume and size is welcome or their lifespans are expected to be extended [54], [55]. On the other hand, for some application occasions with more stringent requirements on the harmonics, the LCL filter will replace the single L filter for grid-connected applications because it features high-order properties, reduced weight, and size, which can attenuate the harmonic more effectively [56]–[58]. Also, the installment of the LC filter between VSCs and the motor terminal is an effective approach to overcome the high change

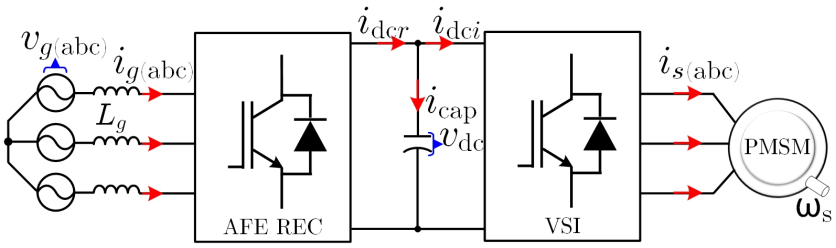

Figure 1.5: The BTB VSCs-fed VSD system.

of dv/dt and over-reflection voltage in the long cable connection [59]–[61]. However, the high-order system raises more complex control problems and poses a higher challenge to the controller design. In addition, although the WBG device-based converter enables the high switching frequency to improve the output voltage/current quality and reduce the filter size, it is not always possible to realize the high switching frequency in the digital controller due to the limited computational capability [62]. Therefore, how to apply the control scheme, especially the advanced method is quite essential to the high switching frequency VSCs. This section thus reviews these typical technical requirements and control challenges in the VSCs-fed VSD application.

1.4.1 Intermediate dc-link Capacitor Current in the BTB VSCs

As seen in Fig. 1.5, the BTB VSCs employ the AFE voltage-source rectifier (VSR) and the voltage-source inverter (VSI)-side motor drive, which is commonly used in the wind turbine system [63], [64] and the EV charger application [65]. The BTB structure brings the benefits such as nearly perfect sinusoidal input currents, nearly unity power factor, and regenerative capability [28].

In the BTB system, the intermediate dc-link capacitor serves as the energy buffer, which is indispensable for supporting stable dc voltage, providing reactive power, reducing the emission of electromagnetic interference (EMI), etc [54], [55]. On the other hand, the dc-link capacitor sustains the high-frequency current switching ripple shock and it shows a high failure rate in the whole system [54]. With more requirements posed on the power density, cost, and

system reliability, capacitors with smaller volume and size are welcome or their lifespans are expected to be extended [54], [55]. The lifetime model of dc-link capacitors developed in [54] includes the equivalent series resistance (ESR) modeling and reveals the effect of the tested temperature and voltage stress, which is given in (1.8).

$$\begin{cases} L \propto V^{-n} \times \exp\left(\frac{E_a}{K_B T}\right) \\ T = T_{\text{amb}} + R_{\text{ha}} \times \sum_{i=1}^{n} \text{ESR}(f_i) \times I_{rms}^2(f_i) \end{cases} \tag{1.8}$$

where L represents the estimated lifetime, V is the maximum voltage across capacitors, K_B is the Boltzmann's constant, E_a is the activation energy, n is the voltage stress exponent, T is the hotspot temperature, T_{amb} is the ambient temperature, R_{ha} is the equivalent thermal resistance from hotspot to ambient, $\text{ESR}(f_i)$ represents the equivalent series resistance at frequency f_i and $I_{rms}(f_i)$ is the RMS value of the ripple current at frequency f_i. Under a rated DC-link voltage level, the ripple current flowing through the capacitor contributes to the self-healing process and the root-mean-square (RMS) current is crucial to the rise of the hotspot temperate [54], [55]. Therefore, the reduction of the RMS current in the dc-link capacitor has been the focus to reduce the capacitor size or extend the lifespan under different PWM strategies.

In the BTB VSCs, the instantaneous dc-link capacitor current is the difference between the dc-side output current of the VSR and that of the VSI. Essentially, the VSC dc-side current pulse is determined by the corresponding switching state and three-phase current. Therefore, the capacitor current contains multiple frequency components from both sides, where its spectrum shape and RMS value are directly related to the imposed PWM strategy on the two sides. For example, according to the analytical expression under the widely used carrier-based space vector pulse width modulation (SVPWM) scheme, the high-order ripple components dominate in the capacitor current, which includes the carrier frequency and carrier-sideband harmonics [66], [67].

1.4.2 Power Quality for Grid-Connected Application

To improve the harmonic profile of the grid-connected VSCs, the high-order LCL filter is commonly used to replace the single L filter. However, the LCL filter introduces the inherent resonance problem, which brings challenges to the stability of the grid-connected VSC. The resonant current spikes will be excited by the switching harmonics from either the converter or the background harmonic in the grid voltage. Therefore, the controller design should effectively suppress the filter resonance and simultaneously reject the current harmonics caused by the unhealthy grid. Existing AD control with additional feedback has been extensively accepted and researched for the LCL-filtered VSC. The dynamic response of injected current in these AD schemes is expected to be limited since the cascaded control loops are adopted with either PI or proportional-resonant (PR) regulators [68]–[71]. Besides, the design complexity is increased, e.g., with digital filter and virtual-impedance concept involved. In addition to the natural resonance problem of the LCL filter, the unhealthy grid condition will significantly affect the injected current performance. The background harmonic voltage in the grid will excite the harmonic currents [72], [73]. Moreover, the unbalanced grid condition can cause the prominent triple-order harmonic in the current [74]. Therefore, the controller should be able to maintain sinusoidal current even under distorted and unbalanced grid conditions.

1.4.3 Resonance Suppression in Motor Drives With Inverter Output LC Filter

The high-frequency switching transition of VSC will generate adverse effects on the motor side, such as the high value of dv/dt, additional power loss, and insulation failure of stator windings. The high change of dv/dt normally causes reflection overvoltage and EMI problems during the long-cable transmission. Especially with the increased application of SiC and GaN-based inverters, the switching devices can be operated with a more fast transition [75]. As a result, the critical cable length could lead to 150% of the dc bus voltage stress on

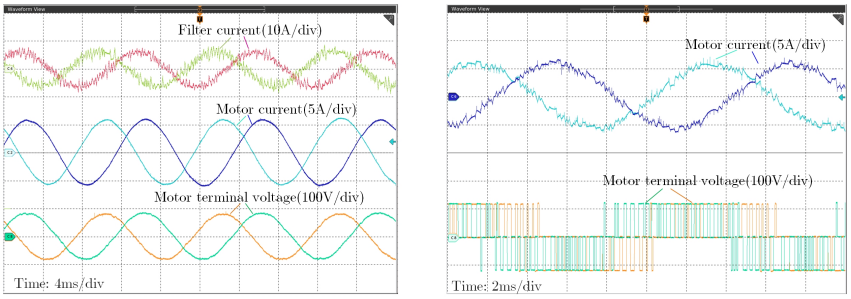

(a) (b)

Figure 1.6: An experimental case of the VSC-fed PMSM system. (a) With LC filter (b) Without LC filter.

the motor terminal and even cause the interturn short-circuit fault [76]. The installment of the LC filter between VSC and motor could be an alternative way to overcome the mentioned problems. For low voltage motors fed by inverters with switching frequency above 4kHz, the utilization of LC filter is quite necessary and common [77], [78]. In [61], the author has summarized that the reduced inverter-side current, reduced RMS current ripple and low temperature of the dc-link capacitor, reduction of distortions in stator flux, and reduction of air-gap torque pulsation of the motor could be obtained by using the LC filter. A scaled-down experimental test for the same PMSM system with/without the LC filter is provided in Fig. 1.6. It can be seen that the motor terminal voltage and stator current waveform are improved significantly due to the LC filter. The high dv/dt problem and the high-frequency noise in stator current are both effectively mitigated. Consequently, the voltage and current applied to the motor are closer to the sinusoidal waveform, which is beneficial to the longer life of the motor.

However, the LC filter, together with the motor inductor, will induce the additional LCL resonance problem. Due to the low circuit impedance, the voltage and current oscillations will appear, which reduces the stability of the drive system. Similar to the grid-connected side, the AD schemes applied to the motor side are designed based on linear cascaded loops with high complexity. Moreover, since the additional feedback loops are incorporated, the control parameters are difficult to tune due to the different loop bandwidths.

1.4.4 Computational Challenge for High Switching Frequency VSCs

The WBG switching device enables high switching frequency operation, bringing benefits such as improved control bandwidth and reduced current/voltage ripples, smaller filter size requirements, and enhanced system efficiency. Besides, the high-frequency WBG-based integrated motor drive system enjoys less volume and reduced manufacturing cost, which could be potentially used in aerospace, robotics, automobiles, etc [62], [78]–[80]. Hence, with the adoption of SiC and GaN devices, it is desirable to exploit the benefits provided by the high switching frequency. For example, the bulky DC electrolytic capacitors can be replaced by the film capacitor to reduce the total volume and cost of electrical vehicles. Also, the high-speed machines with a larger number of poles bring high power density, which requires a high switching frequency control. The direct approach to increasing the switching frequency of the power converter is to set a higher sampling frequency. However, this way is restricted by multiple factors in practical applications.

The first constraint comes from the analog to digital conversion (ADC) operation. Considering the expense, it will be not convenient to measure, process (digital filter), and store the sampled data at a fast rate for general digital signal processors (DSPs), enlarging the sampling period [81], [82]. As a result, the ADC process consumes a certain time. On the other hand, enough computational margin should be reserved for the controller execution and thus adopting a sampling frequency above 20kHz usually becomes quite challenging. As shown in Fig. 1.7, the digital controller not purely contains the execution stage for the main control algorithm, i.e., MPC, and many peripheral sampling and logic modules are incorporated simultaneously. Therefore, another limiting factor is the busy tasks. As flexibility and scalability are required and the diverse requirement of power converter control should be met, complex control objectives can be achieved by incorporating more specific subfunctions into the framework of the control scheme [83]. For example, to maintain sinusoidal currents under the distorted grid, the harmonic penalization items with

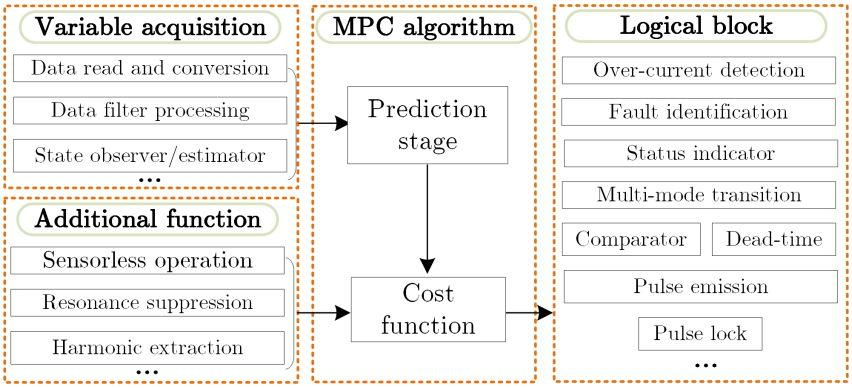

Figure 1.7: The typical interrupt tasks in a digital controller for an MPC-based power converter application.

online discrete Fourier transformation (DFT) are designed into the controller [84]. To suppress the resonance problem of a high-order filter, the AD strategy is accompanied [85]. Besides, to reduce the hardware cost and delay, the alternative observer or estimator works together with the main controller, where the application can be commonly found in the motor drive sensorless control [86]. In addition to the main algorithm, the over-current detection, protection module, multi-mode operation transition, etc., are all necessary components needed to be incorporated in the practical application. As a result, a longer sampling/interrupt (S/I) interval should be ensured to facilitate the easy realization of the tasks in DSPs. With more complex converter topologies, increased switching states, and high-order system modeling, a high sampling frequency becomes more challenging. The fast-speed field-programmable gate arrays (FPGAs) show advantages over DSPs in terms of handling multiple parallel tasks and high sampling operation. However, DSPs still gain wide application in the industry thanks to the C environment programming and simpler debugging stage, which brings shorter development times, especially for advanced control techniques

Therefore, the expected high switching frequency in power converters is always a great challenge for the controller design. The reason is that the S/I interval is too short for a digital processor to accomplish heavy interrupt tasks [62]. Consequently, the benefits provided by the WBG device have not been fully realized in the industry, especially when it is combined with MPC

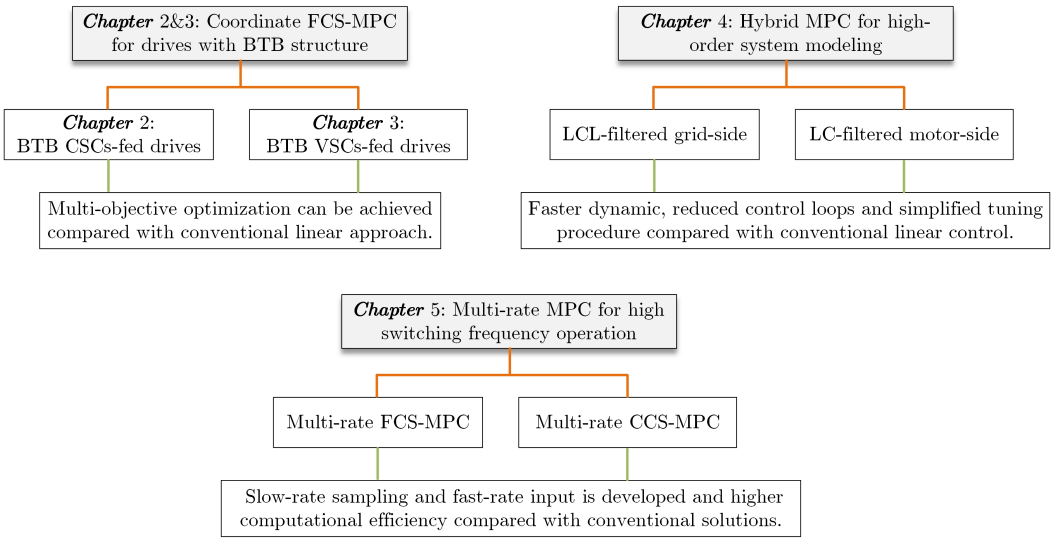

Figure 1.8: Overview of the research structure in this thesis

strategies.

1.5 Research Objectives and Contributions

Conventional linear control shows limitations for high-performance ac drives and increased control loops for drive systems with high-order modeling. On the other hand, existing MPC works have not fully developed their potential for BTB structure optimization and lacked investigation for high-order systems. Therefore, this thesis aims to solve these prominent control problems in the MV CSCs and low-power VSCs-fed VSD systems by proposing improved MPC frameworks, as shown in Fig. 1.8. The main research is developed based on the following three objectives.

1) **The coordinate control by using the FCS-MPC will be designed for the BTB power converters-fed drives to achieve multi-objective optimization.**

Conventional linear control structures show limited performance for BTB systems with multi-objective optimization demand and nonlinear characteristics. Therefore, the FCS-MPC with improved cost function design will be developed for both the BTB CSCs and VSCs-fed motor drives, which are arranged into *chapter 2* and *chapter 3* respectively. The coordinate control for

both the rectifier and inverter side is proposed to optimize multiple objectives simultaneously. Specifically, the cost function will be designed to have better resonance damping, grid-side harmonic rejection, and CM resonance mitigation in transformerless CSCs-fed drives. For the BTB VSCs, the design of the cost function considers the dc-link capacitor current ripple optimization in addition to the power control of two sides, and it is expected to achieve improved results compared to the conventional carrier-based PWM scheme.

2) **The multivariable control property of MPC endows it with great flexibility and scalability to handle the LCL-filtered modeling, which can be developed to achieve faster dynamic and simplified tuning procedures compared to multi-loop linear structure.**

The conventional linear way requires increased control loops for complex system modeling. On the other hand, existing MPC research was mainly reported on the first-order L-filtered power converters and relatively little effort has been applied to the LC/CL/LCL-filtered cases. In this thesis, the multivariable control property of MPC with great flexibility and scalability will be exploited to handle the MIMO modeling. The FCS-MPC and CCS-MPC will be respectively designed for the motor-side and grid-side equipped with high-order filters, which is presented in *chapter 4*. It is thus expected to achieve faster dynamics, reduced control loops, and simplified tuning procedures compared with linear schemes.

3) **The multi-rate MPC with slow-rate sampling information but a fast-rate control input will be developed to reduce the computational difficulty for high switching frequency power converters.**

The high sampling/interrupt frequency for high switching frequency operation becomes a great challenge because such a short period imposes big computational difficulty in the programming code execution. Therefore, *chapter 5* designs the multi-rate technique into the MPC formulation, where the switching frequency can be significantly increased with a low sampling/interrupt frequency. In this case, the quite long interrupt period allows the easy realization of the control algorithm and an abundant computational margin can remain in the digital platform, which will present higher computational efficiency than

conventional ways.

The detailed research objectives and contributions of each chapter are clarified as follows.

In chapter 2, the FCS-MPC will be designed for the CSCs-fed VSD system. Firstly, considering the low switching frequency operation and the multi-objective optimization, the FCS-MPC will be designed for CSR by directly regulating the multi-variable in the second-order system, which can achieve a simplified concept and lower computational burden than the existing virtual-impedance-based FCS-MPC. To main good robustness of the FCS-MPC applied to CSR, the observer will be designed to estimate the lumped disturbance caused by parameter mismatch online. Also, the proposed FCS-MPC will effectively mitigate the low-order harmonics when CSR works under distorted grid conditions with an acceptable computational burden, which can be realized by adding selective harmonic orders of grid current feedback into the controller. On the other hand, when applying the FCS-MPC to the BTB CSCs-fed motor drive, the CMV effect on the CSC system and the CM resonance in both the high-speed region and low-speed region will be analyzed. Then, the cost function will be designed for the power command tracking, filter resonance damping, and CM current suppression simultaneously. Therefore, the size of the CM choke adopted in the transformerless CSCs operation can be smaller due to the reduced CM current.

In chapter 3, the FCS-MPC will be proposed to reduce the capacitor RMS current in the BTB VSCs-fed VSD system, which aims to extend the designed capacitor lifespan or reduce the DC-link size with improved power density. The conventional modulator-based control involves the inherent carrier-based switching operation, and hence the dominant harmonics at carrier frequency multiplier and carrier sideband are introduced into the capacitor current. The synchronous carriers adopted at the two sides can eliminate the carrier frequency multiplier harmonic but the carrier sideband component still remains. Through the proposed FCS-MPC, the direct switching pulse generation without using the carrier can give a distinctive capacitor current spectrum and the possible current pulse cancellation between the VSR and VSI sides can

be conveniently designed through the cost function. Besides, the acceptable grid-current quality and motor performance will be maintained by designing a suitable weighting factor. The simulated and experimental results will be performed to highlight the effectiveness and benefits of the proposed method in terms of capacitor RMS current reduction compared to the synchronous carrier-based scheme and also significant improvements over an existing predictive manner.

In chapter 4, the MPC scheme will be proposed to solve the control problems in the LCL-filtered grid-connected VSCs and the motor-side VSCs equipped with the LC filter. For the grid-connected VSCs application, the CCS-MPC will be designed because of the constant switching frequency, such that the discrete current spectrum can meet the harmonic standard. The cost function can be designed to involve the grid current, inverter-side current, and capacitor voltage tracking, which gives the optimized control law according to the minimization of the cost function. In this process, the weighting factors can be exactly arranged to place the desired closed-loop poles with guaranteed system stability. The hybrid cost function with modified reference will also be proposed to reject the harmonics caused by the unhealthy grid condition. The control delay can be compensated by using the forecast reference and the predictive state variable estimated by the observer. The proposed scheme features multi-variable control properties and it performs the intuitive concept, reduced tuning complexity, and faster dynamic response compared to the existing capacitor current-based AD scheme. On the other hand, for the LC filtered VSCs-fed VSD application, the FCS-MPC will be designed to realize a motor-friendly waveform and overcome the resonance problem effectively. The cost function design will be analyzed in the time domain with the intuitive concept, which regulates the trajectory of multi-variable in the system. The robustness of the controller to parameter variations of the filter will also be verified.

In chapter 5, the multi-rate MPC (MR-MPC) will be developed to solve the computational issue brought by the high switching frequency operation for the WBG switching device. Due to the short computational time, the high

S/I frequency demand is always a great challenge for the DSPs because such a short period imposes a big difficulty in the programming code execution. Therefore, existing MPC schemes are usually applied when the switching frequency is below 20kHz, which cannot exploit the full potential of the WBG power converters. The MR-MPC enables the S/I trigger and switching device transition to be performed at different rates. Compared to the existing MPC schemes, the main feature of the proposed MR-MPC is that the high-dimension control sequence is solved and applied within each S/I interval. As a result, the high switching frequency objective can be easily achieved with a low S/I frequency configuration, which can significantly relieve the execution of the heavy interrupt tasks in DSPs. The multi-rate technique will be applied to both the typical FCS-MPC and the CCS-MPC framework, and the modeling process and solving procedure for the control input will be developed in combination with their respective characteristics. The VSCs-fed VSD system will be taken as the case study to verify the effectiveness and advantage of the proposed MR-MPC schemes.

Chapter 2

FCS-MPC Scheme for Medium-Voltage BTB CSCs-fed Motor Drives

This chapter designs the FCS-MPC for the CSCs-fed PMSM drive system to solve the control problems, including the LC/CL filter resonance, grid-side selective harmonic rejection, and the CM resonance in the transformerless operation. The FCS-MPC framework can address the multiple control objectives simultaneously with the intuitive concept and the direct switching pulse generation manner suits the low switching frequency CSCs.

Firstly, the predictive modeling of both CSR and the CSI-fed PMSM sides will be developed. Subsequently, this chapter proposes an improved FCS-MPC method for high-power CSR, where the predefined cost function directly takes grid-side current and capacitor voltage as the regulating objectives to suppress the LC resonance and grid current distortions. The relationship and differences between the proposed cost function and its form with the AD function are analyzed in detail. Besides, to keep sinusoidal grid current for CSR even working under severely distorted supply voltage, specific harmonic orders of grid current suppression items are added to the proposed cost function. Furthermore, to improve the system robustness to parameter mismatch in CSR, the disturbance observer is designed to estimate the additional capacitor voltage reference and the lumped input disturbance caused by parameter mismatch. Also, the MPC scheme is further assessed by increasing the prediction horizon

length to reveal the resonance principle with different state feedback types.

Secondly, the FCS-MPC scheme is designed to tackle the CM resonance in the transformerless BTB CSCs system. In the low-speed region, besides restraining the PTP magnitude of the CMV at the CSR side, the third-order harmonic of the CMV generated by the CSI is extracted and then penalized in the cost function to further suppress the CM current. With the increase of the motor speed, the control objective of the CSI side controller switches to the PTP magnitude of CMV suppression because of the alleviation of the CM resonance. The capacitor voltage of the CSI side is regulated via the cost function as well, which can mitigate the current harmonic distortion and improve system stability. The simulation with 1MVA rated power and the scaled-down experiment shows the effectiveness of the proposed scheme.

2.1 The Modeling for the BTB CSCs-fed PMSM System

This section builds the discrete modeling equation for the CSR and CSI side respectively and the future state variables of the system can be obtained, which lays the fundamentals for the predictive controller design. The control scheme for the CSR side can be developed under either the stationary $\alpha\beta$ frame or the synchronous dq frame. The control scheme for the motor side is typically developed under the synchronous dq frame.

2.1.1 Predictive Model of the CSR-Side

The main topology of a high-power CSR is depicted in Fig. 2.1. Star-connected grid supplies abc three-phase voltage to the converter through line impedance R_r, input filter L_r and C_{fr} respectively. Large inductive choke L_{dc} is put at the dc-side. S_{1r}, S_{3r}, S_{5r} represent the switching state of three upper switches while S_{4r}, S_{6r}, S_{2r} represent those of three bottom switches in the converter.

The switching state of CSR at any time instant should satisfy the constraint that only two switches conduct, one in the upper half of the bridge and the other in the bottom half of the bridge [27]. Therefore, the single bridge CSR

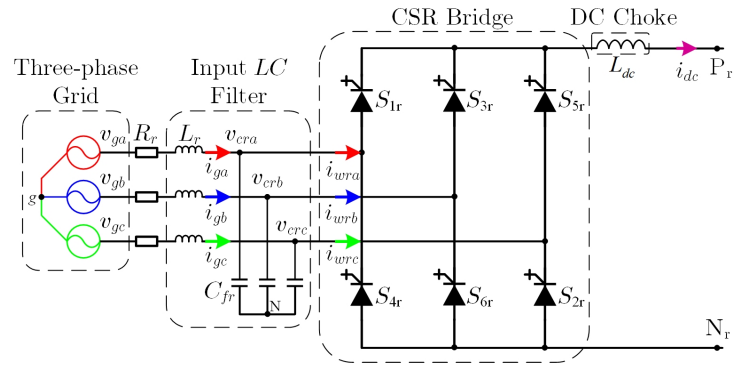

Figure 2.1: Typical configuration of high-power CSR.

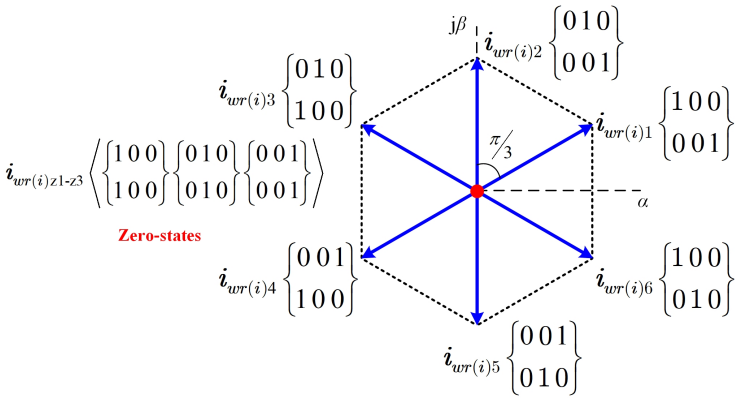

Figure 2.2: Space current vector diagram of CSC in stationary $\alpha\beta$ frame.

can provide nine current vectors, whose switching state are defined as the binary value of $\boldsymbol{I}_{wi}$=[S_{1r} S_{3r} S_{5r}; S_{4r} S_{6r} S_{2r}]. "1" indicates the corresponding switch is on, while "0" indicates the switch is off. The current vectors under stationary $\alpha\beta$ space can be expressed with the switching functions as

$$\boldsymbol{i}_{wr\alpha\beta} = i_{wr\alpha} + j i_{wr\beta} = \frac{2}{3}(i_{wra} + \chi i_{wrb} + \chi^2 i_{wrc}) \tag{2.1}$$

where χ=exp($j\frac{2\pi}{3}$), i_{wra}=(S_{1r}-S_{4r})i_{dc}, i_{wbr}=(S_{3r}-S_{6r})i_{dc} and i_{wcr}=(S_{5r}-S_{2r})i_{dc}. The $\alpha\beta$ space current vectors can be described in Fig. 2.2. According to the former definition, the CSR bridge contains six active vectors and three zero vectors. The space plane pattern is divided into six sectors and the space angle range in each sector is $\frac{\pi}{3}$.

The control strategy for the CSR side can be developed under either the stationary $\alpha\beta$ frame or the synchronous dq frame. The abc three-phase variable ξ_{abc} can be transformed into the variable $\xi_{\alpha\beta}$ under $\alpha\beta$ reference frame by the

Clarke transformation $\xi_{\alpha\beta} = T_{abc2\alpha\beta}\xi_{abc}$, and the matrix $T_{abc2\alpha\beta}$ is

$$T_{abc2\alpha\beta} = \frac{2}{3}\begin{bmatrix} 1 & \frac{1}{2} & -\frac{1}{2} \\ 0 & \frac{\sqrt{3}}{2} & -\frac{\sqrt{3}}{2} \end{bmatrix} \tag{2.2}$$

For the CSR modeling under the $\alpha\beta$ frame, the grid current $\boldsymbol{i_g}$=$[i_{g\alpha}\ i_{g\beta}]^{\mathrm{T}}$ and filter capacitor voltage $\boldsymbol{v_c}$=$[v_{cr\alpha}\ v_{cr\beta}]^{\mathrm{T}}$ are selected as the state variables. According to the Kirchhoff voltage and current laws, the state-space model of the CSR can be described by the following continuous-time equation:

$$\frac{d\boldsymbol{x_g}}{dt} = \mathbf{A_g}\boldsymbol{x_g} + \mathbf{B_g}\boldsymbol{u_g} + \mathbf{E_g}\boldsymbol{v_g} \tag{2.3}$$

where $\boldsymbol{x_g}$=$[i_{g\alpha}\ i_{g\beta}\ v_{cr\alpha}\ v_{cr\beta}]^{\mathrm{T}}$. The input vector is the CSR current $\boldsymbol{u_g}$=$[i_{wr\alpha}\ i_{wr\beta}]^{\mathrm{T}}$ and grid voltage vector is $\boldsymbol{v_g}$=$[v_{g\alpha}\ v_{g\beta}]^{\mathrm{T}}$. The system matrix $\mathbf{A_g}$, input matrix $\mathbf{B_g}$, and disturbance matrix $\mathbf{E_g}$ are given by

$$\mathbf{A_g} = \begin{bmatrix} -\frac{R_r}{L_r} & 0 & -\frac{1}{L_r} & 0 \\ 0 & -\frac{R_r}{L_r} & 0 & -\frac{1}{L_r} \\ \frac{1}{C_{fr}} & 0 & 0 & 0 \\ 0 & \frac{1}{C_{fr}} & 0 & 0 \end{bmatrix}, \mathbf{B_g} = \begin{bmatrix} 0 & 0 \\ 0 & 0 \\ -\frac{1}{C_{fr}} & 0 \\ 0 & -\frac{1}{C_{fr}} \end{bmatrix}, \mathbf{E_g} = \begin{bmatrix} \frac{1}{L_r} & 0 \\ 0 & \frac{1}{L_r} \\ 0 & 0 \\ 0 & 0 \end{bmatrix} \tag{2.4}$$

According to the zero-order hold (ZOH) principle, the continuous-time equation (2.3) can be discretized to obtain the predictive state equation as

$$\boldsymbol{x_g}(k+1) = \mathbf{G_g}\boldsymbol{x_g}(k) + \mathbf{H_g}\boldsymbol{u_g}(k) + \mathbf{F_g}\boldsymbol{v_g}(k) \tag{2.5}$$

where $\mathbf{G_g}$=exp($\mathbf{A_g}T_s$), $\mathbf{H_g}$=($\mathbf{G_g}$-$\mathbf{I_g}$)$\mathbf{A_g}^{-1}\mathbf{B_g}$, $\mathbf{F_g}$=($\mathbf{G_g}$-$\mathbf{I_g}$)$\mathbf{A_g}^{-1}\mathbf{E_g}$ and $\mathbf{I_g}$ is the identity matrix with the same dimension of $\mathbf{G_g}$. T_s denotes the sampling time. Considering the one-step delay in the digital controller, the prediction of the state variable should move forward by one step correspondingly [87], i.e., the predictive variable at $(k$+2$)th$ instant will be evaluated in the cost function.

The $\alpha\beta$ stationary variable can be transformed into the dq reference frame, i.e., $\xi_{dq} = T_{\alpha\beta2dq}\xi_{\alpha\beta}$, and the matrix $T_{\alpha\beta2dq}$ is

$$T_{\alpha\beta2dq} = \begin{bmatrix} \cos\theta_e & \sin\theta_e \\ -\sin\theta_e & \cos\theta_e \end{bmatrix} \tag{2.6}$$

where θ_e can be the electrical angle of the grid voltage or the motor rotor position. In dq frame, the three-phase quantities would have constant value under

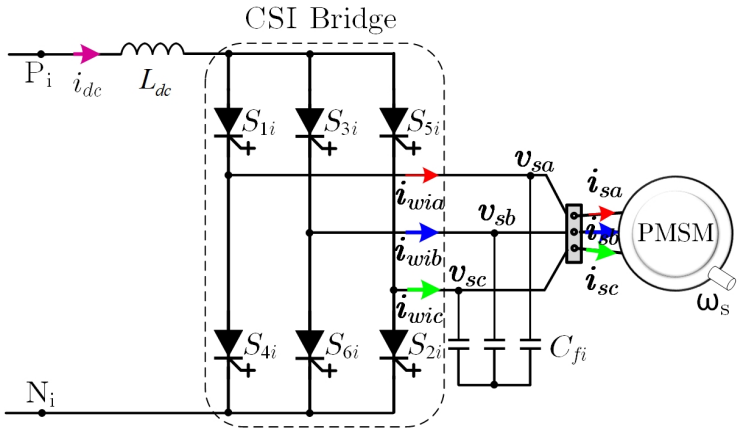

Figure 2.3: Typical configuration of CSI-fed PMSM.

steady-state. The dynamic modeling of the CSR system can be described in the synchronous dq frame as

$$\frac{d\boldsymbol{x_{gdq}}}{dt} = \mathbf{A_{gdq}}\boldsymbol{x_{gdq}} + \mathbf{B_g}\boldsymbol{u_{gdq}} + \mathbf{E_g}\boldsymbol{v_{gdq}} \tag{2.7}$$

where the state vector $\boldsymbol{x_{gdq}}$=$[i_{gd}\ i_{gq}\ v_{crd}\ v_{crq}]^{\mathrm{T}}$, input vector $\boldsymbol{u_{gdq}}$=$[i_{wrd}\ i_{wrq}]^{\mathrm{T}}$ and grid vector $\boldsymbol{v_{gdq}}$=$[v_{gd}\ v_{gq}]^{\mathrm{T}}$. The system matrix $\mathbf{A_{gdq}}$ under the dq frame is expressed as follows.

$$\mathbf{A_{gdq}} = \begin{bmatrix} -\frac{R_r}{L_r} & \omega_g & -\frac{1}{L_r} & 0 \\ -\omega_g & -\frac{R_r}{L_r} & 0 & -\frac{1}{L_r} \\ \frac{1}{C_{fr}} & 0 & 0 & \omega_g \\ 0 & \frac{1}{C_{fr}} & -\omega_g & 0 \end{bmatrix} \tag{2.8}$$

2.1.2 Predictive Model of the CSI-fed PMSM Side

Fig. 2.3 shows the detailed configuration of the CSI-fed PMSM system. For the surface-mounted PMSMs, the dynamic model of stator current $\boldsymbol{i_s}$=$[i_{sd}\ i_{sq}]^{\mathrm{T}}$ in the dq reference frame is expressed as:

$$\begin{cases} \frac{di_{sd}}{dt} = \frac{1}{L_s}(v_{sd} - R_s i_{sd} + \omega_s L_s i_{sq}) \\ \frac{di_{sq}}{dt} = \frac{1}{L_s}(v_{sq} - R_s i_{sq} - \omega_s L_s i_{sd} - \omega_s \psi_f) \end{cases} \tag{2.9}$$

where R_s is the stator resistor and ψ_f represents the magnitude of rotor flux ψ_r. ω_s is the electrical angular velocity and can be obtained through the encoder. $\boldsymbol{v_s}$=$[v_{sd}\ v_{sq}]^{\mathrm{T}}$ represents the stator voltage vector. For the CSI side,

the dynamic model of the CL filter can be expressed as

$$\begin{cases} \frac{dv_{sd}}{dt}=\frac{1}{C_{fi}}\left(i_{wid}-i_{sd}+\omega_s C_{f_i} v_{sq}\right) \\ \frac{dv_{sq}}{dt}=\frac{1}{C_{fi}}\left(i_{wiq}-i_{sq}-\omega_s C_{f_i} v_{sd}\right) \end{cases} \tag{2.10}$$

Based on (2.9) and (2.10), the state-space model of the CSI-fed PMSM in continuous time-domain can be summarized as

$$\frac{d\boldsymbol{x_s}}{dt} = \mathbf{A_s}\boldsymbol{x_s} + \mathbf{B_s}\boldsymbol{u_s} + \mathbf{E_s} \tag{2.11}$$

where the state vector $\boldsymbol{x_s}$=$[i_{sd}\ i_{sq}\ v_{sd}\ v_{sq}]^{\mathrm{T}}$. The input vector refers to the CSI current $\boldsymbol{u_s}$=$[i_{wid}\ i_{wiq}]^{\mathrm{T}}$. The input vector $\boldsymbol{u_s}$ is determined by the dc-link current and the applied switching state of CSI side. The time-varying system matrix $\mathbf{A_s}$, input matrix $\mathbf{B_s}$ and disturbance matrix $\mathbf{E_s}$ are given by

$$\mathbf{A_s} = \begin{bmatrix} -\frac{R_s}{L_s} & \omega_s & \frac{1}{L_s} & 0 \\ -\omega_s & -\frac{R_s}{L_s} & 0 & \frac{1}{L_s} \\ -\frac{1}{C_{fi}} & 0 & 0 & \omega_s \\ 0 & -\frac{1}{C_{fi}} & -\omega_s & 0 \end{bmatrix}, \mathbf{B_s} = \begin{bmatrix} 0 & 0 \\ 0 & 0 \\ \frac{1}{C_{fi}} & 0 \\ 0 & \frac{1}{C_{fi}} \end{bmatrix}, \mathbf{E_s} = \begin{bmatrix} 0 \\ -\frac{\omega_s}{L_s}\psi_f \\ 0 \\ 0 \end{bmatrix} \tag{2.12}$$

Likewise, the continuous-time equation (2.11) can be discretized to obtain the predictive form (2.13) with the assumption that the input $\boldsymbol{u_s}$ is constant during each control interval.

$$\boldsymbol{x_s}(k+1) = \mathbf{G_s}\boldsymbol{x_s}(k) + \mathbf{H_s}\boldsymbol{u_s}(k) + \mathbf{F_s} \tag{2.13}$$

where $\mathbf{G_s}$=exp($\mathbf{A_s}T_s$), $\mathbf{H_s}$=($\mathbf{G_s}$-$\mathbf{I_s}$)$\mathbf{A_s}^{-1}\mathbf{B_s}$, $\mathbf{F_s}$=($\mathbf{G_s}$-$\mathbf{I_s}$)$\mathbf{A_s}^{-1}\mathbf{E_s}$ and $\mathbf{I_s}$ is the identity matrix with the same dimension of $\mathbf{G_s}$. Also, the predictive variable at $(k+1)th$ instant will be compensated and then the cost function of the CSI side will evaluate the predictive information $\boldsymbol{x_s}(k+2)$.

2.2 FCS-MPC Scheme for CSR-Side Under Normal and Distorted Gird Conditions

This section designs and improves the FCS-MPC for the CSR side under the stationary $\alpha\beta$ frame. The prominent control problems, including the LC filter resonance and grid-side harmonic rejection, are solved. A comparison with the existing predictive scheme with the AD function is performed to show the enhancement of the proposed control.

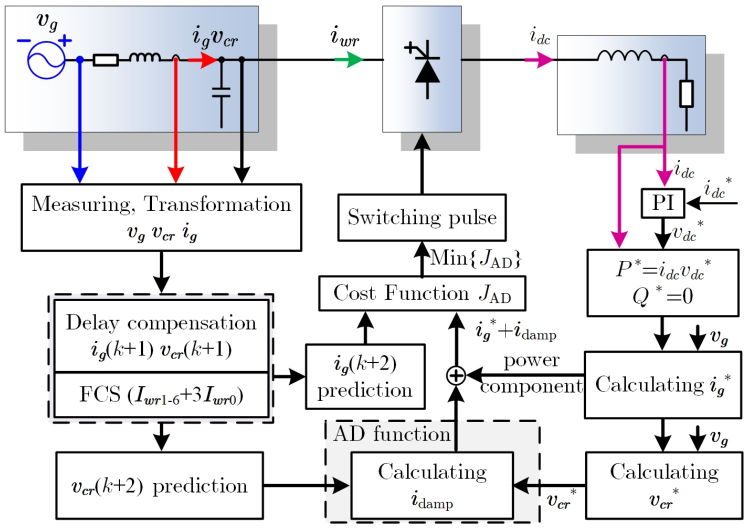

Figure 2.4: The diagram of FCS-MPC$_{\mathrm{AD}}$ scheme for CSR.

2.2.1 Existing FCS-MPC With Active Damping Function

The CSR features the second-order characteristic and multivariable feedback is necessary to suppress the LC filter resonance. In [88], the very basic form of FCS-MPC has been applied to CSR without considering the LC resonance issue. In [89], a modified FCS-MPC is analyzed to achieve the maximum achievable input power factor, and an extended predictive control version of grid-side current by including an AD current reference is proposed. The damping current reference is derived by the means of the AD notion and is calculated by the division between harmonic components of capacitor voltage and pre-defined virtual resistor.

The control flowchart diagram of the FCS-MPC algorithm with AD function (denoted as FCS-MPC$_{\mathrm{AD}}$) for CSR is shown in Fig. 2.4 and is executed under the stationary $\alpha\beta$ frame. The predictive control scheme is performed in the following steps.

1) Measuring the grid voltages, capacitor voltage, and grid current at kth sampling instant;

2) One-step delay is compensated by calculating the grid currents at $(k+1)$th sampling instant, and then predicting the grid currents at $(k+2)$th sampling instant for all candidate current vectors in the control set (nine current vec-

tors);

3) Evaluating the cost function value J_{AD} for each prediction result;

4) Choosing the best current vector with the minimum value of J_{AD} as the output to control the switching devices.

Once the prediction model and control horizons are determined, the cost function remains the only tuning tool to control the future behavior of the converter. In [89], to dampen the parallel LC resonance, the cost function J_{AD} is designed as

$$\begin{aligned} J_{\mathrm{AD}} = &\left[\boldsymbol{i}_{\boldsymbol{g}}^{*}+\boldsymbol{i}_{\mathbf{damp}}-\boldsymbol{i}_{\boldsymbol{g}}(k+2)\right]^{\mathrm{T}}\left[\boldsymbol{i}_{\boldsymbol{g}}^{*}+\boldsymbol{i}_{\mathbf{damp}}-\boldsymbol{i}_{\boldsymbol{g}}(k+2)\right]+ \\ &\lambda_{sfr}\left|\boldsymbol{I}_{\boldsymbol{wr}}(k+1)-\boldsymbol{I}_{\boldsymbol{wr}}(k)\right| \end{aligned} \tag{2.14}$$

where $\boldsymbol{i}_{\boldsymbol{g}}^{*}=[i_{g\alpha}^{*}\ i_{g\beta}^{*}]^{\mathrm{T}}$ is the grid current reference vector. The cost function consists of two terms. The first term penalizes the predicted grid current error at the $(k+2)th$ instant quadratically. The second term penalizes the switching effort between two consecutive instants to reduce switching frequency. The positive weighting factor λ_{sfr} is a tunable parameter that adjusts the trade-off between the grid current tracking accuracy and the switching frequency. The active power reference P^{*} comes from the PI regulator of dc-link current and reactive power reference Q^{*} is usually set at zero to achieve unity power factor. According to the generalized equation for instantaneous power calculation at the grid-side [90], the reference value of grid current can be derived respectively as follows

$$\begin{cases} i_{g\alpha}^{*} = \frac{2}{3}\frac{P^{*}v_{g\alpha}+Q^{*}v_{g\beta}}{v_{g\alpha}^{2}+v_{g\beta}^{2}} \\ i_{g\beta}^{*} = \frac{2}{3}\frac{P^{*}v_{g\beta}-Q^{*}v_{g\alpha}}{v_{g\alpha}^{2}+v_{g\beta}^{2}} \end{cases} \tag{2.15}$$

In the conventional AD scheme [45], the HPF is indispensably used to extract the harmonic component of capacitor voltage, which is then divided by the pre-defined virtual resistor to calculate $\boldsymbol{i}_{\mathbf{damp}}$. The benefit of FCS-MPC$_{\mathrm{AD}}$ proposed in [89] is that it avoids using HPF, and deriving the damping current reference as follows

$$\boldsymbol{i}_{\mathbf{damp}} = \frac{\boldsymbol{v}_{\boldsymbol{cr}}(k+1)-\boldsymbol{v}_{\boldsymbol{cr}}^{*}}{R_{\mathrm{damp}}} \tag{2.16}$$

Since $\boldsymbol{v}_{\boldsymbol{cr}}^{*}$ represents the fundamental reference value of capacitor voltage, it

can be calculated according to

$$\begin{cases} v^*_{cr\alpha} = v_{g\alpha} + \omega_g L_{fr} i^*_{g\beta} \\ v^*_{cr\beta} = v_{g\beta} - \omega_g L_{fr} i^*_{g\alpha} \end{cases} \tag{2.17}$$

where ω_g is the grid angular frequency, R_{damp} should be selected appropriately since large R_{damp} cannot achieve the desired damping effects while small R_{damp} will cause an unstable system [27].

FCS-MPC$_{\text{AD}}$ uses the same principle with the convention AD notion by emulating a virtual resistor in parallel with the capacitor. It introduces the damping current component into the fundamental current reference, which may affect the actual power tracking accuracy and deteriorate the steady performance of CSR especially when it works at a low switching frequency.

2.2.2 Proposed Cost Function With Direct Feedback

The proposed FCS-MPC scheme utilizes the inherent advantage of FCS-MPC that several state variables can be simultaneously controlled via a single cost function. To this end, the capacitor voltage reference tracking is included in the cost function directly in addition to the grid current power reference tracking, which is shown as

$$J_{\text{proposed}} = \left[\boldsymbol{x}^*_{\boldsymbol{g}} - \boldsymbol{x}_{\boldsymbol{g}}(k+2)\right]^{\text{T}} \mathbf{W} \left[\boldsymbol{x}^*_{\boldsymbol{g}} - \boldsymbol{x}_{\boldsymbol{g}}(k+2)\right] + \lambda_{sfr} \left|\boldsymbol{I}_{\boldsymbol{wr}}(k+1) - \boldsymbol{I}_{\boldsymbol{wr}}(k)\right| \tag{2.18}$$

where the reference vector $\boldsymbol{x}^*_{\boldsymbol{g}}$=$[i^*_{g\alpha}\ i^*_{g\beta}\ v^*_{cr\alpha}\ v^*_{cr\beta}]^{\text{T}}$. The predictive state variable can be obtained through discrete modeling (2.3). The weighting factor matrix $\mathbf{W}$ assigns different penalized priorities between the grid current and capacitor voltage, and

$$\mathbf{W} = \begin{bmatrix} 1 & 0 & 0 & 0 \\ 0 & 1 & 0 & 0 \\ 0 & 0 & \lambda_{v_{cr}} & 0 \\ 0 & 0 & 0 & \lambda_{v_{cr}} \end{bmatrix} \tag{2.19}$$

The positive weighting factor $\lambda_{v_{cr}}$ is a tunable parameter that adjusts the trade-off between the capacitor voltage reference tracking accuracy and other items. Comparing J_{proposed} and J_{AD}, it can be found that both grid current and capacitor voltage are predicted and controlled in these two cost functions.

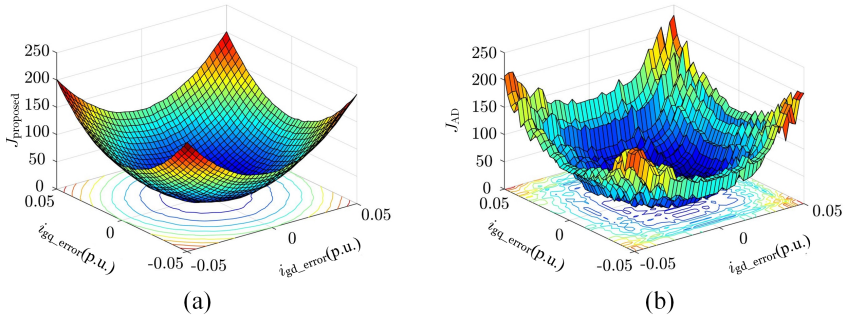

Figure 2.5: Geometrical representations of the cost functions (depicted for a typical 1MVA CSR system). (a)J_{proposed}. (b)J_{AD}.

In addition, by substituting (2.16) into (2.14), the reciprocal value of virtual resistor $1/R_{\text{damp}}$ in (2.14) can be also treated as a kind of weighting factor, and then (2.14) looks equivalent to (2.18). However, there are some key differences between them.

In (2.14), the damping current $\boldsymbol{i}_{\mathbf{damp}}$ represents the harmonic component of capacitor voltage scaled by R_{damp} and is added to the fundamental current reference, which implies a coupling relationship exists between fundamental reference tracking and harmonic component since the first item penalizes the predicted current error quadratically. Therefore, $\boldsymbol{i}_{\mathbf{damp}}$ will always interfere with fundamental reference tracking. On the contrary, the second item in (2.18) implies that the harmonic component of capacitor voltage would be suppressed as small as possible, where the fundamental and harmonic components are controlled independently. Moreover, ignoring the switching effort in these two cost functions firstly, Fig. 2.5 gives the contour map of J_{proposed} and J_{AD} with respect to dq-axis grid currents by keeping the same weighting coefficients for the capacitor voltage to achieve the equivalent comparison, i.e. $\lambda_{v_{cr}}=1/R_{\text{damp}}^2$. It is seen that the cost functions of these two controllers are not equivalent, despite the switching cost. This difference is illustrated by the different shapes of their corresponding contour lines. It can be seen that the proposed cost function can achieve a very smooth shape, whereas the contour map of cost function J_{AD} looks spiky (lots of local solutions). Furthermore, it can be seen that the overall cost value in J_{AD} is larger than that of J_{proposed}, especially when the current tracking error is larger.

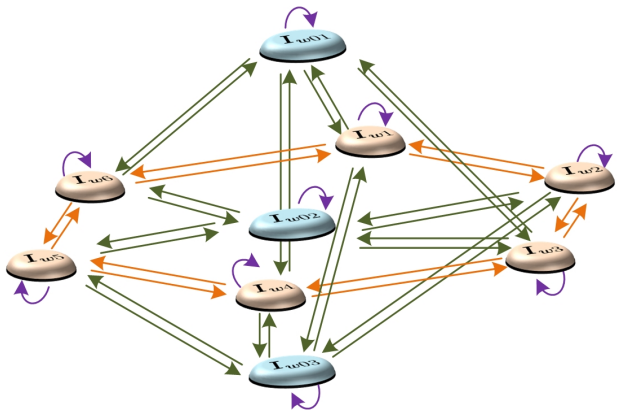

Figure 2.6: Demonstration for switching state transition in the proposed FCS-MPC.

To avoid large di/dt in CSR, the number of switching state changes in CSR should be reduced as much as possible during each commutation, which implies that only one switch can be switched at most or without any switching action. Therefore, according to the transition rules for switching states in Fig. 2.6, only five current vectors are taken into the FCS at the next predictive horizon. Thus, the number of enumeration execution times in the proposed FCS-MPC can be reduced consequently, which relieves the computational burden. For example, if the switching state in kth sampling interval is $\boldsymbol{i_{wr1}}$, then the FCS in the next sampling interval is determined as $\boldsymbol{I_{wr1}}$, $\boldsymbol{I_{wr2}}$, $\boldsymbol{I_{wr6}}$, and two zero vectors $\boldsymbol{I_{wr01}}$, $\boldsymbol{I_{wr03}}$. Another benefit of following the graph in Fig. 2.6 is that the maximum average switching frequency can be restricted as well.

For the implementation of the proposed FCS-MPC, a full-order observer for CSR can be taken to estimate the capacitor voltage $\boldsymbol{v_{cr}}$, thus reducing the number of voltage sensors. The full-order observer is similar to those used to estimate load current in [91] and stator flux of motor in [92]. The observer mainly introduces the sampling error feedback of grid current based on the measured output, thus realizing noise rejection and improving the accuracy of estimation and prediction for the control algorithm. According to the state space model in (2.3), the capacitor voltage observer can be expressed as

$$\begin{cases} \frac{d\boldsymbol{x_{ob}}}{dt} = \mathbf{A_g}\boldsymbol{x_{ob}} + \mathbf{B_g}\boldsymbol{u_g} + \mathbf{E_g}\boldsymbol{v_g} - \mathbf{L}(\boldsymbol{y_g} - \boldsymbol{y_{ob}}) \\ \boldsymbol{y_{ob}} = \mathbf{C}\boldsymbol{x_{ob}} \end{cases} \tag{2.20}$$

where, $\boldsymbol{y_g}$=$\mathbf{C}\boldsymbol{x_g}$ and $\mathbf{C}$=[1 0 0 0; 0 1 0 0]; $\boldsymbol{x_{ob}}$=$[i_{g\alpha\_ob}\ i_{g\beta\_ob}\ v_{cr\alpha\_ob}\ v_{cr\beta\_ob}]^{\mathrm{T}}$

is the observed variables and $\boldsymbol{y_{ob}}$ is the output of the designed observer. $\mathbf{L}$ represents the feedback gain matrix for sampling error, which is 4×2 order matrix. The linear quadratic (LQ) optimal principle [93] can be employed to determine $\mathbf{L}$ with a guaranteed stability margin, thus $\mathbf{L}$ can be calculated offline according to

$$\mathbf{L} = -\mathbf{P}\mathbf{C}^{\mathrm{T}}\mathbf{R}^{-1} \tag{2.21}$$

Here $\mathbf{P}$ can be derived by solving the Riccati equation, i.e.

$$\mathbf{A_g}\mathbf{P} + \mathbf{P}\mathbf{A_g}^{\mathrm{T}} - \mathbf{P}\mathbf{C}^{\mathrm{T}}\mathbf{R}^{-1}\mathbf{C}\mathbf{P} + \mathbf{Q} = \mathbf{0} \tag{2.22}$$

$\mathbf{Q}$ and $\mathbf{R}$ are positive definite diagonal matrices and represent the weighting values on the state variables and inputs respectively. Therefore, $\mathbf{Q}$ and $\mathbf{R}$ need to be tuned to ensure the control system achieves satisfactory performance. Assuming $\boldsymbol{x_d}$ is the deviation between the actual value and the observed value of state variables respectively, i.e. $\boldsymbol{x_d}$=$\boldsymbol{x_g}$-$\boldsymbol{x_{ob}}$, therefore, the dynamic model for error vector $\boldsymbol{x_d}$ can be derived as follows according to (2.3) and (2.20).

$$\frac{d\boldsymbol{x_d}}{dt} = (\mathbf{A_g} + \mathbf{L}\mathbf{C})\boldsymbol{x_d} \tag{2.23}$$

The Lyapunov function-based analysis is used to prove the stability of the observer [93]. Define the energy function as

$$E_{\mathrm{LF}} = \boldsymbol{x_d}^{\mathrm{T}}\mathbf{P}^{-1}\boldsymbol{x_d} \tag{2.24}$$

which shows that E_{LF} is positive definite and then the derivative of E_{LF} can be calculated as

$$\begin{aligned}
\tfrac{dE_{\mathrm{LF}}}{dt} &= \tfrac{d\boldsymbol{x_d}^{\mathrm{T}}\mathbf{P}^{-1}\boldsymbol{x_d}}{dt} = \tfrac{d\boldsymbol{x_d}^{\mathrm{T}}}{dt}\mathbf{P}^{-1}\boldsymbol{x_d} + \boldsymbol{x_d}^{\mathrm{T}}\mathbf{P}^{-1}\tfrac{d\boldsymbol{x_d}}{dt} \\
&= \boldsymbol{x_d}^{\mathrm{T}}\mathbf{P}^{-1}(\mathbf{P}\mathbf{A_g}^{\mathrm{T}} + \mathbf{A_g}\mathbf{P} - 2\mathbf{P}\mathbf{C}^{\mathrm{T}}\mathbf{R}^{-1}\mathbf{C}\mathbf{P})\mathbf{P}^{-1}\boldsymbol{x_d} \\
&\leq -\boldsymbol{x_d}^{\mathrm{T}}\mathbf{P}^{-1}\mathbf{Q}\mathbf{P}^{-1}\boldsymbol{x_d}
\end{aligned} \tag{2.25}$$

It can be seen that the derivative of E_{LF} is always negative definite, which implies that the observer is asymptotically stable.

Fig. 2.7 demonstrates the proposed FCS-MPC scheme for CSR under normal grid conditions. Compared to the conventional FCS-MPC$_{\mathrm{AD}}$ scheme in Fig. 2.4, the simple structure under normal grid operations is reserved. Thanks

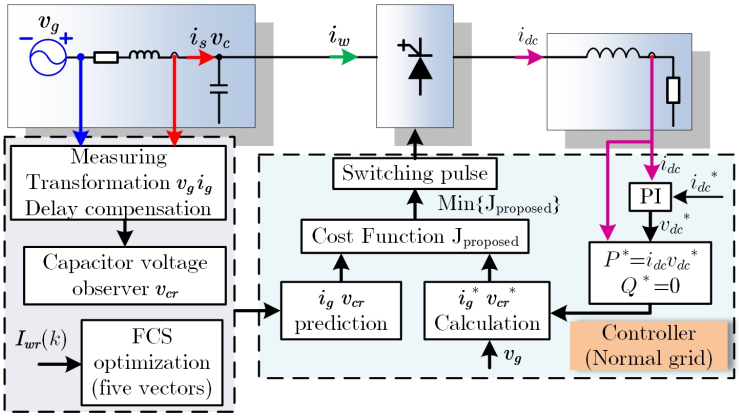

Figure 2.7: The diagram of proposed FCS-MPC scheme for CSR.

to the inherent advantage of FCS-MPC, multi-objectives can be managed by a single cost function. For the proposed cost function (2.18), $\lambda_{v_{cr}}$ can be turned firstly to obtain a satisfactory damping effect for resonance, and $\lambda_{v_{cr}}$=$1/R_{\text{damp}}^2$ guides the design of $\lambda_{v_{cr}}$ as well. Then, the desired average switching frequency can be reached by gradually increasing λ_{sfr}.

2.2.3 Proposed Cost Function With Selective Harmonic Rejection

The power quality of the grid voltage supply will influence the performance of CSR directly, where specific harmonic orders of series resonance will be excited in grid current easily (for example 5^{th} or 7^{th} harmonic). Although the control scheme taking grid current and capacitor voltage as the feedback can effectively suppress the resonance from the CSR side, more suitable and reliable strategies should be considered to furthermore improve the waveform quality of grid currents under distorted grid voltage conditions. For the FCS-MPC under distorted grid conditions with dominant 5^{th} and 7^{th} supply harmonic voltage, a modified cost function is employed to take the fundamental current reference tracking, capacitor voltage reference tracking, and selective current harmonic suppression items to reduce grid current distortion and thus improving the

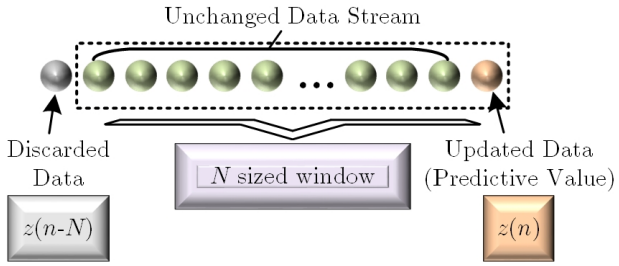

Figure 2.8: Realizing process of SDFT in the digital controller.

waveform quality, which is shown as

$$J_{\text{distorted\_grid}} = \left[\boldsymbol{x}^*_{\textbf{g\_distorted}} - \boldsymbol{x_g}(k+2)\right]^{\mathrm{T}} \mathbf{W} \left[\boldsymbol{x}^*_{\textbf{g\_distorted}} - \boldsymbol{x_g}(k+2)\right] + \sum_{H}^{5,7} \lambda_{i_{gH}} \left[|\boldsymbol{i_{gH}}(k+2)|\right]^2 + \lambda_{sfr} \left|\boldsymbol{I_{wr}}(k+1) - \boldsymbol{I_{wr}}(k)\right| \tag{2.26}$$

where the reference vector $\boldsymbol{x}^*_{\textbf{g\_distorted}}=[i^*_{g\alpha F}\ i^*_{g\beta F}\ v^*_{cr\alpha}\ v^*_{cr\beta}]^{\mathrm{T}}$ and $i^*_{g\alpha F}$ and $i^*_{g\beta F}$ represent the fundamental grid current reference. The selective harmonic current suppression item can be seen as additional feedback in the controller and will improve the grid current waveform quality furthermore.

The harmonic current prediction can be realized by employing the sliding discrete Fourier transformation (SDFT) technique [94], which is suitable for real-time implementation with acceptable computational cost. The principle of SDFT is based on DFT but with the help of a constant N-sized sliding window, the large unnecessary calculation can be avoided since the window serves as a storage buffer for the sampling signal. During each sampling interval, the first data in the window is discarded and the new predictive value enters the window, which implies that only two data points are updated for each SDFT operation during the predictive horizon, then according to the recursive equation, i.e.,

$$S_h(n) = S_h(n-1)e^{j\frac{2\pi h}{N}} - z(n-N) + z(n) \tag{2.27}$$

the predictive harmonic components of the desired signal z can be extracted in real-time. The $S_h(n)$ represents the new spectral component and $S_h(n\text{-}1)$ represents the previous one. z is the input signal and h is a positive integer which refers to the extracted harmonic order of z. The attractive feature

of SDFT is the sliding window employed during each control interval. With the recursive relationship between the updated data and previous data, the realization process for SDFT in the DSPs is relatively easy to be programmed, which is shown in Fig. 2.8. The computational burden is independent of N and (2.27) is only executed once for each signal with only two data updated. In addition, the exponent item $e^{j\frac{2\pi h}{N}}$ can be calculated offline since h and N are both determined in advance.

Under the distorted grid conditions, the control objective is still to obtain sinusoidal current with fundamental grid frequency, and the harmonic voltage will not generate real power since fundamental current and harmonic voltage have different frequencies. Therefore, according to the instantaneous power reference and fundamental component of grid voltage, the reference fundamental current can be calculated as follows.

$$\begin{cases} i^*_{g\alpha F} = \frac{2}{3}\frac{P^* v_{g\alpha F} + Q^* v_{g\beta F}}{v^2_{g\alpha F} + v^2_{g\beta F}} \\ i^*_{g\beta F} = \frac{2}{3}\frac{P^* v_{s\beta F} - Q^* v_{g\alpha F}}{v^2_{g\alpha F} + v^2_{g\beta F}} \end{cases} \tag{2.28}$$

Here the grid fundamental voltage is also measured by the SDFT technique.

Fig. 2.9(a) demonstrates the proposed FCS-MPC scheme for CSR under the distorted grid condition. It is worth mentioning that the magnitude of grid harmonic component $|\boldsymbol{v_{gH}}|$ can be utilized to distinguish whether the grid condition is healthy or distorted, and subsequently decide which controller should be selected, as shown in Fig. 2.9(b).

2.2.4 Simulation and Experimental Results

The proposed FCS-MPC under the $\alpha\beta$ frame is firstly verified to illustrate its effectiveness under normal and distorted grid conditions respectively. A 1-MVA CSR system with typical parameters in Table 2.1 [27] is adopted in MATLAB/Simulink. The proportional gain and integral gain of the outer PI regulator are set as 5 and 500 respectively. The resonance damping effect shown in [27] concludes a rule that R_{damp} for high-power CSR should not be lower than 1.0p.u. Therefore R_{damp} is selected empirically as 2p.u. in [89], which is employed for conventional FCS-MPC$_{\text{AD}}$ as well. Moreover, white

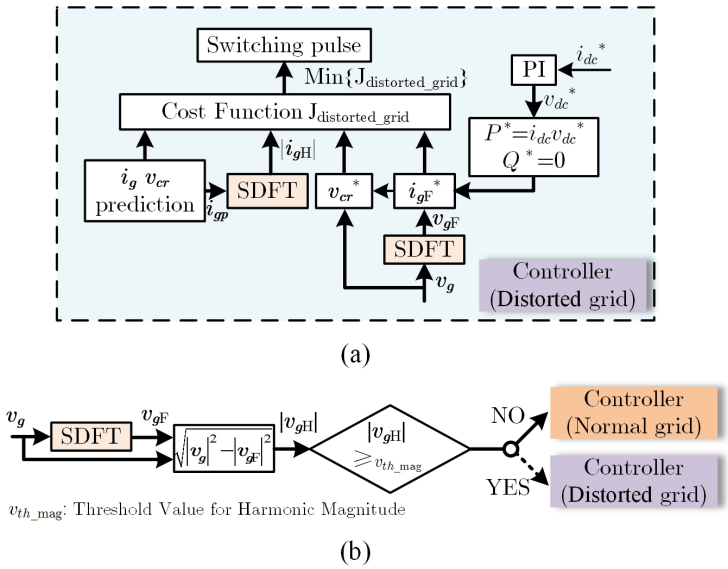

Figure 2.9: Proposed FCS-MPC scheme for CSR. (a) Control stage under distorted grid conditions. (b) Mechanism to detect the distorted grid and shift control.

Gaussian noise is added to the sampling process of grid voltage and current.

Table 2.1: Simulated parameters of the CSR System

Parameters	Simulated value	Experimental value
Rated power	1MVA	10kVA
Rated line to line voltage	4160V60Hz	208V60Hz
Filter inductor	0.1p.u.	0.15p.u.
Filter capacitor	0.4p.u.	0.26p.u.
Line resistor	0.03p.u.	0.1p.u.
DC-link inductor	1.96p.u.	1.74p.u.
DC load resistor	1p.u.	2p.u.
Resonance frequency	300Hz.	300Hz.
Virtual damping resistor	2p.u.	2p.u.

Fig. 2.10 shows the waveforms of phase a grid current for FCS-MPC$_{\mathrm{AD}}$ and proposed FCS-MPC scheme respectively and corresponding frequency spectrum analysis results based on fast Fourier transformation (FFT). The relationship $\lambda_{v_{cr}}=1/R_{\mathrm{damp}}^2$ is kept to achieve an equivalent comparison between these two schemes. Both these two control schemes can suppress the LC resonance in CSR effectively. Since the switching frequency is kept at 1kHz by adjusting weighting factor λ_{sfr}, relatively superior grid current performances

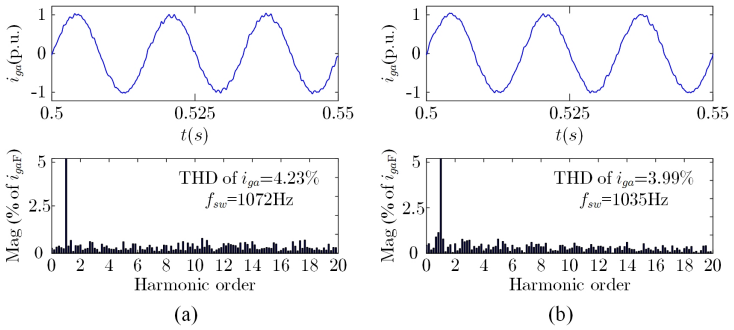

Figure 2.10: Simulated comparison of grid currents (phase a) and corresponding FFT analysis with 1kHz switching frequency. (a) FCS-MPC$_{\mathrm{AD}}$. (b) Proposed FCS-MPC.

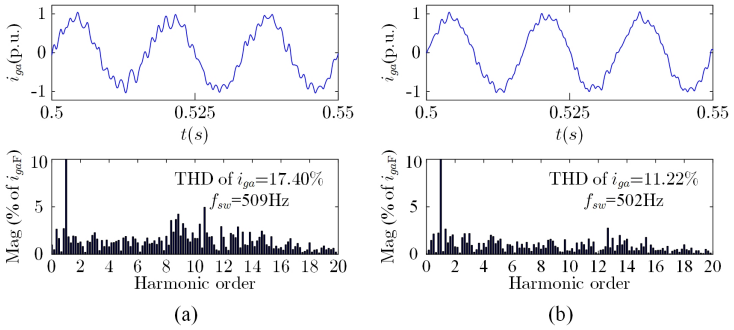

Figure 2.11: Simulated comparison of grid currents (phase a) and corresponding FFT analysis with 500Hz switching frequency. (a) FCS-MPC$_{\mathrm{AD}}$. (b) Proposed FCS-MPC.

are achieved and the fundamental total harmonic distortion (THD) for these two schemes are similar, i.e, 4.33% and 3.99% respectively.

Fig. 2.11 shows the performance of phase a grid current for FCS-MPC$_{\mathrm{AD}}$ and the proposed FCS-MPC scheme when the switching frequency is reduced to 500Hz. It is observed that the grid current waveform and its harmonic spectrum using the proposed FCS-MPC scheme are superior to those of the adopted FCS-MPC$_{\mathrm{AD}}$ under the same switching frequency, which has verified the proposed cost function (2.18) is better than (2.14) with the lower switching frequency. Besides, the cost function (2.18) is more intuitive with lower design complexity.

Fig. 2.12 shows the grid current waveform of the proposed FCS-MPC under distorted grid conditions. Two cases are presented, i.e. grid voltage contains 10% 5^{th} harmonic (resonant frequency), and the other case contains 5% 5^{th} harmonic with 3% 7^{th} harmonic. It is clearly that dominant 5^{th} and 7^{th}

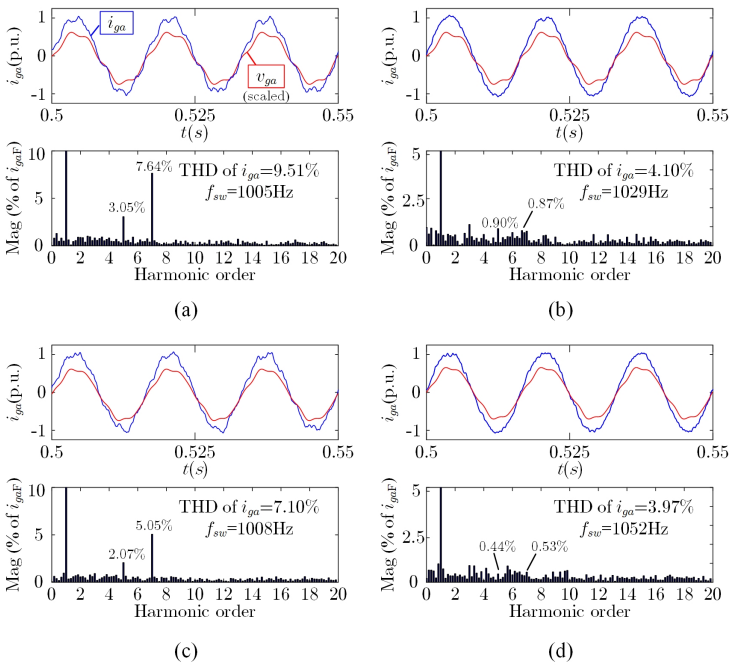

Figure 2.12: Simulated comparison of grid currents and FFT analysis under grid harmonic voltage. (a) 10% 5^{th} harmonic with normal grid controller. (b) 10% 5^{th} harmonic with distorted grid controller. (c) 5% 5^{th} harmonic and 3% 7^{th} harmonic with normal grid controller. (d) 5% 5^{th} harmonic and 3% 7^{th} harmonic with distorted grid controller.

current harmonics are eliminated apparently by adding the selective harmonic penalization item into the cost function, i.e., (2.26). Therefore, it confirms that sinusoidal currents still can be obtained with the proposed controller under distorted grid conditions.

Fig. 2.13 shows the magnitude of 5^{th} and 7^{th} harmonic components of grid current over test time under supply voltage containing 10% 5^{th} harmonic. From 0s to 1s, CSR works under normal grid operation, and the 5^{th} and 7^{th} harmonics are relatively apparent, and thus the THD of grid current is large. At 1s instant, the SDFT of fundamental grid voltage extraction is enabled, where the current reference changes from (2.15) to the fundamental component, i.e., (2.28). Thus, the 7^{th} harmonic is reduced but the 5^{th} harmonic remains the same magnitude. At 2s instant, the SDFT of harmonic grid current prediction is enabled and then added into the cost function, which begins to suppress the 5^{th} harmonic current. Therefore, based on these two improvements, desired performance of grid current can be achieved under distorted grid conditions, and the effectiveness of the proposed operation is verified.

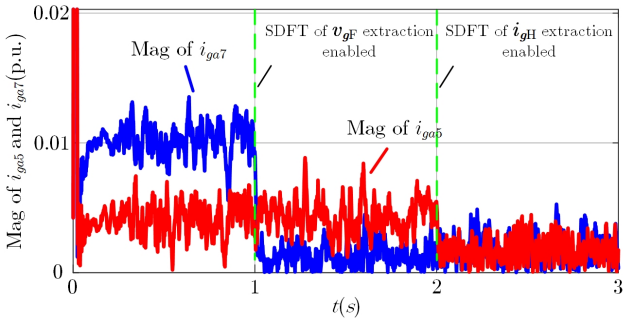

Figure 2.13: Magnitude of 5^{th} and 7^{th} harmonic of grid current under different operations.

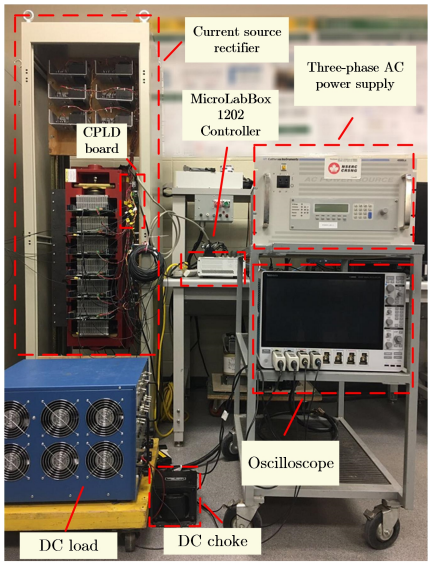

Figure 2.14: Experimental setup of 10-kVA CSR.

Fig. 2.14 shows a scaled 10-kVA CSR hardware prototype. The IGCTs-based CSR (IGCT module number: 5SHZ 0860F0005) is digitally controlled by a MicroLabBox 1202 controller with a complex programmable logic device (CPLD) system, which is employed to verify the proposed FCS-MPC scheme experimentally. The detailed setup parameters are given in Table 2.1. The proportional gain and integral gain of the outer PI loop in the experiment are set as 2 and 200 respectively.

Fig. 2.15 shows the experimental waveforms of dc-link current, grid current, grid voltage, and capacitor voltage obtained from FCS-MPC$_{\mathrm{AD}}$ and the proposed FCS-MPC scheme. It is observed that the performance gap of these two schemes is not particularly large but the proposed FCS-MPC gains grid currents with smaller THD 5.17% and a better damping effect.

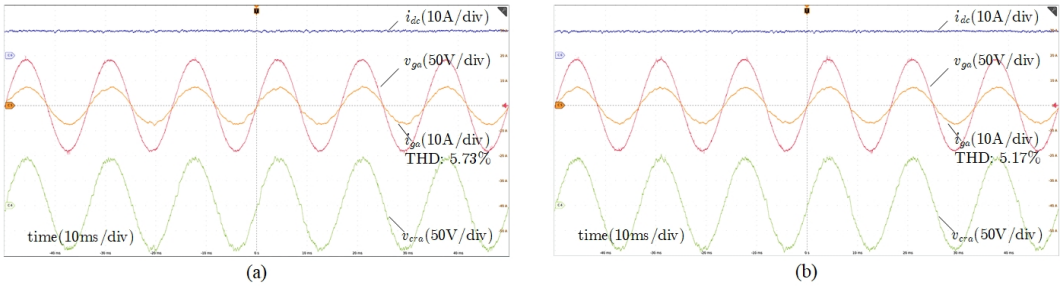

Figure 2.15: Experimental waveforms comparison with 1kHz switching frequency. (a) FCS-MPC$_{\mathrm{AD}}$. (b) Proposed FCS-MPC.

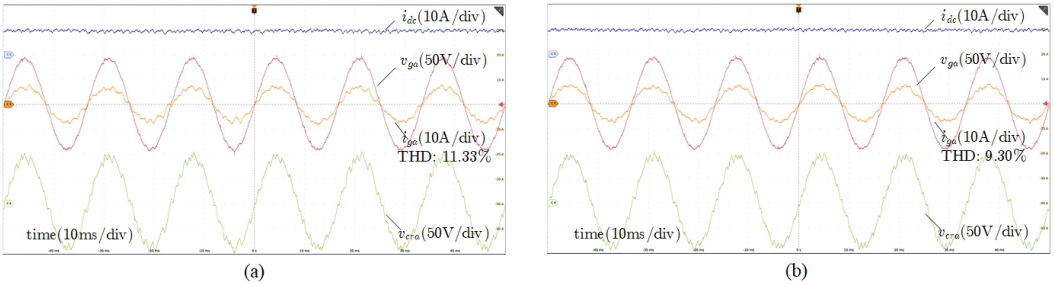

Figure 2.16: Experimental waveforms comparison with 500Hz switching frequency. (a) FCS-MPC$_{\mathrm{AD}}$. (b) Proposed FCS-MPC.

Similarly, Fig. 2.16 shows the experimental waveforms of dc-link current, grid current, grid voltage, and capacitor voltage, except that the switching frequency of FCS-MPC$_{\mathrm{AD}}$ and proposed FCS-MPC are both kept at 500Hz. It is observed that the grid current THD of the proposed FCS-MPC (9.30%) is smaller than FCS-MPC$_{\mathrm{AD}}$ (11.33%). The experimental results are consistent with the theoretical analysis and simulated results.

Fig. 2.17 shows the experimental waveform and FFT analysis of grid current of proposed FCS-MPC when the grid voltage contains 5% 5^{th} harmonic. It is worth mentioning that 5% 5^{th} harmonic is relatively large since the LC filter is in short-circuit status for the specific frequency. Fig. 2.18 gives the result for grid current when grid voltage contains 5% 5^{th} harmonic and 3% 7^{th} harmonic. Similar to simulated results, dominant 5^{th} and 7^{th} current harmonics are eliminated apparently by employing the modifications under the distorted grid, which can be clearly seen from their corresponding harmonic spectrums. Therefore, the proposed FCS-MPC with selective harmonic rejection can effectively improve the grid current quality under distorted grid

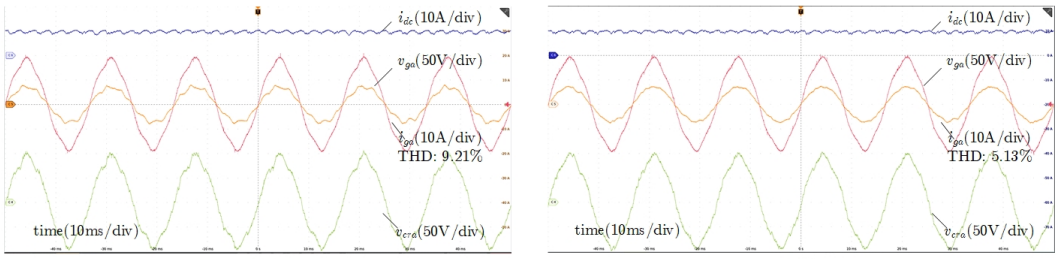

Figure 2.17: Experimental waveforms comparison under 5% 5^{th} grid harmonic voltage. (a) Proposed FCS-MPC for the normal grid. (b) Proposed FCS-MPC for the distorted grid.

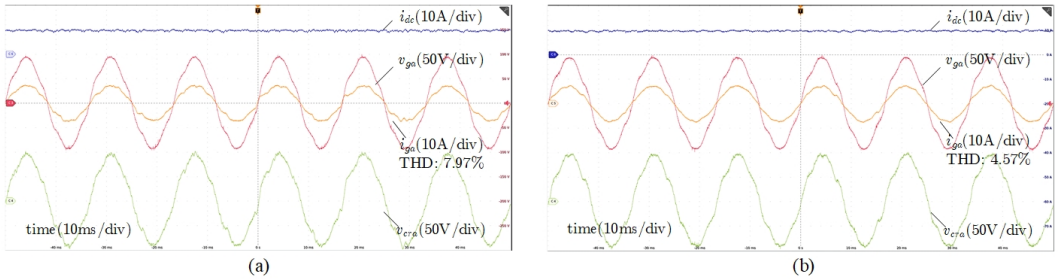

Figure 2.18: Experimental waveforms comparison under 5% 5^{th} and 3% 7^{th} grid harmonic voltage. (a) Proposed FCS-MPC for the normal grid. (b) Proposed FCS-MPC for the distorted grid.

conditions.

2.3 FCS-MPC Scheme With Enhanced Robustness for CSR-Side

Considering the challenge of the MPC scheme, the system robustness to the parameter mismatch is investigated and the disturbance observer is designed to enhance the robustness. To this end, the tracking error model of CSR is firstly built under the synchronous *dq* frame, where the constant state variable can intuitively show the error change subjected to the specific parameter mismatch case. Based on this, the observer is developed to estimate the lumped disturbance and contributes to the prediction error compensation. The observer-based disturbance estimation can also be universally applied to the CSI-fed motor side. Finally, the potential of applying the FCS-MPC to CSR with a long prediction horizon length is revealed.

2.3.1 Proposed Disturbance Observer-Based FCS-MPC

To suppress the filter resonance, both the grid current and capacitor voltage are regulated through the cost function in the proposed FCS-MPC. However, for the high-order system, the effect of parameter mismatch is rarely investigated in the MPC-based scheme. Undeniably, the variation of system parameters will cause the prediction error within each control interval. As a result, the accuracy of input vector selection will be reduced and thus the system performance will degrade [95]. Moreover, the impact caused by parameter mismatch will be worse for the FCS-MPC schemes applied in the CSR because the capacitor voltage reference is required in the cost function, which uses the value of inductance. As a result, the tracking error of the capacitor voltage will be further increased with the inductance value mismatch. Therefore, the robustness of FCS-MPC should be enhanced to ensure the performance under mismatched parameters.

The system state variable is expected to track the steady-state reference, including grid current reference $\boldsymbol{i_g^*}= i_{gd}^*+\mathrm{j}i_{gq}^*$ and capacitor voltage reference $\boldsymbol{v_{cr}^*}= v_{crd}^*+\mathrm{j}v_{crq}^*$. According to the active power P^* and reactive power Q^*, the dq-axes grid current reference can be calculated as

$$\begin{cases} i_{gd}^* = \frac{2}{3}\frac{P^* v_{gd}+Q^* v_{g\mathrm{q}}}{v_{g\mathrm{d}}^2+v_{g\mathrm{q}}^2} \\ i_{gq}^* = \frac{2}{3}\frac{P^* v_{gd}-Q^* v_{gq}}{v_{gd}^2+v_{gq}^2} \end{cases} \tag{2.29}$$

Furthermore, the dq-axes capacitor voltage reference can be inferred as follows based on the internal modeling.

$$\begin{cases} v_{crd}^* = -R_g i_{gd}^* + \omega_g L_r i_{gq}^* + v_{gd} \\ v_{crq}^* = -R_g i_{gq}^* - \omega_g L_r i_{gd}^* + v_{gq} \end{cases} \tag{2.30}$$

According to the dynamic modeling (2.7) and the reference of grid current and capacitor voltage, the dynamic equation of the state tracking error can be built as

$$\frac{d\tilde{\boldsymbol{x}}_{\mathbf{gdq}}}{dt} = \mathbf{A}_{\mathbf{gdq}}\tilde{\boldsymbol{x}}_{\boldsymbol{gdq}} + \mathbf{B}_{\mathbf{g}}\boldsymbol{u}_{\boldsymbol{gdq}} + \mathbf{B}_{\mathbf{g}}\boldsymbol{u}_{\boldsymbol{dis}} \tag{2.31}$$

where the error vector $\tilde{\boldsymbol{x}}_{\boldsymbol{gdq}}=[\tilde{i}_{gd}\ \tilde{i}_{gq}\ \tilde{v}_{crd}\ \tilde{v}_{crq}]^{\mathrm{T}}$ and $\tilde{i}_{gd}=i_{gd}$-i_{gd}^*, $\tilde{i}_{gq}=i_{gq}$-i_{gq}^*, $\tilde{v}_{crd}=v_{crd}$-v_{crd}^*, $\tilde{v}_{crq}=v_{crq}$-v_{crq}^*. The input disturbance vector $\boldsymbol{u}_{\boldsymbol{dis}}=[i_{wrd\_dis}\ i_{wrq\_dis}]^{\mathrm{T}}$,

which is expressed as

$$\begin{cases} i_{wrd\_dis} = -i^*_{gd} - \omega_g C_{fr} v^*_{crq} + m_{\mathrm{d}} \\ i_{wrq\_dis} = -i^*_{gq} + \omega_g C_{fr} v^*_{crd} + m_{\mathrm{q}} \end{cases} \tag{2.32}$$

where m_{d} and m_{q} are the lumped disturbance, including the parameter mismatch effect and unknown noise. As can be seen in (2.8), the value of inductance and capacitance are mainly used as denominators in matrix elements. Considering the magnitude order of LC parameters, a small change will cause a significant mismatch in the system modeling. Therefore, the mismatched LC filter will affect the prediction accuracy of the state variables. Besides, the accuracy of the capacitor voltage reference will also be affected by the mismatched inductance. To overcome the adverse effect caused by the parameter mismatch of the LC filter, both the capacitor voltage reference and the input disturbance are estimated online through observers, which work parallel with the controller to compensate for the steady-state tracking error. In this process, the dynamic of the capacitor voltage reference and the input disturbance are assumed to be slow compared to the fast sampling.

According to the dynamic modeling (2.7), the following modeling can be built to describe the dynamic of grid current and capacitor voltage reference.

$$\begin{cases} \frac{d\boldsymbol{x_t}}{dt} = \mathbf{A_t}\boldsymbol{x_t} + \mathbf{B_t}\boldsymbol{u_t} \\ \boldsymbol{y_t} = \mathbf{C_t}\boldsymbol{x_t} \end{cases} \tag{2.33}$$

where $\boldsymbol{x_t}$=$[\tilde{i}_{gd}\ \tilde{i}_{gq}\ v^*_{crd}\ v^*_{crq}]^{\mathrm{T}}$, $\boldsymbol{u_t}$=$[v_{crd}\ v_{crq}]^{\mathrm{T}}$, $\boldsymbol{y_t}$=$[\tilde{i}_{gd}\ \tilde{i}_{gq}]^{\mathrm{T}}$, and

$$\mathbf{A}_{\mathrm{t}} = \begin{bmatrix} -\frac{R_r}{L_r} & \omega_g & \frac{1}{L_r} & 0 \\ -\omega_g & -\frac{R_r}{L_r} & 0 & \frac{1}{L_r} \\ 0 & 0 & 0 & 0 \\ 0 & 0 & 0 & 0 \end{bmatrix}, \mathbf{B}_{\mathrm{t}} = \begin{bmatrix} -\frac{1}{L_r} & 0 \\ 0 & -\frac{1}{L_r} \\ 0 & 0 \\ 0 & 0 \end{bmatrix}, \mathbf{C_t} = \begin{bmatrix} 1 & 0 & 0 & 0 \\ 0 & 1 & 0 & 0 \end{bmatrix} \tag{2.34}$$

The discrete-time expression of (2.33) can be written as

$$\boldsymbol{x_{t\_ob}}(k+1) = \mathbf{A_{td}}\boldsymbol{x_{t\_ob}}(k) + \mathbf{B_{td}}\boldsymbol{u_t}(k) + \mathbf{L_{td}}(y_t - \mathbf{C_t}\boldsymbol{x_{t\_ob}}) \tag{2.35}$$

where the estimated vector $\boldsymbol{x_{t\_ob}}$=$[\tilde{i}_{gd\_ob}\ \tilde{i}_{gq\_ob}\ v^*_{crd\_ob}\ v^*_{crq\_ob}]^{\mathrm{T}}$ and the discrete matrices $\mathbf{A_{td}} = e^{\mathbf{A}_{\mathrm{t}}T_s} \approx \sum_{n=0}^{2} \frac{\mathbf{A_t}^n {T_s}^n}{n!}$ and $\mathbf{B_{td}} \approx \sum_{n=1}^{2} \frac{\mathbf{A_t}^{n-1} {T_s}^n}{n!}\mathbf{B_t}$. The feedback

matrix $\mathbf{L_{td}}$ can be directly designed based on the Kalman filtering process [96], where the steady-state gain can be expressed as

$$\mathbf{L_{td}}(\infty) = \mathbf{A_{td}}\mathbf{P_{td}}\mathbf{C_t}^{\mathrm{T}}(\mathbf{R_{td}} + \mathbf{C_t}\mathbf{P_t}\mathbf{C_t}^{\mathrm{T}})^{-1} \tag{2.36}$$

and $\mathbf{P_{td}}$ can be solved from the following Riccati equation

$$\mathbf{P_{td}} = \mathbf{A_{td}}^{\mathrm{T}}[\mathbf{P_{td}} - \mathbf{P_{td}}\mathbf{C_t}(\mathbf{R_{td}} + \mathbf{C_t}^{\mathrm{T}}\mathbf{P_{td}}\mathbf{C_t})^{-1}\mathbf{C_t}^{\mathrm{T}}\mathbf{P_{td}}]\mathbf{A_{td}} + \mathbf{Q_{td}} \tag{2.37}$$

In this case, the observer closed-loop matrix $\mathbf{A_{td}} - \mathbf{L_{td}}\mathbf{C_t}$ can be stable. Also, the matrix $\mathbf{Q_{td}}$ and $\mathbf{R_{td}}$ represent the covariance matrices of the measurement noise and modeling mismatch respectively, which adjust the tradeoff between the noise rejection and bandwidth.

To improve the prediction accuracy, the unknown input $\boldsymbol{u_{dis}}$ is also estimated by designing the observer. Based on (2.7), the following dynamic modeling can be obtained.

$$\begin{cases} \frac{d\boldsymbol{x_o}}{dt} = \mathbf{A_o}\boldsymbol{x_o} + \mathbf{B_o}\boldsymbol{u_o} \\ \boldsymbol{y_o} = \mathbf{C_o}\boldsymbol{x_o} \end{cases} \tag{2.38}$$

where $\boldsymbol{x_o}$=$[\tilde{v}_{crd}\ \tilde{v}_{crq}\ i_{wrd\_dis}\ i_{wrq\_dis}]^{\mathrm{T}}$, $\boldsymbol{u_o}$=$[\tilde{i}_{gd} - i_{wrd}\ \tilde{i}_{gd} - i_{wrq}]^{\mathrm{T}}$, $\boldsymbol{y_o}$=$[\tilde{v}_{crd}\ \tilde{v}_{crq}]^{\mathrm{T}}$ and

$$\mathbf{A_o} = \begin{bmatrix} 0 & \omega_g & -\frac{1}{C_{fr}} & 0 \\ -\omega_g & 0 & 0 & -\frac{1}{C_{fr}} \\ 0 & 0 & 0 & 0 \\ 0 & 0 & 0 & 0 \end{bmatrix}, \mathbf{B_o} = \begin{bmatrix} \frac{1}{C_{fr}} & 0 \\ 0 & \frac{1}{C_{fr}} \\ 0 & 0 \\ 0 & 0 \end{bmatrix}, \mathbf{C_o} = \begin{bmatrix} 1 & 0 & 0 & 0 \\ 0 & 1 & 0 & 0 \end{bmatrix} \tag{2.39}$$

The discrete-time expression of the disturbance observer (2.38) is

$$\boldsymbol{x_{o\_ob}}(k+1) = \mathbf{A_{od}}\boldsymbol{x_{o\_ob}}(k) + \mathbf{B_{od}}\boldsymbol{u_o}(k) + \mathbf{L_{od}}(\boldsymbol{y_o} - \mathbf{C_o}\boldsymbol{x_{o\_ob}}) \tag{2.40}$$

where the estimated vector $\boldsymbol{x_{o\_ob}}$=$[\tilde{v}_{crd\_ob}\ \tilde{v}_{crq\_ob}\ i_{wrd\_dis\_ob}\ i_{wrq\_dis\_ob}]^{\mathrm{T}}$ and $\mathbf{A_{od}} = e^{\mathbf{A_o}T_s} \approx \sum_{n=0}^{2} \frac{\mathbf{A_o}^n T_s{}^n}{n!}$, $\mathbf{B_{od}} \approx \sum_{n=1}^{2} \frac{A_o{}^{n-1} T_s{}^n}{n!}\mathbf{B_o}$. Also, the feedback matrix $\mathbf{L_{od}}$ is designed according to

$$\mathbf{L_{od}}(\infty) = \mathbf{A_{od}}\mathbf{P_{od}}\mathbf{C_o}^{\mathrm{T}}(\mathbf{R_{od}} + \mathbf{C_o}\mathbf{P_{od}}\mathbf{C_o}^{\mathrm{T}})^{-1} \tag{2.41}$$

and $\mathbf{P_{od}}$ can be solved by the Riccati equation. Also, the matrix $\mathbf{Q_{od}}$ and $\mathbf{R_{od}}$ can be taken as the tuning parameters.

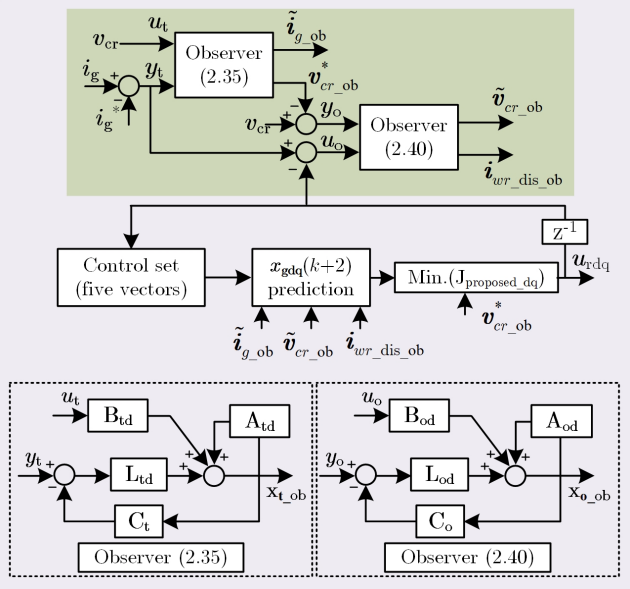

Figure 2.19: Disturbance-observer-based FCS-MPC scheme for CSR.

It is worth mentioning that the observer (2.35) and (2.40) also estimate the state tracking error of grid-current and capacitor voltage, which are provided in the one-step forward predictive manner based on the *kth* step sampling information. Therefore, the delay compensation in the FCS-MPC can be replaced by the estimated state error from the observer. Fig. 2.19 shows the diagram of the observer-based FCS-MPC scheme, and the robustness can be strengthened through the disturbance compensation.

It should be noted that the cost function under the *dq* frame still directly takes the tracking error of the grid current and capacitor voltage as the control objectives, i.e.,

$$J_{\text{proposed\_dq}} = \tilde{\boldsymbol{x}}_{\boldsymbol{gdq}}^{\text{T}} \mathbf{W} \tilde{\boldsymbol{x}}_{\boldsymbol{gdq}} + \lambda_{sfr} \left| \boldsymbol{I}_{\boldsymbol{wr}}(k+1) - \boldsymbol{I}_{\boldsymbol{wr}}(k) \right| \tag{2.42}$$

2.3.2 Long Prediction Horizon with Only Grid Current Feedback

Based on the multivariable regulation, the FCS-MPC scheme with one-step forward prediction can achieve good performance in the CSR system. To further reveal the potential of FCS-MPC, the tracking process of grid current and the predictive stage are analyzed. Furthermore, the predictive horizon length is increased to estimate the controller performance in the CSR system.

Fig. 2.20 presents the trajectory evolution of the grid current using the FCS-MPC scheme but under different scenarios. Due to the second-order feature, the change of capacitor voltage is constrained to be continuous. Consequently, the derivative of the grid current cannot change suddenly, which also expresses the continuous property. In Fig. 2.20(a), the one-step forward prediction-based FCS-MPC scheme with the regulation of both grid-current and capacitor voltage is applied. In this case, the two freedom degrees of the current, including the magnitude and derivative are regulated well. For example, considering the current time at the kth instant, the trajectory of grid current may be driven to five possible candidates based on the control set. As can be seen, the trajectory point with the minimum magnitude error is not always selected at each instant, such as the $(k+1)th$ instant. The reason is that the optimal trajectory presents the tradeoff between the derivative and magnitude error. In Fig. 2.20(b), the one-step forward prediction-based FCS-MPC scheme is still applied but without the capacitor voltage regulation. Therefore, the cost function selects the input vector only according to the magnitude error of the grid current. As can be seen at $(k+1)th$ instant, the trajectory point with minimum magnitude error is selected, but the grid current derivative is not regulated. As a result, all available inputs will generate large deviations from the reference at $(k+2)th$ instant, which cannot restore the tendency of grid current. Therefore, even though the point with the minimum magnitude error is always selected, the resonance will appear. Fig. 2.20(c) presents the trajectory with only grid current regulation but the prediction horizon has been extended. In this case, the trajectory leading to resonance can be detected at kth, which will be abandoned by the controller because all of the instantaneous tracking errors within the horizon will be added up as the evaluation criteria. Finally, according to the RHP, the first element in the control input sequence resulting in the optimal trajectory will be applied. Thus, it can be inferred that the long horizon prediction can improve the CSR performance with only grid current regulation.

In summary, both the magnitude and derivative of grid current are needed to be regulated well with the one-step forward prediction. On the other hand,

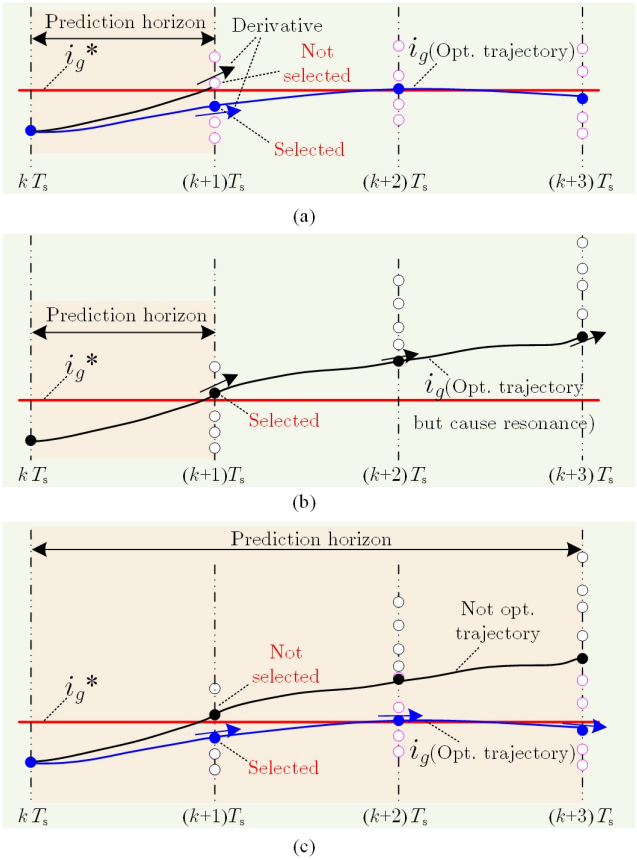

Figure 2.20: The trajectory of grid current under the FCS-MPC scheme. (a) One-step prediction with capacitor voltage regulation. (b) One-step prediction without capacitor voltage regulation. (c) Long-horizon prediction without capacitor voltage regulation.

the longer horizon length endows the controller with the ability to only regulate the magnitude error since the grid current tendency can be predicted in advance. In this case, the capacitor voltage tracking item does not need to be included in the cost function and the capacitor voltage reference can be eliminated, thus enhancing the robustness of the control scheme.

Ignoring the input disturbance in (2.31), the long horizon prediction results can be formulated as follows.

$$\tilde{\mathbf{X}}_{\mathbf{gdq}}(k) = \mathbf{\Phi}\tilde{\boldsymbol{x}}_{\boldsymbol{gdq}}(k) + \mathbf{\Xi}\mathbf{U}_{\mathbf{gdq}}(k) \tag{2.43}$$

where $\tilde{\mathbf{X}}_{\mathbf{gdq}}(k)$=$[\tilde{\boldsymbol{x}}_{\boldsymbol{gdq}}(k+1)\ \tilde{\boldsymbol{x}}_{\boldsymbol{gdq}}(k+2)\ ,...,\ \tilde{\boldsymbol{x}}_{\boldsymbol{gdq}}(k+N)]^{\mathrm{T}}$, $\mathbf{U}_{\mathbf{gdq}}(k)$=$[\boldsymbol{u}_{\boldsymbol{gdq}}(k)$ $\boldsymbol{u}_{\boldsymbol{gdq}}(k+1)\ ,...,\ \boldsymbol{u}_{\boldsymbol{gdq}}(k+N-1)]^{\mathrm{T}}$, $\mathbf{\Phi} = \left[\ \mathbf{A}_{\mathbf{gdq}}\ \ \mathbf{A}_{\mathbf{gdq}}{}^{2}\ ,...,\ \mathbf{A}_{\mathbf{gdq}}{}^{N}\ \right]^{\mathrm{T}}$,

$$\boldsymbol{\Xi}=\begin{bmatrix} \mathbf{B_g} & & & \\ \mathbf{A_{gdq}}\mathbf{B_g} & \mathbf{B_g} & & \\ \vdots & & & \\ \mathbf{A_{gdq}}^{N-1}\mathbf{B_g} & \mathbf{A_{gdq}}^{N-2}\mathbf{B_g} & \dots & \mathbf{B_g} \end{bmatrix}$$ and N is the length of the predictive horizon.

According to (2.43), it can be seen that the prediction within the horizon contains two components, i.e. the one depending on the state error $\tilde{\boldsymbol{x}}_{\boldsymbol{gdq}}$ and the other reflecting the response from the available input combinations in the future steps. During each sampling interval, the first item $\boldsymbol{\Phi}\tilde{\boldsymbol{x}}_{\boldsymbol{gdq}}(k)$ can be pre-calculated and taken as constant while the second item contains the future response. Therefore, if the second item cannot cover the possible responses, the optimal control input sequence may be missed because the cost function only evaluates the subset of the response range. For CSR modeling in (2.31), matrix $\mathbf{A_{gdq}}$ is full rank and the length of the state vector is 4. Besides, checking that $rank[\mathbf{B_g}\ \mathbf{A_{gdq}}\mathbf{B_g}] = 4$ and thus the reachable subspace $R_{(\mathbf{A_{gdq}},\mathbf{B_g})|k}$ of CSR system at time instant kth can be expressed as [97]

$$R_{(\mathbf{A_{gdq}},\mathbf{B_g})|k} = \text{span}\,[\mathbf{B_g}\ \ \mathbf{A_{gdq}}\mathbf{B_g}] \tag{2.44}$$

where span$[x_1,\ x_2,\ \ldots,\ x_m]$ represents the subspace generated by the linear combinations of $x_1,\ x_2,\ \ldots,\ x_m$. Therefore, the one-step forward prediction only evaluates the subset of span $[\mathbf{B_g}]$, whose scope is much smaller than the reachable subspace. Thus, it is difficult for the controller to select the input resulting in optimal trajectory, especially under the case with only grid current regulation. With two-step prediction (N=2) adopted, the total 25 combinations of span $[\mathbf{B_g}\ \mathbf{A_{gdq}}\mathbf{B_g}]$ are evaluated, which can significantly extend the evaluated range. Further, the longer the prediction horizon ($N\geq$2), the more responses in the subspace are evaluated, thus improving system performance.

2.3.3 Simulation and Experimental Results

To intuitively observe the tracking errors of state variables caused by the LC parameter mismatch effect, a simulated case for the state tracking error of the CSR system is shown in Fig. 2.21, where the line-to-line grid peak voltage is 110V and the dc-link current reference is set as 7.2A with 500W active power

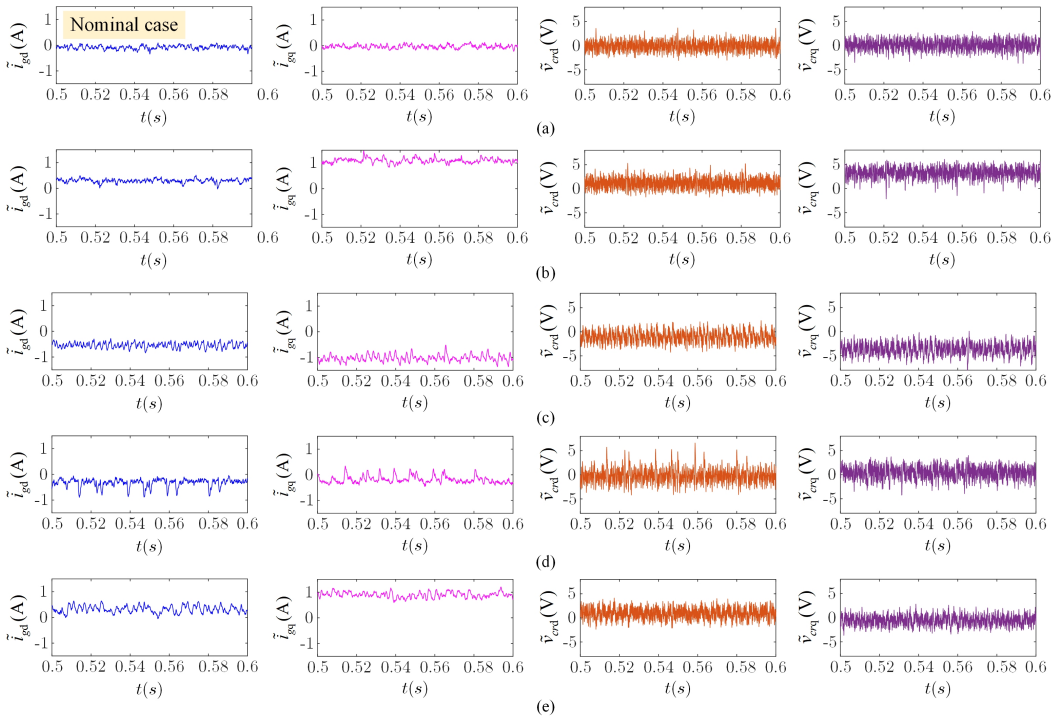

Figure 2.21: The simulated tracking error of grid current and capacitor voltage using one-step prediction FCS-MPC scheme. (a) Without parameter mismatch. (b) δ_{L}=+66.67%. (c) δ_{L}=-66.67%. (d) δ_{C}=+50%. (e) δ_{C}=-50%.

generated and the reactive power is set as 0Var to maintain the unity power factor. The parameter mismatch effect is tested by increasing or decreasing the adopted value of the LC filter in the controller. The parameter mismatch percent can be defined as

$$\delta_{\mathrm{L}} = \frac{L_{\Delta}}{L_r} \quad , \quad \delta_{\mathrm{C}} = \frac{C_{\Delta}}{C_{fr}} \tag{2.45}$$

where L_{Δ} and C_{Δ} are the mismatched part of the inductance and capacitance value. As shown in Fig. 2.21(a), all of the state tracking errors are close to zero with the nominal inductance and capacitance value used in the controller. Fig. 2.21(b) and Fig. 2.21(c) present the situation with mismatched inductance used, resulting in non-zero tracking errors of both grid current and capacitor voltage, which come from the prediction error and the incorrect capacitor voltage reference. The different deviation directions of inductance value will lead to the opposite change of the error in both the grid current and capacitor voltage. Fig. 2.21(d) and Fig. 2.21(e) present the situation with mismatched capacitance used and the non-zero errors have been caused

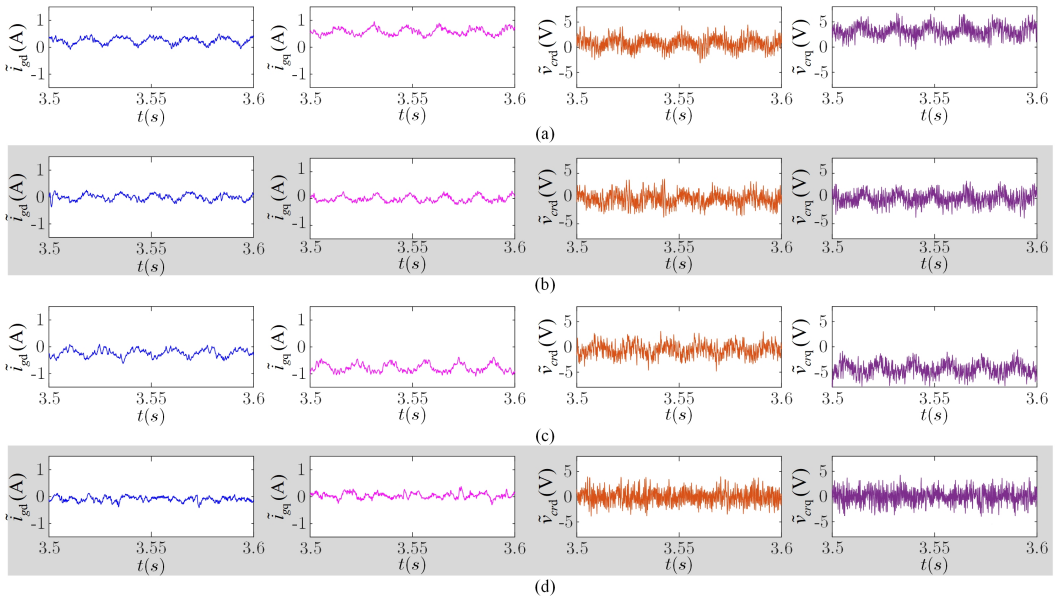

Figure 2.22: The experimental tracking error of grid current and capacitor voltage using one-step prediction FCS-MPC scheme with inductance mismatch. (a)/(b) Inactive/active proposed observer with δ_{L}=+66.67%. (c)/(d) Inactive/active proposed observer with δ_{L}=-66.67%

by the prediction error. It can be seen that the increased/decreased inductance or decreased/increased capacitance used in the controller will generate a similar deviated error in grid current. Especially, the q-axis current component is affected most, which implies that the unity power factor cannot be maintained. To verify the effectiveness of the proposed method under the inductance mismatch situation, Fig. 2.22 shows the experimental tracking error of grid current and capacitor voltage with/without using the dual observer. A new grid-connected CSR hardware prototype, which adopts the SiC-MOSFET (number: C3M0065100K) as the switching device has been adopted. The digital controller is MicroLabBox 1202 and the tested switching frequency is 1.5kHz. The filter inductance is 3mH and the filter capacitance is 160μF. The tracking error data is captured by the control desk project. As can be seen in Fig. 2.22(a), with the increased inductance value used in the controller, the prediction error and the incorrect capacitor voltage reference appear, resulting in the non-zero tracking error in both grid current and capacitor voltage. When the proposed observer becomes active in Fig. 2.22(b), the zero tracking error of the state variable can be guaranteed, where the prediction error is com-

pensated and the capacitor voltage reference is generated from the observer. Similarly, the state tracking error with reduced inductance value is compared through Fig. 2.22(c) and Fig. 2.22(d), which verifies that the proposed method is always effective to deal with the inductance mismatch.

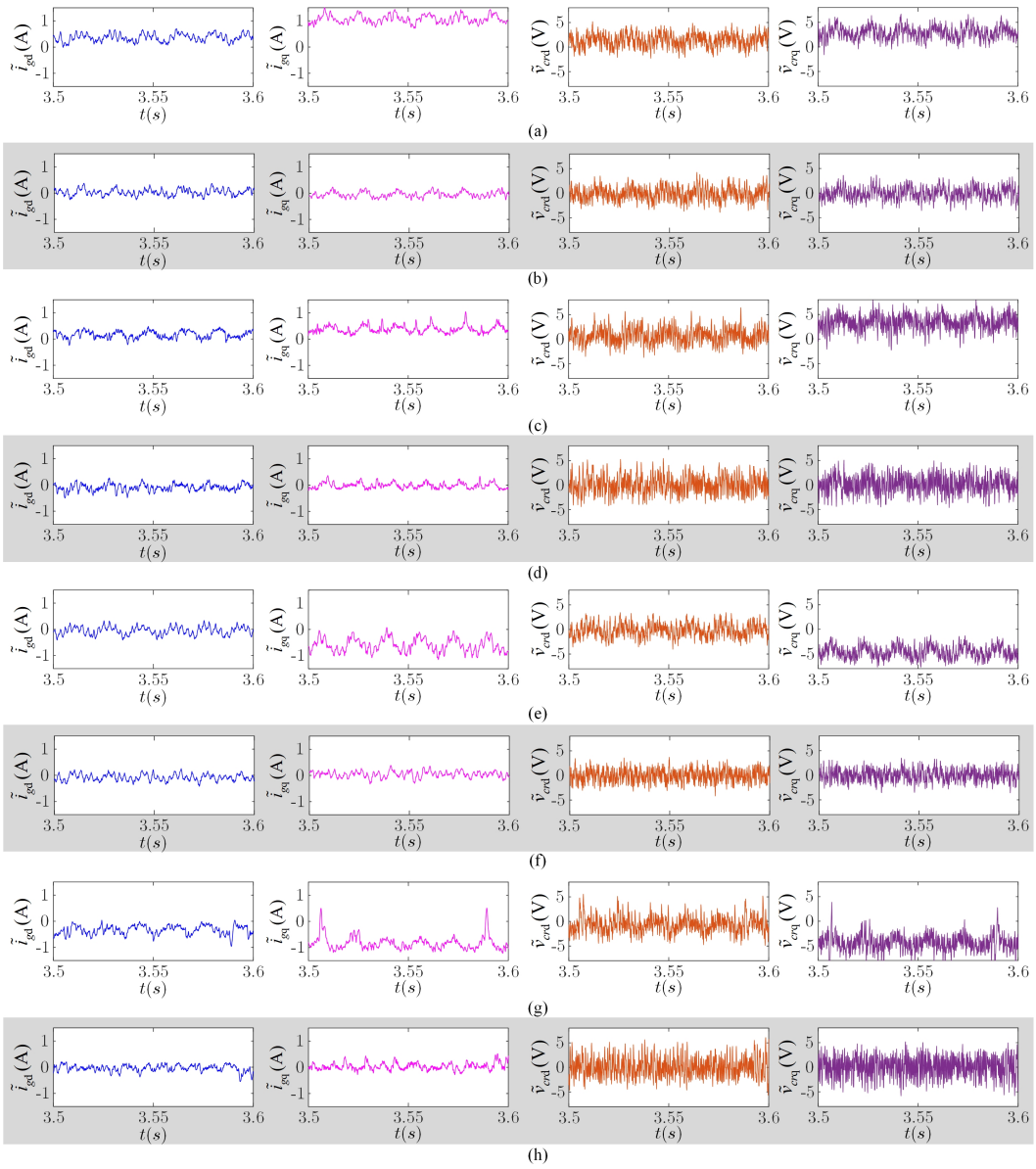

Figure 2.23: The experimental tracking error of grid current and capacitor voltage using one-step prediction FCS-MPC with inductance and capacitance mismatch. (a)/(b) Inactive/active observer with δ_L=+66.67% and δ_C=-50%. (c)/(d) Inactive/active observer with δ_L=+66.67% and δ_C=+50%. (e)/(f) Inactive/active observer with δ_L=-66.67% and δ_C=-50%. (g)/(h) Inactive/active observer with δ_L=-66.67% and δ_C=+50%.

Fig. 2.23 compares the tracking error of grid current and capacitor voltage

with the inductance and capacitance mismatch simultaneously. Undeniably, the state tracking error exists in all of these cases. By enabling the proposed dual observer, the tracking error of grid current and capacitor voltage can be reduced to zero. Therefore, it verified that the robustness of the proposed method for CSR application can be effectively improved.

To observe the effect of the long prediction horizon and verify the analysis in Fig. 2.20, the performance of FCS-MPC with different state variable regulation and prediction horizon length are compared in Fig. 2.24, where the experimental waveform and FFT analysis of grid current and line-to-line capacitor voltage are presented. As can be seen in Fig. 2.24(a), the FCS-MPC with one-step forward prediction can achieve satisfactory results by regulating both the grid current and capacitor voltage. Although the controller only evaluates five kinds of prediction response, the freedom degrees of the current, i.e. the magnitude and derivative are both effectively regulated. Furthermore, Fig. 2.25(b) shows the CSR performance with one-step FCS-MPC but the weighting factor for capacitor voltage has been set as zero. As a result, the resonance problem appears and the grid current quality has been significantly distorted. Therefore, it verifies that only grid current feedback in the CSR system is not sufficient by using the one-step FCS-MPC. The derivative of the grid current cannot be changed arbitrarily due to the capacitor constraint. The FCS-MPC with the extended predictive horizon, including two-step and three-step length, have been tested, where still only the grid current is regulated in the cost function. As can be seen in Fig. 2.24(c), the CSR performance can be significantly improved compared to Fig. 2.24(b). The range of the predictive response has been enlarged, which makes the controller abandon the resonant trajectory. The predictive response is closer to the subspace span[$\mathbf{B_r}$ $\mathbf{A_{rdq}B_r}$] with a three-step prediction, further improving the grid current quality with reduced THD in Fig. 2.24(d). Therefore, under the condition that with only grid current feedback, the long-horizon FCS-MPC can guarantee closed-loop stability and significantly improve the power quality compared to the one-step case. In addition, the three-step FCS-MPC can achieve good current quality comparable to the one-step FCS-MPC scheme with both grid current and

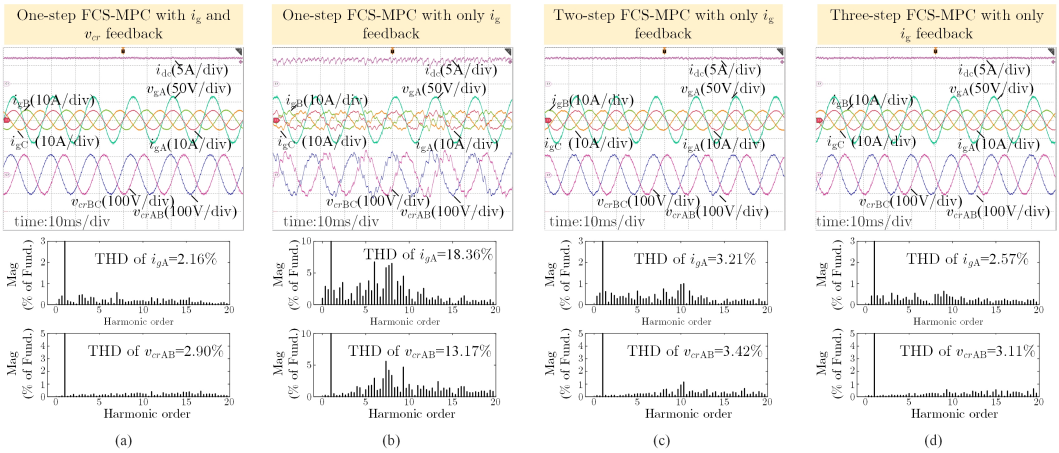

Figure 2.24: The steady-state experimental waveform of CSR system and FFT analysis of grid currents and line-to-line capacitor voltage. (a) One-step prediction FCS-MPC with both grid-current and capacitor voltage feedback. (b) One-step prediction FCS-MPC with only grid-current feedback. (c) Two-step prediction FCS-MPC with only grid-current feedback. (d) Three-step prediction FCS-MPC with only grid-current feedback.

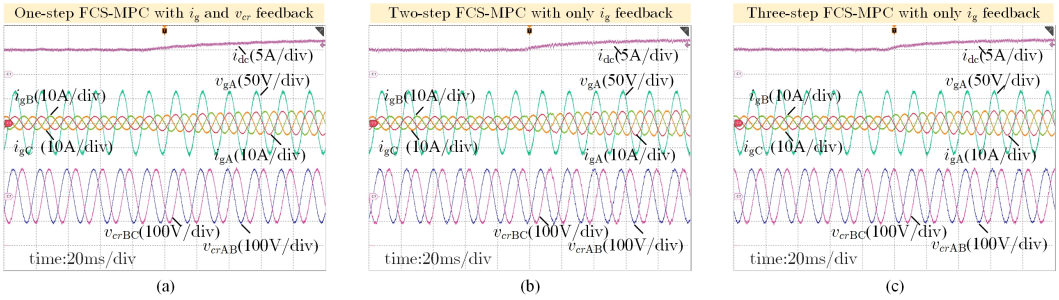

Figure 2.25: The dynamic test of CSR system. (a) One-step FCS-MPC with both grid-current and capacitor voltage feedback. (b) Two-step FCS-MPC with only grid-current feedback. (c) Three-step FCS-MPC with only grid-current feedback.

capacitor voltage feedback.

The dynamic test of the multivariable feedback one-step FCS-MPC and longer horizon prediction FCS-MPC with only grid current feedback are presented in Fig. 2.25. All of these three cases achieve smooth transient without resonance spikes. Therefore, the CSR performance can be guaranteed with only grid current feedback by extending the predictive length, which brings benefits including the elimination of weighting factors for capacitor voltage and the reduced effect caused by the mismatched inductance.

It is worth mentioning that the benefits of the multistep prediction applied to the second-order system have been focused and thus the further optimization of the computational time reduction is not a core. To facilitate the

realization of long prediction length, advanced branch and bound searching processes, such as the sphere decoding method can be applied [98].

2.4 FCS-MPC for Transformerless CSCs-fed PMSM Drives

The integrated dc-link choke can replace the bulky transformer in CSCs-fed motor drive systems to bear the CMV. However, the CM resonance will be excited by the specific harmonics in the CMV, which causes excessive CM current in the loop. In this section, the FCS-MPC scheme is proposed to tackle the CM resonance and filter resonance simultaneously. In the low-speed region, besides restraining the PTP magnitude of the CMV at the rectifier side, the third-order harmonic of the CMV generated by the inverter is extracted and then penalized in the cost function to further suppress the CM current. With the increase of the motor speed, the control objective of the inverter side controller switches to the PTP magnitude of CMV suppression because of the alleviation of the CM resonance. The simulation with 1MVA rated power and the scaled-down experiment shows that the proposed scheme can suppress the CM resonance, which contributes to a smaller size of the CM choke.

2.4.1 Expression and Properties of CMV Generated by CSCs

The CMV generated by CSR and CSI sides are defined respectively as [53]

$$V_{cmr} = \frac{V_{\mathrm{P}_r-g} + V_{\mathrm{N}_r-g}}{2} \ , \ V_{cmi} = \frac{V_{\mathrm{P}_i-o} + V_{\mathrm{N}_i-o}}{2} \tag{2.46}$$

where V_{cmr} and V_{cmi} represent the CMV at CSR and CSI sides. $V_{\mathrm{P_r}-g}$ and $V_{\mathrm{N_r}-g}$ represent the voltage of two dc terminals $\mathrm{P_r}$ and $\mathrm{N_r}$ respectively, with respect to the CSR-side ground g, as seen in Fig. 2.1. $V_{\mathrm{P_i}-o}$ and $V_{\mathrm{N_i}-o}$ represent the voltage of two dc terminal $\mathrm{P_i}$ and $\mathrm{N_i}$, respectively, with respect to the motor-side neutral point o. Also, V_{cmr} and V_{cmi} can be calculated as follows

[99]

$$V_{cmr} = \frac{1}{2} \cdot [S_{1r} + S_{4r} \;\; S_{3r} + S_{6r} \;\; S_{5r} + S_{2r}] \begin{bmatrix} v_{ga} \\ v_{gb} \\ v_{gc} \end{bmatrix},$$
$$V_{cmi} = \frac{1}{2} \cdot [S_{1i} + S_{4i} \;\; S_{3i} + S_{6i} \;\; S_{5i} + S_{2i}] \begin{bmatrix} v_{sa} \\ v_{sb} \\ v_{sc} \end{bmatrix} \tag{2.47}$$

In (2.47), the capacitor voltage of the CSR side can be substituted with the grid voltage. It can be found that the CMV generated by the zero-switching state will equal to the phase voltage while the active switching state will generate CMV magnitude with half of the phase voltage. Therefore, the overall shape of CMV is determined by the amplitude envelope of the capacitor voltage and the applied switching state.

In general, for the FCS-MPC scheme for CSC application, the transition between the active switching states is restrained to the adjacent vectors to limit large di/dt. Besides, since three redundant zero vectors exist in a CSC, the selection of zero vectors should follow the principle that maintains the minimum number of transitions with the previous switching state. For example, if the switching vector in the last interval is $\boldsymbol{i_{wr(i)1}}$ and zero vector will be chosen, then $\boldsymbol{i_{wr(i)z1}}$ and $\boldsymbol{i_{wr(i)z3}}$ can be alternatives. However, these two zero-states are still redundant since there is no further control freedom to determine which one should be selected. Therefore, to ensure that the switching device of each phase can act evenly, the assignment of zero vector in the general FCS-MPC scheme can use the transition rule from the SVM strategy for CSC, where the transition of switching vectors is concluded in Table 2.2.

To clearly show the property of the CMV generated by the CSC, the simulated waveform of the CMV and three-phase capacitor voltage of the CSI side is presented in Fig. 2.26, where the switching state is switched according to Table 2.2. It can be found that the CMV shape is the envelope of the capacitor voltage. Besides, the CMV waveform contains the zero-sequence components and the dominant harmonic order is the third [53].

Table 2.2: Transition of the switching vectors for the general FCS-MPC scheme

The vector in last interval	The candidate vectors in the next interval
$\boldsymbol{i_{wr(i)1}}$	$\boldsymbol{i_{wr(i)6}}$ $\boldsymbol{i_{wr(i)1}}$ $\boldsymbol{i_{wr(i)2}}$ $\boldsymbol{i_{wr(i)z3}}$
$\boldsymbol{i_{wr(i)2}}$	$\boldsymbol{i_{wr(i)1}}$ $\boldsymbol{i_{wr(i)2}}$ $\boldsymbol{i_{wr(i)3}}$ $\boldsymbol{i_{wr(i)z2}}$
$\boldsymbol{i_{wr(i)3}}$	$\boldsymbol{i_{wr(i)2}}$ $\boldsymbol{i_{wr(i)3}}$ $\boldsymbol{i_{wr(i)4}}$ $\boldsymbol{i_{wr(i)z1}}$
$\boldsymbol{i_{wr(i)4}}$	$\boldsymbol{i_{wr(i)3}}$ $\boldsymbol{i_{wr(i)4}}$ $\boldsymbol{i_{wr(i)5}}$ $\boldsymbol{i_{wr(i)z3}}$
$\boldsymbol{i_{wr(i)5}}$	$\boldsymbol{i_{wr(i)4}}$ $\boldsymbol{i_{wr(i)5}}$ $\boldsymbol{i_{wr(i)6}}$ $\boldsymbol{i_{wr(i)z2}}$
$\boldsymbol{i_{wr(i)6}}$	$\boldsymbol{i_{wr(i)5}}$ $\boldsymbol{i_{wr(i)6}}$ $\boldsymbol{i_{wr(i)1}}$ $\boldsymbol{i_{wr(i)z1}}$
$\boldsymbol{i_{wr(i)z1}}$	$\boldsymbol{i_{wr(i)1}}$ $\boldsymbol{i_{wr(i)3}}$ $\boldsymbol{i_{wr(i)4}}$ $\boldsymbol{i_{wr(i)6}}$ $\boldsymbol{i_{wr(i)z1}}$
$\boldsymbol{i_{wr(i)z2}}$	$\boldsymbol{i_{wr(i)2}}$ $\boldsymbol{i_{wr(i)3}}$ $\boldsymbol{i_{wr(i)5}}$ $\boldsymbol{i_{wr(i)6}}$ $\boldsymbol{i_{wr(i)z2}}$
$\boldsymbol{i_{wr(i)z3}}$	$\boldsymbol{i_{wr(i)1}}$ $\boldsymbol{i_{wr(i)2}}$ $\boldsymbol{i_{wr(i)4}}$ $\boldsymbol{i_{wr(i)5}}$ $\boldsymbol{i_{wr(i)z3}}$

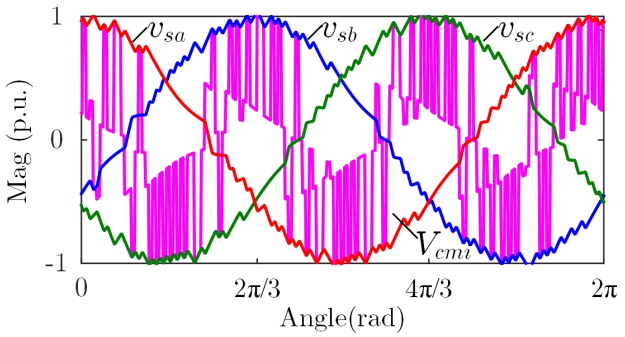

Figure 2.26: The typical waveform of the CMV at the CSI side.

2.4.2 Common Mode Resonance in Transformerless CSCs

The CMV in the MV drive system can be blocked by the isolated transformer but with the expense of system cost and weight. The integrated dc-link choke, including differential inductance and CM inductance, has been proposed in [52] to replace the isolated transformer. The differential inductance L_{diff} can reduce the dc-link current ripple while the CM inductance L_{cm} is responsible

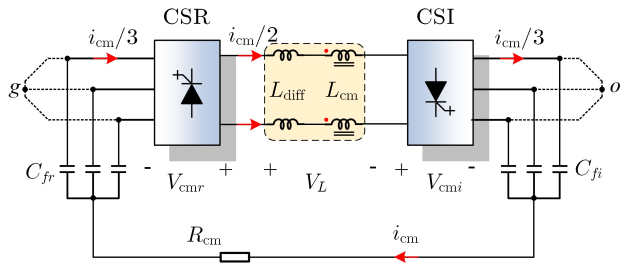

Figure 2.27: The CM loop in the transformerless CSC-fed PMSM drive.

for CMV suppression and the CM current limitation. According to Fig. 1.3, the CM loop circuit can be redrawn in Fig. 2.27, which essentially is an RLC loop. As can be seen, V_{cmr} and V_{cmi} are the two voltage sources in the CM loop. Therefore, according to the Kirchhoff voltage law, the whole CMV of the drive system V_{og}, namely the voltage between the neutral point o of PMSM with respect to the ground g can be expressed as

$$V_{og} = V_{cmr} - V_{cmi} - V_L \tag{2.48}$$

where V_L represents the voltage drop on the integrated dc-link choke. The total CMV V_{og} can be significantly reduced since the dominant voltage component of $V_{cmr} - V_{cmi}$ is canceled out by V_L. Moreover, the CM current i_{cm} can be calculated as

$$i_{cm} = \frac{V_{cmr} - V_{cmi}}{Z_{cm}} \tag{2.49}$$

where Z_{cm} is the total impedance of the CM loop. Therefore, the CM current i_{cm} will be entirely determined by V_{cmr}, V_{cmi} and Z_{cm}. It should be pointed out that the positive/negative rail only contains half of the total CM current flowing in the same direction [52]. According to the properties of CMV in CSC, the third-order harmonic voltage is the dominant component in both V_{cmr} and V_{cmi}, i.e., V_{cmr_3} and V_{cmi_3}. Thus, it can be deduced that i_{cm} will contain the dominant component with the triple stator frequency of the motor side and the 180Hz component from the CSR side (the grid voltage frequency is 60Hz).

The CM loop contains the inductive choke and two sides capacitors of the CSC, which implies the CM series resonance will be easily excited by the CMV component with a specific frequency. The resonant frequency can be calculated as

$$\begin{cases} f_{cm\_res} = \frac{1}{2\pi\sqrt{L_{eq}C_{eq}}}\text{Hz} \\ L_{eq} = L_{cm} + \frac{L_{diff}}{2} \\ C_{eq} = 3 \cdot \frac{C_{fr} \cdot C_{fi}}{C_{fr} + C_{fi}} \end{cases} \tag{2.50}$$

where L_{eq} and C_{eq} represent the equivalent inductance and capacitance of the CM loop. As shown in [52], the typical resonance frequency of the CM loop is

designed in the range of 0.528-0.744p.u., namely f_{cm_res} is from 31.5 to 44.7 Hz. The frequency of V_{cmr_3} is constant at 180Hz, which is higher than the resonant frequency f_{cm_res}. Therefore, the CM current induced by the CSR side is not very severe since the CMV component with 180Hz can be blocked by the CM choke. However, due to the speed of motor changes, the frequency of V_{cmi_3} will change correspondingly. Assuming that the stator frequency of the motor is approximately kept at 10-15Hz, the prominent third-order component with a frequency ranging from 30 to 45Hz will appear in V_{cmi}. As a result, the severe CM current will be induced in the CM loop, which may cause the magnetic saturation of the CM choke. Furthermore, the CMV stress on the motor will increase and the insulation challenge will be produced [53]. The core size of the CM choke is directly related to the PTP magnitude of i_{cm}. As investigated in [53], if a toroid core is adopted and the PTP magnitude of i_{cm} is reduced by half, the core cross-sectional area, mean length per turn, and total copper loss of the choke can be reduced by 60%, 37%, 22.25% respectively, which contributes to the size reduction of the CM choke.

2.4.3 Proposed Cost Function With CM Resonance Suppression

To reduce the CM current in the CSCs-fed PMSM system, the cost functions of the FCS-MPC for both CSR and CSI sides are designed. For the CSR side, to suppress the LC filter resonance, the grid current and the capacitor voltage tracking at the CSR side are regulated simultaneously through the cost function (2.18). On the other hand, because the frequency of dominant component V_{cmr_3} is constant at 180Hz and the amplitude of grid voltage is constant as well, the component of i_{cm} induced by V_{cmr} will not change much. The peak of i_{cm} can be reduced if the PTP magnitude of V_{cmr} is suppressed well. Based on these two control objectives, the cost function for the CSR side can be designed as follows

$$\begin{aligned} J_{\mathrm{CSR}} = &\left[\boldsymbol{x}_{\boldsymbol{g}}^{*} - \boldsymbol{x}_{\boldsymbol{g}}(k+2)\right]^{\mathrm{T}} \mathbf{W} \left[\boldsymbol{x}_{\boldsymbol{g}}^{*} - \boldsymbol{x}_{\boldsymbol{g}}(k+2)\right] + \\ &\lambda_{sfr} \left|\boldsymbol{I}_{\boldsymbol{wr}}(k+1) - \boldsymbol{I}_{\boldsymbol{wr}}(k)\right| + \lambda_{V_{cmr}} \left|V_{cmr}(k+1)\right| \end{aligned} \tag{2.51}$$

where $\lambda_{V_{cmr}}$ is the positive weighting factor for the penalization of PTP magnitude of V_{cmr}. The predictive V_{cmr} can be calculated according to the definition in (2.47).

For the CSI-fed PMSM side, the electromagnetic torque T_e and stator flux ψ_s can be controlled implicitly by regulating the stator current of PMSM. However, because the CL resonance may occur and cause harmonic distortion, the feedback of stator voltage (capacitor voltage) should be introduced into the cost function as well. Therefore, the first component of the cost function for the CSI side is designed as

$$J_{\text{CSI1}} = [\boldsymbol{x}_{\boldsymbol{s}}^* - \boldsymbol{x}_{\boldsymbol{s}}(k+2)]^{\text{T}} \mathbf{W}_{\mathbf{s}} [\boldsymbol{x}_{\boldsymbol{s}}^* - \boldsymbol{x}_{\boldsymbol{s}}(k+2)] + \lambda_{sfi} |\boldsymbol{I}_{\boldsymbol{wi}}(k+1) - \boldsymbol{I}_{\boldsymbol{wi}}(k)| \tag{2.52}$$

where the second item penalizes the switching frequency with the weighting factor λ_{sfi}. The q-axis reference i_{sq}^* comes from the outer PI loop for motor speed regulation and the d-axis reference i_{sd}^* is set as 0 to achieve the operation with the maximum torque current ratio. The positive weighting factor matrix $\mathbf{W_s}$ is used to tune the priority of stator voltage tracking and thus the filter resonance can be controlled. The steady-state reference of stator voltage can be derived as

$$\begin{cases} v_{sd}^* = R_s i_{sd}^* - \omega_s L_s i_{sq}^* \\ v_{sq}^* = R_s i_{sq}^* + \omega_s L_s i_{sd}^* + \omega_s \psi_f \end{cases} \tag{2.53}$$

Since the CM resonance will be excited by V_{cmi} when the motor runs in the low-speed region, the CMV control strategy is different from that of the CSR side. The CM current will be mainly amplified by the third-order component V_{cmi_3} at the CSI side. Therefore, it is important to eliminate V_{cmi_3} when the motor runs at a low speed. To achieve this goal, the cost function is designed as follows to limit V_{cmi_3} but not the PTP magnitude of V_{cmi} in the low-speed region

$$J_{\text{CSI2\_LS}} = \lambda_{V_{cmi\_3}} |V_{cmi\_3}(k+1)| \tag{2.54}$$

where $\lambda_{V_{cmi\_3}}$ is the positive weighting factor for the penalization of the magnitude of V_{cmi_3}. As can be seen in (2.54), to effectively suppress the magnitude of V_{cmi_3}, the extraction of harmonic information is needed. The SDFT can

be employed to predict the harmonic information and be realized in real-time with a low computational cost. The principle of SDFT is to store the data of the signal into a buffer with a constant dimension. With the signal updated, the new predictive data of the signal is sent into the buffer while the first data in the buffer is discarded. Based on the recursive expression

$$|V_{cmi\_h}(k+1)| = |V_{cmi\_h}(k)|\, e^{j\frac{2\pi h}{N}} - V_{cmi}(k-N) + V_{cmi}(k) \tag{2.55}$$

the predictive harmonic component can be calculated, where the positive integer h refers to the extracted harmonic order of V_{cmi}, i.e., h=3. As the motor speed increases, the CM resonance will be alleviated since the stator frequency will gradually move away from the resonant range of the CM loop. Therefore, the third-order component V_{cmi_3} can be blocked effectively by the CM choke and i_{cm} will reduce consequently. In this case, the control objective should switch from the elimination of V_{cmi_3} to the suppression of the PTP magnitude of V_{cmi}. As a result, the PTP value of i_{cm} will be reduced in the high-speed region, which contributes to the reduction of the CM choke size. According to this principle, the cost function for the high-speed region with PTP magnitude suppression of V_{cmi} is designed as

$$J_{\text{CSI2\_HS}} = \lambda_{V_{cmi}} |V_{cmi}(k+1)| \tag{2.56}$$

Finally, the cost function design for the CSI-fed PMSM side is expressed as

$$J_{\text{CSI}} = J_{\text{CSI1}} + J_{\text{CSI2}} \quad J_{\text{CSI2}} = \begin{cases} J_{\text{CSI\_LS}} & \omega_s < \omega_B \\ J_{\text{CSI\_HS}} & \omega_s \geq \omega_B \end{cases} \tag{2.57}$$

where ω_B is the speed boundary to distinguish whether the motor is running in the low-speed region or the high-speed region.

The proposed FCS-MPC scheme for the CSCs-fed PMSM drive system is shown in Fig. 2.28. The PI loop of the CSR side regulates the dc-link current by generating the active power reference, and then the current and capacitor voltage references can be derived. The predictive information of state variables and the value of V_{cmr} can be calculated. Subsequently, the variable $\boldsymbol{i_g}$ and $\boldsymbol{v_{cr}}$ are regulated to track their reference and the PTP magnitude of V_{cmr} value is suppressed via the cost function (2.51). For the CSI side, the

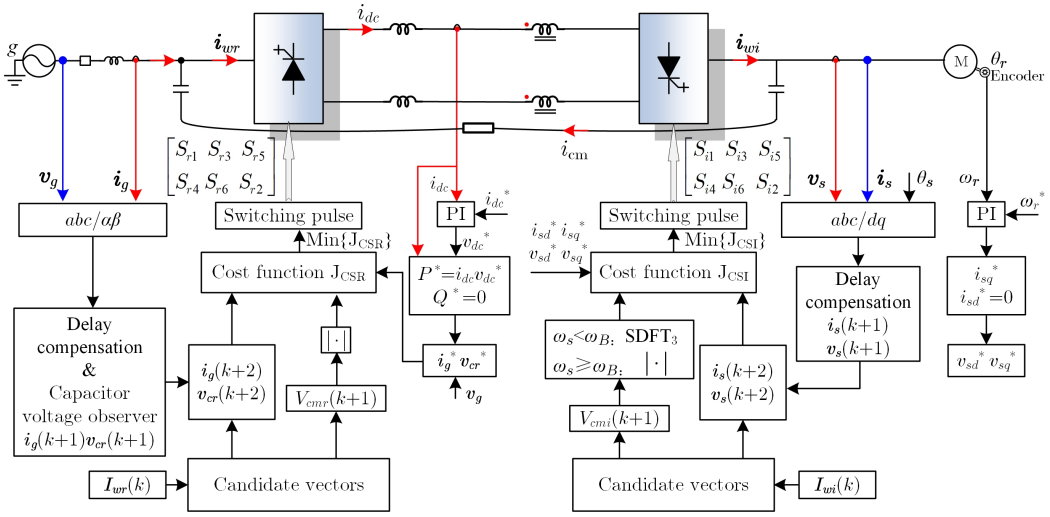

Figure 2.28: The proposed FCS-MPC scheme for transformerless CSCs-fed PMSM drive.

outer speed loop generates the dq-axis current reference and then the capacitor voltage reference can be calculated. The information of V_{cmi} is predicted by the candidate switching state. The control objective for the CSI side CMV depends on the speed region of PMSM. When the speed is lower than the defined boundary value ω_B, the CM resonance suppression is prioritized, and thus V_{cmi_3} is extracted and then penalized in the cost function. With the increased speed of the PMSM, the CMV control objective switches to the PTP magnitude suppression of V_{cmi}. The regulation of CMV at both CSR and CSI sides provides the freedom to decide which zero vectors will be selected. Thus, all of the three zero-vectors $\boldsymbol{i_{wr(i)z1}}$, $\boldsymbol{i_{wr(i)z2}}$ and $\boldsymbol{i_{wr(i)z3}}$ can be included in the next control interval.

The proposed FCS-MPC takes the advantage of multi-objective optimization for the transformerless CSC-fed drive system. Since both the capacitor voltage of CSR and CSI sides are controlled effectively, the LC/CL filter resonance is mitigated with reduced complexity compared to the existing AD schemes. Moreover, the control scheme concentrates on all CMV generated in the system, where the CM current reduction is the core. Therefore, the size of the CM choke employed in the drive system can be reduced, which saves cost and improves total efficiency.

2.4.4 Simulation and Experimental Results

In order to verify the performance of the proposed FCS-MPC scheme for the transformerless CSCs-fed PMSM drives, a simulated system with 1MVA rated power is realized in the MATLAB/Simulink. The system parameters are shown in Table 2.3. The sampling frequency for the whole system is 12kHz. The weighting factors used in the simulation are $\lambda_{v_{cr}}$=0.0008, $\lambda_{V_{cmr}}$=0.002, $\lambda_{v_{ci}}$ =0.0015 and $\lambda_{V_{cmi}}$ =0.001 respectively. The weighting factors λ_{sfr} and λ_{sfi} are tuned to maintain the 1kHz switching frequency of CSC.

Table 2.3: Simulated and experimental parameters of the transformerless CSCs-fed PMSM drive system

	Parameters	Simulated value	Experimental value
CSR	Grid voltage (line-to-line)	4160V	90V
	Nominal power	1MVA	10kVA
	Grid frequency	60Hz	60Hz
	Line inductance L_r	4.58mH	2.5mH
	Input filter capacitance C_{fr}	76.64μF	160μF
DC link	Differential-mode inductance L_{diff}	31.5mH	40mH
	Common-mode inductance L_{cm}	400mH	100mH
	CM resistance R_{cm}	15Ω	5Ω
	CM resonance frequency f_{cm_res}	30Hz	32Hz
CSI-PMSM	Output capacitance C_{fi}	46μF	120μF
	Rated power of PMSM	1MVA	1kW
	Rated stator frequency	80Hz	100Hz
	Rated torque of PMSM	8000N·m	8N·m
	Stator inductance L_s	5.46mH	3.1mH
	Permanent fluxψ_f	8.45Wb	0.15Wb
	Pole pairs	4	5
	Monent of inertia J	18kg·m^2	0.0012kg·m^2

The verification of CM current when PMSM runs in the low-speed region is performed in Fig. 2.29. The rotor speed n_r is kept at 150r/min and thus the stator frequency is 10Hz, which implies the V_{cmi} will contain a dominant 30Hz component and the CM resonance will be amplified at this speed. The load torque is 4000N·m to simulate the light load and low-speed operation.

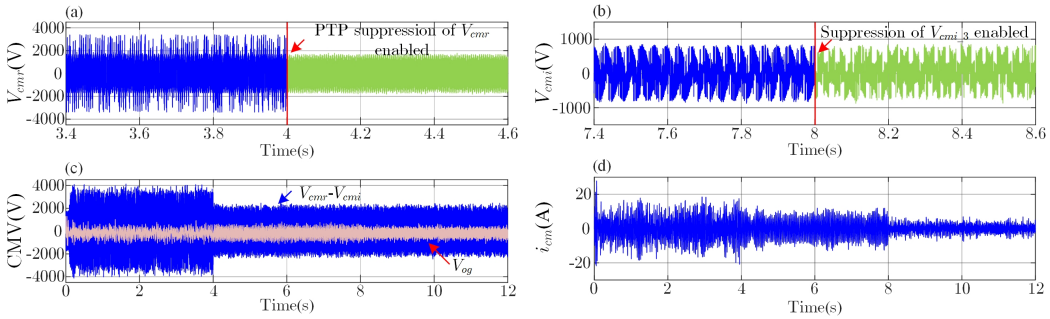

Figure 2.29: The simulated performance in the low-speed region. (a) The waveform of V_{cmr}, (b) The waveform of V_{cmi}. (c) The system CMV with and without the integrated dc-link choke. (d) The waveform of the CM current.

At the 4s instance, the suppression of the PTP magnitude of V_{cmr} is enabled, where the weighting factor $\lambda_{V_{cmr}}$ changes from 0 to 0.002. Therefore, the effect of the reduced V_{cmr} on the performance of CM current can be shown. The suppression for V_{cmi_3} is enabled at the 8s instance, where the weighting factor $\lambda_{V_{cmi\_3}}$ changes from 0 to 0.001. Fig.2.29 (a) and (b) shows the waveform of V_{cmr} and V_{cmi} respectively. As can be seen, the PTP magnitude of V_{cmr} is reduced effectively at the 4s instance when the penalization item in the cost function is enabled. Consequently, the PTP magnitude of i_{cm} is mitigated at the instant 4s, which can be seen in Fig. 2.29(d). Besides, the suppression of the third-order harmonic V_{cmi_3} is realized via the cost function and thus the PTP magnitude of i_{cm} is significantly reduced. To show the effect of the CM choke, the waveform V_{cmr}-V_{cmi}, which represents the CMV of the system without the CM loop, and V_{og} with the CM loop are compared in Fig. 2.29(c). It can be seen the majority of the system CMV is blocked by the CM choke, and thus the voltage stress generated on the motor neutral point is effectively reduced. Since i_{cm} is suppressed by the proposed FCS-MPC scheme, the size of the choke and the CM loop resistance can be lower.

To further verify the performance improvement of i_{cm}, Fig. 2.30 gives the zoom-in view of i_{cm} and the corresponding spectrum using the FFT analysis. Moreover, the spectrum of the system CMV V_{og} is presented. It can be seen in Fig. 2.30(a) that without any CMV suppression strategy, the dominant components of i_{cm} are the 30Hz harmonic and 180Hz harmonic, which are

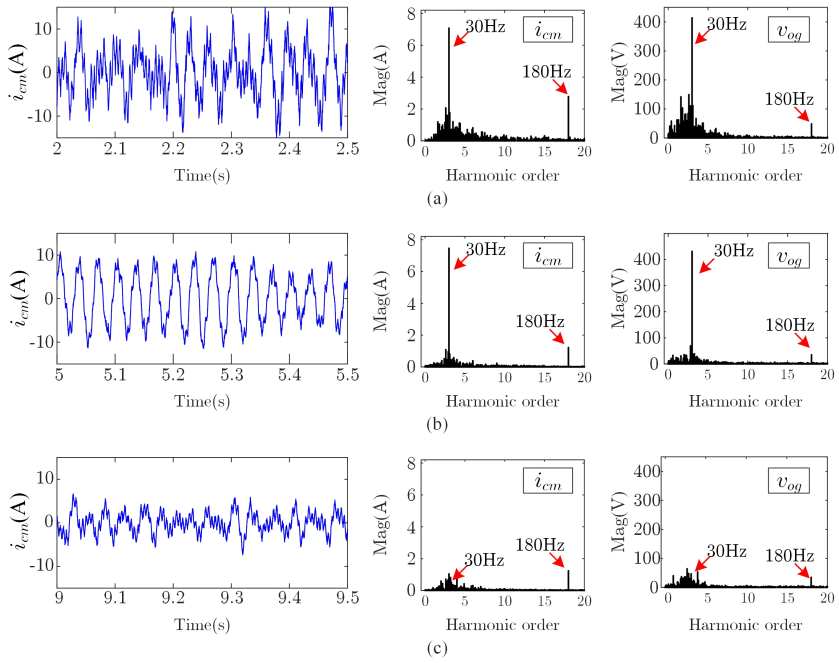

Figure 2.30: The waveform of CM current and the corresponding FFT spectrums under different CMV scenes. (a) Without suppression of PTP magnitude of V_{cmr} and V_{cmi_3}. (b) With only the suppression of PTP magnitude of V_{cmr}. (c) With the suppression of PTP magnitude of V_{cmr} and V_{cmi_3} simultaneously.

generated by the V_{cmi_3} and V_{cmr_3} respectively. However, since the resonant frequency of the CM loop is 30Hz, the CM current at this frequency is amplified. While the component with 180Hz is blocked because of the relatively large impedance of the CM loop. In Fig. 2.30(b), with the PTP magnitude suppression of V_{cmr}, the low-order harmonics, as well as the 180Hz component of V_{og}, are reduced. It can be also found that the magnitude of the 180Hz component in i_{cm} is approximately reduced by half, and the low-order harmonics are eliminated as well. In Fig. 2.30(c), with the suppression of the third-order harmonic V_{cmi_3}, the 30Hz component in V_{og} is reduced significantly. As a result, the CM resonance is attenuated effectively. Therefore, with the suppression of the PTP magnitude of V_{cmr} and the third-order harmonic V_{cmi_3} concurrently, the peak of i_{cm} is maintained low when the motor runs in the low-speed region.

The verification of CM current when PMSM runs at a high speed is performed in Fig. 2.31. The PMSM runs at 960r/min speed with 8000N·m load torque and the stator frequency is 80Hz. The arrangement of simulation time

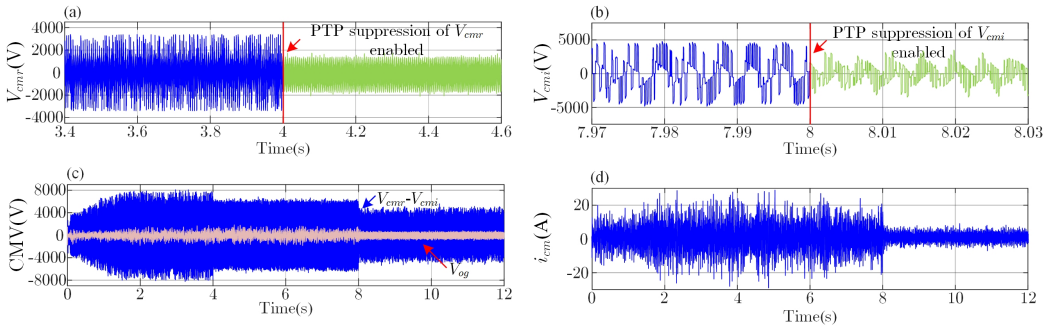

Figure 2.31: The simulated performance in the high-speed region. (a) The waveform of V_{cmr} before and after the PTP magnitude suppression. (b) The waveform of V_{cmi} before and after the PTP magnitude suppression. (c) The CMV waveform of the system with and without the integrated dc-link choke. (d) The waveform of the CM current.

for the CSR side is the same as the low-speed condition. At the 8s instance, the CMV penalization item in the cost function of the CSI side is replaced by the suppression of the PTP magnitude of V_{cmi}. Fig. 2.31 (a) and (b) show the waveform of V_{cmr} and V_{cmi} respectively. The PTP magnitude of V_{cmr} and V_{cmi} are reduced respectively at the 4s instance and 8s instance when the suppression item in the cost function is enabled. With the use of the CM choke, the total CMV of the system V_{og} can be significantly eliminated as seen in Fig. 2.31(c). Moreover, the magnitude of i_{cm} is reduced accordingly with the reduction of the CMV of both sides, which can be seen in Fig. 2.31(d).

Fig. 2.32 shows a scaled IGCT-based hardware prototype for CSC-fed PMSM drives. The MicroLabBox 1202 controller is employed to verify the proposed FCS-MPC scheme experimentally. The detailed setup parameters are given in Table 2.3. The sampling frequency for the whole system is set as 12kHz. The weighting factors used in the experiment are $\lambda_{v_{cr}}$=0.001, $\lambda_{V_{cmr}}$=0.001, $\lambda_{v_{ci}}$ =0.0012 and $\lambda_{V_{cmi}}$ =0.001.

The experimental waveform of speed, torque, phase current, and CM current are shown in Fig. 2.33 when the PMSM runs with a 12Hz stator frequency and a 3N·m load torque. Moreover, the spectrum of the CM current is also presented. It can be seen in Fig. 2.33(a) that without any CMV suppression strategy, the dominant components of i_{cm} are the 36Hz harmonic and the 180Hz harmonic, which are generated by the V_{cmi_3} and V_{cmr_3} respectively. In Fig. 2.33(b), It can be also found that the magnitude of the 180Hz component

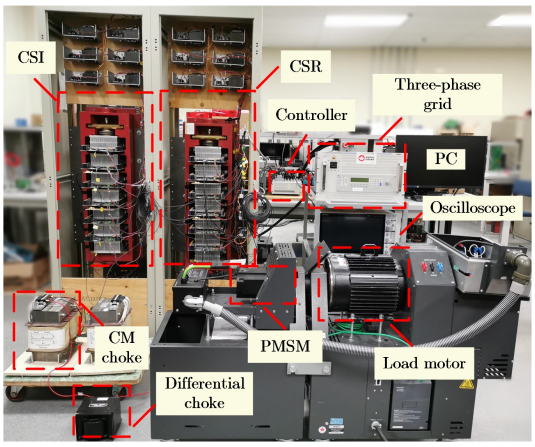

Figure 2.32: Experimental setup of the IGCTs-based CSCs-fed PMSM drive system.

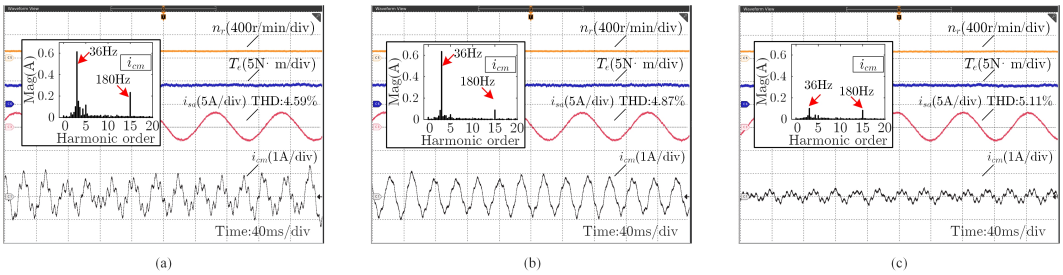

Figure 2.33: The experimental waveform of speed, torque, phase stator current, CM current and the corresponding FFT spectrums of CM current under different CMV scenes. (a) Without any suppression. (b) With only the suppression of PTP magnitude of V_{cmr}. (c) With the suppression of PTP magnitude of V_{cmr} and V_{cmi_3} simultaneously.

in i_{cm} is approximately reduced by half with the PTP magnitude suppression of V_{cmr}, and the low-order harmonics are eliminated as well. Furthermore, with the suppression of V_{cmi_3}, the CM resonance is attenuated effectively which can be found from the spectrum of i_{cm} in Fig. 2.33(c). Therefore, when the motor runs in the low-speed region, the CM resonance and the peak of CM current can be reduced effectively by the proposed scheme. Moreover, the THD of the phase stator current does not change much with the CM current control. The stator current performs well without resonance.

Fig. 2.34 shows the experimental waveforms of speed, torque, phase current, and CM current when the PMSM runs at 30Hz stator frequency and a 6N·m load torque. Firstly, the spectrum of CM current in Fig. 2.34(a) is compared with that in Fig. 2.33(a). It can be seen that the CM resonance has been alleviated with the higher motor speed, which is the result of the in-

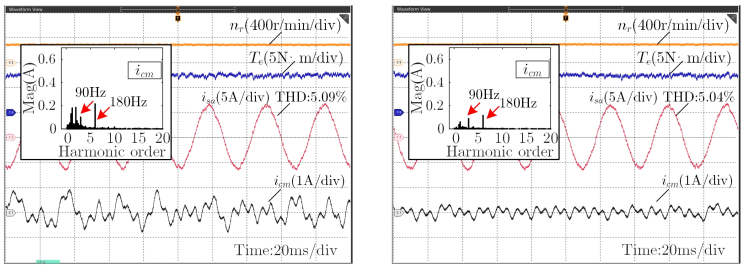

Figure 2.34: The experimental waveform under different CMV scenes with 30Hz stator frequency. (a) Without any suppression. (b) With the suppression of PTP magnitude of V_{cmr} and V_{cmi} simultaneously.

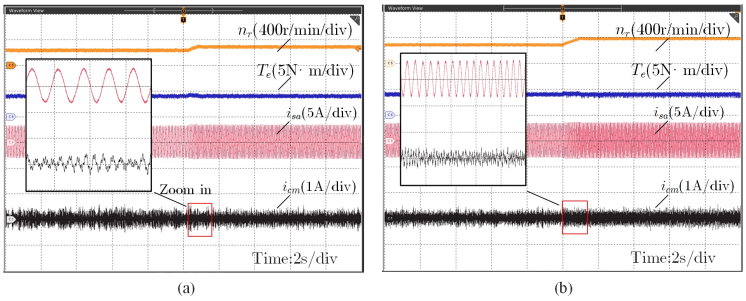

Figure 2.35: The dynamic performance of the proposed FCS-MPC. (a) The stator frequency changes from 12Hz to 15Hz (The low-speed region). (b) The stator frequency changes from 15Hz to 20Hz (The control objective of CSI-side changes from suppression of V_{cmi_3} to the PTP magnitude of V_{cmi}).

creased loop impedance and the CM choke effectively blocking the third-order component. Therefore, the control objective for the CSI side can switch to the PTP magnitude suppression of V_{cmi}. As can be seen in Fig. 2.34(b), with the suppression of the PTP magnitude of both V_{cmr} and V_{cmi}, the CM current can be reduced significantly.

The experiment for dynamic tests are shown in Fig. 2.35. In Fig. 2.35(a), with the stator frequency changing from 12Hz to 15Hz, the third-order harmonic component is always suppressed and thus the peak value of the CM current is low without any large spikes during the dynamic process. In Fig. 2.35(b), when the stator frequency further increases to 20Hz, the control objective of the CSI side switches to the PTP magnitude suppression of V_{cmi}, and the peak value of the CM current is still maintained at a low level without obvious spikes.

2.5 Summary

This chapter firstly proposes an improved FCS-MPC scheme for the high-power CSR in the MV motor drive application. Under normal grid conditions, the proposed FCS-MPC directly takes grid current and capacitor voltage reference tracking into the cost function without using the AD concept. Under distorted grid conditions, two targeted improvements are employed, which are realized through extracting the fundamental grid voltage to modify the current reference and adding the predictive harmonic current suppression items into the cost function, which can reduce harmonics magnitude and improve grid current quality with an acceptable computational burden. Furthermore, to improve the robustness of the one-step FCS-MPC, the observer is proposed to estimate the capacitor voltage reference and unknown input disturbance. The experimental results have verified that the zero tracking error can be always achieved under various parameter mismatch scenarios. In addition, the performance of longer horizon FCS-MPC with only grid current feedback has been assessed. The results show that the long horizon prediction guarantees CSR performance, providing the benefits such as a simplified design stage without weighting factors and additional capacitor voltage reference estimation. Finally, this chapter proposes the FCS-MPC scheme applied to the transformerless CSCs-fed PMSM drives system. The multi-objective optimization is realized through the designed cost function for both CSR and CSI sides. The LC/CL filter resonance is mitigated by directly controlling the capacitor voltage at two sides. The PTP magnitude of the CMV generated from the CSR side is always suppressed. The effect of the CMV generated from the CSI side at different speed ranges is analyzed. In the low-speed range, the control objective suppresses the third-order harmonic of CMV since the CM resonance will be excited. Whereas, in the high-speed range, the CSI side switches to the suppression of the PTP magnitude of CMV. From the simulated results for the 1MVA drive system and the scaled-down experiments, it can be concluded that the proposed MPC with transformerless operation can eliminate the voltage stress on the neutral point of the motor, which is maintained as

10%-15% of the CMV generated by the converter. The CM current is reduced significantly, and thereby the core cross-sectional area, mean length per turn, and total copper loss of the choke can be reduced at least by 60%, 37%, and 22.25% respectively, if a toroid core is adopted.

The proposed cost function design with direct multi-variable feedback can also be applied to the second-order LC-filtered VSCs or extended to the third-order LCL-filtered systems. Specifically, the LC-filtered VSCs share the duality property with the CSCs and the inductor current and capacitor voltage can be controlled through the cost function in a similar formulation. The third-order LCL-filtering model introduces an additional state variable, whose trajectory regulation can also be added to the cost function through a new weighting factor. Correspondingly, the disturbance-observer-based control can be universally applied to those applications with robustness enhancement and the same benefits can be brought by the long prediction horizon. The proposed FCS-MPC can be applied to motor drives that share similar problems regarding the specific harmonic order of CMV reduction and CM resonance suppression.

Chapter 3

FCS-MPC With Reduced DC-link Capacitor RMS Current for BTB VSCs-fed Motor Drives

This chapter designs the FCS-MPC for the VSCs-fed PMSM drive system to reduce the intermediate dc-link capacitor RMS current, thus reducing the capacitor size or extending its lifetime. So far, extensive previous research for the capacitor RMS reduction in the BTB system is the carrier-based PWM framework. As a control strategy that is inherently different from the typical way, the elimination of carrier-based switching operation through the FCS-MPC will generate a distinctive capacitor current spectrum with more possible harmonic reduction. Thus, the FCS-MPC is used as the control framework and its full potential is developed to directly optimize the capacitor current performance. The typical SVPWM with the synchronous carrier is selected as the benchmark for the comparison. The state-space modeling of the BTB drive system will be first formulated. Then, the SVPWM scheme with the synchronous carrier will be reviewed and discussed. Next, the FCS-MPC with capacitor current optimization will be proposed, and the weighting factor selection is also introduced. Finally, the comparative simulation and experimental results will be shown to highlight the benefits of the proposed method.

3.1 The Modeling for the BTB VSCs-fed PMSM System

This section builds the predictive equation for the grid-connected VSR and VSI-fed PMSM side respectively and the future grid current and motor current can be obtained, which lays the fundamentals for the predictive controller design. As shown in Fig. 1.5, a pair of the well-known two-level VSC is used as the AFE rectifier and the inverter respectively. The variable speed load takes a PMSM for the case study. The control schemes for the two sides are developed under the synchronous dq frame. The general variables $\xi_{\mathrm{d}q}$ can be calculated from the ξ_{abc} in three-phase abc reference frame by following Park's transformation.

$$\xi_{\mathrm{d}q} = T_{\mathrm{Park}}\xi_{abc} \tag{3.1}$$

where the matrix $T_{\mathrm{Park}} = \frac{2}{3}\begin{bmatrix} \cos\theta & \cos\left(\theta - \frac{2\pi}{3}\right) & \cos\left(\theta + \frac{2\pi}{3}\right) \\ -\sin\theta & -\sin\left(\theta - \frac{2\pi}{3}\right) & -\sin\left(\theta + \frac{2\pi}{3}\right) \end{bmatrix}$ and θ could be the phase angle of grid voltage or the electrical position angle of the PMSM.

3.1.1 Predictive Model of the VSR-Side

For the grid-connected VSR, the phase angle of the grid voltage θ_g is obtained through the phase-locked loop (PLL) block with grid voltage oriented on the d-axis. After the Park's transformation, the grid voltage vector is $\boldsymbol{v_g} = [v_{gd}\ v_{gq}]^{\mathrm{T}}$, and $\boldsymbol{u_g} = [v_{rd}\ v_{rq}]^{\mathrm{T}}$ represents the controllable voltage variable generated by the VSC. The grid current $\boldsymbol{i}_g = [i_{gd}\ i_{gq}]^{\mathrm{T}}$ is selected as the state variables. According to the Kirchhoff voltage and current laws, the state-space model of the rectifier-side can be expressed by the following continuous-time equation

$$\frac{d\boldsymbol{i_g}}{dt} = \mathbf{A_g}\boldsymbol{i_g} + \mathbf{B_g}\boldsymbol{u_g} + \mathbf{H_g}\boldsymbol{v_g} \tag{3.2}$$

where the system matrix $\mathbf{A_g}$, input matrix $\mathbf{B_g}$, and the disturbance matrix $\mathbf{H_g}$ are given by

$$\mathbf{A_g} = \begin{bmatrix} -\frac{R_g}{L_g} & \omega_g \\ -\omega_g & -\frac{R_g}{L_g} \end{bmatrix}, \mathbf{B_g} = \begin{bmatrix} -\frac{1}{L_g} & 0 \\ 0 & -\frac{1}{L_g} \end{bmatrix}, \mathbf{H_g} = \begin{bmatrix} \frac{1}{L_g} & 0 \\ 0 & \frac{1}{L_g} \end{bmatrix} \tag{3.3}$$

The grid-side filter inductance is L_g and R_g is the equivalent serial resistance, and ω_g is the angular frequency of the grid voltage. To facilitate the controller implementation in the digital platform, the continuous modeling (3.3) can be discretized as follows based on the ZOH principle.

$$\boldsymbol{i_g}(k+1) = \mathbf{A_{gd}}\boldsymbol{i_g}(k) + \mathbf{B_{gd}}\boldsymbol{u_g}(k) + \mathbf{H_{gd}}\boldsymbol{v_g}(k) \tag{3.4}$$

where k represents the current sampling step. The discrete matrices can be calculated based on the forward Euler discretization, i.e., $\mathbf{A_{gd}} = (\mathbf{A_g} + \mathbf{I}_2)T_s$, $\mathbf{B_{gd}} = \mathbf{B_g}T_s$, and $\mathbf{H_{gd}} = \mathbf{H_g}T_s$. The $\mathbf{I}_2$ is the two-dimension identity matrix and T_s denotes the time length of the sampling interval.

3.1.2 Predictive Model of the VSI-fed PMSM Side

For the surface-mounted PMSMs, the continuous modeling in the synchronous dq frame can be expressed as follows.

$$\frac{d\boldsymbol{i_s}}{dt} = \mathbf{A_s}\boldsymbol{i_s} + \mathbf{B_s}\boldsymbol{u_s} + \mathbf{E_s} \tag{3.5}$$

where the stator current vector $\boldsymbol{i_s} = [i_{sd}\ i_{sq}]^{\mathrm{T}}$ and and the VSC input voltage vector $\boldsymbol{u}_s = [v_{id}\ v_{iq}]^{\mathrm{T}}$. The system matrix $\mathbf{A_s}$, input matrix $\mathbf{B_s}$ and disturbance matrix $\mathbf{E_s}$ are respectively given by

$$\mathbf{A_s} = \begin{bmatrix} -\frac{R_s}{L_s} & \omega_s \\ -\omega_s & -\frac{R_s}{L_s} \end{bmatrix}, B_s = \begin{bmatrix} \frac{1}{L_s} & 0 \\ 0 & \frac{1}{L_s} \end{bmatrix}, E_s = \begin{bmatrix} 0 \\ -\frac{\omega_s \psi_f}{L_s} \end{bmatrix} \tag{3.6}$$

where R_s is the stator resistance, L_s is the stator inductance, ψ_f represents the magnitude of rotor flux, and ω_s is the electrical angular velocity obtained through the encoder. Similarly, the discretized modeling can be from (3.6) based on the ZOH principle, i.e.,

$$\boldsymbol{i_s}(k+1) = \mathbf{A_{sd}}\boldsymbol{i_s}(k) + \mathbf{B_{sd}}\boldsymbol{u_s}(k) + \mathbf{E_{sd}} \tag{3.7}$$

where $\mathbf{A_{sd}} = (\mathbf{A_s} + \mathbf{I}_2)T_s$, $\mathbf{B_{sd}} = \mathbf{B_s}T_s$, and $\mathbf{E_{sd}} = \mathbf{E_s}T_s$.

3.2 Conventional Carrier-based SVPWM scheme

The typical control scheme applied to the BTB VSCs-fed PMSM drive system contains the controller stage and the modulator block. The controller generates

the reference voltage command and the modulator block transforms it into the switching signal for the converters [100]. In this process, the switching state of the VSC maps the three-phase current into the current pulse at the dc side, and the instantaneous dc-side current of both the rectifier and inverter sides determines the dc-link capacitor current. Thus, the capacitor current is essentially determined by the applied modulator. In this chapter, the deadbeat control is selected as the controller stage for both sides and the SVPWM is used as the modulator to realize the conventional carrier-based PWM scheme. Compared to the typical PI-based VOC for the rectifier side and the FOC for the motor side [101], [102], the deadbeat controller provides the benefits such as faster dynamic response and simplified parameter tuning procedure. Besides, the reference voltage calculated in a deadbeat way can be subsequently used in the proposed FCS-MPC to facilitate the candidate switching state searching.

3.2.1 Deadbeat Control Law

Fig. 3.1 shows the detailed diagram of the deadbeat control plus the carrier-based SVPWM scheme. Firstly, the DC-link capacitor voltage is controlled through the outer PI loop at the rectifier side, which generates the d-axis grid current reference for the inner control loop. To implement the power balance control and improve the dynamic capacitor current performance, the inverter-side power is calculated and then the feedforward current component i_{gd_ff} is superimposed to obtain the final d-axis current reference i_{gd}^*. The q-axis grid current reference i_{gq}^* is set as zero to achieve the unity power factor.

With the grid current reference $\boldsymbol{i_g^*} = [i_{gd}^* \; i_{gq}^*]^{\mathrm{T}}$ and the real-time sampling current information, the desired reference voltage in the deadbeat control way can be inversely calculated according to (3.4). However, considering the digital delay in practical application, the one-step forward compensation should be introduced and the predictive grid current at the $(k{+}2)th$ instant is controlled to track the given reference value. To this end, the $(k{+}1)th$ instant predictive current is firstly calculated based on the reference voltage determined from

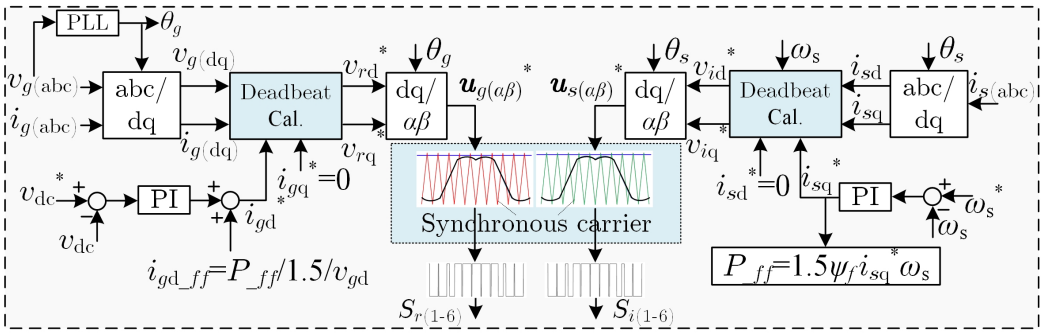

Figure 3.1: The deadbeat+carrier-based SVPWM control scheme for the BTB VSCs-fed drive system.

the last sampling interval, i.e.,

$$\boldsymbol{i_g}(k+1) = \mathbf{A_{gd}}\boldsymbol{i_g}(k) + \mathbf{B_{gd}}\boldsymbol{u_g^*}(k-1) + \mathbf{H_{gd}}\boldsymbol{v_g}(k) \tag{3.8}$$

where $\boldsymbol{u_g^*} = [v_{rd}^*\ v_{rq}^*]^{\mathrm{T}}$ is the optimal voltage input. Based on the grid current reference $\boldsymbol{i_g^*}(k+2)$ and the predictive equation for the rectifier side, the optimal reference voltage for the kth instant can be derived as follows.

$$\boldsymbol{u_g^*}(k) = \left(\mathbf{B_{gd}}^{\mathrm{T}}\mathbf{B_{gd}}\right)^{-1}\mathbf{B_{gd}}^{\mathrm{T}}\left[\boldsymbol{i_g^*}(k+2) - \mathbf{A_{gd}}\boldsymbol{i_g}(k+1) - \mathbf{H_{gd}}\boldsymbol{v_g}(k)\right] \tag{3.9}$$

Substituting (3.8) into (3.9), the deadbeat control law for the rectifier side can be expressed as follows.

$$\begin{aligned}\boldsymbol{u_g^*}(k) = &\left(\mathbf{B_{gd}}^{\mathrm{T}}\mathbf{B_{gd}}\right)^{-1}\mathbf{B_{gd}}^{\mathrm{T}} \\ &\cdot\left[\boldsymbol{i_g^*}(k+2) - \mathbf{A_{gd}}^2\boldsymbol{i_g}(k) - \mathbf{A_{gd}}\mathbf{B_{gd}}\boldsymbol{u_g^*}(k-1) - \right. \\ &\left.\left(\mathbf{A_{gd}}\mathbf{H_{gd}} + \mathbf{H_{gd}}\right)\boldsymbol{v_g}(k)\right]\end{aligned} \tag{3.10}$$

In this process, the $(k+2)th$ instant grid current reference can be obtained through the Lagrangian extrapolation [103]. Also, the dq-axes grid voltage components are constant, and thus $\boldsymbol{v_g}(k+1) = \boldsymbol{v_g}(k)$ can be adopted for derivation of control law. Finally, the dq-axes reference voltages v_{rd}^* and v_{rq}^* are transformed into the components in the stationary $\alpha\beta$ frame, which are then generated through the modulator block.

Similar to the derivation for the AFE rectifier side, the deadbeat control law for the motor side control with delay compensation can be expressed as

follows.

$$\begin{aligned}\boldsymbol{u_s^*}(k) = &\left(\mathbf{B_{sd}}^{\mathrm{T}}\mathbf{B_{sd}}\right)^{-1}\mathbf{B_{sd}}^{\mathrm{T}} \\ &\cdot\left[\boldsymbol{i}_s^*(k+2) - \mathbf{A_{sd}}^2\boldsymbol{i_s}(k) - \mathbf{A_{sd}}\mathbf{B_{sd}}\boldsymbol{u_s^*}(k-1) - \right. \\ &\left.(\mathbf{A_{sd}}\mathbf{E_{sd}} + \mathbf{E_{sd}})\right]\end{aligned} \tag{3.11}$$

where $\boldsymbol{u_s^*} = [v_{id}^*\ v_{iq}^*]^{\mathrm{T}}$ is the optimal voltage input for the inverter, $\boldsymbol{i_s^*} = [i_{sd}^*\ i_{sq}^*]^{\mathrm{T}}$ is the stator current reference. The mechanical dynamics of the PMSM are assumed to be slow compared to the fast sampling operation, i.e., $\omega_s(k+1) \approx \omega_s(k)$. For the stator current reference, the d-axis reference i_{sd}^* is set as 0 to achieve the maximum torque current ratio operation and the q-axis reference i_{sq}^* is generated from the outer PI speed loop. The $(k+2)th$ instant current reference still can be predicted through the Lagrangian extrapolation. The dq-axes reference voltages v_{id}^* and v_{iq}^* are transformed into the stationary $\alpha\beta$ frame to implement the modulation process.

3.2.2 Capacitor Current With the Synchronous Carrier

The modified PWM switching patterns for the single converter stage have been proposed to reduce the capacitor RMS current, such as the dual carrier-based PWM for the hybrid active neutral point clamped inverter [104] and the optimal carrier phase-shift strategy for the paralleled inverters [105], etc. Nonetheless, these specific PWM adjustments for single-stage converter cannot be applied to the BTB drive case because it is the DC-side current pulse cancellation between the rectifier and inverter that determine the capacitor current ripple. Specifically, for the BTB drives, the improved discontinuous PWM (DPWM) was proposed in [106], where the inverter-side switching sequence was adjusted to make the generated dc-side current pulse cancel that of the AFE side. Although the capacitor current ripple of the proposed DPWM is smaller than that of the conventional one, it does not give a significant improvement compared to the SVPWM. Moreover, the DPWM is limited to the high-power application while in low-power occasions and high switching frequency applications, the SVPWM is still the most commonly used [66]. According to the investigation in [66], [107], the SVPWM with the synchronous carrier is an optimal approach for the BTB drives to reduce the capacitor cur-

rent ripple as much as possible, where both the carrier frequency and phase shift at the two sides should be kept the same. In [108] and [109], the harmonic phase feedback control is applied to the BTB drives to cancel the first/second carrier band harmonic in the capacitor current. The order of desired harmonic is extracted through the digital bandpass filter from the dc-link current, which complicates the tuning procedure and deteriorates the dynamic system response. Most importantly, only the sole specific carrier band harmonics can be set as the control objective in this method, which cannot handle other dominant components in the capacitor current.

The SVPWM is a typical modulation scheme used for the two-level VSC because of the best harmonic profile performance [100]. With the obtained control law (3.10) and (3.11), the SVPWM is adopted at the rectifier and inverter sides to transform the reference voltage into switching signals. As a result, the fundamental frequency of the dc-side current pulse of the rectifier/inverter is three times that of the corresponding AC side. For a single VSC, the dc-side current pulse i_{dc} can be given through the double Fourier series as follows [66], [100]

$$\begin{aligned} i_{dc} = |i_0| + \sum_{n=1}^{\infty} |i_n| \cos\left[n\omega_0(t-t_0) + \theta_n\right] + \\ \sum_{m=1}^{\infty}\sum_{n=1}^{\infty} |i_{mn}| \cos\left[(m\omega_c + n\omega_0)(t-t_0) + \theta_{mn}\right] \end{aligned} \tag{3.12}$$

where $|i_0|$ is the DC component; $|i_n|$ and θ_n are the magnitude and phase of the fundamental and baseband harmonics, ω_0 and t_0 represent the fundamental frequency and initial time; i_{mn} and θ_{mn} are the magnitude and phase of the carrier frequency and carrier sideband harmonics, ω_c is the carrier frequency. Based on (3.12), the capacitor current expression in the BTB system under the carrier-based PWM can be obtained, i.e.,

$$\begin{aligned} & i_{cap} = i_{dcr} - i_{dci} = |i_{0r}| - |i_{0i}| \\ & + \sum_{n=1}^{\infty} \left\{|i_r| \cos\left[n\omega_g(t-t_r) + \theta_{nr}\right] - |i_i| \cos\left[n\omega_s(t-t_i) + \theta_{ni}\right]\right\} \\ & + \sum_{m=1}^{\infty}\sum_{n=1}^{\infty} \left\{|i_{mnr}| \cos\left[(m\omega_{cr} + n\omega_g)(t-t_r) + \theta_{mnr}\right] - \right. \\ & \left. |i_{mni}| \cos\left[(m\omega_{ci} + n\omega_s)(t-t_i) + \theta_{mni}\right]\right. \end{aligned} \tag{3.13}$$

The dc components of the two sides are equal due to the power balance, which

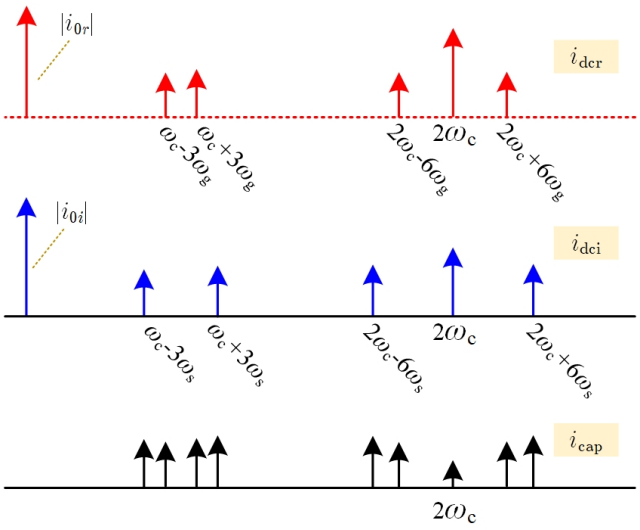

Figure 3.2: The spectrum of the rectifier dc-side current, inverter dc-side current, and capacitor current using the carrier-based PWM.

implies the item $|i_{0r}| - |i_{0i}| = 0$. In the capacitor current, the dominant component is the carrier frequency multiplier and carrier sideband harmonics [66]. Since the AFE rectifier and inverter sides have different fundamental frequencies, it is always difficult for the carrier-based PWM to reduce the baseband and the carrier sideband harmonics through the current cancellation between the two sides [66]. Fortunately, it is possible to cancel the harmonics of the carrier frequency multiplier in the capacitor current through the configuration of the triangle carriers for two sides. Fig. 3.2 shows the spectrum of the dc side current of the rectifier and inverter sides. The difference between these two spectrums results in the spectrum of dc-link capacitor current. Firstly, the dc components of the rectifier and inverter sides can cancel each other out due to the same magnitude. In addition, it can be seen that the same carrier frequency adopted for both the rectifier and inverter sides can eliminate the harmonics of the carrier frequency multiplier. However, the carrier sideband harmonics are still retained. The carrier frequency multiplier harmonics can be specifically obtained from (3.13) with n=0 [66], i.e.,

$$i_{\mathrm{cap\_ch}} = |i_{m0r}| \cos\left[m\omega_{cr}(t - t_r) + \theta_{m0r}\right] - |i_{m0i}| \cos\left[m\omega_{ci}(t - t_i) + \theta_{m0i}\right] \quad (3.14)$$

Under the case that the carrier with the same phase shift is applied to both the rectifier and inverter, the minimized magnitude in (3.14) can be obtained, i.e.,

Table 3.1: Simulated and experimental parameters

Parameters	Value
Grid voltage/frequency	60V/60Hz
Grid inductance/resistance	10mH/0.2Ω
DC-link capacitance	2.8mF
DC-link voltage	180V
Rotor motor stator frequency	100Hz
Number of pole pairs	5
Rotor flux	0.15Wb
Stator inductance/resistance	3.1mH/0.5Ω
Rated load torque	8N·m

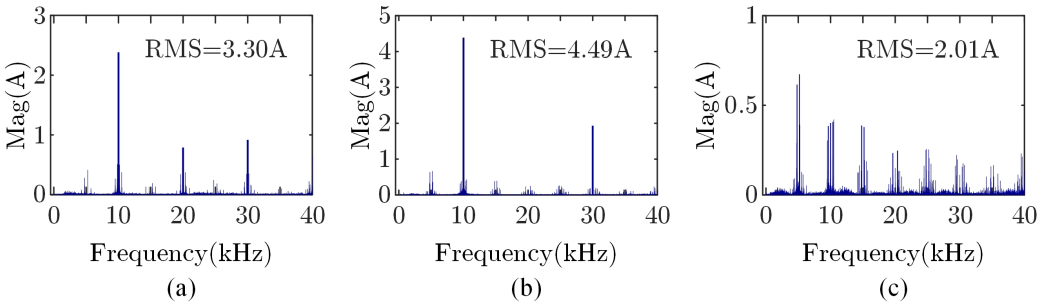

Figure 3.3: The spectrum of dc-link capacitor current in the BTB drive system under different carrier configuration cases. (a) 10kHz carrier at rectifier side and 5kHz carrier at inverter side. (b) 5kHz carrier at two sides but 90° phase shift angle between these two carriers. (c) The 5kHz synchronous carrier at two sides.

$|i_{\text{cap\_ch}}|_{\min} = \sqrt{|i_{m0r}|^2 + |i_{m0i}|^2 - 2\,|i_{m0r}|\,|i_{m0i}|}$. Therefore, the synchronous carrier with both the same frequency and phase shift should be implemented in the BTB drive system to reduce the capacitor current ripple and RMS value.

The simulated dc-link capacitor current spectrum is shown in Fig. 3.3 to verify the effect caused by the carrier relationship between the two sides, and the parameters of the BTB drive system are listed in Table 3.1.

In Fig. 3.3(a), the 10kHz carrier is applied to the rectifier side while the 5kHz carrier is for the inverter side. As a result, the dominant carrier frequency multiplier harmonics, such as the 10kHz, 20kHz, and 30kHz are retained in the dc-link capacitor current and the RMS value is 3.30A. In Fig. 3.3(b), the carrier with the same frequency 5kHz is applied to both sides, however, a 90°

phase shift angle exists between these two carriers, and the resulted capacitor current spectrum contains the dominant carrier frequency component, especially the harmonic at second carrier band 10kHz. Finally, in Fig. 3.3(c), the synchronous carrier is applied to both sides with the same frequency 5kHz and zero phase shift angle is maintained. It can be observed all of the dominant carrier frequency multiplier harmonics have been eliminated due to the good cancellation between the two sides and the minimized RMS value of 2.01A is obtained. Thus, the carrier-based PWM applied to the BTB drive system should be implemented with the synchronous carrier for the capacitor RMS current reduction. However, as seen in Fig. 3.3(c), the carrier sideband harmonics are still retained in the spectrum and they cannot be reduced through the carrier-based PWM scheme.

3.3 Proposed FCS-MPC With Reduced Dc-link Capacitor RMS Current

Although the predictive strategy has become an attractive control scheme for power converters, rare research investigates the dc-link capacitor current performance in BTB drive system under the FCS-MPC, and the benefit compared to the typical carrier-based PWM has not been revealed. To further reduce the dc-link capacitor RMS current and suppress the dominant harmonic component in the carrier-based PWM scheme, the FCS-MPC is developed such that the direct switching pulse generation principle without using the carrier-based modulation can be utilized to give a completely different capacitor current spectrum. In addition, since the nonlinear control objective can be conveniently designed into the cost function, further harmonic cancellation in the capacitor current can be achieved through the FCS-MPC.

3.3.1 Proposed Unified Cost Function Design

The general procedure of the FCS-MPC is to firstly predict the future state variable information under each candidate control input, and then a cost function is designed to penalize the tracking error between the predictive variable

and corresponding reference. The cost function evaluates the effect of each switching state combination individually and the one resulting in the minimum cost value will be selected as the optimal input applied to the power converter [103]. For the two-level VSC, it provides seven different switching voltage vectors and the manipulated voltage input can be aggregated in the control set, i.e., $V_{r\_1,\ldots,7} = \{v_{r\_1} \;\; v_{r\_2} \; ... \; v_{r\_7}\}$. Each specific voltage input in the synchronous dq frame corresponds to the unique switching state of the VSC.

Since the reference voltage commands through the deadbeat control way have been obtained in (3.10) and (3.11), an alternative cost function can be developed to evaluate the quadratic error distance between each voltage input and the desired reference voltage. Hence, the discrete switching state resulting in the closest voltage to such a command will be selected. Based on the deadbeat control law, the cost function for the current control at two sides can be expressed as follows.

$$J_{\mathrm{AC}} = \left[\boldsymbol{u_{g\_n}} - \boldsymbol{u_g^*}(k)\right]^{\mathrm{T}} \left[\boldsymbol{u_{g\_n}} - \boldsymbol{u_g^*}(k)\right] + \left[\boldsymbol{u_{s\_m}} - \boldsymbol{u_s^*}(k)\right]^{\mathrm{T}} \left[\boldsymbol{u_{s\_m}} - \boldsymbol{u_s^*}(k)\right] \tag{3.15}$$

where n=1,2,...,7 and m=1,2,...,7. To reduce the capacitor RMS current, the penalization of instantaneous capacitor current ripple should also be designed into the cost function. To this end, the predictive ac-side current of the rectifier can be obtained based on the compensated three-phase grid current in (3.8), i.e.,

$$\boldsymbol{i_g}(k+2) = \mathbf{A_{gd}}\boldsymbol{i_g}(k+1) + \mathbf{B_{gd}}\boldsymbol{u_{g\_n}}(k) + \mathbf{H_{gd}}\boldsymbol{v_g}(k) \tag{3.16}$$

The three-phase grid current then can be obtained through the inverse Park's transformation and the predictive dc-side current of the rectifier can be calculated as follows.

$$i_{dcr}(k+2) = S_{ra}i_{ga}(k+2) + S_{rb}i_{gb}(k+2) + S_{rc}i_{gc}(k+2) \tag{3.17}$$

where the binary variables S_{ra}, S_{rb}, and S_{rc} represent the switching state of each phase leg in the rectifier. When the upper switching device of the leg is 'ON', S_{rx}=1 (x=a,b,c) while S_{rx} =0 if it is 'OFF'. Similarly, the predictive

dc-side current of the inverter can be calculated through

$$\boldsymbol{i_s}(k+2) = \mathbf{A_{sd}}\boldsymbol{i_s}(k+1) + \mathbf{B_{sd}}\boldsymbol{u_{s\_m}}(k) + \mathbf{E_{sd}} \tag{3.18}$$

and

$$i_{dci}(k+2) = S_{ia}i_{sa}(k+1) + S_{ib}i_{sb}(k+1) + S_{ic}i_{sc}(k+1) \tag{3.19}$$

where the binary variables S_{ia}, S_{ib}, and S_{ic} represent the switching state of each phase leg in the inverter. When the upper switching device of the leg is 'ON', S_{ix}=1 (x=a,b,c) while S_{ix} =0 if it is 'OFF'. The compensated current $\boldsymbol{i_s}(k+1)$ is obtained based on the sampling current and optimal control input from the last interval.

The predictive capacitor current can be calculated as follows based on (3.17) and (3.19), i.e.,

$$i_{cap}(k+2) = i_{dcr}(k+2) - i_{dci}(k+2) \tag{3.20}$$

To penalize the switching ripple of the capacitor current, the cost function for this aim is developed as follows.

$$J_{\mathrm{DC}} = [i_{cap}(k+2) - 0]^2 \tag{3.21}$$

Based on (3.15) and (3.21), the unified cost function for the BTB drive system is

$$J_{\mathrm{Proposed}} = J_{\mathrm{AC}} + W_{\mathrm{DC}}J_{\mathrm{DC}} \tag{3.22}$$

where W_{DC} is the scalar weighting factor to connect the different cost function items and assign the priority between them. An extremely large W_{DC} implies that the capacitor current ripple is over suppressed but the AC-side current control in the BTB drive system will be affected. On the other hand, over small W_{DC} fails to achieve the objective regarding the capacitor current RMS reduction. Therefore, the W_{DC} stands for a tradeoff between these two control objectives and the optimal value needs to be adopted. A general rule to assign the same priority for the different control items can be used to speed up the selection of W_{DC}. The cost function (3.15) penalizes the compared error in

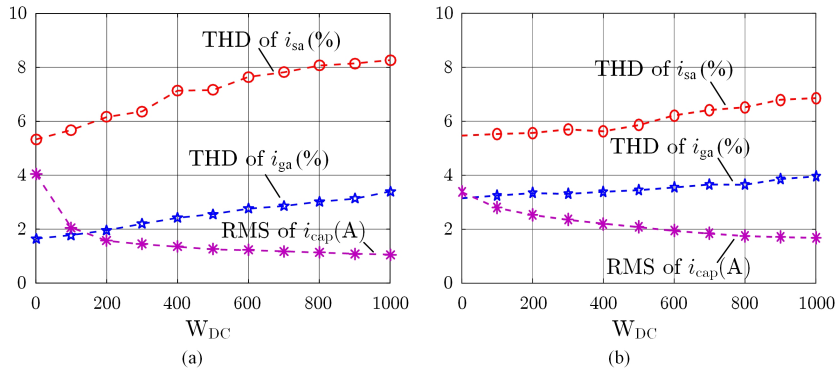

Figure 3.4: The dc-link capacitor RMS current, THD of grid current, and THD of PMSM stator current under different weighting factors W_{DC}. (a) The speed of PMSM is 1000rpm under rated torque. (b) The speed of PMSM is 500rpm under rated torque.

the order of voltage magnitude while the cost function (3.21) penalizes the compared error in the order of current magnitude. Based on the deadbeat control law, the control gain between the voltage and the current at two sides are L_g/T_s and L_s/T_s respectively. These two numbers give orders of magnitude in the range of a few hundred for W_{DC}. Based on this, the numerical value of simulated capacitor RMS current, the THD of grid current, and the THD of the PMSM stator current are presented in Fig. 3.4 under the different values of the weighting factor W_{DC}. Firstly, the capacitor RMS current can be significantly reduced by giving a non-zero weighting factor W_{DC} and the larger W_{DC}, the lower the RMS current. However, both the THD of grid current and PMSM stator current slightly increase along with a larger W_{DC}, due to more priority assigned to the capacitor current ripple suppression. Besides, when the W_{DC} is larger than 500, the decreasing trend of capacitor RMS current gradually turns flattened. Therefore, to maintain an acceptable three-phase grid/stator current quality and reduced capacitor RMS current, the W_{DC} is selected as 500 to present a good tradeoff. It is worth mentioning that the magnitude limitation for the state variable is usually included in the cost function to prevent the overcurrent/overvoltage issue. In this work, the core part is focused on the dc-side capacitor current optimization and ac-side current control, and the state variable magnitude violation is not a big concern since the MPC endows the state variables with fast reference

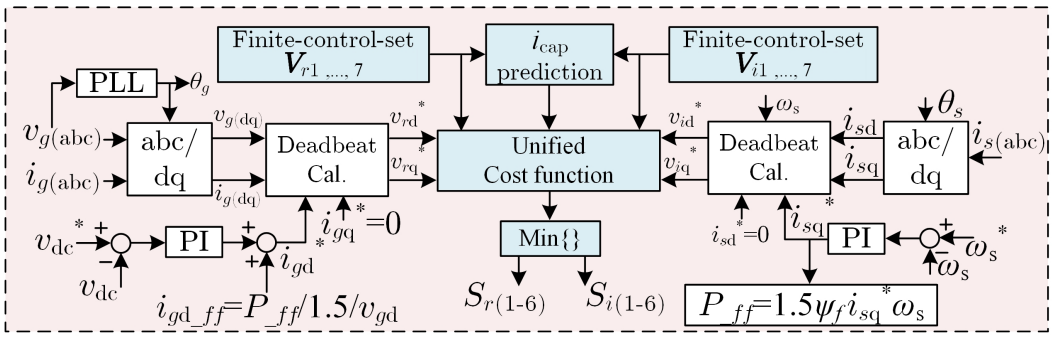

Figure 3.5: The proposed FCS-MPC with reduced capacitor RMS current.

tracking ability usually within several sampling intervals. Also, the extra over current/voltage protection logic is implemented in the programming code to guarantee a reliable operation, which is similar to the function provided by adding the state variable limitation into the cost function.

The control diagram of the proposed FCS-MPC with reduced capacitor RMS current is shown in Fig. 3.5. Compared to the carrier-based PWM scheme in Fig. 3.1, the modulation block has been replaced by direct switching pulse generation. The elimination of the carrier devotes to a completed different capacitor current spectrum with the carrier-based scheme, where the dominant harmonic, such as both the carrier frequency multiplier and carrier sideband component can be suppressed in the proposed FCS-MPC.

3.3.2 Comparison With the Distributed FCS-MPC

The proposed FCS-MPC for the BTB drive system is essentially a kind of centralized controller, which treats the AFE rectifier and inverter as a single power converter. As a result, the optimal switching states for both sides are determined together through a double cycle loop. In this case, the explicit capacitor current can be predicted and its instantaneous ripple can be suppressed through the centralized cost function (3.22). This kind of control manner typically demands more computational resources than the distributed way, where the control for rectifier and inverter sides are implemented separately. To show the performance difference, the FCS-MPC with split cost function implementation for the rectifier and inverter is also implemented for

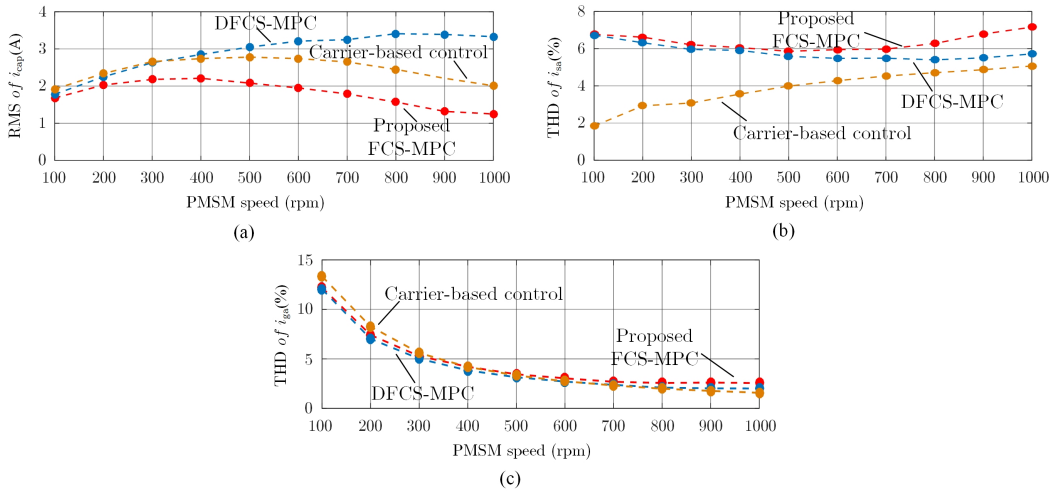

Figure 3.6: Simulation comparison of the capacitor RMS current, grid current THD, and PMSM stator current THD at wide motor speed change. (a) The capacitor RMS current. (b) Grid current THD. (c) PMSM stator current THD.

comparison, and each cost function on both sides contains the dc-side current pulse suppression. This kind of FCS-MPC realized separately will be called the distributed FCS-MPC(DFCS-MPC) in the following contents. Theoretically, it is the separate dc-side current pulse of the rectifier and inverter that can be improved while the dc-link capacitor current has not been directly controlled in the DFCS-MPC. From this point of view, the proposed FCS-MPC is more powerful for capacitor RMS current reduction. The numerical performance in terms of the capacitor RMS current will be compared in the next section.

3.4 Simulation and Experimental Results

To fairly investigate the property of control schemes, the 5kHz switching frequency is configured for both sides in the carrier-based SVPWM scheme. The FCS-MPC scheme adopts the 30kHz sampling frequency to obtain an average 5kHz switching frequency when the PMSM operates at 1000rpm and 8N·m load torque.

A simulated summary in terms of capacitor RMS current, grid current THD, and PMSM stator current THD has been presented in Fig. 3.6. The proposed FCS-MPC can achieve a lower capacitor RMS current than that of the synchronous carrier-based PWM, especially at the higher motor speed

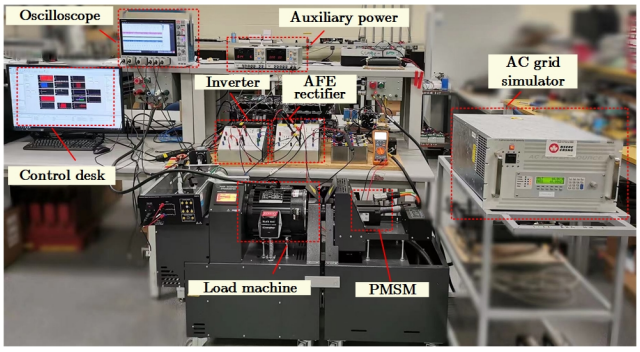

Figure 3.7: Experimental setup of the BTB VSCs-fed PMSM drive system.

range. Although the DFCS-MPC suppresses the dc-side current of two sides, its performance for the RMS reduction is not as good as the proposed method. Regarding the grid-side THD comparison, the proposed FCS-MPC can always maintain an average switching frequency 5kHz at the AFE side, and thus similar results are kept with the carrier-based PWM. On the other hand, the FCS-MPC has a higher motor-side THD in the low-speed range due to the significantly lower switching frequency than that of the carrier-based PWM. A fair comparison at 1000rpm point can be performed where the FCS-MPC has an average 5kHz switching frequency on the inverter. The FCS-MPC has a slightly increased stator current THD but it can be accepted.

Fig. 3.7 shows the hardware prototype of the BTB VSCs-fed PMSM drive system with parameters designed in Table 3.1. The VSC is configurated by the IGBT power modules. The programming code of the proposed controller is implemented in the MicroLabBox 1202 digital platform, where the ADC and PWM pulse emission are realized on the programmable FPGA (Xilinx Kintex-7 XC7K325T) and the control algorithm are programmed on the OorlQ P5020 processors.

Fig. 3.8 shows the experimental results under different control schemes when the motor operates at the 1000rpm and 8N·m load torque. In Fig. 3.8 (a), the deadbeat control law is realized using the asynchronous carrier-based SVPWM, where the carrier of the inverter side is 90° behind that of the rectifier side. As a comparison, the deadbeat control with the synchronous carrier-based SVPWM is given in Fig. 3.8(b). Through these two situations,

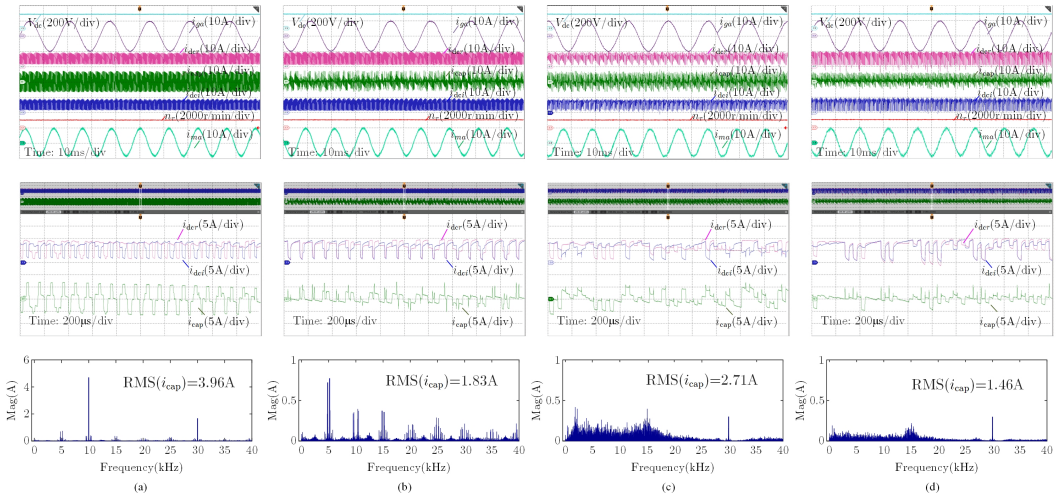

Figure 3.8: Experimental DC-link voltage, grid current, DC-side current pulse of rectifier, capacitor current, DC-side current pulse of inverter, PMSM speed, and the stator current (PMSM:1000rpm and 8N·m). (a) The asynchronous carrier-based SVPWM. (b) The synchronous carrier-based SVPWM. (c) DFCS-MPC. (d) The proposed FCS-MPC.

it can be seen that the synchronous carrier maintained at two sides can significantly reduce the carrier frequency multiplier harmonics, which verifies the effectiveness of the previous analysis. In Fig. 3.8 (c), the DFCS-MPC is presented. Firstly, it can be observed that the dc-side current pulse of both the rectifier and inverter side becomes sparse compared to the SVPWM scheme, which is due to the cost function item for current ripple suppression at each side. However, since the DFCS-MPC suppresses the separate DC-side current pulse at two sides, the capacitor current is not directly controlled and its RMS value is even larger than that of the synchronous carrier-based scheme. The result using the proposed FCS-MPC is shown in Fig. 3.8(d), where the smallest capacitor RMS current has been obtained. It can be seen that the dc pulses of the rectifier side and capacitor side are almost maintained in the same phase, leading to a good cancellation and hence, smaller capacitor current ripple. The dominant remained carrier sideband harmonics in Fig. 3.8(b) have been eliminated in Fig. 3.8(d), which verifies the effectiveness of the proposed method. The harmonic at the 30kHz frequency is caused by the regular sampling process.

Fig. 3.9 shows the experimental comparison between the synchronous carrier-based SVPWM and the proposed FCS-MPC when the PMSM operates

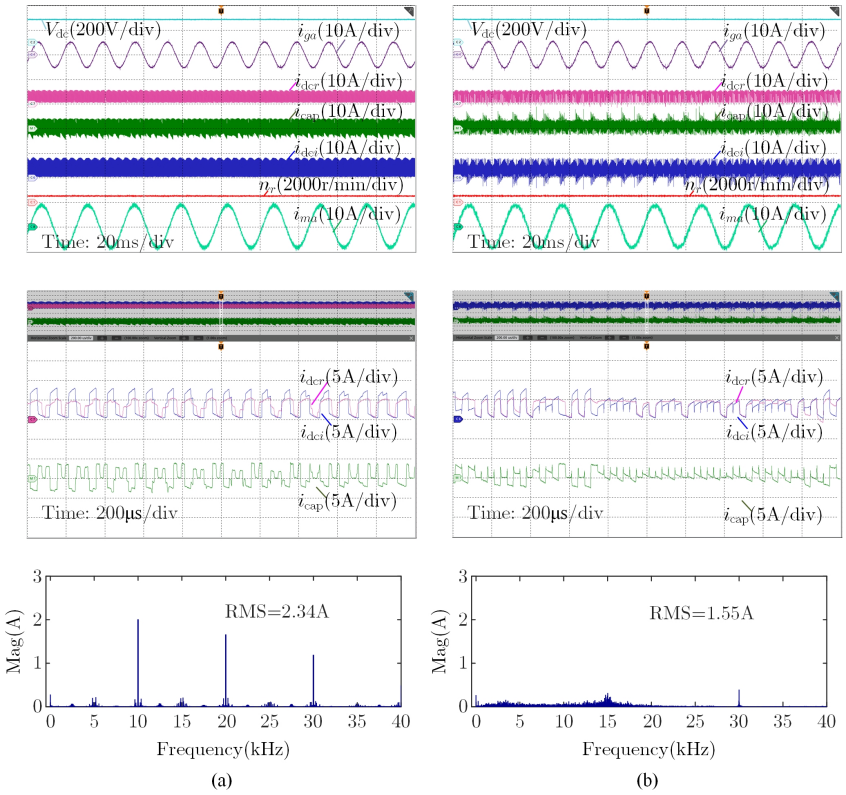

Figure 3.9: Experimental results for medium speed case (PMSM:500rpm and 8N·m). (a) The synchronous carrier-based SVPWM. (b) The proposed FCS-MPC.

at a medium speed case, i.e., 500rpm, and the load torque 8N·m. Firstly, it can be seen that the dominant carrier-frequency multiplier harmonics appear in Fig. 3.9(a) even though the synchronous carrier is still maintained at two sides, which is different from that in Fig. 3.8(b). The reason is that the magnitude of the grid-side three-phase current and that of the motor stator current have a significant difference under the PMSM medium speed case, while the comparable three-phase current magnitude at two sides in Fig. 3.8(b). Fortunately, the proposed FCS-MPC can still achieve a lower capacitor RMS current, as seen in Fig. 3.9(b) and the dominant harmonics can be eliminated in the spectrum. The grid-side current THD of these two schemes are similar, i.e., 3.31% using the SVPWM scheme and 3.83% using the proposed FCS-MPC. The motor-side stator current THD using the proposed FCS-MPC is 6.50% and that of using the SVPWM scheme is 4.03%.

Figs. 3.10 and 3.11 show the dynamic experimental waveforms of proposed

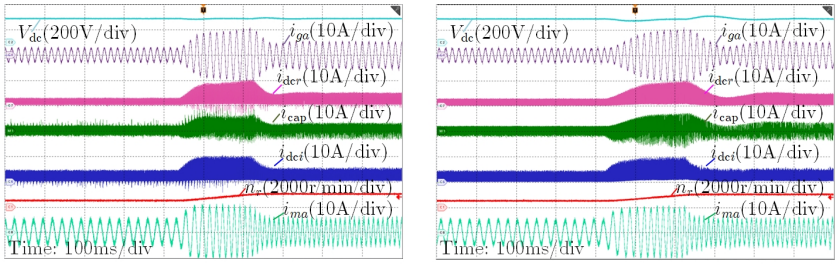

Figure 3.10: Dynamic response with PMSM speed change from 500rpm to 1000rpm of proposed FCS-MPC and synchronous-carrier SVPWM scheme.

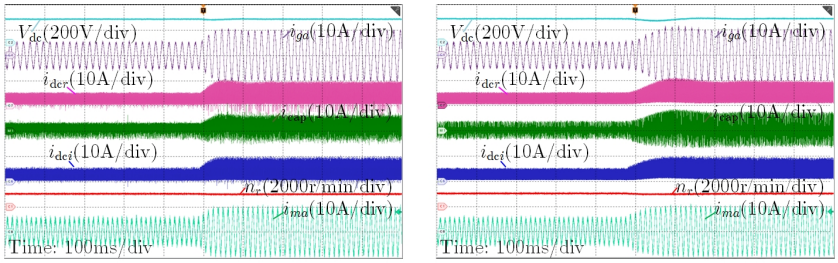

Figure 3.11: Dynamic response with PMSM load change from 4N·m to 8N·m of proposed FCS-MPC and synchronous-carrier SVPWM scheme.

FCS-MPC and synchronous carrier-based SVPWM, where the respect transient change is given to the PMSM speed (from 500rpm to 1000rpm) and the load torque (from 4N·m to 8N·m). The proposed control performs well during the transient process and the capacitor current is controlled with smaller ripples.

The numerical comparison has been summarized in Table 3.2 for a fast review. The proposed FCS-MPC obtains the smallest capacitor RMS current while maintaining the similar grid current THD with the carrier-based scheme. The THD of motor current slight increase but still can be acceptable. The computational time of the proposed FCS-MPC is a bit longer but it is comparable with that of other schemes.

The typical modeling-based approach for the capacitor lifetime estimation is based on the following equation [110]

$$\begin{aligned} L &= L_0 \cdot K_T \cdot K_R \cdot K_V \\ &= L_0 \cdot 2^{\frac{T_0 - T_A}{10K}} \cdot K_i \left[1 - \left(\frac{I_A / f_{\text{correction}}}{I_R}\right)^2\right]^{\frac{\Delta T_0}{10K}} \cdot \left(\frac{U_A}{U_R}\right)^{-n} \end{aligned} \tag{3.23}$$

where K_T represents the temperature factor; K_R represents the ripple current

Table 3.2: Numerical comparison for the carrier-based PWM, proposed FCS-MPC and DFCS-MPC (PMSM: 1000rpm 8N·m).

Indices	Carrier-based	DFCS-MPC	Proposed FCS-MPC
Switching frequency	5kHz(fixed)	5kHz(ave.)	5kHz(ave.)
THD(i_g)	2.16%	2.64%	2.22%
THD(i_s)	5.96%	6.38%	7.52%
RMS(i_{cap})	1.83	2.71	1.46
Computation time	21.72μs	20.8μs	23.6μs

factor and K_V represents the voltage factor. In the specific calculation, the L is the estimated lifetime; L_0 is the lifetime under nominal load at upper category temperature; T_0 is the rated temperature; T_A is the ambient temperature; K_i represents the safety factor; I_A is the actual rated ripple current; I_R is the ripple current at upper category temperature; $f_{\text{correction}}$ is the frequency correction factor that makes the ripple current stress occurring at all the frequencies equivalent to the effect at the nominal frequency; ΔT_0 is the core temperature rise of the capacitor; U_A is the actual operating voltage and U_R is the rated voltage. Based on the typical frequency correction factor $f_{\text{correction}}$=1.1 and considering a rated ripple current I_R=2A, the lifetime of capacitor using the FCS-MPC scheme can be 1.2 times and 1.55 times the carrier-based SVPWM when the PMSM speed is 1000rpm and 500rpm respectively.

3.5 Summary

This chapter investigates the performance of the dc-link capacitor current in the BTB drive system using the FCS-MPC and reveals its advantages compared to the typical carrier-based PWM. Typically, the synchronous carrier-based PWM in such a system can reduce the dominant harmonics at the carrier frequency multiplier but the carrier sideband harmonics still exist. To further eliminate the remains harmonics and reduce the capacitor RMS current, the direct dc-side pulse current cancellation between two sides is designed into the cost function of FCS-MPC. The simulated and experimental results show that

the FCS-MPC can give a 20%-35% lower capacitor RMS current than the synchronous carrier-based SVPWM, which contributes to a smaller size of dc-link or extended lifespan of the existing capacitor. In addition, the quality of the three-phase grid current and the motor stator current can be acceptable. The effectiveness of the proposed compared to the existing distributed type is also presented.

The proposed method can be adopted as a general framework for other BTB applications, such as wind power conversion systems. The proposed FCS-MPC shows more flexibility in terms of nonlinear objective optimization compared to the conventional linear control approach.

Chapter 4

Hybrid Model Predictive Voltage and Current Control for LCL-filtered VSCs

For the VSCs in the grid-connected application, the line filter is required between the VSCs bridge and the terminal of the grid to improve the quality of the power. Compared to the single inductive L filter, the LCL filter features high-order properties, and reduced weight and size, which can attenuate the harmonic more effectively. However, the LCL filter introduces the inherent resonance problem, which brings challenges to the stability of the grid-connected system. The resonant current spikes will be excited by the switching harmonics from the VSCs or the background harmonic in the grid voltage. On the other hand, the installment of the LC filter between VSI and motor can significantly reduce the dv/dt and make the voltage and current applied to the motor closer to sinusoidal, which is beneficial to a longer life of the motor. However, the LC filter, together with the motor inductor, will induce the additional LCL resonance problem and thus cause voltage and current oscillations. To exploit the benefits brought by the LCL filter for the grid-connected and motor-side applications, this chapter designs the MPC scheme with hybrid voltage and current control to solve the resonance problem.

Firstly, the CCS-MPC is designed for the grid-connected VSCs and the cost function involves the grid current, inverter-side current, and capacitor voltage tracking. The optimized control law is generated according to the minimiza-

tion of the designed cost function. In this process, the weighting factors are exactly arranged to place the desired closed-loop poles with guaranteed system stability. The hybrid cost function with modified reference is also proposed to reject the harmonics caused by the unhealthy grid condition.

Secondly, for the LC filtered VSCs-fed motor drive application, the FCS-MPC is designed to realize the speed command tracking while suppressing the filter resonance simultaneously. The cost function design will be analyzed in the time-domain with the intuitive concept, which regulates the trajectory of multivariable in the system. The experimental results prove that the proposed FCS-MPC scheme can achieve a motor-friendly waveform and overcome the resonance problem effectively. The robustness of the controller to parameter variations of the filter is also verified.

4.1 CCS-MPC for Grid-Connected VSCs with LCL Filter

In this section, the CCS-MPC is adopted as the framework for LCL-filtered grid-connected VSI, which aims to suppress the resonance and adapt to the unhealthy grid condition with sinusoidal current maintained. The control law is derived according to the optimal analytical solution of the cost function, which contains the hybrid current and capacitor voltage tracking. The driving pulse is further generated by the sinusoidal PWM (SPMW) stage. The proposed CCS-MPC scheme will be compared with the conventional capacitor current-based AD scheme and the FCS-MPC scheme to show the benefits. To this end, the system modeling and discretization for the LCL-filtered grid-connected VSI will be firstly introduced. Then, the CCS-MPC elements, including parameter design and stability analysis will be presented. Next, the modification of the CCS-MPC to deal with unhealthy grid conditions will be proposed and finally, some simulated and experimental results will be shown to verify the proposed points.

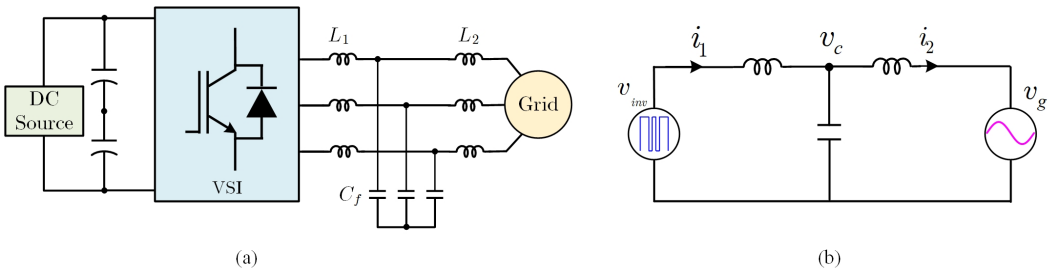

Figure 4.1: (a) The topology of grid-connected VSI with LCL filter. (b) The equivalent circuit of LCL-filtered VSI in the stationary $\alpha\beta$ coordinate frame.

4.1.1 Predictive Model of LCL-filtered Grid System

Fig. 4.1(a) shows the typical configuration of the VSI equipped with an LCL filter, which transfers the power from the dc side to the grid. The components of LCL filter for each phase are denoted as L_1, C_f, and L_2, which are inverter-side inductance, filter capacitance, and grid-side inductance respectively. Fig. 4.1(b) shows the equivalent circuit in the stationary $\alpha\beta$ coordinate frame, where the state variables are defined as

$$\begin{cases} \boldsymbol{v_{inv}} = v_{inv\alpha} + jv_{inv\beta} & \boldsymbol{i_1} = i_{1\alpha} + ji_{1\beta} \\ \boldsymbol{v_c} = v_{c\alpha} + jv_{c\beta} & \boldsymbol{i_2} = i_{2\alpha} + ji_{2\beta} \\ \boldsymbol{v_g} = v_{g\alpha} + jv_{g\beta} & \end{cases} \tag{4.1}$$

According to Kirchhoff voltage and current laws, the state-space model of the system in continuous time can be described as

$$\frac{d\boldsymbol{x_g}}{dt} = \mathbf{A_g}\boldsymbol{x_g} + \mathbf{B_g}\boldsymbol{v_{inv}} + \mathbf{E_g}\boldsymbol{v_g} \tag{4.2}$$

where the state vector $\boldsymbol{x_g} = [\boldsymbol{i_1}\ \boldsymbol{v_c}\ \boldsymbol{i_2}]^{\mathrm{T}}$. The matrix $\mathbf{A_g}$, $\mathbf{B_g}$, and $\mathbf{E_g}$ are given as follows.

$$\mathbf{A_g} = \begin{bmatrix} -\frac{R_1}{L_1} & -\frac{1}{L_1} & 0 \\ \frac{1}{C_f} & 0 & -\frac{1}{C_f} \\ 0 & \frac{1}{L_2} & -\frac{R_2}{L_2} \end{bmatrix} \quad \mathbf{B_g} = \begin{bmatrix} \frac{1}{L_1} \\ 0 \\ 0 \end{bmatrix} \quad \mathbf{E_g} = \begin{bmatrix} 0 \\ 0 \\ -\frac{1}{L_2} \end{bmatrix} \tag{4.3}$$

R_1 and R_2 are the equivalent series resistance of inductance L_1 and L_2 respectively, which can be ignored in the controller design due to the small value. According to the ZOH principle, the modeling (4.2) can be discretized to obtain the predictive equation as

$$\boldsymbol{x_g}(k+1) = \mathbf{A_{gd}}\boldsymbol{x_g}(k) + \mathbf{B_{gd}}\boldsymbol{v_{inv}}(k) + \mathbf{E_{gd}}\boldsymbol{v_g}(k) \tag{4.4}$$

where k represents the current time instant. Assuming that the sampling interval is T_s, the discrete matrix $\mathbf{A_d}$, $\mathbf{B_d}$, and $\mathbf{E_d}$ are expressed as

$$\mathbf{A_{gd}} = e^{\mathbf{A_g}T_s}, \ \ \mathbf{B_{gd}} = \int_0^{T_s} e^{\mathbf{A_g}\tau}\mathbf{B_g}d\tau, \ \ \mathbf{E_{gd}} = \int_0^{T_s} e^{\mathbf{A_g}\tau}\mathbf{E_g}d\tau \tag{4.5}$$

4.1.2 Proposed Cost Function With Hybrid Current and Voltage Control

In the grid-connected VSI with the single L filter, the grid current is the sole control objective, which can be regulated well by the cost function [111], [112]. However, considering the third-order characteristic and the coupling dynamics among the components of LCL filter, the control objective with only the regulation of grid current is insufficient to realize resonance damping. The cost function shows great potential to regulate several variables simultaneously [113]–[115], and the hybrid current and voltage control are designed firstly in this part.

The cost function should realize the grid current reference tracking and thus implicitly ensure the normal power injection. Therefore, the item for grid current regulation is designed as

$$J_1 = [i^*_{2\alpha}(k+1) - i_{2\alpha}(k+1)]^2 + \left[i^*_{2\beta}(k+1) - i_{2\beta}(k+1)\right]^2 \tag{4.6}$$

According to the demanded power and measured grid voltage, the reference of grid current can be calculated as

$$\begin{cases} \boldsymbol{i^*_2}(k) = i^*_{2\alpha}(k) + ji^*_{2\beta}(k) \\ i^*_{2\alpha}(k) = \frac{2}{3}\frac{P^* v_{g\alpha}(k) + Q^* v_{g\beta}(k)}{v^2_{g\alpha}(k) + v^2_{g\beta}(k)} \\ i^*_{2\beta}(k) = \frac{2}{3}\frac{P^* v_{g\beta}(k) - Q^* v_{g\alpha}(k)}{v^2_{g\alpha}(k) + v^2_{g\beta}(k)} \end{cases} \tag{4.7}$$

where P^* is the active power reference, and Q^* is the reactive power reference, which is set at zero in this work to achieve the utility power factor. Considering the internal modeling expressed in (4.2), the reference for capacitor voltage and inverter-side current can be derived respectively as

$$\begin{cases} \boldsymbol{v^*_c}(k) = v^*_{c\alpha}(k) + jv^*_{c\beta}(k) \\ v^*_{c\alpha}(k) = v_{g\alpha}(k) - \omega_g L_2 i^*_{2\beta}(k) \\ v^*_{c\beta}(k) = v_{g\beta}(k) + \omega_g L_2 i^*_{2\alpha}(k) \end{cases} \tag{4.8}$$

and

$$\begin{cases} \boldsymbol{i_1^*}(k) = i_{1\alpha}^*(k) + j i_{1\beta}^*(k) \\ i_{1\alpha}^*(k) = i_{2\alpha}^*(k) - \omega_g C_f v_{\mathrm{c}\beta}^*(k) \\ i_{1\beta}^*(k) = i_{2\beta}^*(k) + \omega_g C_f v_{\mathrm{c}\alpha}^*(k) \end{cases} \tag{4.9}$$

where ω_g is the fundamental angular frequency of grid.

As the coupled dynamics among the LCL components, the grid current will be affected by the capacitor voltage and inverter-side current. For example, the derivative of the grid current is directly related to the capacitor voltage. Therefore, it is necessary to ensure the trajectory of capacitor voltage and inverter-side current are both maintained close to their reference value. The regulation for capacitor voltage regulation and inverter-side current can be realized by designing the cost function as follows.

$$J_2 = \left[v_{c\alpha}^*(k+1) - v_{c\alpha}(k+1)\right]^2 + \left[v_{c\beta}^*(k+1) - v_{c\beta}(k+1)\right]^2 \tag{4.10}$$

and

$$J_3 = \left[i_{1\alpha}^*(k+1) - i_{1\alpha}(k+1)\right]^2 + \left[i_{1\beta}^*(k+1) - i_{1\beta}(k+1)\right]^2 \tag{4.11}$$

One of the significant advantages of MPC is that multiobjective optimization can be easily realized by the pre-defined cost function. To simultaneously controlled all state variables near the corresponding reference, the final cost function with hybrid current and voltage control can be written as

$$J = J_1 + \mathrm{w}_{v_c} J_2 + \mathrm{w}_{i_1} \mathrm{g}_3 = \left[\boldsymbol{x_g}(k+1) - \boldsymbol{x_g^*}(k+1)\right]^{\mathrm{T}} \mathbf{W_g} \left[\boldsymbol{x_g}(k+1) - \boldsymbol{x_g^*}(k+1)\right] \tag{4.12}$$

where the reference vector $\boldsymbol{x_g^*} = [\boldsymbol{i_1^*}\ \boldsymbol{v_c^*}\ \boldsymbol{i_2^*}]^{\mathrm{T}}$. The positive semidefinite matrix $\mathbf{W_g}$=diag(w_{i_1}, w_{v_c}, 1), including weighting factors w_{v_c} for capacitor voltage and w_{i_1} for inverter-side current, which assigns the different priorities to penalize each tracking error.

It can be seen that the concept of cost function design is intuitive, i.e, all predictive state variables are controlled to track their corresponding reference. Supposing that the state variable vector $\boldsymbol{x}$ tracks $\boldsymbol{x^*}$ well, then the resonance problem will be solved.

4.1.3 Optimized Control Law

Substituting the predictive equation (4.4) into the cost function (4.12) and performing the gradient of (4.12) with respect to $\boldsymbol{v_{inv}}$ equals to zero. The unconstrainted control law can be expressed as

$$\boldsymbol{v_{inv\_unc}}(k)= (\mathbf{B_{gd}}^{\mathrm{T}}\mathbf{W_g}\mathbf{B_{gd}})^{-1}\mathbf{B_{gd}}^{\mathrm{T}}\mathbf{W_g}\left[\boldsymbol{x_g^*}(k+1) - \mathbf{A_{gd}}\boldsymbol{x_g}(k) - \mathbf{E_{gd}}\boldsymbol{v_g}(k)\right] \tag{4.13}$$

It can be found that besides the information of state variables and grid voltage at the kth instant is needed, the reference value at $(k+1)th$ instant is also required, which can be obtained as

$$\boldsymbol{x_g^*}(k+1) = \boldsymbol{x_g^*}(k)e^{j\omega_g T_s} \tag{4.14}$$

Since the cost function penalizes the tracking error of state variables quadratically, the control law in (4.13) corresponds to the minimum value of the cost function (4.12). Different from FCS-MPC, the CCS-MPC uses the modulator to synthesize the desired voltage command. Considering the maximum voltage V_{inv_lim} generated by the modulator, the constraint for the control law should be effective when $\boldsymbol{v_{inv\_unc}}$ is out of the allowable region of the modulator, i.e.,

$$|\boldsymbol{v_{inv\_unc}}| = \sqrt{v_{inv\alpha\_unc}^2 + v_{inv\beta\_unc}^2} \leq V_{inv\_\mathrm{lim}} \tag{4.15}$$

Therefore, the optimized control law sent into the SPWM block is expressed as

$$\boldsymbol{v_{inv}^*}(k) = \begin{cases} \boldsymbol{v_{inv\_unc}}(k) & |\boldsymbol{v_{inv\_unc}}| \leq V_{inv\_\mathrm{lim}} \\ \frac{\boldsymbol{v_{inv\_unc}}(k)}{|\boldsymbol{v_{inv\_unc}}(k)|}V_{inv\_\mathrm{lim}} & |\boldsymbol{v_{inv\_unc}}| > V_{inv\_\mathrm{lim}} \end{cases} \tag{4.16}$$

In this way, the exhaustive searching process for candidate vectors in FCS-MPC is eliminated, and the optimized control law with the minimum cost function value is ensured.

Although the optimized control law (4.13) is determined at the kth instant, it cannot be executed immediately by the VSI due to the computational time and PWM delay. Considering the one-step delay, the predictive model is rewritten as

$$\boldsymbol{x_g}(k+1) = \mathbf{A_{gd}}\boldsymbol{x_g}(k) + \mathbf{B_{gd}}\boldsymbol{v_{inv}^*}(k-1) + \mathbf{E_{gd}}\boldsymbol{v_g}(k) \tag{4.17}$$

Therefore, the one-step delay should be compensated by the controller otherwise the system performance will deteriorate. To do this, the state variables at the $(k+1)th$ instant will be estimated firstly, and then the cost function will evaluate the state variables at the $(k+2)th$ instant, i.e.,

$$J_{\text{com}} = \left[\boldsymbol{x_g}(k+2) - \boldsymbol{x_g^*}(k+2)\right]^{\text{T}} \mathbf{W_g} \left[\boldsymbol{x_g}(k+2) - \boldsymbol{x_g^*}(k+2)\right] \tag{4.18}$$

Correspondingly, the unconstrainted control law with delay compensation will be updated as follows.

$$\boldsymbol{v_{inv\_unc}}(k) = (\mathbf{B_{gd}}^{\text{T}} \mathbf{W_g} \mathbf{B_{gd}})^{-1} \mathbf{B_{gd}}^{\text{T}} \mathbf{W_g} \left[\boldsymbol{x_g^*}(k+2) - \mathbf{A_{gd}} \boldsymbol{x_g}(k+1) - \mathbf{E_{gd}} \boldsymbol{v_g}\right] \tag{4.19}$$

The two-step ahead sinusoidal reference can be obtained by

$$\boldsymbol{x_g^*}(k+2) = \boldsymbol{x_g^*}(k) e^{j\omega_g 2T_s} \tag{4.20}$$

The dynamic of grid voltage can be considered to be slow compared to the sampling process. The state variable information at the $(k+1)th$ instant can be estimated by designing a state observer.

4.1.4 Weighting Factor Design

The weighting factors are usually determined in FCS-MPC by trial and error. On the contrary, the essence of the CCS-MPC is a linear control strategy. Thus, it is possible to analyze the closed-loop performance by examining the poles of the system. The simulated and experimental parameters of the LCL-filtered grid-connected VSI are given in Table 4.1.

Since the computational delay has been compensated, the closed-loop state-space modeling can be obtained by substituting the control law (4.13) into (4.4), i.e.,

$$\boldsymbol{x_g}(k+1) = \mathbf{\Phi_g} \boldsymbol{x_g}(k) + \mathbf{\Gamma_g} \boldsymbol{i_2^*}(k) + \mathbf{\Xi_g} \boldsymbol{v_g}(k) \tag{4.21}$$

where $\mathbf{\Phi_g} = \left[\mathbf{I_3} - \mathbf{B_{gd}} (\mathbf{B_{gd}}^{\text{T}} \mathbf{W_g} \mathbf{B_{gd}})^{-1} \mathbf{B_{gd}}^{\text{T}} \mathbf{W_g}\right] \mathbf{A_{gd}}$,

$\mathbf{\Gamma_g} = \mathbf{B_{gd}} (\mathbf{B_{gd}}^{\text{T}} \mathbf{W_g} \mathbf{B_{gd}})^{-1} \mathbf{B_{gd}}^{\text{T}} \mathbf{W_g} \mathbf{T_g}$,

$\mathbf{\Xi_g} = \mathbf{E_{gd}} + \mathbf{B_{gd}} (\mathbf{B_{gd}}^{\text{T}} \mathbf{W_g} \mathbf{B_{gd}})^{-1} \mathbf{B_{gd}}^{\text{T}} \mathbf{W_g} (\mathbf{R_g} - \mathbf{E_{gd}})$,

Table 4.1: Simulated and experimental parameters of the LCL-filtered VSI system

Parameters	Value
DC-link voltage	300V
DC-link capacitance	3300μF
Gird fundamental frequency	60Hz
Gird peak voltage	115V
Inverter-side inductance	3mH
Filter capacitance	30μF
Grid-side inductance	1mH
Resonant frequency	1061Hz
Sampling frequency	6kHz

$\mathbf{T_g} = \begin{bmatrix} 1-\omega_g^2 L_2 C_f & j\omega_g L_2 & 1 \end{bmatrix}^{\mathrm{T}}$ and $\mathbf{R_g} = [j\omega_g C_f \;\; 1 \;\; 0]^{\mathrm{T}}$. $\mathbf{I_3}$ is the identity matrix with 3-dimension. It can be seen that the system matrix $\mathbf{A_{gd}}$ of the open-loop model has been modified into the closed-loop matrix $\mathbf{\Phi_g}$. The closed-loop poles can be obtained by solving the characteristic equation as

$$|\lambda \mathbf{I_3} - \mathbf{\Phi_g}| = 0 \tag{4.22}$$

Since the control law is related to the weighting factor matrix $\mathbf{W_g}$, the values of the w_{i_1} and w_{v_c} will affect the closed-loop system performance. Only the system poles under the α-axis component are investigated since the β-axis counterpart is completely the same. The open-loop poles of system are plotted in Fig. 4.2(a), which illustrates the open-loop system is unstable with poles lying on the boundary of the unit circle. The closed-loop poles of system, i.e., the solution of (4.22) are plotted in Fig. 4.2(b) with w_{i_1}=0.3 and w_{v_c}=0.03 respectively. It can be seen that all closed-loop poles are moved into the unit circle with a zero pole and two complex poles. The system stability is improved and the damping ratio is configured around 0.6, which is slightly smaller than the optimum value 0.707 to obtain a relatively faster response [71]. To further show the impact of the weighting factors, the root loci are plotted in Fig. 4.2(c) and Fig. 4.2(d) as w_{i_1} and w_{v_c} changes respectively. It can be seen in Fig. 4.2(c) that with a larger w_{v_c}, the two complex poles move closer to the origin, resulting in a faster dynamic response. However, considering the sensitivity to the noise in the real controller, the value of w_{v_c} is selected as

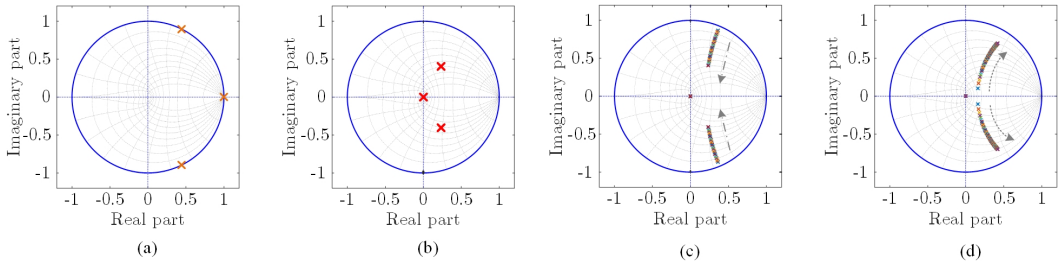

Figure 4.2: The poles map of the system. (a) Open-loop poles. (b) Closed-loop poles (w_{i_1}=0.3, w_{v_c}=0.03). (c) The closed-loop root loci with w_{v_c} changes from 0.03 to 0.4. (d) The closed-loop root loci with w_{i_1} changes from 0.2 to 1.

0.03. On the contrary, with a larger w_{i_1}, the two complex poles move away from the origin, which reduces the stability margin of the system. Besides, the oscillations caused by disturbance will be more obvious due to the lower damping ratio. It is consistent with the analysis in Fig. 4.2(c), which implies the penalization strength for capacitor voltage tracking error becomes weak when a larger w_{i_1} is adopted. Therefore, the value of w_{i_1} is selected as 0.3 with the closed-loop poles designed in Fig. 4.2(b).

The discrete transfer function from the grid current reference $\boldsymbol{i_2^*}$ to the actual current $\boldsymbol{i_2}$ can be derived as

$$\frac{i_2(z)}{i_2^*(z)} = \mathbf{C}(z\mathbf{I_3} - \mathbf{\Phi_g})^{-1}\mathbf{\Gamma_g} \tag{4.23}$$

where C=[0 0 1]$^{\mathrm{T}}$. The bode plot of (4.23) is shown in Fig. 4.3, which shows the proposed CCS-MPC can achieve zero tracking error for wide bandwidth. While in case the feedforward compensation is not fully included, e.g., the third gain coefficient in $\mathbf{\Gamma_g}$ is set as zero, the steady-state tracking error will exist. Therefore, compared to the direct state feedback way, the proposed MPC can achieve better closed-loop performance since the optimized control law corresponds to the minimization of the cost function. To realize the optimized control law, the information of all state variables needs to be known. In this work, the full-order state observer is incorporated, which not only can reduce the number of sensors but can compensate for the control delay by using the estimated state value. According to the separation principle, the state observer and the controller can be designed independently [97]. The state observer in

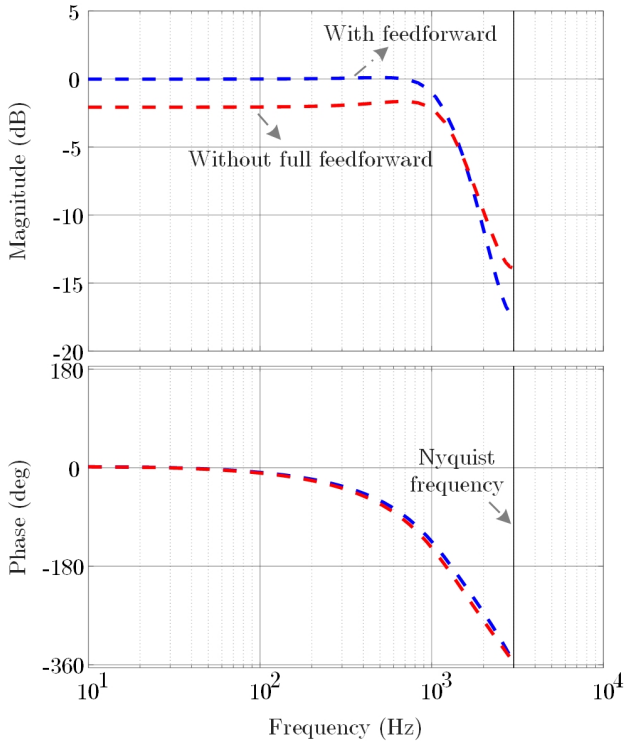

Figure 4.3: The bode plot of the transfer function (4.23) with and without full feedforward compensation.

the discrete time-domain is expressed as

$$\begin{cases} \hat{\boldsymbol{x}}_g(k+1) = \mathbf{A_{gd}}\hat{\boldsymbol{x}}_g(k) + \mathbf{B_{gd}}\boldsymbol{v}^*_{\boldsymbol{inv}}(k-1) + \mathbf{E_{gd}}\boldsymbol{v_g}(k) + \mathbf{K_{ob}}\left[\boldsymbol{y(k)} - \hat{\boldsymbol{y}}\boldsymbol{(k)}\right] \\ \boldsymbol{y}(k) = \mathbf{C}\boldsymbol{x}(k) \\ \hat{\boldsymbol{y}}(k) = \mathbf{C}\hat{\boldsymbol{x}}_g(k) \end{cases} \tag{4.24}$$

where $\mathbf{K_{ob}}$ is the gain matrix for the observer and $\hat{\boldsymbol{x}}_{\boldsymbol{g}} = [\hat{\boldsymbol{i}}_{\mathbf{1}}\ \hat{\boldsymbol{v}}_{\boldsymbol{c}}\ \hat{\boldsymbol{i}}_{\mathbf{2}}]^{\mathrm{T}}$ is the estimated state vector. Defining $\boldsymbol{x_e}$=$\boldsymbol{x_g}$-$\hat{\boldsymbol{x}}_{\boldsymbol{g}}$ represent the estimated error of the observer, and thus the dynamic of $\boldsymbol{x_e}$ can be described as

$$\boldsymbol{x_e}(k+1) = \left(\mathbf{A_{gd}} - \mathbf{K_{ob}}\mathbf{C}\right)\boldsymbol{x_e}(k) \tag{4.25}$$

It can be found the eigenvalues of the closed-loop matrix $\mathbf{A_{gd}} - \mathbf{K_{ob}}\mathbf{C}$ will determine the dynamic response of the state observer. The pole placement design can be applied to obtain the value of $\mathbf{K_{ob}}$. Although the eigenvalues which are closer to the origin will bring a faster response, the noise rejection ability will be weakened. In this work, the poles of the observer are designed according to a rule of thumb that the dynamic of the observer should be faster than

the controller. The closed-loop poles of the controller are [0 0.2353+j0.4026 0.2353-j0.4026], which are shown in Fig. 4.2(b). Therefore, the distance between the observer poles and the origin is selected as one-third of the distance between the controller poles and the origin. In this case, the poles designed for the state observer are determined as [0 0.1359+j0.2324 0.1359-j0.2324]. By using the 'place' order in MATLAB, the gain matrix $\mathbf{K_{ob}}$ is determined as $[0.4211\ 0.8718\ 1.6156]^{\mathrm{T}}$.

4.1.5 Modified Reference for Grid-Side Harmonic Rejection

MPC provides a flexible mode to design the cost function such that to suit the different sceneries. Therefore, to maintain sinusoidal current when the unhealthy grid voltage appears, the modification of the controller is proposed in this section. Compared to the previous design structure of the controller, only the reference with two-step ahead compensation needs to be updated under the distorted and unbalanced grid voltage.

The distorted grid is assumed to contain the dominant 5^{th}, 7^{th}, 11^{th}, and 13^{th} harmonic order voltage besides the fundamental component. The open-loop model of LCL-filtered VSI is sensitive to the background harmonic in the grid since the resonant peak will be induced. The output admittance of the VSI can be defined as the transfer function from the grid voltage to the grid current. The smaller admittance implies the strong harmonic rejection ability of the system. Fig. 4.4 plots the bode diagram of the output admittance of VSI with the open-loop plant and closed-loop controller respectively. It can be seen that the open-loop admittance has a peak at the resonant frequency, where the grid voltage with the same frequency will cause a significant harmonic. The resonant peak has been significantly eliminated in the closed-loop equation (4.21), as can be seen from the blue line in Fig. 4.4. Therefore, the proposed MPC controller can effectively reject the harmonics response from the distorted grid voltage, but two modifications are still proposed to improve the current performance under a distorted grid.

The first one is that the current reference generation should only contain

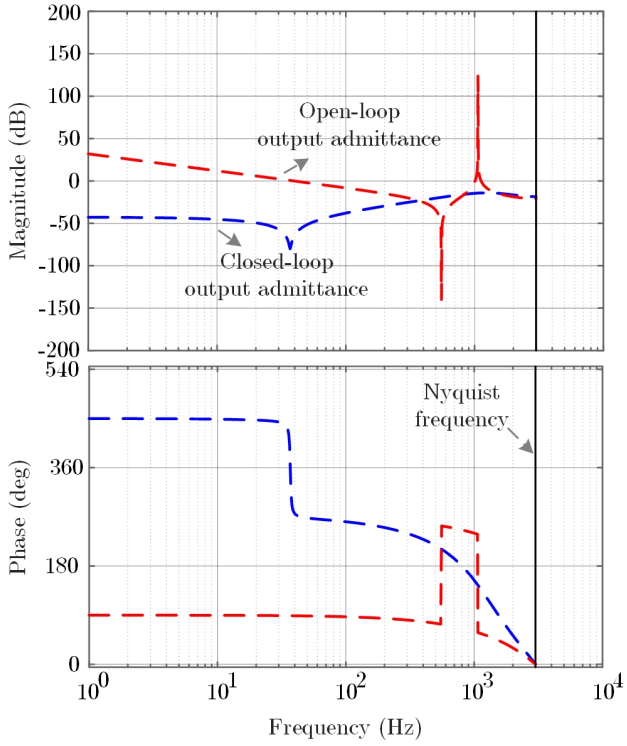

Figure 4.4: The bode plot of the output admittance of the open-loop model and closed-loop model.

the fundamental component otherwise the harmonic counterpart will also be tracked accurately as seen in Fig. 4.3. To exact the fundamental and harmonics of the grid voltage, the SDFT tool is chosen here. Compared to the resonant filters, which may easily introduce phase errors, the SDFT can achieve more accurate extraction results [116]. The basic diagram of the digital realization for SDFT is shown in Fig. 4.5, where a constant N-sized sliding window is used to store the information of the signal. The discrete transfer function for the *hth* order harmonic can be expressed as

$$H_{\mathrm{SDFT}}(z) = \frac{1 - z^{-N}}{1 - e^{j2\pi h/N} z^{-1}} \tag{4.26}$$

With the fundamental grid voltage $v_{g\alpha\_1}$ and $v_{g\beta\_1}$ obtained, the fundamental grid current reference under distorted grid conditions can be generated as

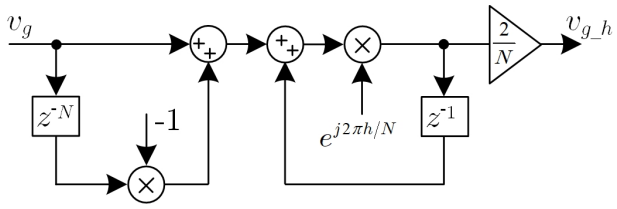

Figure 4.5: The realization diagram for the hth harmonic extraction using SDFT.

follows

$$\begin{cases} \boldsymbol{i}^*_{\mathbf{2\_1}}(k) = i^*_{2\alpha\_1}(k) + j i^*_{2\beta\_1}(k) \\ i^*_{2\alpha\_1}(k) = \frac{2}{3}\frac{P^* v_{g\alpha\_1}(k) + Q^* v_{g\beta 1\_}(k)}{v^2_{g\alpha\_1}(k) + v^2_{g\beta\_1}(k)} \\ i^*_{2\beta\_1}(k) = \frac{2}{3}\frac{P^* v_{g\beta\_1}(k) - Q^* v_{g\alpha\_1}(k)}{v^2_{g\alpha\_1}(k) + v^2_{g\beta\_1}(k)} \end{cases} \tag{4.27}$$

Since the current reference in (4.27) is still sinusoidal, the two-step ahead compensation for control delay can still be obtained by

$$\boldsymbol{i}^*_{\mathbf{2\_1}}(k+2) = \boldsymbol{i}^*_{\mathbf{2\_1}}(k) e^{j\omega_g 2T_s} \tag{4.28}$$

Correspondingly, the cost function for the grid current regulation under distorted grid conditions is designed as

$$J_{1\mathrm{D}} = \left[i^*_{2\alpha\_1}(k+2) - i_{2\alpha}(k+2)\right]^2 + \left[i^*_{2\beta\_1}(k+2) - i_{2\beta}(k+2)\right]^2 \tag{4.29}$$

Another modification for the controller under the distorted grid conditions is to ensure the capacitor voltage can replicate the harmonic components of the grid voltage. In this case, as much as the harmonics in the grid current can be rejected. The cost function for the capacitor voltage regulation under distorted grid conditions is designed as

$$J_{2\mathrm{D}} = \left[v^*_{c\alpha\_H}(k+2) - v_{c\alpha}(k+2)\right]^2 + \left[v^*_{c\beta\_H}(k+2) - v_{c\beta}(k+2)\right]^2 \tag{4.30}$$

where ${v_{c\alpha\_H}}^*$ and ${v_{c\beta\_H}}^*$ are the reference for capacitor voltage tracking, which contains the harmonic component from the grid. Normally, the grid harmonic component can be obtained by subtracting the fundamental voltage from the total grid voltage. However, considering the two-step ahead compensation for the reference still needed to be realized and the background harmonic voltage of the grid has different frequencies, the compensation is realized independently for each harmonic component. For example, the 5^{th}, 11^{th} harmonic voltage

with the negative sequence and 7^{th}, 13^{th} harmonic voltage with the positive sequence can be compensated as

$$\begin{cases} v_{g\_1}(k+2) = v_{g\_1}(k)e^{j\omega_g 2T_s} \\ v_{g\_5}(k+2) = v_{g\_5}e^{-j5\omega_g 2T_s} \\ v_{g\_7}(k+2) = v_{g\_7}(k)e^{j7\omega_g 2T_s} \\ v_{g\_11}(k+2) = v_{g\_11}(k)e^{-j11\omega_g 2T_s} \\ v_{g\_13}(k+2) = v_{g\_13}(k)e^{j13\omega_g 2T_s} \end{cases} \tag{4.31}$$

Therefore, the reference $v_{c\alpha\_H}{}^*$ and $v_{c\beta\_H}{}^*$ can be calculated as

$$\begin{cases} \boldsymbol{v^*_{c\_H}}(k = v^*_{c\alpha\_H}(k) + jv^*_{c\beta\_H}(k) \\ v^*_{c\alpha\_H}(k) = \sum\limits_{h}^{1,5,7,11,13} v_{g\alpha\_h}(k) - \omega_g L_g i^*_{2\beta\_1}(k) \\ v^*_{c\beta\_H}(k) = \sum\limits_{h}^{1,5,7,11,13} v_{g\beta\_h}(k) + \omega_g L_g i^*_{2\alpha\_1}(k) \end{cases} \tag{4.32}$$

Furthermore, the reference for inverter-side current is the sum of the grid current and capacitor current, which can be calculated as

$$\begin{cases} \boldsymbol{i^*_{1\_H}}(k) = i^*_{1\alpha\_H}(k) + ji^*_{1\beta\_H}(k) \\ i^*_{1\alpha\_H}(k) = (1 - {\omega_g}^2 L_2 C_f)\, i^*_{2\alpha\_1}(k) + \omega_g C_f \left(- \sum\limits_{h}^{1,7,13} h\overrightarrow{v_{g\beta h}}(k) + \sum\limits_{h}^{5,11} h\overrightarrow{v_{g\beta h}}(k) \right) \\ i^*_{1\beta\_H}(k) = (1 + {\omega_g}^2 L_2 C_f)\, i^*_{2\beta\_1}(k) + \omega_g C_f \left(\sum\limits_{h}^{1,7,13} h\overrightarrow{v_{g\alpha h}}(k) - \sum\limits_{h}^{5,11} h\overrightarrow{v_{g\alpha h}}(k) \right) \end{cases} \tag{4.33}$$

and the cost function for the inverter-side current regulation under distorted grid conditions is designed as

$$J_{3\mathrm{D}} = \left[i^*_{1\alpha\_H}(k+2) - i_{1\alpha}(k+2)\right]^2 + \left[i^*_{1\beta\_H}(k+2) - i_{1\beta}(k+2)\right]^2 \tag{4.34}$$

Finally, the total cost function can be written as

$$J_{\mathrm{D}} = J_{1\mathrm{D}} + \mathrm{w}_{v_c} J_{2\mathrm{D}} + \mathrm{w}_{i_1} J_{3\mathrm{D}} \tag{4.35}$$

The optimized control law can also be derived by performing the gradient of (4.35) with respect to $\boldsymbol{v_{inv}}$ equals to zero.

The unbalanced grid voltage will cause the prominent triple-order harmonic in the grid current [117]. In this section, the capability of MPC to tackle

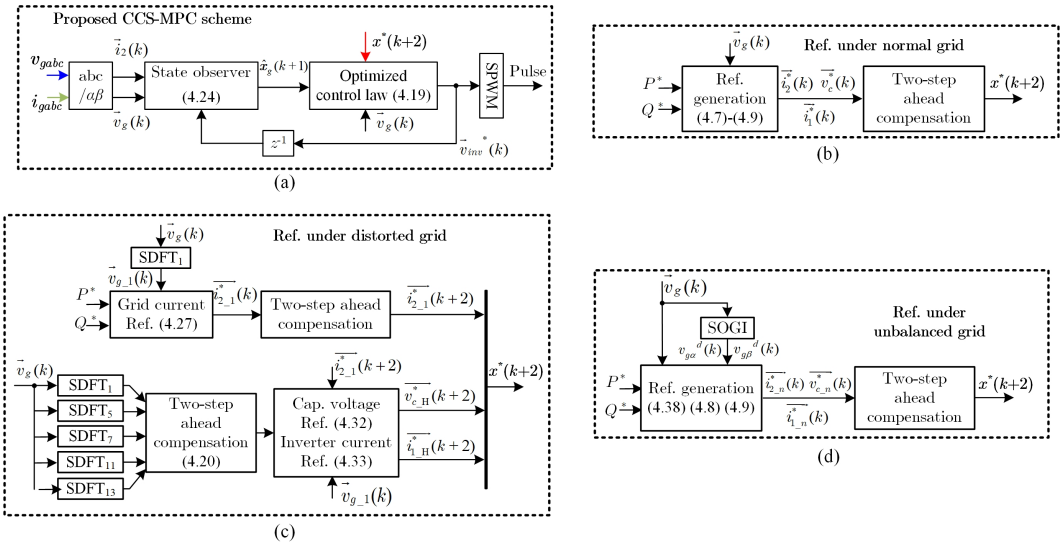

Figure 4.6: Diagram of the proposed MPC scheme with hybrid current and voltage control. (a) The unified structure of the proposed controller. (b) The reference generation under normal grid condition. (c) The reference generation under distorted grid condition. (d) The reference generation under unbalanced grid condition.

the unbalanced grid condition is extended for LCL-filtered VSI. To maintain a simple concept and avoid using the positive/negative sequence extraction block, the modification of the instantaneous reactive power is used to generate the grid current reference [75], which is realized in this work to verify its application versatility on a high-order plant. To do this, the variable x_d is defined, which lags x by 90 electrical degrees. For grid voltage, it can be expressed as

$$\begin{cases} v_{g\alpha} = V_1 cos(\omega t + \varphi_1) \;\; v_{g\alpha}^d = V_1 sin(\omega t + \varphi_1) \\ v_{g\beta} = V_2 cos(\omega t + \varphi_2) \;\; v_{g\beta}^d = V_2 sin(\omega t + \varphi_2) \end{cases} \tag{4.36}$$

and the instantaneous active and reactive powers are defined as

$$\begin{cases} P_n = \frac{3}{2}(v_{g\alpha} i_{g\alpha} + v_{g\beta} i_{g\beta}) \\ Q_n = \frac{3}{2}(v_{g\alpha}^d i_{g\alpha} + v_{g\beta}^d i_{g\beta}) \end{cases} \tag{4.37}$$

Substituting (4.36) into (4.37) and making the dc component of P_n equals P^* while the coefficients before the ripple component and the dc component of Q_n equal zero at the same time. Therefore, the reference for grid current under

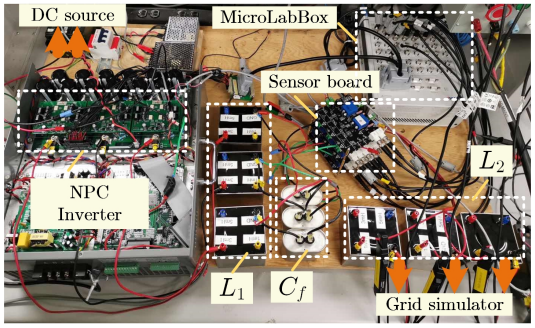

Figure 4.7: Experimental setup of the LCL filtered VSI system.

unbalanced grid conditions can be derived as

$$\begin{cases} \boldsymbol{i^*_{2\_n}}(k) = i^*_{2\alpha\_\mathrm{n}}(k) + j i^*_{2\beta\_\mathrm{n}}(k) \\ i^*_{2\alpha\_n}(k) = \frac{2}{3}\frac{-P^* v^d_{g\beta}(k)}{(v_{g\beta}v^d_{g\alpha} - v_{g\alpha}v^d_{g\beta})} \\ i^*_{2\beta\_\mathrm{n}}(k) = \frac{2}{3}\frac{P^* v^d_{g\alpha}(k)}{(v_{g\beta}v^d_{g\alpha} - v_{g\alpha}v^d_{g\beta})} \end{cases} \tag{4.38}$$

The delay variable of the grid voltage $v^d_{g\alpha}$ and $v^d_{g\beta}$ can be obtained by using the second-order generalized integrator (SOGI) block. The reference of capacitor voltage $\boldsymbol{v^*_{c\_n}}(k)$ and inverter-side current $\boldsymbol{i^*_{1\_n}}(k)$ can be derived in (4.8) and (4.9) respectively by replacing $\boldsymbol{i^*_2}(k)$ with $\boldsymbol{i^*_{2\_n}}(k)$. Since all references are sinusoidal, the two-step ahead compensation can be directly adopted. Similarly, the optimized control law can be then obtained by using the new reference generated.

The diagram of the proposed MPC scheme with hybrid current and voltage control for LCL-filtered grid-connected VSI is shown in Fig. 4.6. The system with resonance damping and harmonic rejection ability is incorporated, and the control delay is compensated by the forecast reference and estimated state variables from the observer. It can be seen that the proposed controller is implemented with an intuitive concept and only the reference of the state variables needs to be modified under unhealthy grid voltage conditions.

4.1.6 Simulation and Experimental Results

The proposed controller is simulated by using the MATLAB/Simulink firstly with the parameter shown in Table 4.1. Then, it is verified experimentally

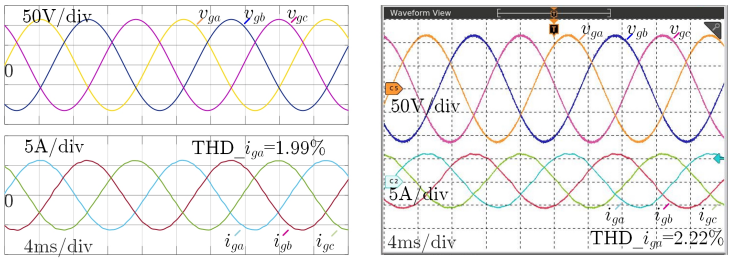

Figure 4.8: Simulation and experimental results of grid current with 1kW injected power under the sinusoidal grid voltage (a) Simulated grid current. (b) Experimental grid current.

by MicroLabBox 1202 digital controller with the same parameter used. A three-level neutral-point-clamped (NPC) inverter configurated by IGBT power modules (Infineon F3L75R07W2E3) is connected to the ac grid simulator. The SPWM block with a common-mode signal injection is used to generate the optimized control law from the controller while maintaining the balance of dc-link voltage. Fig. 4.7 shows the adopted hardware prototype for the three-level NPC inverter connected to the grid through the LCL filter.

Fig. 4.8 shows the simulated and experimental results of the grid current. It can be seen that both the simulated and experimental grid currents are maintained as sinusoidal waveforms without resonance oscillations. The THD value of the injected current is lower, i.e, 1.99% in simulation and 2.22% in the experiment. Therefore, the proposed CCS-MPC scheme can ensure the normal power injection at the steady-state with satisfactory current performance. For comparison, if the weighting factor w_{vc} for capacitor voltage tracking is set as 0, then the system cannot work normally and the ac grid simulator indicates the 'fault' mode in the experiment.

To verify the resonance damping ability of the proposed MPC controller. The dynamic response of the grid current by using simulation and experiment are shown in Fig. 4.9, where the active power reference changes from 500W to 1kW. With the closed-loop poles designed in Fig. 4.2(b), the resonance peak caused by the disturbance can be effectively reduced, as seen in Fig. 4.9(a) and Fig. 4.9(c). For comparison, the weighting factor for capacitor voltage regulation w_{v_c} is reduced to 0.003 with the results shown in Fig. 4.9(b)

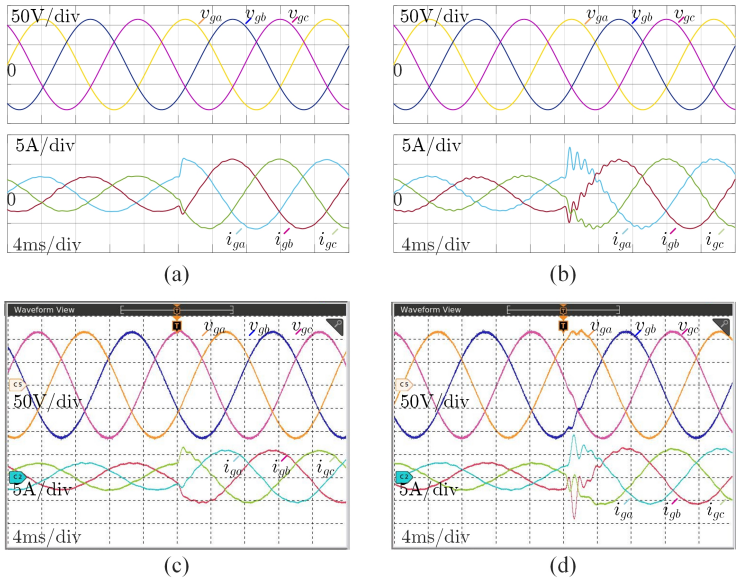

Figure 4.9: Simulation and experimental results of grid voltage and current with the injected power changes from 500W to 1kW (a) Simulation (w_{v_c} =0.03). (b) Simulation (w_{v_c}=0.003). (c) Experiment (w_{v_c}=0.03). (d) Experiment (w_{v_c}=0.003).

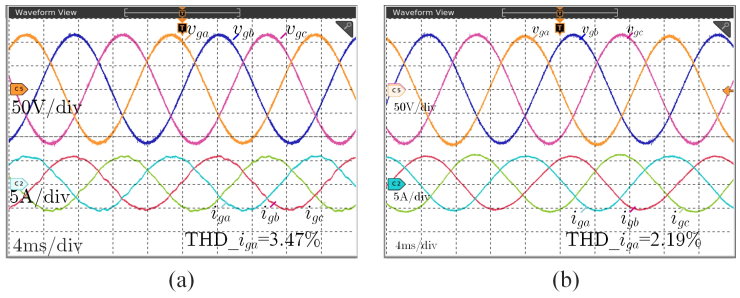

Figure 4.10: Experimental results of grid current with 1kW injected power (a) FCS-MPC with sampling frequency 30kHz. (b) PI-based AD scheme with capacitor current feedback.

and Fig. 4.9(d) respectively. Since the closed-loop poles are far away from the origin with a reduced w_{v_c}, the stability margin of the system is reduced. Besides, the resonance peak becomes prominent due to the smaller damping ratio. Therefore, with the suitable parameter designed, the proposed MPC can significantly dampen the resonance peak and improve system security.

To show the contribution of the proposed scheme, the other two typical schemes applied to the LCL filtered grid-connected inverter are compared. The steady-state performance with 1kW injected power of the FCS-MPC and PI-based AD scheme with capacitor current feedback are shown in Fig. 4.10. The spectrum of grid current has been presented in Fig. 4.11. The FCS-MPC

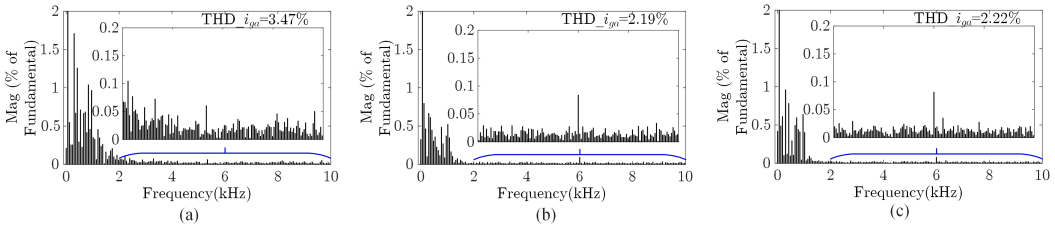

Figure 4.11: The spectrum of experimental grid current with 1kW injected power (a) FCS-MPC with sampling frequency 30kHz. (b) PI-based AD scheme with capacitor current feedback. (c) Proposed MPC scheme.

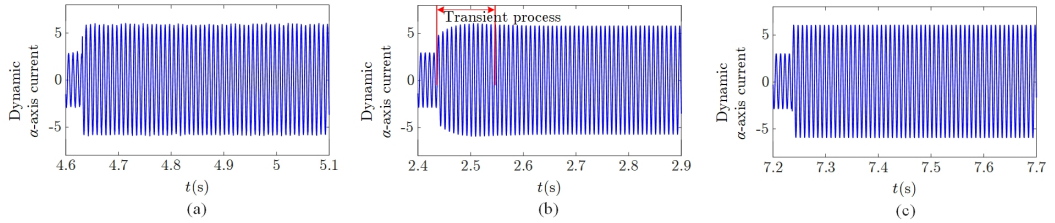

Figure 4.12: Dynamic experimental results of α-axis grid current with the injected power changes from 500W to 1kW (a) FCS-MPC with sampling frequency 30kHz. (b) PI-based AD scheme with capacitor current feedback. (c) Proposed MPC scheme.

scheme exhaustively searches the optimized input vector according to the proposed cost function (4.12). As a result, the FCS-MPC needs almost 25μs to execute the algorithm. Therefore the sampling frequency 30kHz is adopted in FCS-MPC to ensure enough computation resources for the algorithm execution. Besides, since there is no modulation stage incorporated in FCS-MPC, the switching frequency is unfixed (almost 4.5kHz with lkW power injection) and the resulted spectrum of the injected current is spread. As can be seen in Fig. 4.10(a), the steady-state current performance of FCS-MPC is worse than that of the proposed scheme. The capacitor current feedback-based AD scheme utilized the cascaded way, where the PI regulator is adopted for the injected current. The parameters of PI are adjusted according to the symmetrical optimum whereas the LCL filter is approximated to the L filter [118]. Besides, the damping coefficient is determined by the root loci of the closed-loop transfer function. As can be seen in Fig. 4.10(b), this AD scheme can also achieve a satisfactory steady-state current. The dynamic α-axis current tracking performances of the three schemes are shown in Fig. 4.12. It can be seen that both the proposed scheme and FCS-MPC show faster current track-

ing performance than that of the AD scheme. It is worth mentioning that the AD scheme has at least four parameters including the proportional gain, integral gain, saturation value of the PI regulator, and damping coefficient that need to be designed. On the contrary, only two weighting factors w_{i_1} and w_{v_c} need to be designed in the proposed MPC scheme. Therefore, compared to this AD scheme, a faster dynamic response and reduced tuning complexity can be achieved by the proposed scheme. Finally, the comparison of FCS-MPC, PI-based AD and the proposed MPC scheme is summarized in Table 4.2.

Table 4.2: Comprehensive comparison for FCS-MPC, PI-based AD and proposed MPC scheme

Indices	FCS-MPC	PI-based AD	Proposed MPC
Steady-state performance	general	good	good
Dynamic response	fast	slow	fast
Parameter number	two	four	two
Weighting factor tuning	difficult	-	easy
Computational burden	high	low	low
Sampling frequency	high	low	low
Switching frequency	unfixed	constant	constant
Bandwidth	high	limited	high
Design concept	intuitive	complex	intuitive
Multivariable control	easy	difficult	easy

Fig. 4.13 shows the grid current waveform under the distorted grid conditions, which contains 2% 5^{th}, 2% 7^{th}, 1% 11^{th}, and 1% 13^{th} order harmonic voltage. Firstly, the performance of grid current is tested by using the proposed CCS-MPC without any modification. It can be seen in Fig. 4.13(a) and Fig. 4.13(c) that the current waveform is significantly polluted by the grid harmonic voltage with simulated THD 10.93% and experimental THD 13.88% respectively. To clear the harmonic components in grid current, the proposed two modifications are applied, i.e., the reference is changed to the distorted grid condition and the capacitor voltage is forced to replicate the grid harmonic voltage by the cost function. As a result, it can be seen in Fig. 4.13(b) and Fig. 4.13(d) that the sinusoidal current can still be maintained with low THD obtained. Therefore, the proposed modification within the MPC framework

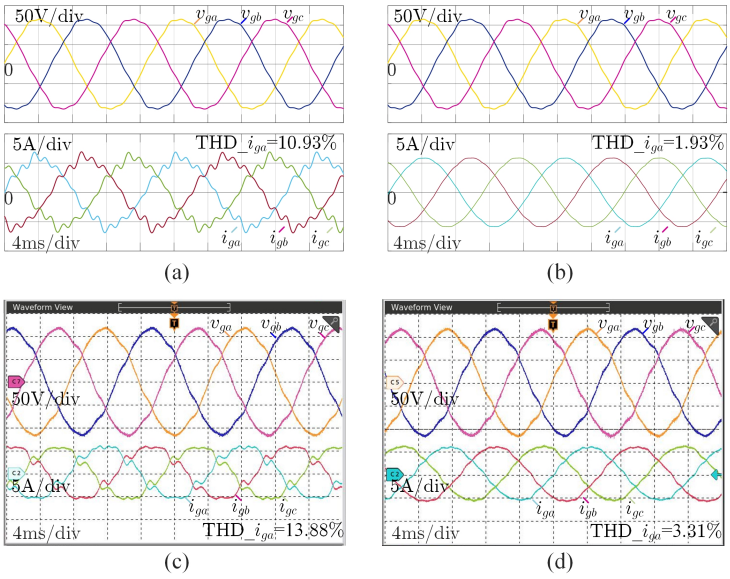

Figure 4.13: Simulation and experimental results of grid current using the proposed CCS-MPC with 1kW injected power under distorted grid conditions (a) Simulation without modification. (b) Simulation with reference modification. (c) Experiment without modification. (d) Experiment with reference modification.

can effectively reject the harmonics caused by the distorted grid conditions.

Fig. 4.14 shows the grid current waveform under the unbalanced grid conditions, where the phase a grid voltage is reduced to 80% percent of the other two phases. The performance of grid current is tested by directly using the proposed CCS-MPC without reference modification. As expected in Fig. 4.14(a) and Fig. 4.14(c), the prominent triple-order harmonic appears in the grid current, resulting in simulated THD 7.34% and experimental THD 7.81% respectively. By modifying the reference of grid current in (4.38), the sinusoidal current is obtained in Fig. 4.14(b) and Fig. 4.14(d) with THD 1.90% and 1.82% respectively. Therefore, the proposed scheme can effectively reject the harmonics caused by unbalanced grid conditions. Moreover, as seen in Fig. 4.14(e), the proposed controller reacts quickly to the voltage sags with a good transient process.

With the weighting factors $w_{i_1}(0.3)$ and $w_{v_c}(0.03)$ designed for the proposed MPC, the performance of the controller affected by the mismatch of the plant parameters is investigated. The real value of the inverter-side inductance is 3mH used, and the closed-loop root loci is plotted in Fig. 4.15(a) when the used

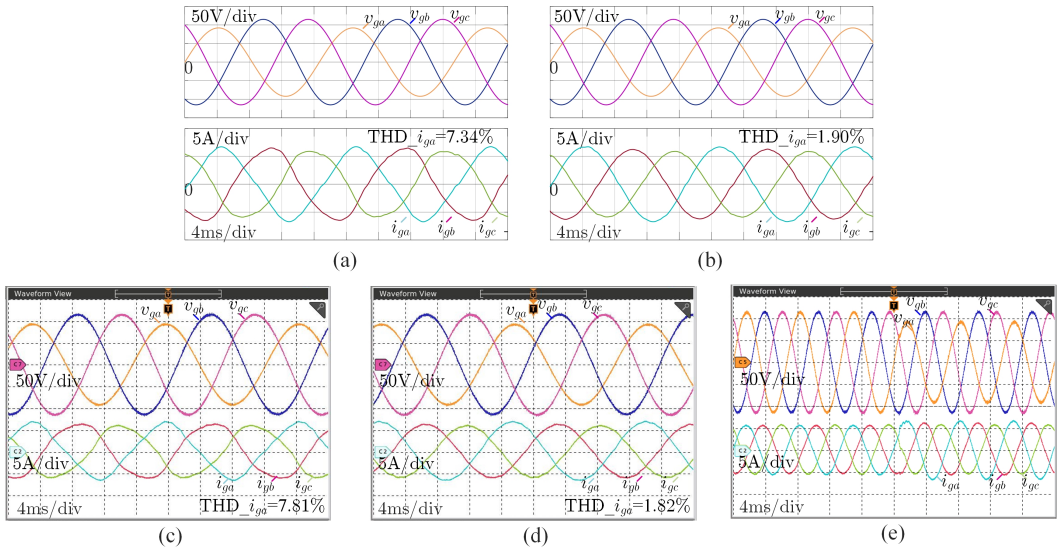

Figure 4.14: Simulation and experimental results of grid current using the proposed CCS-MPC with 1kW injected power under unbalanced grid conditions (a) Simulation without modification. (b) Simulation with reference modification. (c) Experiment without modification. (d) Experiment with reference modification. (e) The dynamic current response in case of voltage sags.

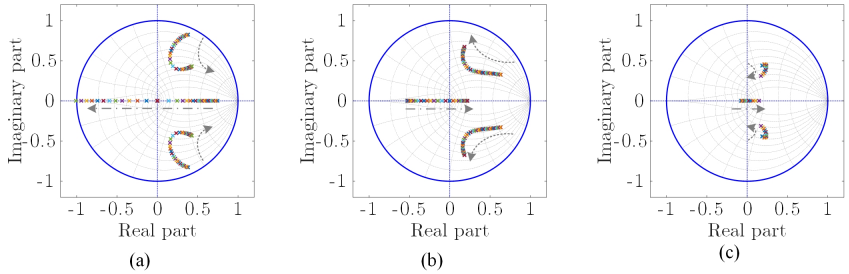

Figure 4.15: The closed-loop root loci with mismatched plant parameters. (a) The used L_1 value changes from 33.33% to 140% of the real value. (b) The used C_f value changes from 33.33% to 166.67% of the real value. (c) The used L_2 value changes from 50% to 150% of the real value.

value in the controller changes from 33.33% to 140% of the real value. It can be seen that with a reduced value of L_1 used, the stability margin of the system and the damping ratio are reduced. When the used value reaches 140%, the pole lies out of the unit cycle, and the system becomes unstable. However, for a wide range of L_1 changes, the system performance can be ensured. Similarly, the closed-loop root loci is plotted in Fig. 4.15(b) when the used capacitance value in the controller changes from 33.33% to 166.67% of the real value. The damping ratio will reduce considerably with the increased capacitance, resulting in more resonance peaks during the dynamic process. Fig. 4.15(c)

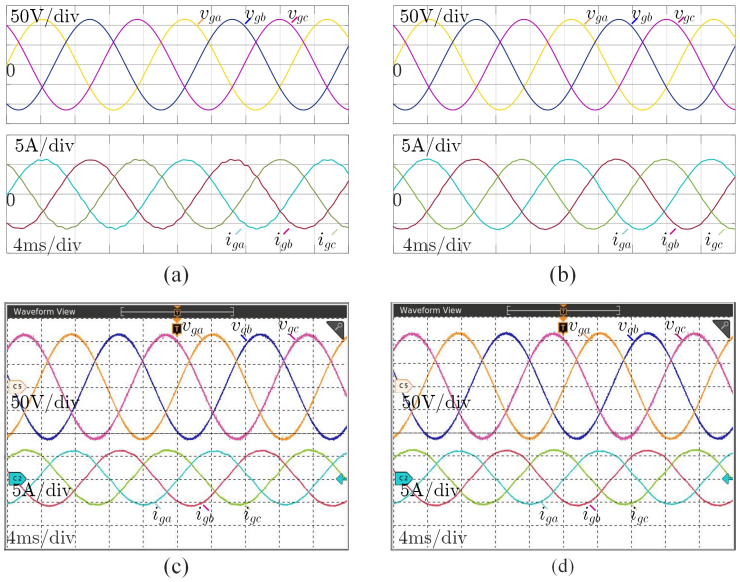

Figure 4.16: Simulation and experimental results of grid current with 1kW injected power under grid-side inductance mismatch (a) Simulation with 0.5mH L_2. (b) Simulation with 1.5mH L_2. (c) Experiment with 0.5mH L_2. (d) Experiment with 1.5mH L_2.

plots the closed-loop root loci when the used grid-side inductance value in the controller changes from 50% to 150% of the real value. The damping ratio will change slightly but still with guaranteed system performance. A study case of the grid-side inductance mismatch is shown in Fig. 4.16 with 50% and 150% of the real value used. It can be seen that the system performance does not change too much compared to Fig. 4.8.

4.2 FCS-MPC for VSC-fed PMSM With Output LC Filter

In this section, the FCS-MPC is designed for the three-level NPC inverter-fed PMSM drive system with an LC filter, as shown in Fig. 4.17. Firstly, the state trajectory between the first-order system (without filter) and the high-order plant is compared in the time domain. Therefore, the design principle of the cost function for filter resonance suppression can be revealed intuitively. Secondly, to reduce the hardware cost, the Kalman-filter-based state estimation is adopted with the compensation for control input delay. Finally, to make an easy realization in the digital platform, the cost function is further optimized

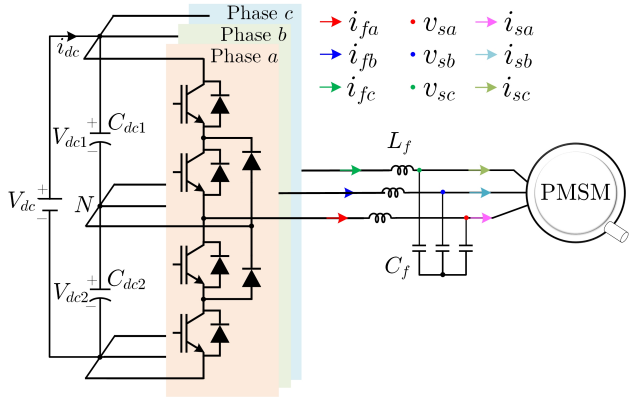

Figure 4.17: Three-level NPC inverter-fed PMSM drive system with an output LC filter.

to a simplified form. An exhaustive and detailed description of the proposed FCS-MPC controller is presented.

4.2.1 Predictive Model of PMSM Side With LC filter

The dynamic modeling in Fig. 4.17 can be described as

$$\frac{d\boldsymbol{x_s}}{dt} = \mathbf{A_s}\boldsymbol{x} + \mathbf{B_s}\boldsymbol{u_s} + \mathbf{E_s} \tag{4.39}$$

where the state vector $\boldsymbol{x_s} = [i_{sd}\ i_{sq}\ v_{sd}\ v_{sq}\ i_{fd}\ i_{fq}]^{\mathrm{T}}$ and the input vector $\boldsymbol{u_s} = [v_{invd}\ v_{invq}]^{\mathrm{T}}$. The time-varying matrix $\mathbf{A_s}$, $\mathbf{B_s}$, and the disturbance matrix $\mathbf{E_s}$ are given by

$$\begin{aligned}
\mathbf{A_s} &= \begin{bmatrix}
-\frac{R_s}{L_s} & \omega_e & \frac{1}{L_s} & 0 & 0 & 0 \\
-\omega_e & -\frac{R_s}{L_s} & 0 & \frac{1}{L_s} & 0 & 0 \\
-\frac{1}{C_f} & 0 & 0 & \omega_e & \frac{1}{C_f} & 0 \\
0 & -\frac{1}{C_f} & -\omega_e & 0 & 0 & \frac{1}{C_f} \\
0 & 0 & -\frac{1}{L_f} & 0 & -\frac{R_f}{L_f} & \omega_e \\
0 & 0 & 0 & -\frac{1}{L_f} & -\omega_e & -\frac{R_f}{L_f}
\end{bmatrix}, \\
\mathbf{B_s} &= \begin{bmatrix}
0 & 0 \\ 0 & 0 \\ 0 & 0 \\ 0 & 0 \\ \frac{1}{L_f} & 0 \\ 0 & \frac{1}{L_f}
\end{bmatrix}, \quad \mathbf{E_s} = \begin{bmatrix}
0 \\ -\frac{\omega_e \psi_f}{L_s} \\ 0 \\ 0 \\ 0 \\ 0
\end{bmatrix}
\end{aligned} \tag{4.40}$$

v_{sd}, v_{sq}, and i_{sd}, i_{sq} represent the dq-axes stator voltage and current respectively. R_s and L_s represent the stator resistance and inductance for the

surface-mounted PMSM. ω_e is the synchronous angular velocity. ψ_f represents the magnitude of rotor flux. v_{invd}, v_{invq}, and i_{fd}, i_{fq} represent the dq-axes inverter-side voltage and current respectively. L_f and C_f represent the filter inductance and capacitance respectively. R_f is the equivalent series resistance of L_f, which is ignored in this work due to the quite small value. Besides, the worst situation without any internal damping factor will make the system more unstable.

Assuming that the sampling interval is T_s and the current time step is k, the modeling (4.39) is discretized based on the ZOH principle to obtain the predictive equation as

$$\boldsymbol{x_s}(k+1) = \mathbf{A_{sd}}\boldsymbol{x_s}(k) + \mathbf{B_{sd}}\boldsymbol{u_s}(k) + \mathbf{E_{sd}} \tag{4.41}$$

Considering the high-order feature of (4.39) and the coupling dynamic between state variables, the Taylor series expansion of the discrete matrices are reserved to the third-order item to improve the accuracy of state prediction, i.e.,

$$\mathbf{A_{sd}} \approx \sum_{n=0}^{3} \frac{\mathbf{A_s}^n T_s^n}{n!} \ , \ \mathbf{B_{sd}} \approx \sum_{n=1}^{3} \frac{\mathbf{A_s}^{n-1} T_s^n}{n!}\mathbf{B_s} \ , \mathbf{E_{sd}} \approx \sum_{n=1}^{3} \frac{\mathbf{A_s}^{n-1} T_s^n}{n!}\mathbf{E_s} \tag{4.42}$$

Considering the inaccurate disturbance $\tilde{\mathbf{E}}_{\mathbf{sd}}$ and other constant disturbance $\boldsymbol{\eta}_{\mathbf{d}}$ in the system model, i.e.,

$$\boldsymbol{x_s}(k+1) = \mathbf{A_{sd}}\boldsymbol{x_s}(k) + \mathbf{B_{sd}}\boldsymbol{u_s}(k) + \tilde{\mathbf{E}}_{\mathbf{sd}} + \boldsymbol{\eta}_{\mathbf{d}} \tag{4.43}$$

The integral operation is embedded into the predictive equation to improve the accuracy [119], which can eliminate the effect that comes from the slow-varying disturbance. Applying the differential operation to both sides of (4.43), we have

$$\begin{aligned} \boldsymbol{x_s}(k+1) - \boldsymbol{x_s}(k) = \mathbf{A_{sd}}\left[\boldsymbol{x_s}(k) - \boldsymbol{x_s}(k-1)\right] + \mathbf{B_{sd}}\left[\boldsymbol{u_s}(k) - \boldsymbol{u_s}(k-1)\right] \\ + \tilde{\mathbf{E}}_{\mathbf{sd}} - \tilde{\mathbf{E}}_{\mathbf{sd}} + \boldsymbol{\eta}_{\mathbf{d}} - \boldsymbol{\eta}_{\mathbf{d}} \end{aligned} \tag{4.44}$$

or equivalently

$$\Delta\boldsymbol{x_s}(k+1) = \mathbf{A_{sd}}\Delta\boldsymbol{x_s}(k) + \mathbf{B_{sd}}\Delta\boldsymbol{u_s}(k) \tag{4.45}$$

where the dynamic of ω_e is assumed as constant($d\omega_e/dt = 0$). $\Delta \boldsymbol{x_s}(k)$=$\boldsymbol{x_s}(k)$-$\boldsymbol{x_s}(k\text{-}1)$, $\Delta \boldsymbol{u_s}(k)$=$\boldsymbol{u_s}(k)$-$\boldsymbol{u_s}(k\text{-}1)$ are the incremental component of state variable and control input respectively. Therefore, the predictive state variables can be obtained through the augmented equation

$$\boldsymbol{x_s}(k+1) = \boldsymbol{x_s}(k) + \mathbf{A_{sd}}\Delta \boldsymbol{x_s}(k) + \mathbf{B_{sd}}\Delta \boldsymbol{u_s}(k) \tag{4.46}$$

Each phase leg $l \in \{a,\ b,\ c\}$ has three voltage levels that can be selected, i.e., $0.5V_{dc}(\lambda_l{=}1)$, $0(\lambda_l{=}0)$, and $\text{-}0.5V_{dc}(\lambda_l{=}\text{-}1)$, where λ_l represent the switching variable of each leg. Therefore, the dynamic equation of the two dc-link capacitor voltages V_{dc1} and V_{dc2} can be expressed as [120]

$$\begin{bmatrix} \frac{dV_{dc1}}{dt} \\ \frac{dV_{dc2}}{dt} \end{bmatrix} = \begin{bmatrix} -\frac{\Gamma_{1a}}{C_{dc1}} - \frac{\Gamma_{1b}}{C_{dc1}} - \frac{\Gamma_{1c}}{C_{dc1}} \\ -\frac{\Gamma_{2a}}{C_{dc2}} - \frac{\Gamma_{2b}}{C_{dc2}} - \frac{\Gamma_{2c}}{C_{dc2}} \end{bmatrix} \begin{bmatrix} i_{fa} \\ i_{fb} \\ i_{fc} \end{bmatrix} + \begin{bmatrix} \frac{i_{dc}}{C_{dc1}} \\ \frac{i_{dc}}{C_{dc2}} \end{bmatrix} \tag{4.47}$$

where

$$\Gamma_{1l} = \frac{\lambda_l(\lambda_l+1)}{2} \quad \Gamma_{2l} = \frac{\lambda_l(1-\lambda_l)}{2}.$$

i_{fa}, i_{fb}, i_{fc} and i_{dc} represent the three-phase inverter-side currents and dc-link current, as noted in Fig. 4.17. The two dc-link capacitances used are same, i.e., C_{dc1}=C_{dc2}=C_{dc}. Therefore, the dynamic equation for the voltage deviation ΔV_{dc} between V_{dc1} and V_{dc2} can be obtained as

$$\begin{aligned} \tfrac{d\Delta V_{dc}}{dt} &= \tfrac{dV_{dc1}}{dt} - \tfrac{dV_{dc2}}{dt} \\ &= \tfrac{1}{C_{dc}}\left[(\Gamma_{2a}-\Gamma_{1a})\, i_{fa} + (\Gamma_{2b}-\Gamma_{1b})\, i_{fb} + (\Gamma_{2c}-\Gamma_{1c})\, i_{fc}\right] \end{aligned} \tag{4.48}$$

Using the first-order Euler discretization, the predictive dc-link voltage deviation can be obtained as

$$\begin{aligned} \Delta V_{dc}(k+1) = \Delta V_{dc}(k) + \tfrac{T_s}{C_{dc}}[&(\Gamma_{2a}-\Gamma_{1a})\, i_{fa}(k) + \\ &(\Gamma_{2b}-\Gamma_{1b})\, i_{fb}(k) + (\Gamma_{2c}-\Gamma_{1c})\, i_{fc}(k)] \end{aligned} \tag{4.49}$$

4.2.2 Proposed Cost Function With Multivariable Control

The typical cascaded way for the motor drive controller is adopted in this work, where the outer speed loop uses the PI regulator to generate the q-axis current reference i^*_{sq}. The d-axis current reference i^*_{sd} is set as 0 to achieve

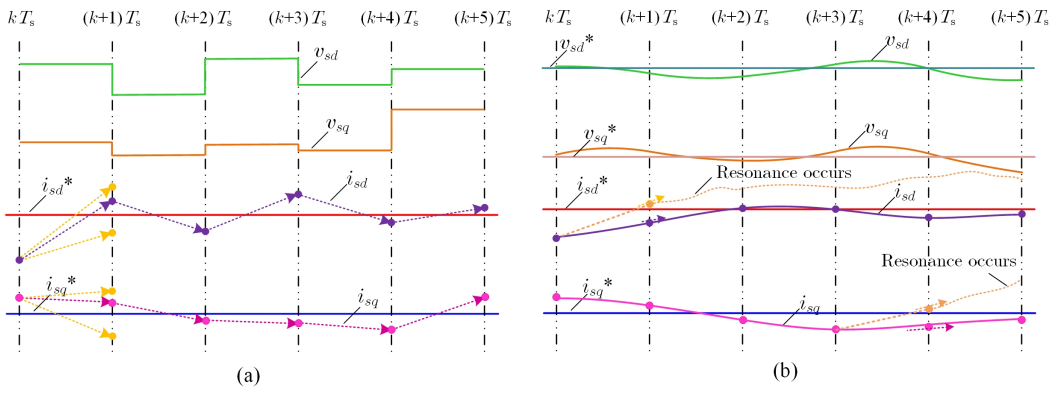

Figure 4.18: The trajectory evolution of stator current in the MPC realization process (a) Motor drive without additional filter (first-order system) and (b) Motor drive with LC filter.

the maximum torque current ratio. The inner loop only includes a single FCS-MPC controller without a multiloop path. To demonstrate the resonance problems caused by the additional filter, the trajectory of state variables is firstly analyzed.

The cost function should realize the *dq*-axes stator current reference tracking and thus implicitly ensure the tracking of speed reference. Therefore, the first item in the cost function is designed as

$$J_1 = \left[i_{sq}^* - i_{sq}(k+1)\right]^2 + \left[i_{sd}^* - i_{sd}(k+1)\right]^2 \tag{4.50}$$

To dampen the filter resonance, the existing AD schemes are realized with additional feedback, e.g., capacitor current or converter-side current are introduced. Besides, the virtual-impedance-based harmonic loop is also combined, where the design is a transfer-function-based process with a modulator applied. To provide an intuitive principle of the resonance generation and suppression, the compared trajectory of state variables in the drive system with and without additional filter (first-order system) are demonstrated in the time-domain firstly, as seen in Fig. 4.18. In Fig. 4.18(a), where the motor drive without LC filter is considered, the control objective only includes the *dq*-axes current reference tracking and the manipulated voltage vector which can achieve the minimized current tracking error will be selected at each sampling instant. Therefore, the derivative of current can change suddenly subjected to the applied input stator voltage without any physical constraints. While for the

motor terminal connected with LC filter, the stator voltage is maintained as a continuous variable due to the effect of the capacitor. In the system modeling (4.39), v_{sdq} can be treated as the virtual input for the control of i_{sdq}. Since v_{sdq} cannot change instantaneously, the derivative of i_{sdq} are forced to maintain as continuous at each sampling instant. As seen in Fig. 4.18(b), with the dq-axes current reference tracking as the sole objective, the virtual input v_{sdq} will contribute to the minimized error between the actual current trajectory and references. However, the derivative of the current remains uncontrolled at each sampling instant. Therefore, in the case of the current trajectory evolved from the last instant, although the input v_{sdq} which can achieve the smallest current deviation is still selected, the current trajectory trend cannot be remedied. In other words, due to the continuous constraint of the current derivatives, all available virtual inputs v_{sdq} will generate a relatively large current deviation in the next interval. Furthermore, the current trajectory will deviate more and more from the desired reference, which causes the filter resonance phenomenon. Therefore, besides the current reference tracking at each sampling instant, the capacitor voltage, which is directly related to the current derivative should also be regulated effectively. As can be seen in Fig. 4.18(b), the derivatives of the stator current reference are zero since the constant value under dq frame. According to the dynamic equation of stator current

$$\begin{cases} \frac{di_{sd}}{dt} = -\frac{R_s}{L_s} i_{sd} + \omega_e i_{sq} + \frac{1}{L_s} v_{sd} \\ \frac{di_{sq}}{dt} = -\omega_e i_{sd} - \frac{R_s}{L_s} i_{sq} + \frac{1}{L_s} v_{sq} - \frac{\omega_e \psi_f}{L_s} \end{cases}, \tag{4.51}$$

the capacitor voltage reference can be obtained by making the derivatives of the stator current in (4.51) equal zero. Therefore, we have

$$\begin{cases} v_{sd}^* = R_s i_{sd}^* - \omega_e L_s i_{sq}^* \\ v_{sq}^* = R_s i_{sq}^* + \omega_e L_s i_{sd}^* + \omega_e \psi_f \end{cases} \tag{4.52}$$

As a result, the cost function that regulates the capacitor voltage tracking is expressed as

$$J_2 = \left[v_{sq}^* - v_{sq}(k+1)\right]^2 + \left[v_{sd}^* - v_{sd}(k+1)\right]^2 \tag{4.53}$$

Similarly, the derivative of the capacitor voltage is kept continuous due to the physical constraint of the filter inductor. The instantaneous values of capacitor voltage are regulated in (4.53) without the derivative control. Therefore, to remedy the trajectory of capacitor voltage, the inverter-side current, which is directly related to the derivative of capacitor voltage, should also be regulated. The inverter-side current reference corresponds to the zero derivatives of capacitor voltage can be generated as

$$\begin{cases} i_{fd}^{*} = i_{sd}^{*} - \omega_e C_f v_{sq}^{*} \\ i_{fq}^{*} = i_{sq}^{*} + \omega_e C_f v_{sd}^{*} \end{cases} \tag{4.54}$$

The cost function that regulates the inverter-side current tracking is expressed as

$$J_3 = \left[i_{fq}^{*} - i_{fq}(k+1)\right]^2 + \left[i_{fd}^{*} - i_{fd}(k+1)\right]^2 \tag{4.55}$$

Therefore, the cost function for the state variables regulation is designed as

$$J_{\mathrm{AC}} = J_1 + \mathrm{w}_{v_s} J_2 + \mathrm{w}_{i_f} J_3 = \left[\boldsymbol{x_s}(k+1) - \boldsymbol{x_s^{*}}\right]^{\mathrm{T}} \mathbf{W} \left[\boldsymbol{x_s}(k+1) - \boldsymbol{x_s^{*}}\right] \tag{4.56}$$

where the reference vector $\boldsymbol{x_s^{*}} = [i_{sd}^{*}\ i_{sq}^{*}\ v_{sd}^{*}\ v_{sq}^{*}\ i_{fd}^{*}\ i_{fq}^{*}]^{\mathrm{T}}$. The matrix $\mathbf{W}$ assigns the different weighting factors to penalize each tracking error, which can be expressed as $\mathbf{W} = \mathrm{diag}(1,\ 1,\ w_{vs},\ w_{vs},\ w_{if},\ w_{if})$ since the diagonal property. The dimension of $\mathbf{W}$ is 6 and also it is positive semidefinite. It can be seen in (4.56) that the weighting factor for stator current is set as 1 and thus only two weighting factor w_{if} and w_{vs} need to be tuned in this stage.

The dc-link voltage balance can be achieved by exploiting the redundancy provided by small vectors and zero vectors of NPC inverter [121]. To do this, the penalization item for the deviation between V_{dc1} and V_{dc2} is added into the cost function. The final cost function for the NPC-fed PMSM drive with LC filter is expressed as

$$J_{\mathrm{s}} = \left[\boldsymbol{x_s}(k+1) - \boldsymbol{x_s^{*}}\right]^{\mathrm{T}} \mathbf{W} \left[\boldsymbol{x_s}(k+1) - \boldsymbol{x_s^{*}}\right] + \mathrm{w}_{bal} \left[\Delta V_{dc}(k+1)\right]^2 \tag{4.57}$$

The weighting factor plays a vital role in the connection among physical variables with different units, dimensions, and rates of change. In (4.57), three weighting factors need to be tuned, i.e., w_{vs}, w_{if}, and w_{bal}. Firstly, the value

Table 4.3: Simulated and experimental parameters of the NPC inverter-fed PMSM drive system

Parameters	Value
DC-link voltage	240V
DC-link capacitance: C_{dc1} C_{dc2}	3300μF
Rated power	1.1kW
Rated stator frequency	100Hz
Number of pole pairs	5
Rotor flux	0.15Wb
Stator resistance	0.5Ω
Stator inductance	3.1mH
filter capacitance	60μF
filter inductance	3mH
Resonant frequency	375Hz
Sampling frequency	15kHz

of w_{bal} is designed according to the tradeoff between state variables regulation and dc-link voltage balance. The function J_{AC} has the same value for the redundant switching states. According to their different effect on the dc-link voltage deviation, the function J_{M} can distinguish which one should be applied by setting w_{bal}>0. In this work, the simulated and experimental parameters for the NPC inverter-fed PMSM system are shown in Table 4.3. The simulated performances of dc-link voltage are compared in Fig. 4.19 by setting three values of w_{bal} at 0.2s, i.e., 2×10^{-7}, 2×10^{-4}, and 2×10^{4}. It can be seen that when w_{bal} is set as 2×10^{-7} and 2×10^{-4}, the two dc-link voltages are both balanced well at the steady-state, and the speed and torque of motor are not affected too much during the dynamic process. However, when w_{bal} is increased to 2×10^{4} in Fig. 4.19(c), the dynamic performance of motor is sacrificed for the faster response of dc-link voltage balance although the steady-state is still well regulated. In practical application, since the dc-link voltage balance is always controlled, the value of w_{bal} can be tuned as a smaller value. Therefore, the value 2×10^{-4} is selected for w_{bal} to maintain enough margin for the dc-link voltage balance. It is worth to mention that the proposed FCS-MPC scheme at the steady-state shows high robustness to w_{bal}, which can be set easily within a wide range.

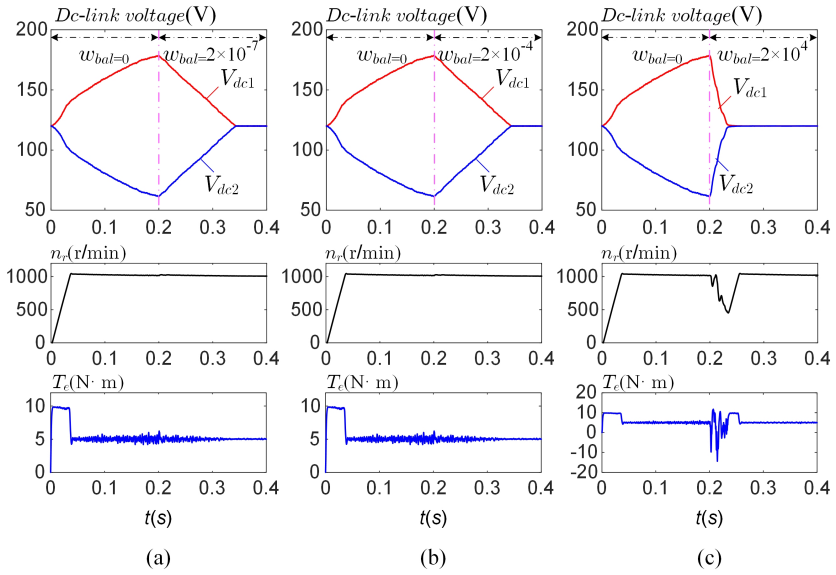

Figure 4.19: The simulated performance of dc-link voltage, motor speed, and torque by using different values of w_{bal} at 0.2s. (a) w_{bal}=2×10^{-7}. (b) w_{bal}=2×10^{-4}. (c) w_{bal}=2×10^{4}.

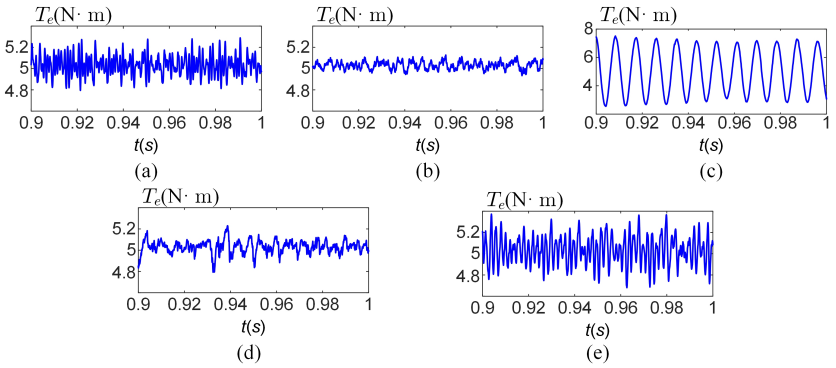

Figure 4.20: The simulated performance of motor torque with different weighting factors used. (a) w_{vs}=0.0003, w_{if}=0.001. (b) w_{vs}=0.003, w_{if}=0.001. (c) w_{vs}=0.03, w_{if}=0.001. (d)w_{vs}=0.003, w_{if}=0.0001. (e) w_{vs}=0.003, w_{if}=0.01.

Secondly, the adjustment of weighting factor w_{vs} and w_{if}, which are directly related to the state variables, is more important to the system stability. To speed up the tuning process, we can start from the assumption that the same priority is assigned for all tracking errors of state variables. Since the additional filter, the waveforms of stator current and stator voltage are smooth due to the high-order filtering. Considering the maximum change of inverter output voltage is $2V_{dc}/3$, the ripple of inverter-side current is roughly estimated as $2V_{dc}T_s/(3L_f)$. The ripples of capacitor voltage and stator current are roughly calculated as $2V_{dc}{T_s}^2/(3L_fC_f)$ and $2V_{dc}{T_s}^3/(3L_fC_fL_s)$ respectively. Since the

cost function penalizes the tracking error quadratically, the square of the ratio of stator current ripple to inverter-side current ripple is set as the turning point for w_{if}, i.e., $T_s^4/(C_f L_s)^2$. Similarly, the square of the ratio of stator current ripple to capacitor voltage ripple is set as the turning point for w_{vs}, i.e., $T_s^2/{L_s}^2$. Therefore, the weighting factor can be further adjusted in order to achieve the desired resonance damping performance. Generally, the resonance damping ability of system can be enhanced with larger w_{if} and w_{vs} adopted. Besides, it is worth to mention that both w_{if} and w_{vs} drive the state trajectory in the same trend, which can simplify the tuning process. According to the parameters in Table 4.3, w_{if} and w_{vs} can be tuned from 0.00057 and 0.00046 respectively. The final value of w_{if} and w_{vs} are set as 0.001 and 0.003 through the simulated comparison of motor torque in Fig. 4.20, where several sets of w_{if} and w_{vs} are adopted. Either the insufficient damping ability or the overdamping situation will cause the oscillations in the motor torque.

4.2.3 Control Scheme Implementation

To dampen the filter resonance, the capacitor voltage and inverter-side current are both controlled, which means the information of $v_{sdq}(k)$ and $i_{fdq}(k)$ need to be known. To reduce the number of sensors, the Kalman filter-based state estimation is adopted. Considering the one-step delay in the digital controller, the discrete-time observer is expressed as

$$\begin{cases} \hat{\boldsymbol{x}}_s(k+1) = \mathbf{A_{sd}}\hat{\boldsymbol{x}}_s(k) + \mathbf{B_{sd}}\boldsymbol{u_s}(k-1) + \mathbf{E_{sd}} + \mathbf{K_{ob}}\left[\boldsymbol{y}(k) - \hat{\boldsymbol{y}}(k)\right] \\ \boldsymbol{y}(k) = \mathbf{C}\boldsymbol{x_s}(k) \\ \hat{\boldsymbol{y}}(k) = \mathbf{C}\hat{\boldsymbol{x}}_s(k) \end{cases} \tag{4.58}$$

where the matrix $\mathbf{C}$ is given by

$$\mathbf{C} = \begin{bmatrix} 1 & 0 & 0 & 0 & 0 & 0 \\ 0 & 1 & 0 & 0 & 0 & 0 \end{bmatrix}$$

and $\hat{\boldsymbol{x}}_s = [\hat{i}_{sd}\ \hat{i}_{sq}\ \hat{v}_{sd}\ \hat{v}_{sq}\ \hat{i}_{fd}\ \hat{i}_{fq}]^{\mathrm{T}}$ is the estimated state vector. Due to the digital delay, the optimized voltage vector $\boldsymbol{u_s}(k-1)$ determined from the last control interval will be applied at the k instant. To compensate for the delay, the one-step forward state variable is estimated in a predictive manner by using

(4.58), which can be used directly as the start point for the prediction of state variable. It should be noted that the prediction process uses all the estimated value from the observer. The feedback gain $\mathbf{K}_{ob}$ is a 6×2-dimension matrix. Considering the modeling matrix in (4.41) is time-varying, the gain $\mathbf{K}_{ob}$ is calculated recursively as [122]

$$\begin{cases} \mathbf{K_{ob}}(k) = \mathbf{P_p}(k)\mathbf{C}^{\mathrm{T}}\left[\mathbf{C}\mathbf{P_p}(k)\mathbf{C}^{\mathrm{T}} + \mathbf{R}\right]^{-1} \\ \mathbf{P_p}(k+1) = \mathbf{A_{sd}}\left[\mathbf{I} - \mathbf{K_{ob}}(k)\mathbf{C}\right]\mathbf{P_p}(k){\mathbf{A_{sd}}}^{\mathrm{T}} + \mathbf{Q} \end{cases} \tag{4.59}$$

where $\mathbf{I}$ is the 6^{th} order identity matrix and $\mathbf{P_p}$ represents the auto-covariance matrix for the predictive state variables. The auto-covariance matrices for the modeling mismatch and measurement noise are $\mathbf{Q}$ and $\mathbf{R}$ respectively, which can be set as diagonal matrices and need to be tuned properly. The larger $\mathbf{Q}$ implies that the larger variations between the predictive state and real state, which causes stronger update of the estimated vector. The auto-covariance matrices of noise in the experimental test are set as $\mathbf{Q}$=diag(0.0001, 0.0001, 0.0003, 0.0003, 0.001, 0.001) and $\mathbf{R}$=diag(0.0001, 0.0001). The Kalman-filter based state estimation makes compensation for the state variables. Therefore, the designed cost function evaluates the trajectory of state variables at the $(k+2)th$ instant, which are calculated according to

$$\boldsymbol{x_s}(k+2) = \hat{\boldsymbol{x}}_s(k+1) + \mathbf{A_{sd}}\Delta\hat{\boldsymbol{x}}_s(k+1) + \mathbf{B_{sd}}\Delta\boldsymbol{u_s}(k) \tag{4.60}$$

In the typical implementation of FCS-MPC scheme, the candidate control inputs are substituted into the predictive model and then the corresponding effect will be evaluated via the cost function. This kind of way put the repeated state prediction into the circulation, which causes numerous computing operations in the digital controller. To further reduce the computational burden, the unconstrained solution of cost function J_{AC} in (4.56) is found firstly. By making the gradient of J_{AC} equals to zero, i.e.,

$$\nabla J_{\mathrm{AC}}\left[\boldsymbol{x_s}(k+2),\ \Delta\boldsymbol{u_s}(k)\right] = 0 \tag{4.61}$$

where ∇ represents the derivative of J_{AC} with respect to $\Delta\boldsymbol{u_s}(k)$. Substituting

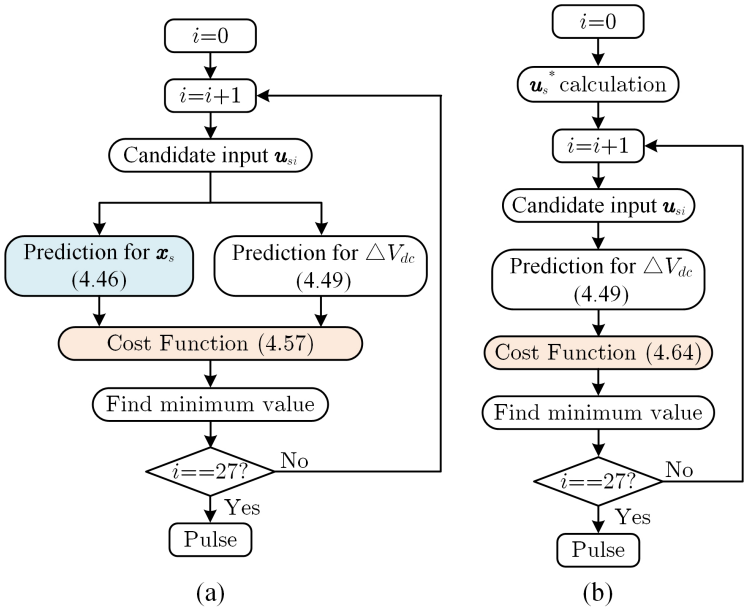

Figure 4.21: The flow chart of the FCS-MPC realization (a) Using the cost function (4.57). (b) Using simplified cost function (4.64).

(4.60) into (4.61), the unconstrained solution $\Delta \boldsymbol{u}_{\boldsymbol{s}}^*(k)$ can be expressed as

$$\Delta \boldsymbol{u}_{\boldsymbol{s}}^*(k)=(\mathbf{B_{sd}}^{\mathrm{T}}\mathbf{W}\mathbf{B_{sd}})^{-1}\mathbf{B_{sd}}^{\mathrm{T}}\mathbf{W}\left[(\boldsymbol{x}_{\boldsymbol{s}}^*-\hat{\boldsymbol{x}}_s(k+1))-\mathbf{A_{sd}}\Delta\hat{\boldsymbol{x}}_s(k+1)\right] \tag{4.62}$$

Thus, the optimized voltage reference can be obtained as

$$\boldsymbol{u}_{\boldsymbol{s}}^*(k)=\boldsymbol{u}_{\boldsymbol{s}}(k-1)+\Delta \boldsymbol{u}_{\boldsymbol{s}}^*(k) \tag{4.63}$$

Finally, the cost function (4.57) can be simplified as

$$J_{\mathrm{Ss}}=\left[\boldsymbol{u}_{\boldsymbol{s}}(k)-\boldsymbol{u}_{\boldsymbol{s}}^*(k)\right]^{\mathrm{T}}\left[\boldsymbol{u}_{\boldsymbol{s}}(k)-\boldsymbol{u}_{\boldsymbol{s}}^*(k)\right]+\mathrm{w}_{bal}[\Delta V_{dc}(k+1)]^2 \tag{4.64}$$

Fig. 4.21 shows the comparison between FCS-MPC using the cost function (4.57) and the simplified form (4.64) respectively. It can be seen that by directly comparing each input with $\boldsymbol{u}_{\boldsymbol{s}}^*(k)$ in Fig. 4.21(b), the repeated prediction process in Fig. 4.21(a) for state variable $\boldsymbol{x}_{\boldsymbol{s}}(k+2)$ in the circulation can be eliminated. Therefore, the computational burden is reduced.

The proposed FCS-MPC scheme for NPC-fed PMSM drives is presented in Fig. 4.22, where only the stator current, electrical rotor angle θ_e, and two

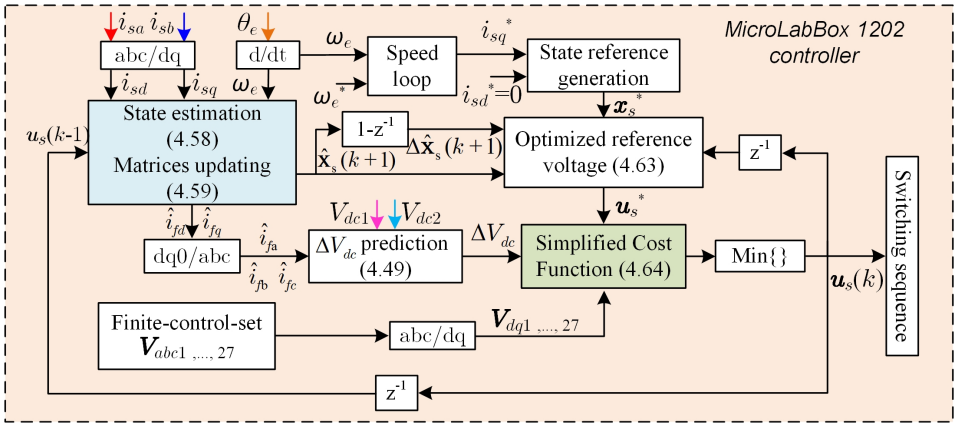

Figure 4.22: The proposed FCS-MPC controller for NPC-fed PMSM drives with LC filter.

dc-link voltages need to be measured. The speed command tracking can be satisfied while the filter resonance is suppressed by cost function (4.64).

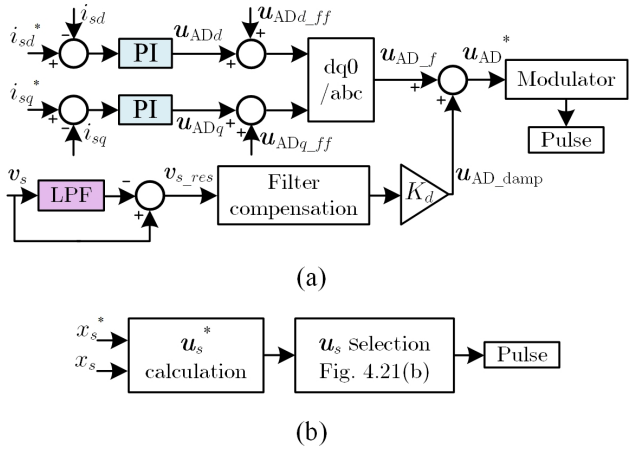

Figure 4.23: The inner loop comparison of (a) AD scheme with linear modulator. (b) The proposed FCS-MPC.

To clearly show the advantage of the proposed scheme, the comparison between the inner loop of proposed FCS-MPC and conventional AD scheme [123] are shown in Fig. 4.23. The conventional AD scheme generates the fundamental control component $\boldsymbol{u}_{\mathrm{AD\_}f}$ by PI regulators in a cascaded way ($\boldsymbol{u}_{\mathrm{AD}dq\_ff}$ are the dq-axes feedforward component), and the resonant component of the measured capacitor voltage $\boldsymbol{v}_{s\_res}$ is extracted through a low-pass filter (LPF). The harmonic voltage with the filter compensation is further multiplied by the damping coefficient K_d to obtain the damping variable $\boldsymbol{u}_{\mathrm{AD\_}damp}$. The final reference $\boldsymbol{u}^*_{\mathrm{AD}}$ sent into the modulator is the superposition of $\boldsymbol{u}_{\mathrm{AD\_}f}$ and $\boldsymbol{u}_{\mathrm{AD\_}damp}$.

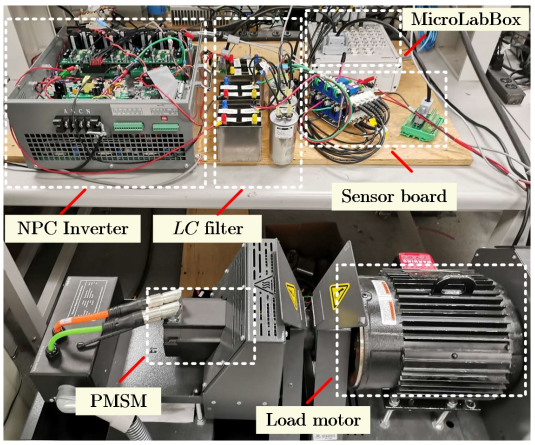

Figure 4.24: Experimental setup of the three-level NPC inverter-fed PMSM drive with LC filter.

In this AD scheme, the parameters of the PI regulator (the anti-windup mechanism is required), the cutoff frequency of LPF, and K_d are all needed to be tuned properly. Moreover, the AD scheme cannot accurately extract the resonant voltage component when the switching frequency is low. While the inner loop of the proposed FCS-MPC only includes the optimization process of voltage vectors without any other control paths or harmonic extraction block. It is worth to mention that the conventional AD scheme only introduces the capacitor voltage as the additional feedback while the inverter-side current is not controlled. On the contrary, all state variables are controlled effectively through the proposed cost function (4.64). Therefore, the proposed controller expresses more flexibility, high bandwidth as well as low tuning complexity (only two parameters w_{vs} and w_{if} needs to be determined).

4.2.4 Simulation and Experimental Results

Fig. 4.24 shows the adopted hardware prototype for the three-level NPC inverter-fed PMSM drive system with LC filter. The FCS-MPC scheme is realized using the MicroLabBox 1202 controller with the parameter shown in Table 4.3. The inverter setup configurated by IGBTs power modules (Infineon F3L75R07W2E3) is used to drive the PMSM.

Fig. 4.25(a) shows the Kalman-filter based state estimation at the steady-state operation of PMSM (rotor speed 1000r/min, load torque 5N·m). The

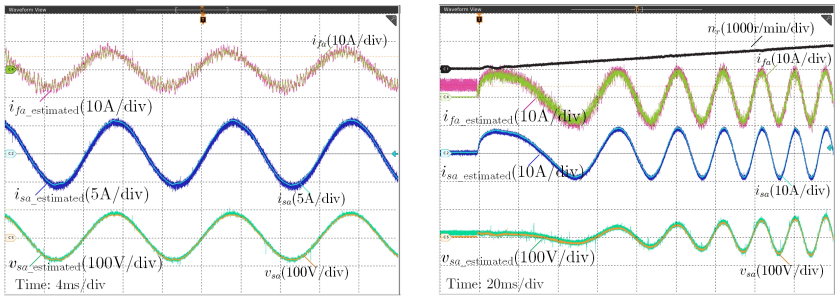

Figure 4.25: Experimental results for Kalman-filter-based state estimation (a) Steady-state operation of PMSM (rotor speed 1000r/min, load torque 5N·m.), (b) Start-up process of PMSM (the rotor speed starts from still to 1000r/min).

dynamic process is shown in Fig. 4.25(b) with speed changes from zero to 1000r/min. The estimated state variables are generated on the oscilloscope using the 16-bit Digital/Analog output channels while the real values are directly measured by probes. It can be seen that both in the steady-state and dynamic process, the estimated value of i_{fa}, v_{sa}, and i_{sa} are all consistent well with the real state information.

To verify the design process for the cost function (4.64). Fig. 4.26 shows the experimental results with different control situations for state variables when the motor operates at 1000r/min (rotor speed) with 5N·m load torque. Firstly, the system performance is shown in Fig. 4.26(a) with inverter-side current, capacitor voltage, and stator current all controlled effectively. The weighting factors assigned for capacitor voltage and inverter-side current are w_{vs}=0.003 and w_{if}=0.001, respectively. The average switching frequency is about 3.3kHz. It can be seen that both stator current and capacitor voltage maintain sinusoidal waveform with low THD value. Although the ripples of inverter-side current exist, no resonance phenomenon occurs. Fig. 4.26(b) shows the state performance with a decreased weighting factor for inverter-side current control, i.e., w_{if}=0.0002. It can be seen that larger ripples appear in the inverter-side current due to insufficient control. Consequently, the THD of capacitor voltage and stator current increase a bit, but no obvious resonance occurs since the capacitor voltage is still regulated effectively. Therefore, the inverter-side current control can improve the damping performance of system. The weight-

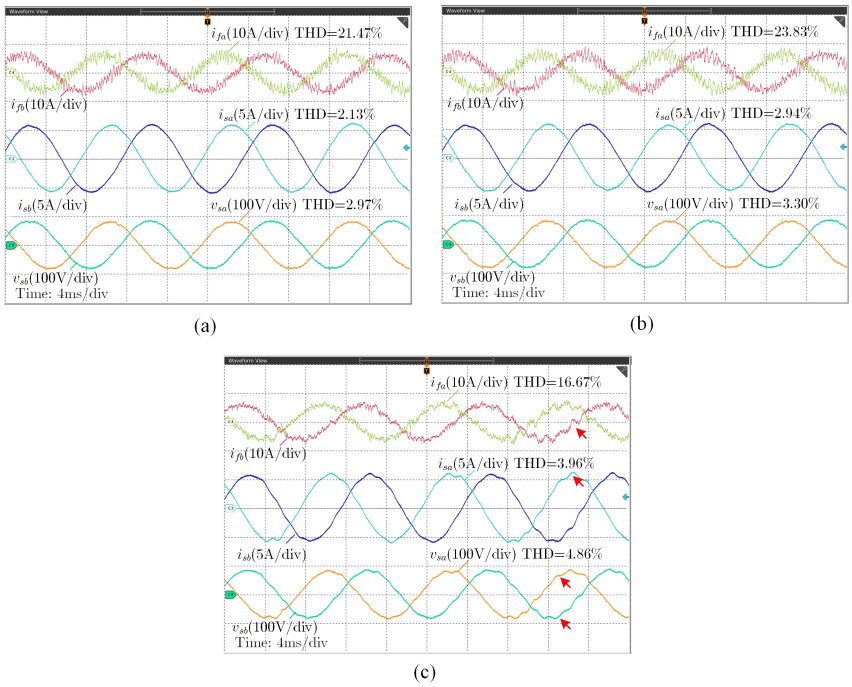

Figure 4.26: Experimental results for filter resonance suppression verification using different weighting factors (a) w_{vs}=0.003 and w_{if}=0.001, (b) w_{vs}=0.003 and w_{if}=0.0002. (c) w_{vs}=0.0003 and w_{if}=0.001.

ing factors w_{vs} is decreased gradually since the instability problem will easily be caused. The performance of state variables is shown in Fig. 4.26(c) when w_{vs}=0.0003. It can be seen that the obvious resonance phenomenon appears, and the THD of capacitor voltage and stator current increases considerably, which implies the insufficient control of capacitor voltage will cause a more significant effect on the system than that of inverter-side current. It is worth to mention that the THD of inverter-side current becomes lower (16.67%) in Fig. 4.26(c). This is the result of more priority are assigned for the inverter-side current reference tracking with the smaller weighting factor assigned for capacitor voltage.

The dynamic performance of the FCS-MPC scheme is shown in Fig. 4.27, including the start-up process when the PMSM speeds up to 1000r/min from the still state and the dynamic process with a sudden change of load torque. It can be seen that the dynamic performance during the start-up process is satisfactory without resonant oscillations in Fig. 4.27(a). Moreover, with the external load torque suddenly changed between 0N·m and 5N·m in Fig.

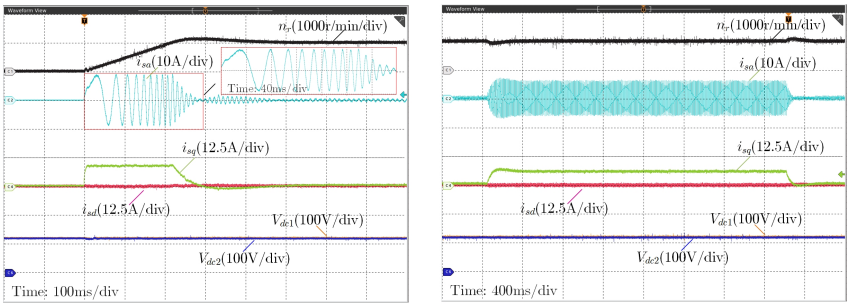

Figure 4.27: Experimental results for dynamic performance test (a) The start-up process of PMSM that speeds up to 1000r/min, (b) The dynamic process with a sudden change of the load torque.

4.27(b), the dq-axes current shows a smooth response without any unstable resonance. Besides, the dc-link voltage V_{dc1} and V_{dc2} are always maintained as the same without any unbalance.

The results for the robustness test are shown in Fig. 4.28, where the $\pm 40\%$ parameters variation of the filter inductance and capacitance are considered. The parameters mismatch includes the values used in the controller, which are lower and higher than the real value. From the compared results with Fig. 12(a), the system performance is stable without obvious differences, and no resonance phenomenon occurs as well. The FCS-MPC scheme for the NPC inverter-fed PMSM drive with LC filter shows high robustness to the parameter variation of filter.

4.3 Summary

The MPC scheme with hybrid current and voltage control is proposed in this chapter to address the resonance problems in the LCL-filtered grid-connected application and the motor drive equipped with the output LC filter. For the grid-connected case, the resonance oscillation caused by the LCL filter is well dampened with the proposed cost function, and the digital delay is also effectively compensated with improved system performance. The harmonic caused by the unhealthy grid conditions are effectively rejected by the modified reference of state variables. The proposed MPC exhibits the merit

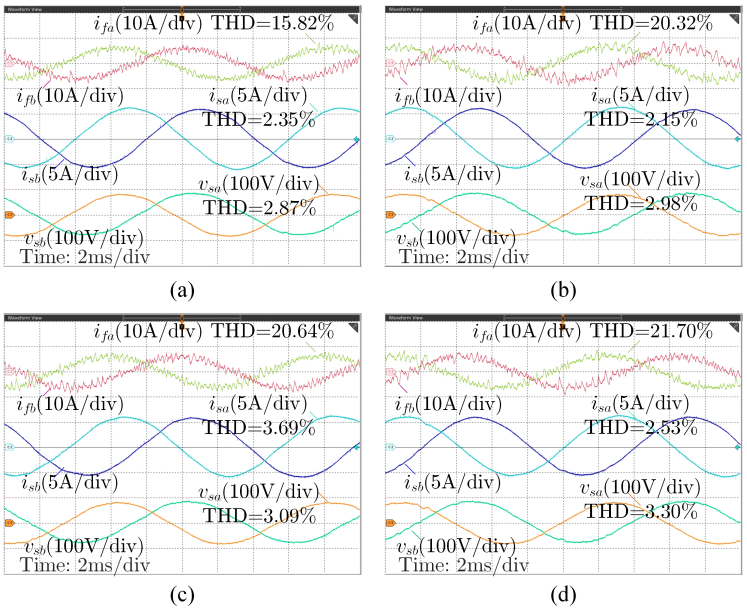

Figure 4.28: Robustness test of the FCS-MPC. (a) The inductance used is 60% of the real value, (b) The inductance used is 140% of the real value. (c) The capacitance used is 60% of the real value. (b) The capacitance used is 140% of the real value.

including intuitive concept, low computational burden, faster dynamic and flexible adaptability, which has been verified by the simulation and experimental tests. The proposed scheme can be extended to other multivariable plants with the coupling dynamic involved, such that the control structure and parameter design can be simplified with an optimized process.

On the other hand, different from the linear AD schemes applied to suppress the resonance in the motor drive system with an LC filter, this chapter analyzes the resonance mechanism and suppression strategy in the time domain, which shows a more clear and intuitive design process for the cost function. The detailed description and realization steps of the proposed FCS-MPC scheme have been presented. Compared to the linear AD scheme, the proposed design shows reduced complexity and a simplified tuning process. The multivariable control is designed into the cost function without any other cascaded/feedforward paths or harmonic extraction blocks. High bandwidth can be obtained by using the single inner loop controller. The hardware cost is saved since the Kalman filter-based state estimation is used, which also compensates for the one-step delay in the digital controller. The search process for

the voltage vector is optimized with the unconstrained solution obtained first, which reduces the computational burden significantly. The proposed scheme can be extended to motor drive applications designed with high-order filters, like the SiC or GaN-based inverter-fed, where the high dv/dt is the main challenge in the long-cable transmission.

Chapter 5

Multi-rate Model Predictive Control for High Switching Frequency Power Converters

For both the FCS-MPC and CCS-MPC, the high S/I frequency demand is a great challenge because such a short period imposes big computational difficulty in the programming code execution. Particularly, due to the modulator-free structure, the FCS-MPC needs a high S/I frequency (20kHz-50kHz) for power converters application, while the typical converter switching frequency is around 20-25% of the sampling frequency. To extend it to the high switching frequency converter application, it is not always practical to increase the sampling rate by considering the computational burden in DSPs. Therefore, increasing the switching frequency without using a high sampling frequency is a critical task for FCS-MPC, particularly applied to SiC and GaN-based high switching frequency power converters. To solve this problem, this chapter proposes the multi-rate FCS-MPC (MRFCS-MPC), where the control frequency is allowed to be higher than the sampling frequency. Consequently, the switching frequency can be significantly increased without changing the sampling frequency. The proposed scheme inherits the ability to handle complex control objectives from the traditional FCS-MPC. The lifting model is built to predict the fast rate information of state variables based on the low sampling output. Then, the fast rate control inputs within one sampling interval are solved efficiently with a good tradeoff between computational burden and

optimized system performance.

This chapter also proposes a multi-rate CCS-MPC (MRCCS-MPC) scheme, where the S/I trigger and switching device transition can be performed at different rates. Compared to the existing typical CCS-MPC schemes, the main feature of the proposed MRCCS-MPC is that the high-dimension control sequence is solved and applied within each S/I interval. As a result, the high switching frequency objective can be easily achieved with a low S/I frequency configuration, which can significantly relieve the execution of the heavy interrupt tasks in DSPs. The applied control sequence through the MRCCS-MPC is solved according to the minimization of the cost function, which results in a more optimal solution than the MRFCS-MPC.

5.1 Dual Time-rate Prediction and Lifting Operation

In most cases, the dynamic of the power converter system can be described by the linear time-invariant equation

$$\frac{d\boldsymbol{x}}{dt} = \mathbf{A}\boldsymbol{x} + \mathbf{B}\boldsymbol{u} + \mathbf{E} \tag{5.1}$$

where, in general, the state vector $\boldsymbol{x} \in \mathcal{R}^n$, input vector $\boldsymbol{u} \in \mathcal{R}^p$, output vector $\boldsymbol{y} \in \mathcal{R}^q$ and the system matrix $\mathbf{A}$, input matrix $\mathbf{B}$, disturbance matrix $\mathbf{E}$, and output matrix $\mathbf{C}$ are of compatible dimensions, i.e., $\mathbf{A} \in \mathcal{R}^{n\times n}$, $\mathbf{B} \in \mathcal{R}^{n\times p}$, $\mathbf{E} \in \mathcal{R}^n$ and $\mathbf{C} \in \mathcal{R}^{q\times n}$. For the real-time realization, the MPC predicts the system behavior based on the state-space model in the discrete domain, and the predictive equation can be expressed as

$$\begin{aligned} \boldsymbol{x}(k+1) &= \mathbf{A_s}\boldsymbol{x}(k) + \mathbf{B_s}\boldsymbol{u}(k) + \mathbf{E_s} \\ \boldsymbol{y}(k) &= \mathbf{C}\boldsymbol{x}(k) \end{aligned} \tag{5.2}$$

where k represents the current sampling step. Considering the general sampling interval T_s, the discrete matrices $\mathbf{A}_s$, $\mathbf{B}_s$, and $\mathbf{E}_s$ are calculated as

$$\mathbf{A_s} = e^{\mathbf{A}T_s},\ \mathbf{B_s} = \int_0^{T_s} e^{\mathbf{A}\tau}\mathbf{B}d\tau,\ \mathbf{E_s} = \int_0^{T_s} e^{\mathbf{A}\tau}\mathbf{E}d\tau \tag{5.3}$$

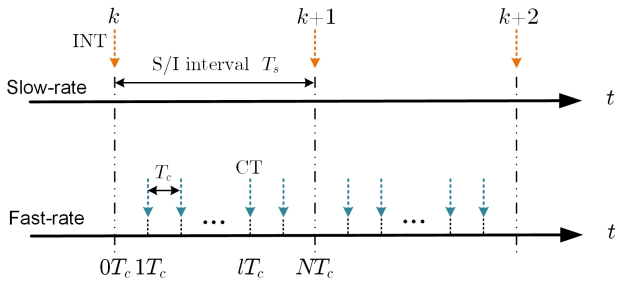

Figure 5.1: The timeline of the multi-rate system.

The state vector $\boldsymbol{x}$ includes the typical state variable, such as inductor current, capacitor voltage, motor torque, speed, flux, etc. The output vector $\boldsymbol{y}$ contains the measurable components. The sampling frequency f_s equals $1/T_s$. The state-space equation (5.2), which is discretized with the time scale T_s, predicts the state variable information in the next S/I interval. To lay the foundation for the MR-MPC, the S/I interval is equally divided into N intervals, and each small interval is defined as the control interval, whose length is defined as T_c. Fig. 5.1 shows the relationship between these two time intervals and the timeline of the interrupt trigger (INT) and the control trigger (CT). Correspondingly, the sampling frequency f_s equals $1/T_s$, and the control frequency f_c equals $1/T_c$. Thus $T_s{=}NT_c$ or $f_c{=}Nf_s$. With the defined control interval T_c, the dynamic model (5.1) can be discretized as

$$\begin{aligned} \boldsymbol{x}_c(l\,|k) &= \mathbf{A}_c\boldsymbol{x}_c(l-1\,|k) + \mathbf{B}_c\boldsymbol{u}_c(l-1\,|k) + \mathbf{E}_c \\ \boldsymbol{y}_c(l\,|k) &= \mathbf{C}\boldsymbol{x}_c(l\,|k) \end{aligned} \tag{5.4}$$

for $l{=}1,\ 2,\ \ldots,\ N$, where l represents the current control step and $l\,|k$ represents the lth control instant during the kth sampling interval. As a comparison, the discrete modeling in (5.2) represents the slow-rate prediction while (5.4) represents the fast-rate prediction due to the short interval. The discrete matrices are expressed as

$$\mathbf{A}_c = e^{\mathbf{A}T_c},\ \mathbf{B}_c = \int_0^{T_c} e^{\mathbf{A}\tau}\mathbf{B}d\tau,\ \mathbf{E}_c = \int_0^{T_c} e^{\mathbf{A}\tau}\mathbf{E}d\tau \tag{5.5}$$

To facilitate the modeling of the system with different time scales involved, the lifting technique is adopted to aggregate the fast rate data stream into a

super vector [124]. Assuming a general signal $\boldsymbol{z}$, i.e.,

$$\boldsymbol{z}(k) = [z(0)\ z(1) \dots z(N-1) | z(N)\ z(N+1) \dots z(2N-1)]^{\mathrm{T}} \tag{5.6}$$

The representation of the lifting vector with entended dimension can be written as

$$\underline{\boldsymbol{z}} = \left\{ \begin{bmatrix} z(0) \\ z(1) \\ \vdots \\ z(N-1) \end{bmatrix}, \begin{bmatrix} z(N) \\ z(N+1) \\ \vdots \\ z(2N-1) \end{bmatrix}, \dots \right\}^{\mathrm{T}} \tag{5.7}$$

5.2 Review of Conventional SRFCS-MPC

The typical FCS-MPC will be called the single-rate FCS-MPC(SRFCS-MPC) in the following contents. The general framework and digital realization of the SRFCS-MPC are reviewed first. In SRFCS-MPC, the control frequency is defined the same as the S/I frequency, and the length of the predictive horizon is set as one sampling interval. With the predictive state variable obtained, the optimization process can be performed to decide the optimized control input $\boldsymbol{u}_{\mathrm{op}}$. The typical cost function penalizes the tracking error between the predictive output $\boldsymbol{y}$ and the corresponding reference $\boldsymbol{y}^*$ quadratically, which can be written as

$$\mathrm{g} = [\boldsymbol{y}(k+1) - \boldsymbol{y}^*(k+1)]^{\mathrm{T}} \mathbf{W} [\boldsymbol{y}(k+1) - \boldsymbol{y}^*(k+1)] \tag{5.8}$$

The weighting factors are included in the matrix $\mathbf{W}$ with diagonal and positive definite properties. The SRFCS-MPC exploits the discrete feature of the power converter to evaluate the effect of each candidate input. Since the power converter provides the finite switching states, the manipulated control input in total number N_u can be aggregated in the control set

$$\mathbf{U}(k) = \{\boldsymbol{u}_1(k)\ \ \boldsymbol{u}_2(k)\ \dots\ \boldsymbol{u}_{N_u}(k)\}\,. \tag{5.9}$$

Fig. 5.2 shows the principle of the SRFCS-MPC, including the operation process and the flowchart of the algorithm. As can be seen in Fig. 5.2(a), in the kth sampling interval, the predictive stage is executed by substituting each

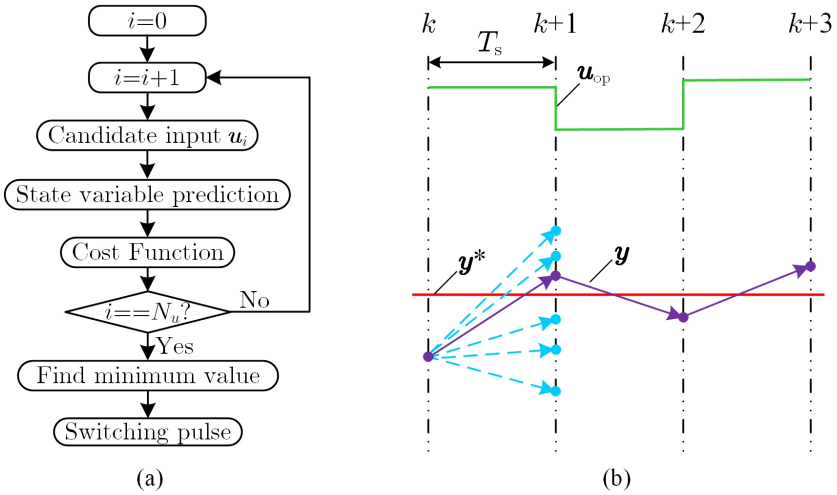

Figure 5.2: The principle of SRFCS-MPC (typical FCS-MPC). (a) The flowchart of the algorithm. (b) The operation process.

candidate input into (5.8) in turn. Therefore, a collection of the cost function value can be obtained, which represents the system response under the effect of each input. Finally, the control input with the minimum cost function value is selected and send into the driving block to generate the switching pulse. In this way, the minimum tracking error between the output $\boldsymbol{y}$ and reference $\boldsymbol{y}^*$ can be achieved at each sampling instant, as seen in Fig. 5.2(b). This process will be repeated in the coming control intervals to realize the rolling optimization in real-time.

The SRFCS-MPC is a kind of direct control strategy without using the modulator. Since the rolling optimization is executed in each sampling interval to select the control input, the control frequency is the same as the sampling frequency. Therefore, only the time scale T_s is adopted in the power converter system, which belongs to the single rate control category.

The detailed realization in the digital controller is shown in Fig. 5.3, where the single-rate control signal is obtained by using the SRFCS-MPC algorithm. The switching pulse is generated by comparing the count value in the register with the triangle carrier. If the register value is larger than the triangle carrier, a high switching level is generated otherwise a low switching level will be generated. It also can be found that the carrier frequency is the same as the sampling frequency. It is worth mentioning that delay compensation is

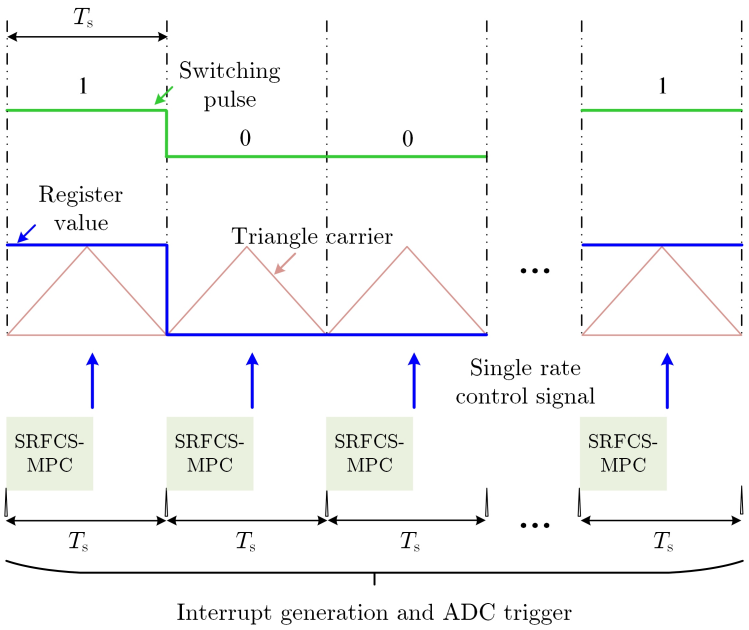

Figure 5.3: The digital realization of SRFCS-MPC.

necessary for the digital realization of FCS-MPC. The commonly adopted way is to estimate the system information by one step forward, i.e., $x(k+1)$, which will be taken as the starting point for the predictive stage. Then the cost function will evaluate the system performance at the $(k+2)th$ instant.

5.3 Proposed Multi-rate FCS-MPC Design

This section extends the typical FCS-MPC framework to the MRFCS-MPC form, where the update frequency of the control input is increased to be faster than that of the system output. The advantage of the proposed multi-rate technique is that no additional parameters or switching pulse patterns need to be designed, and the switching frequency can be significantly enhanced without increasing the sampling frequency. The MRFCS-MPC elements are designed, including the lifting model and lifting control input solving process. The two-level VSI-fed motor drive is taken as the case study to verify the proposed MRFCS-MPC.

5.3.1 Lifting Model With a Fast Rate Control Input

Since the control frequency is different from the sampling frequency, dual-rate time scales exist in the system. To perform the modeling, the lifting technique is an effective tool to deal with the control problem in the multi-rate sampled-data system, where the dimension of a vector can be extended to accommodate the fast signal stream [124]. The multi-rate control has been used in the low switching frequency converters to improve the PWM control accuracy of harmonics [125], and a similar concept is also applicable to WBG device-based high switching converters. In MRFCS-MPC, the control frequency is designed as the integer multiple of the sampling frequency. In this case, the lifting model is built to connect the fast-rate control input and the slow-rate sampling output.

The system output is sampled every T_s duration and the information at the kT_s instant is already available. As can be seen in Fig. 5.1, the state variable at the $0T_c$ control instant is assumed as the starting point at each sampling interval and thus

$$\boldsymbol{x}_c(0\,|k\,) = \boldsymbol{x}_s(k) \tag{5.10}$$

Based on the discrete modeling (5.4), the system state variable at each control instant within the sampling interval from kT_s to $(k+1)T_s$ can be calculated as follows respectively.

$$\begin{aligned} \boldsymbol{x}_c(1\,|k\,) &= \mathbf{A}_c\boldsymbol{x}_c(0\,|k\,) + \mathbf{B}_c\boldsymbol{u}_c(0\,|k\,) + \mathbf{E}_c \\ &= \mathbf{A}_c\boldsymbol{x}_s(k) + \mathbf{B}_c\boldsymbol{u}_c(0\,|k\,) + \mathbf{E}_c \end{aligned} \tag{5.11}$$

$$\begin{aligned} \boldsymbol{x}_c(2\,|k\,) &= \mathbf{A}_c\boldsymbol{x}_c(1\,|k\,) + \mathbf{B}_c\boldsymbol{u}_c(1\,|k\,) + \mathbf{E}_c \\ &= {\mathbf{A}_c}^2\boldsymbol{x}_s(k) + \mathbf{A}_c\mathbf{B}_c\boldsymbol{u}_c(0\,|k\,) + \mathbf{B}_c\boldsymbol{u}_c(1\,|k\,) \\ &\quad +\mathbf{A}_c\mathbf{E}_c + \mathbf{E}_c \end{aligned} \tag{5.12}$$

$$\begin{aligned} &\boldsymbol{x}_c(N\,|k\,) = \mathbf{A}_c\boldsymbol{x}_c(N-1\,|k\,) + \mathbf{B}_c\boldsymbol{u}_c(N-1\,|k\,) + \mathbf{E}_c \\ &= {\mathbf{A}_c}^N\boldsymbol{x}_s(k) + {\mathbf{A}_c}^{N-1}\mathbf{B}_c\boldsymbol{u}_c(0\,|k\,) \\ &\quad +{\mathbf{A}_c}^{N-2}\mathbf{B}_c\boldsymbol{u}_c(1\,|k\,) + ... + \mathbf{B}_c\boldsymbol{u}_c(N-1\,|k\,) \\ &\quad +{\mathbf{A}_c}^{N-1}\mathbf{E}_c + ... + \mathbf{E}_c \end{aligned} \tag{5.13}$$

To aggregate the fast rate information, the output vector and the input vector are lifted as N-dimensional form, i.e.,

$$\underline{\boldsymbol{y}}(k)=\begin{bmatrix}\boldsymbol{y_c}(1\,|k)\\ \boldsymbol{y_c}(2\,|k)\\ \vdots\\ \boldsymbol{y_c}(N\,|k)\end{bmatrix},\underline{\boldsymbol{u}}(k)=\begin{bmatrix}\boldsymbol{u_c}(0\,|k)\\ \boldsymbol{u_c}(1\,|k)\\ \vdots\\ \boldsymbol{u_c}(N-1\,|k)\end{bmatrix} \tag{5.14}$$

Therefore, the lifting model of the dual-rate system can be built as

$$\begin{aligned}\boldsymbol{x}_s(k+1)&=\underline{\mathbf{A}}\boldsymbol{x}_s(k)+\underline{\mathbf{B}\boldsymbol{u}}(k)+\mathbf{E}_s\\ \underline{\boldsymbol{y}}(k)&=\underline{\mathbf{C}}\boldsymbol{x}_s(k)+\underline{\mathbf{D}\boldsymbol{u}}(k)+\underline{\mathbf{E}}\end{aligned} \tag{5.15}$$

where the lifting matrices $\underline{\mathbf{A}}=\mathbf{A}_s$, $\underline{\mathbf{B}}=\begin{bmatrix}\mathbf{A}_c{}^{N-1}\mathbf{B}_c & \mathbf{A}_c{}^{N-2}\mathbf{B}_c & \ldots & \mathbf{A}_c\mathbf{B}_c & \mathbf{B}_c\end{bmatrix}$, and $\underline{\mathbf{C}}=\begin{bmatrix}\mathbf{C}\mathbf{A}_c & \mathbf{C}\mathbf{A}_c{}^2 & \ldots & \mathbf{C}\mathbf{A}_c{}^{N-1} & \mathbf{C}\mathbf{A}_c{}^{N}\end{bmatrix}^{\mathrm{T}}$,

$$\underline{\mathbf{D}}=\begin{bmatrix}\mathbf{C}\mathbf{B}_c & \mathbf{0} & \ldots & \mathbf{0} & \mathbf{0}\\ \mathbf{C}\mathbf{A}_c\mathbf{B}_c & \mathbf{C}\mathbf{B}_c & \ldots & \mathbf{0} & \mathbf{0}\\ \mathbf{C}\mathbf{A}_c{}^2\mathbf{B}_c & \mathbf{C}\mathbf{A}_c\mathbf{B}_c & \ldots & \mathbf{0} & \mathbf{0}\\ & & \vdots & & \\ \mathbf{C}\mathbf{A}_c{}^{N-1}\mathbf{B}_c & \mathbf{C}\mathbf{A}_c{}^{N-2}\mathbf{B}_c & \ldots & \mathbf{C}\mathbf{A}_c\mathbf{B}_c & \mathbf{C}\mathbf{B}_c\end{bmatrix},$$

$$\underline{\mathbf{E}}=\begin{bmatrix}\mathbf{C}\mathbf{E}_c\\ \mathbf{C}\mathbf{A}_c\mathbf{E}_c+\mathbf{C}\mathbf{E}_c\\ \mathbf{C}\mathbf{A}_c{}^2\mathbf{E}_c+\mathbf{C}\mathbf{A}_c\mathbf{E}_c+\mathbf{C}\mathbf{E}_c\\ \vdots\\ \mathbf{C}\sum_{h=0}^{N-1}\mathbf{A}_c{}^h\mathbf{E}_c\end{bmatrix}.$$

5.3.2 Suboptimal Solving Process of the Lifting Control Input

Different from the SRFCS-MPC, the optimized lifting control input $\underline{\boldsymbol{u}}_{\mathrm{op}}(k)$ is applied during the interval from kT_s to $(k+1)T_s$ by using MRFCS-MPC. The N input elements contained in $\underline{\boldsymbol{u}}_{\mathrm{op}}(k)$ are applied sequentially, where the duration of each one is T_c. Two kinds of ways can be adopted to solve the optimized solution $\underline{\boldsymbol{u}}_{\mathrm{op}}(k)$. The first one is to solve all N elements simultaneously. For

each control interval T_c, the number of N_u primary vectors in (5.9) can be applied, which implies N_u^N feasible solutions in total can be obtained during the whole sampling interval T_s. Since the exhaustive enumeration searching process is employed in FCS-MPC, this way will exponentially aggravate the computational burden as the dimension of $\underline{\boldsymbol{u}}(k)$ increases. Another alternative method is to solve these N elements one by one, which belongs to the sub-optimal way. In this case, the first element $\boldsymbol{u}_{\text{cop}}(0\,|k)$ is solved by directly evaluating each primary vector during the first control interval, where the cost function is

$$J_{1|k} = [\boldsymbol{y}_c(1\,|k) - \boldsymbol{y}^*(1\,|k)]^{\mathrm{T}}\mathbf{W}\,[\boldsymbol{y}_c(1\,|k) - \boldsymbol{y}^*(1\,|k)] \tag{5.16}$$

and $\boldsymbol{y}_c(1\,|k)$ can be calculated according to (5.15). After this stage, the first solution is obtained, i.e., $\boldsymbol{u}_{\text{cop}}(0\,|k)$, which corresponds to the minimum value of (5.16). Subsequently, the solving stage moves to the next control interval, where the second element $\boldsymbol{u}_c(1\,|k)$ is solved in the same way. In this case, the control input for the previous control interval is substituted with the already solved optimized solution $\boldsymbol{u}_{cop}(0\,|k)$ to calculate the predictive state information. Namely

$$\begin{aligned}\boldsymbol{x}_c(2\,|k) = \mathbf{A}_c{}^2\boldsymbol{x}_s(k) + \mathbf{A}_c\mathbf{B}_c\boldsymbol{u}_{\text{cop}}(0\,|k)\\ +\mathbf{B}_c u_c(1\,|k) + \mathbf{A}_c\mathbf{E}_c + \mathbf{E}_c\end{aligned} \tag{5.17}$$

and the cost function for the second control interval is

$$J_{2|k} = [\boldsymbol{y}_c(2\,|k) - \boldsymbol{y}^*(2\,|k)]^{\mathrm{T}}\mathbf{W}\,[\boldsymbol{y}_c(2\,|k) - \boldsymbol{y}^*(2\,|k)] \tag{5.18}$$

The process is repeated until the Nth unknown input $\boldsymbol{u}_c(N-1\,|k)$ is solved, and the state information is calculated according to

$$\begin{aligned}\boldsymbol{x}_c(N\,|k) = \mathbf{A}_c{}^N\boldsymbol{x}_s(k) + \mathbf{A}_c{}^{N-1}\mathbf{B}_c\boldsymbol{u}_{\text{cop}}(0\,|k)\\ +\mathbf{A}_c{}^{N-2}\mathbf{B}_c\boldsymbol{u}_{\text{cop}}(1\,|k) + ... + \mathbf{B}_c\boldsymbol{u}_c(N-1\,|k)\\ +\mathbf{A}_c{}^{N-1}\mathbf{E}_c + ... + \mathbf{E}_c\end{aligned} \tag{5.19}$$

Also, the cost function for the Nth control interval is

$$J_{N|k} = [\boldsymbol{y}_c(N\,|k) - \boldsymbol{y}^*(N\,|k)]^{\mathrm{T}}\mathbf{W}\,[\boldsymbol{y}_c(N\,|k) - \boldsymbol{y}^*(N\,|k)] \tag{5.20}$$

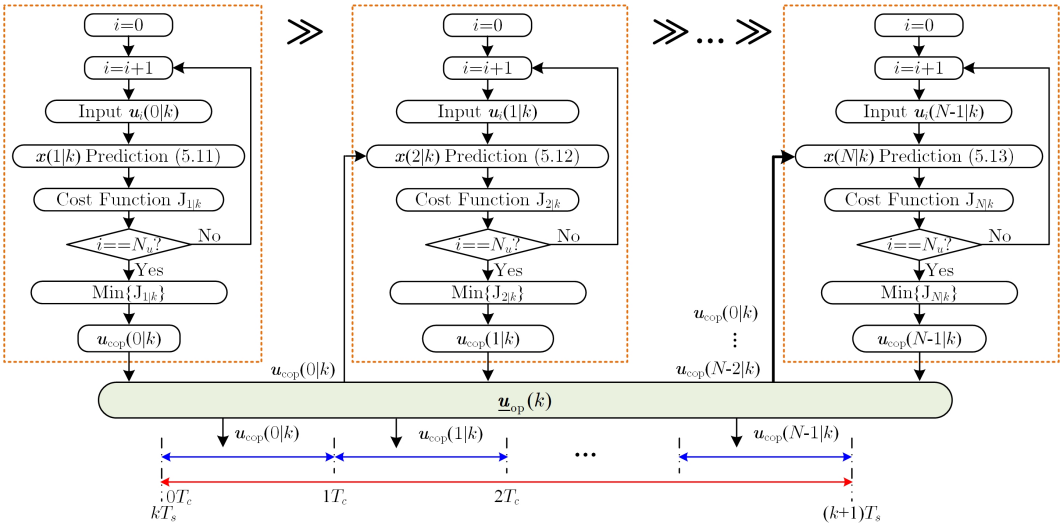

Figure 5.4: The solving flowchart of the lifting control input for MRFCS-MPC.

The above process is presented in Fig. 5.4. where the lifting control inputs within one sampling interval are solved successively. This way maintains a good tradeoff between computational burden and optimized system performance, which can be easily realized through the digital controller.

5.3.3 Digital Realization

Compared to the digital realization of SRFCS-MPC, the carrier frequency in MRFCS-MPC should be increased to be the same as the control frequency f_c since the multiple input signals will be applied during each sampling interval. The sampling frequency and the interrupt generation are kept the same as SRFCS-MPC and the detailed realization is demonstrated in Fig. 5.5. As can be seen, the proposed MRFCS-MPC decides the control inputs with a fast update frequency during each sampling interval T_s. After that, each element in the optimized input vector is successively generated by comparing the corresponding register value with the fast rate triangle carrier. Finally, the switching state during each sampling interval will be updated multiple times, bringing increased switching frequency. Regarding the delay compensation, the lifting control inputs will be applied in the next sampling interval. Therefore, the one-step forward calculation with time scale T_s is realized according

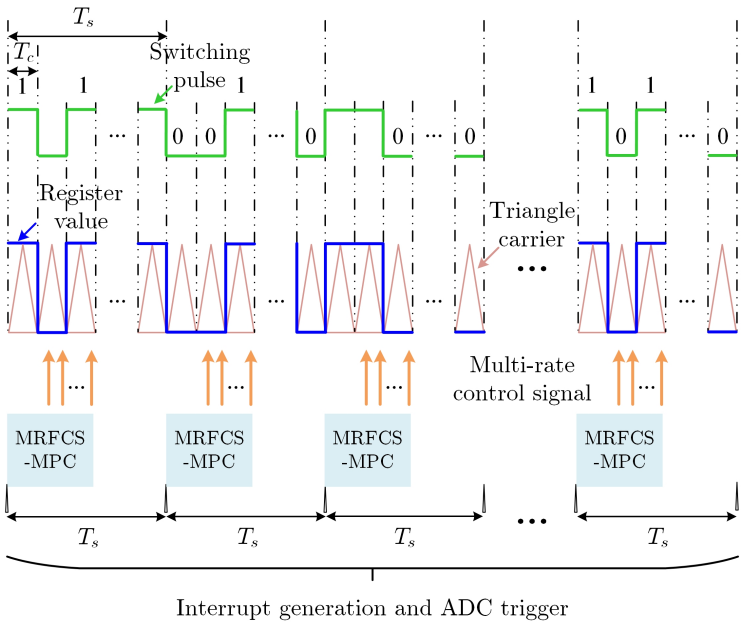

Figure 5.5: The digital realization of proposed MRFCS-MPC.

to the optimized lifting inputs during the last sampling interval, i.e.,

$$\boldsymbol{x}_s(k+1) = \underline{\mathbf{A}}\boldsymbol{x}_s(k) + \underline{\mathbf{B}}\underline{\boldsymbol{u}}_{op}(k) + \mathbf{E}_s \tag{5.21}$$

5.3.4 Experimental Results and Evaluation

The two-level VSI-fed PMSM drive system is taken to verify the proposed MRFCS-MPC scheme. The three-phase variable is transformed to the synchronous dq frame through Park's transformation, Therefore, the dynamic equation (5.1) has $\boldsymbol{x}$=$\boldsymbol{y}$=$[i_{sd}\ i_{sq}]^{\mathrm{T}}$, $\boldsymbol{u}$=$[u_{invd}\ u_{invq}]^{\mathrm{T}}$, and $\mathbf{A} = \begin{bmatrix} -\dfrac{R_s}{L_s} & \omega_e \\ -\omega_e & -\dfrac{R_s}{L_s} \end{bmatrix}$, $\mathbf{B} = \begin{bmatrix} \dfrac{1}{L_s} & 0 \\ 0 & \dfrac{1}{L_s} \end{bmatrix}$, $\mathbf{E} = \begin{bmatrix} 0 \\ -\dfrac{\omega_e \varphi_f}{L_s} \end{bmatrix}$, $\mathbf{C} = \begin{bmatrix} 1 & 0 \\ 0 & 1 \end{bmatrix}$, where i_{sd}, i_{sq} represent the dq-axes stator current respectively and u_{invd}, u_{invq}, represent the dq-axes input voltage generated by VSI. R_s and L_s represent the stator resistance and inductance of the surface-mounted PMSM. ω_e is the synchronous angular velocity. φ_f represents the permanent flux linkage. The kinematic equation of PMSM

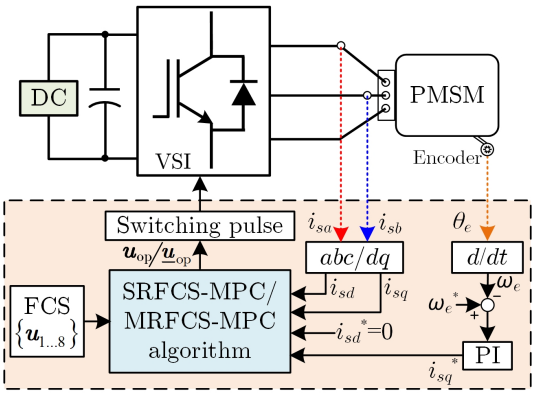

Figure 5.6: Diagram of model predictive current control for PMSM drives.

can be expressed as

$$T_e = 1.5p\varphi_f i_{sq} \tag{5.22}$$

$$J\frac{d\omega_e}{dt} + B\omega_e = T_e - T_l \tag{5.23}$$

where T_e is the electromagnetic torque produced by PMSM and T_l is the load torque. p is the number of pole pairs. J is the machine inertia and B is the viscous friction coefficient. The typical approach, i.e. the FCS-MPC scheme with stator current regulation is adopted for PMSM control [126]–[128], as shown in Fig. 5.6. According to (5.22), the value of T_e can be maximum when all stator current is devoted to the torque generation, i.e. the stator current vector $\boldsymbol{i}_s$=i_{sq}[127]. Therefore, the d-axis current reference i_{sd}^* is set as 0 to achieve the maximum torque current ratio operation. The outer speed loop uses the PI regulator to generate the q-axis current reference i_{sq}^*. The dq-axes current references can be assumed as the same during each sampling interval for both SRFCS-MPC and MRFCS-MPC by considering the slow mechanical dynamic. In this case, the desired torque can be produced by controlling i_{sq} since T_e is directly proportional to the i_{sq} in (5.22). Therefore, to minimize the torque ripple, the tracking error between i_{sq}^* and i_{sq} should be minimized, which is the main objective realized by the inner control loop. Based on this, the cost function of SRFCS-MPC penalizes the dq-axes current tracking error is designed as

$$J = \left[i_{sd}(k+1) - i_{sd}^*(k+1)\right]^2 + \left[i_{sq}(k+1) - i_{sq}^*(k+1)\right] \tag{5.24}$$

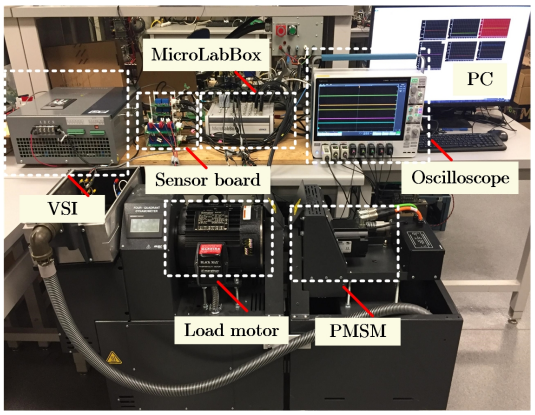

Figure 5.7: Experimental setup of the VSI-fed PMSM drive system.

With the dual time scales T_s and T_c, the stator current prediction equation used in SRFCS-MPC and MRFCS-MPC can be expressed respectively as

$$\begin{bmatrix} i_{sd}(k+1) \\ i_{sq}(k+1) \end{bmatrix} = \mathbf{A}_s \begin{bmatrix} i_{sd}(k) \\ i_{sq}(k) \end{bmatrix} + \mathbf{B}_s \boldsymbol{u}_s(k) + \mathbf{E}_s \tag{5.25}$$

$$\begin{bmatrix} i_{sd}(l+1\,|k) \\ i_{sq}(l+1\,|k) \end{bmatrix} = \mathbf{A}_c \begin{bmatrix} i_{sd}(l\,|k) \\ i_{sq}(l\,|k) \end{bmatrix} + \mathbf{B}_c \boldsymbol{u}_c(l\,|k) + \mathbf{E}_c \tag{5.26}$$

where the discrete matrices are $\mathbf{A}_s = \begin{bmatrix} 1-\frac{R_s T_s}{L_s} & T_s\omega_e \\ -T_s\omega_e & 1-\frac{R_s T_s}{L_s} \end{bmatrix}$, $\mathbf{B}_s = \begin{bmatrix} \frac{T_s}{L_s} & 0 \\ 0 & \frac{T_s}{L_s} \end{bmatrix}$, $\mathbf{E}_s = \begin{bmatrix} 0 \\ -\frac{\omega_e \varphi_f T_s}{L_s} \end{bmatrix}$. $\mathbf{A}_c = \begin{bmatrix} 1-\frac{R_s T_c}{L_s} & T_c\omega_e \\ -T_c\omega_e & 1-\frac{R_s T_c}{L_s} \end{bmatrix}$, $\mathbf{B}_c = \begin{bmatrix} \frac{T_c}{L_s} & 0 \\ 0 & \frac{T_c}{L_s} \end{bmatrix}$, $\mathbf{E}_c = \begin{bmatrix} 0 \\ -\frac{\omega_e \varphi_f T_c}{L_s} \end{bmatrix}$.

Correspondingly, the MRFCS-MPC predicts the lifting current information and then solves the lifting control input by evaluating the cost function N times, whose time scale is changed to T_c, as seen in (5.16), (5.18), and (5.20). The experimental setup is shown in Fig. 5.7, which adopts the MicroLabBox 1202 digital controller. The VSI setup configurated by IGBT power modules (Infineon F3L75R07W2E3) is used to drive the PMSM. The parameters are shown in Table 5.1.

Four kinds of control algorithms are compared for the two-level VSI-fed PMSM drive case, i.e., SRFCS-MPC with 10kHz sampling frequency, SRFCS-MPC with 40kHz sampling frequency, MRFCS-MPC (N=5) with 10kHz sampling frequency, and MRFCS-MPC (N=10) with 10kHz sampling frequency.

Table 5.1: Experimental parameters of the VSI-fed PMSM system

Parameters	Value
DC-link voltage	180V
DC-link capacitance C_{dc}	3300μF
Rated power	1.1kW
Rated stator frequency	100Hz
Number of pole pairs	5
Rotor flux	0.15Wb
Stator resistance	0.5Ω
Stator inductance	3.1mH
Sampling frequency	10kHz
Control frequency (SRFCS-MPC)	10kHz
Control frequency (MRFCS-MPC)	50kHz 100kHz

All control schemes use the same PI parameter for the speed loop. It is worth mentioning that due to the simple inverter topology and system modeling in this case study, the SRFCS-MPC can still be executed with 40kHz sampling frequency. Considering the increased number of switching states in the multilevel converter or complex system plant such as high-order filter involved, it will be challenging to adopt 40kHz sampling frequency. Fig. 5.8 shows the

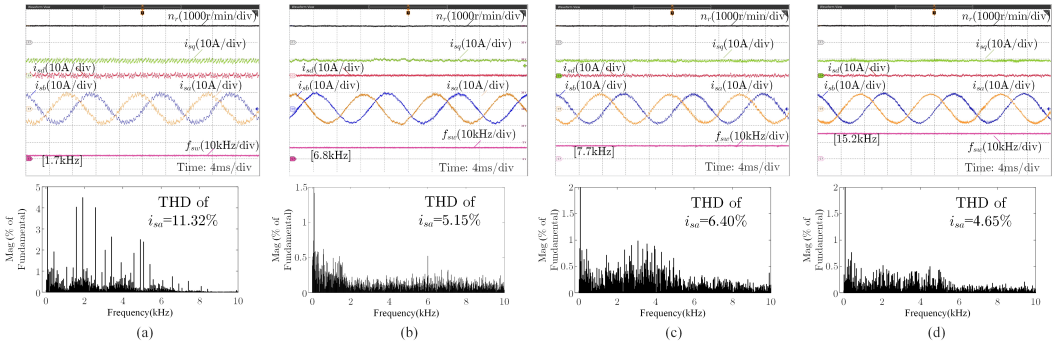

Figure 5.8: The experimental PMSM current waveform and FFT spectrum (rotor speed 1000r/min, load torque 8N·m) (a) SRFCS-MPC(f_s=10kHz). (b) SRFCS-MPC(f_s=40kHz). (c) MRFCS-MPC(f_s=10kHz, f_c=50kHz, N=5). (d) MRFCS-MPC(f_s=10kHz, f_c=100kHz, N=10).

steady-state current waveform of the PMSM by using four kinds of control algorithms respectively, The motors operated at 1000r/min rotor speed and 8N·m load torque. The control schemes with the same sampling frequency

are compared first. It can be seen that the current performance of PMSM is poor by using SRFCS-MPC with a 10kHz sampling frequency. The switching frequency f_{sw} is only 1.7kHz and the large current ripples exist, where the THD of stator current is 11.32%. With the control frequency increased to 50kHz in MRFCS-MPC (N=5), the system performance is enhanced with a 7.7kHz switching frequency. The stator current ripple is lower and the THD reduces to 6.40%. Furthermore, when the 100kHz control frequency is used in MRFCS-MPC (N=10), the switching frequency reaches 15.2kHz. The stator current ripple is further reduced and 4.65% THD can be achieved. Therefore, with the proposed MRFCS-MPC scheme, the system switching frequency can be significantly enhanced with improved performance, and only 10kHz sampling frequency is used. Moreover, with the sampling frequency increased to 40kHz in SRFCS-MPC, the switching frequency is maintained as 6.8kHz and the THD of the stator current is 5.15%. It can be inferred that the effect of MRFCS-MPC is not as good as the SRFCS-MPC with 40kHz sampling frequency under the same switching frequency condition. The reason is that the update frequency of the real-time current feedback is only 10kHz in MRFCS-MPC and the prediction for the intersample instant is executed in an open-loop manner. On the other hand, with a higher sampling frequency used in the SRFCS-MPC, a faster real-time current feedback is provided. Therefore, the time duration for the prediction is shorter, resulting in more accurate control input selection. Fortunately, the proposed MRFCS-MPC still shows benefit in the computational burden especially when the SRFCS-MPC with higher sampling frequency cannot be realized. Fig. 5.9 shows the detailed dq-axes current waveform and the corresponding root mean square error (MSE) value (defined in (5.27)) at steady-state. As can be seen, the MRFCS-MPC can significantly reduce the current ripple of dq-axis currents, i.e. MSE(i_{sq}^*- i_{sq}) and MSE(i_{sd}^*- i_{sd}).

$$\text{MSE}(x^* - x_j) = \sqrt{\frac{1}{N_{total}} \sum_{i=0}^{N_{total}} (x^* - x_j)^2} \tag{5.27}$$

To verify the dynamic performance, the start-up process where the rotor

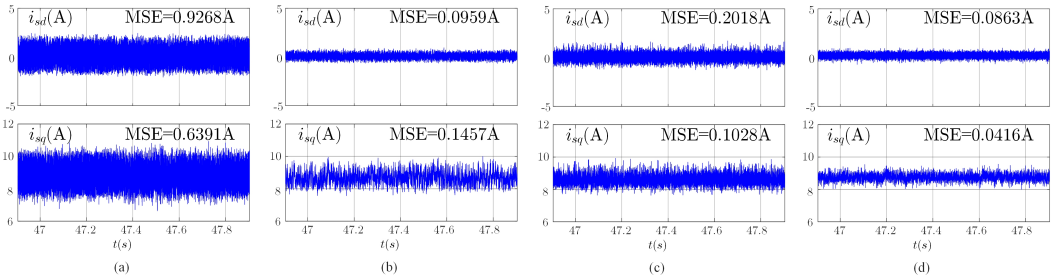

Figure 5.9: The experimental PMSM dq-axes current waveform (a) SRFCS-MPC(f_s=10kHz). (b) SRFCS-MPC(f_s=40kHz). (c) MRFCS-MPC(f_s=10kHz, f_c=50kHz, N=5). (d) MRFCS-MPC(f_s=10kHz, f_c=100kHz, N=10).

speed changes from the standstill state to the 1000r/min is shown in Fig. 5.10. It can be seen that the proposed strategy reduces the current ripple while not affecting the dynamic performance of the original SRFCS-MPC. Furthermore, the dynamic test with step load change from zero to 8N·m is shown in Fig. 5.11. It can be seen that all schemes show a fast response to the external disturbance. To fully investigate the property of the proposed MRFCS-MPC, the zoom-in views of the rotor speed with speed maneuver and load torque change are compared in Fig. 5.12. The initial speed oscillations are caused by the flexible shaft connection between the load machine and PMSM. With the increased control frequency of MRFCS-MPC, the scheme shows a faster response to the speed regulation with higher control bandwidth. The MRFCS-MPC with 100kHz control frequency expresses the minimum speed deviation and restores faster to the nominal speed in Fig. 5.12. Therefore, the proposed MRFCS-MPC maintains the fast dynamic response of the FCS-MPC and also can improve the system response to external disturbance.

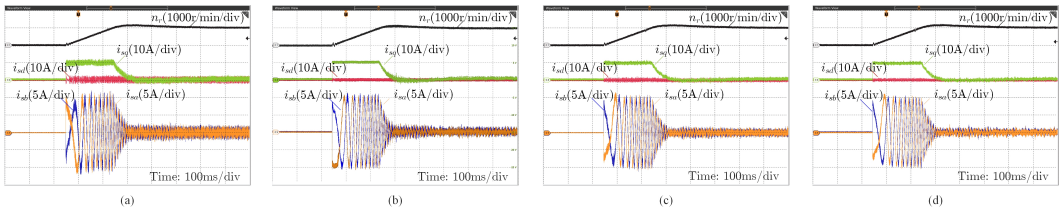

Figure 5.10: The dynamic start-up process test (a) SRFCS-MPC(f_s=10kHz). (b) SRFCS-MPC(f_s=40kHz). (c) MRFCS-MPC(f_s=10kHz, f_c=50kHz, N=5). (d) MRFCS-MPC(f_s=10kHz, f_c=100kHz, N=10).

The proposed MRFCS-MPC is a generic form of the SRFCS-MPC, where

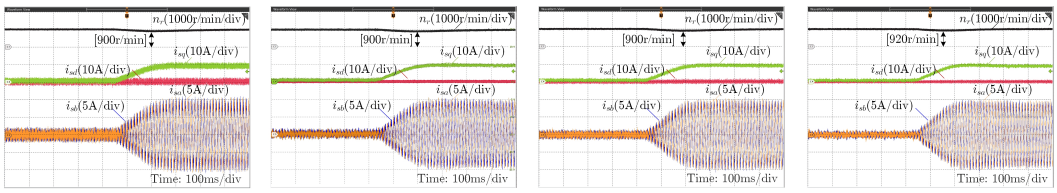

Figure 5.11: The dynamic test with step load change (a) SRFCS-MPC(f_s=10kHz). (b) SRFCS-MPC(f_s=40kHz). (c) MRFCS-MPC(f_s=10kHz, f_c=50kHz, N=5). (d) MRFCS-MPC(f_s=10kHz, f_c=100kHz, N=10).

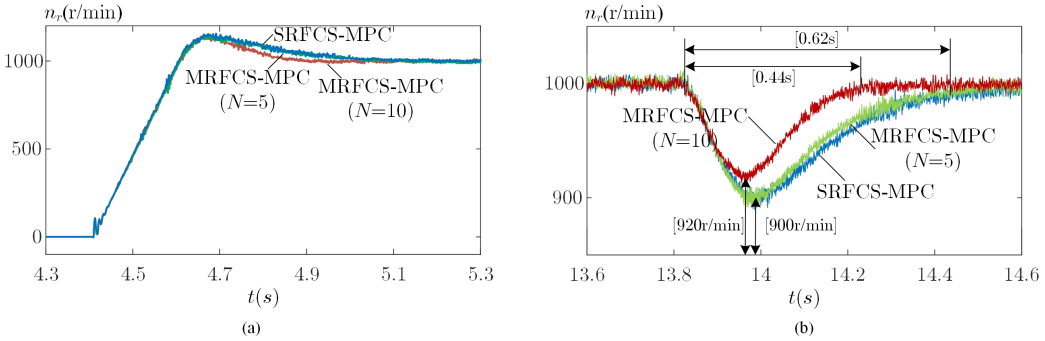

Figure 5.12: The zoom-in view comparison of the dynamic speed response (a) Start-up process with 10kHz sampling frequency. (b) Step load change with 10kHz sampling frequency.

the control frequency is not limited by the sampling frequency. The main advantage of the MRFCS-MPC is that the switching frequency can be significantly increased with unchanged sampling frequency. To evaluate the total computational burden, the execution time of each control scheme is measured by using the dSPACE Profiler, and the result is shown in Table 5.2. The interrupt occupancy is defined as the ratio of the total execution time used to the sampling duration. A higher interrupt occupancy indicates the lower computational margin remains.

In many practical applications, the SRFCS-MPC cannot be realized with a high enough sampling frequency. In this case study, the simple power converter topology two-level VSI is adopted, and only the stator current reference tracking is included in the cost function. Considering more complex systems, additional control objectives, and a general digital platform, the computational burden increase. Besides, due to the frequently varying work mode and magnitude order change of variables in practical application, the real execution time of the control algorithm will vary consequently. Therefore, it is

Table 5.2: The computational burden comparison between SRFCS-MPC and MRFCS-MPC

Indices	Execution time	Interrupt occupancy	THD	f_{sw}
SRFCS-MPC (10kHz)	15.2μs	15.2/100 =15.2%	11.32%	1.7kHz
SRFCS-MPC (40kHz)	15.2μs	15.2/25 =60.8%	5.15%	6.8kHz
MRFCS-MPC (N=5)	19.16μs	19.16/100 =19.16%	6.4%	7.7kHz
MRFCS-MPC (N=10)	26.08μs	26.08/100 =26.08%	4.65%	15.2kHz

recommended to remain at least around 30% computational margin. Based on these factors, it will be difficult to obtain the desired switching frequency by using a high sampling frequency, e.g., 40kHz. In this case, the proposed MRFCS-MPC could be an alternative way, which shows a higher ceiling for the improvement of switching frequency and system performance.

The control frequency is determined by the selection of the number of N in the proposed MRFCS-MPC scheme. In practical application, considering the converter loss, filter size, power level, etc., the switching frequency can be determined. In this case, the number of N can be selected according to the switching frequency requirement. On the other hand, N can be infinite theoretically, and the larger the N, the higher the switching frequency, the better the system performance. However, in real-time implementation, the number of N will be limited by the capability of the DSPs. Besides, due to the parameter mismatch and uncertainties, the cumulative prediction error becomes larger as N increases. On the occasion that FCS-MPC is designed with a disturbance observer, the increase of N can be more efficient. Therefore, the selection of the number of N should be determined by considering the switching frequency requirement, practical computational burden, and modeling accuracy. In the case study, the situation N=10 has been realized and verified, which can be enough for most power converters. To further enhance the switching frequency, the sampling frequency can also be increased appro-

priately, for example, the combination of 20kHz sampling frequency and N=10 can be adopted for MRFCS-MPC.

5.4 Review of Conventional SRCCS-MPC

The multi-rate technique is also developed for the CCS-MPC to address the computational issue in high switching frequency applications. The typical single-rate CCS-MPC (SRCCS-MPC) is firstly reviewed before introducing the MRCCS-MPC. Considering the S/I interval T_s and the current predictive step k, the prediction equation can be derived in (5.2). Assuming that the information of the state variable at the current time step k, i.e., $\boldsymbol{x}(k)$ is available, the future state variable can be predicted for N_p samples ahead, where the number N_p is called the predictive horizon. The predictive variables can be denoted as $\boldsymbol{x}(k+1\,|k)$, $\boldsymbol{x}(k+2\,|k)$, ..., $\boldsymbol{x}(k+m\,|k)$, ..., $\boldsymbol{x}(k+N_p\,|k)$, where $k+m\,|k$ is the future $k+m$ instant started from the current step k. According to (5.2), the general expression of the predictive vector $\boldsymbol{x}(k+m\,|k)$ can be deduced as

$$\begin{aligned}\boldsymbol{x}(k+m\,|k) = {} & \mathbf{A}_s{}^{m}\boldsymbol{x}(k) + \mathbf{A}_s{}^{m-1}\mathbf{B}_s\boldsymbol{u}(k) \\ & + \mathbf{A}_s{}^{m-2}\mathbf{B}_s\boldsymbol{u}(k+1) + \dots \\ & \vdots \\ & + \mathbf{B}_s\boldsymbol{u}(k+m-1) \\ & + \sum_{i=0}^{N_p-1} \mathbf{C}\mathbf{A}_s{}^{i}\mathbf{E}_s\end{aligned} \tag{5.28}$$

Therefore, the predictive outputs $\boldsymbol{y}(k+1\,|k)$, $\boldsymbol{y}(k+2\,|k)$, ..., $\boldsymbol{y}(k+m\,|k)$, ..., $\boldsymbol{y}(k+N_p\,|k)$ can be obtained by substitution, which can be expressed in the compact matrix form as

$$\mathbf{Y}(k+1\,|k) = \boldsymbol{\Phi}_s\boldsymbol{x}(k) + \boldsymbol{\Gamma}_s\mathbf{U}(k) + \boldsymbol{\Xi}_s \tag{5.29}$$

and $\mathbf{Y}(k+1\,|k)$ is the prediction output sequence over the predictive horizon N_p; $\mathbf{U}(k)$ is the control sequence over the control horizon, and the control horizon is taken as the same as the predictive horizon N_p for simplicity in this work. The vector $\mathbf{Y}(k+1\,|k)$, $\mathbf{U}(k)$ and the matrix $\boldsymbol{\Phi}_k$, $\boldsymbol{\Gamma}_k$, $\boldsymbol{\Xi}_k$ are shown in

the following respectively.

$$\mathbf{Y}(k+1\,|k) = [\boldsymbol{y}(k+1\,|k)\ \boldsymbol{y}(k+2\,|k)\ \ldots\ \boldsymbol{y}(k+N_p\,|k)]^{\mathrm{T}} \tag{5.30}$$

$$\mathbf{U}(k) = [\boldsymbol{u}(k)\ \boldsymbol{u}(k+1)\ \ldots\ \boldsymbol{u}(k+N_p-1)]^{\mathrm{T}} \tag{5.31}$$

$$\boldsymbol{\Phi}_s = \left[\mathbf{CA}_s\ \mathbf{CA}_s{}^2\ \mathbf{CA}_s{}^3\ \ldots\ \mathbf{CA}_s{}^{N_p}\right]^{\mathrm{T}} \tag{5.32}$$

$$\boldsymbol{\Gamma}_s = \begin{bmatrix} \mathbf{CB}_s & & & \\ \mathbf{CA}_s\mathbf{B}_s & \mathbf{CB}_s & & \\ \vdots & \vdots & \ddots & \\ \mathbf{CA}_s{}^{N_p-1}\mathbf{B}_s & \mathbf{CA}_s{}^{N_p-2}\mathbf{B}_s & \mathbf{CA}_s{}^{N_p-3}\mathbf{B}_s\ldots & \mathbf{CB}_s \end{bmatrix} \tag{5.33}$$

$$\boldsymbol{\Xi}_s = \left[\mathbf{CE}_s\ \ \mathbf{CA}_s\mathbf{E}_s + \mathbf{CE}_s\ \ \ldots\ \ \sum_{i=0}^{N_p-1} \mathbf{CA}_s{}^{i}\mathbf{E}_s\right]^{\mathrm{T}} \tag{5.34}$$

It can be seen that all of the prediction outputs are calculated in terms of the current state variable information $\boldsymbol{x}(k)$ and the future control input $\boldsymbol{u}(k+i)$, where i=0, 1, ..., N_p-1. The cost function is designed to guarantee that the predictive variable can track the corresponding reference and it can be expressed as

$$J = \Delta\mathbf{Y}(k+1\,|k)^{\mathrm{T}}\boldsymbol{\Theta}\Delta\mathbf{Y}(k+1\,|k) + \mathbf{U}(k)^{\mathrm{T}}\boldsymbol{\Upsilon}\mathbf{U}(k) \tag{5.35}$$

where $\Delta\mathbf{Y}(k+1\,|k) = \mathbf{Y}(k+1\,|k) - \mathbf{Y}^*(k+1\,|k)$. The reference vector contains the desired output within the predictive horizon, i.e.,

$$\mathbf{Y}^*(k+1\,|k) = [\boldsymbol{y}^*(k+1\,|k)\ \boldsymbol{y}^*(k+2\,|k)\ldots\ \boldsymbol{y}^*(k+N_p\,|k)]^{\mathrm{T}} \tag{5.36}$$

$\boldsymbol{\Theta}$ and $\boldsymbol{\Upsilon}$ are the symmetric positive definite matrices, and they represent the weight assigned for the penalization of the output tracking error and the control effort. Furthermore, $\boldsymbol{\Theta}$ and $\boldsymbol{\Upsilon}$ aggregates the $\mathbf{Q}$ and $\mathbf{R}$ in total number N_p respectively, i.e., $\boldsymbol{\Theta} = diag(\mathbf{Q}, \mathbf{Q}, \ldots \mathbf{Q})$ and $\boldsymbol{\Upsilon} = diag(\mathbf{R}, \mathbf{R}, \ldots \mathbf{R})$, where $\mathbf{Q}$ and $\mathbf{R}$ are the weighting factors of the output tracking error and control effort for each predictive step respectively.

The optimal control sequence $\mathbf{U}(k)$ can be obtained according to the minimization of the cost function (5.35). Substituting (5.29) into (5.35) and taking the derivative of J with respect to $\mathbf{U}(k)$ equals zero, i.e.,

$$\frac{\partial J}{\partial \mathbf{U}(k)} = 0 \tag{5.37}$$

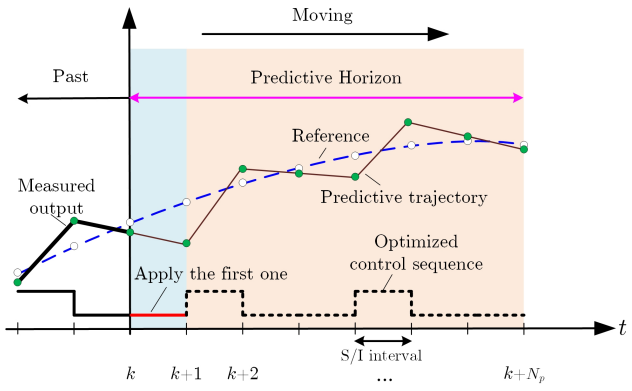

Figure 5.13: The principle of the SR-MPC scheme.

The optimized control sequence can be obtained as

$$\mathbf{U}(k) = (\boldsymbol{\Gamma}_s{}^{\mathrm{T}}\boldsymbol{\Theta}\boldsymbol{\Gamma}_s + \boldsymbol{\Upsilon})^{-1}\boldsymbol{\Gamma}_s{}^{\mathrm{T}}\boldsymbol{\Theta}\left[\mathbf{Y}^* - \boldsymbol{\Phi}_s\boldsymbol{x}(k) - \boldsymbol{\Xi}_s\right] \tag{5.38}$$

Moreover, the condition that the second-order partial derivative of the J, i.e., $\partial^2 J/\partial \mathbf{U}^2(k) > 0$ guarantee the solution resulting in the minimization value of (5.35).

According to the RHP, the first element of $\mathbf{U}(k)$ will be applied to the next S/I interval, thereby the optimized control law is

$$\boldsymbol{u}(k) = \mathbf{W}(\boldsymbol{\Gamma}_s{}^{\mathrm{T}}\boldsymbol{\Theta}\boldsymbol{\Gamma}_s + \boldsymbol{\Upsilon})^{-1}\boldsymbol{\Gamma}_s{}^{\mathrm{T}}\boldsymbol{\Theta}\left[\mathbf{Y}^* - \boldsymbol{\Phi}_s\boldsymbol{x}(k) - \boldsymbol{\Xi}_s\right] \tag{5.39}$$

where $\mathbf{W}$=$[1\ 0\ \ldots 0]^{\mathrm{T}}$ with N_p dimension. The modulator is utilized to synthesize the control input, which is constrained into the allowable region. Assuming that the magnitude of the maximum reachable input is u_{max}, the final input sent into the modulator block is expressed as

$$\boldsymbol{u}^*(k) = \begin{cases} \boldsymbol{u}(k) & |\boldsymbol{u}(k)| \le u_{\max} \\ \frac{\boldsymbol{u}(k)}{|\boldsymbol{u}(k)|}u_{\max} & |\boldsymbol{u}(k)| > u_{\max} \end{cases} \tag{5.40}$$

Fig. 5.13 shows the principle of the MPC scheme at the kth S/I interval. The predictive horizon with length N_p serves as a moving window, within which the future output information is calculated based on the kth step state variable and the control sequence. With the optimized solution, only the first element, i.e. (5.37) is applied to the next S/I interval to provide real-time feedback. In the next S/I interval, the horizon window moves one step forward starting

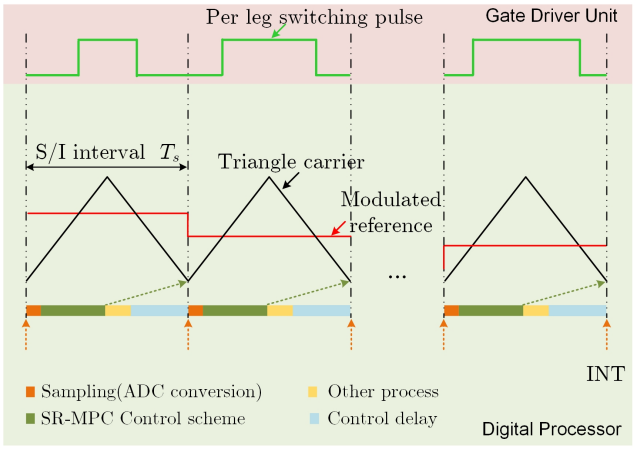

Figure 5.14: The digital realization of the SRCCS-MPC scheme.

from the k+1 instance, and the same procedure will be repeated to obtain the control law $\boldsymbol{u}(k+1)$. With the CCS-MPC framework. The optimized control law will be sent into the modulator block to generate the switching driving pulse during each S/I interval. Fig. 5.14 shows the realization of the SRCCS-MPC in the digital platform. As can be seen, only the time scale T_s exists in the controller, and thus the conventional MPC belongs to the single-rate control category. The control law is converted into the modulated reference, which is compared with the triangle carrier to determine whether a high or low switching level will be given. The algorithm starts with sampling at the bottom of the triangle carrier and ends with the update of the modulation ratio at the beginning of the next triangle carrier. During each S/I interval, the switching device of each leg only acts once, and therefore the switching frequency is constant and equals to the S/I frequency directly. Considering the computational burden of the control scheme, the S/I frequency is limited, which is typically below 20kHz in DSPs. Therefore, the switching frequency of the SRCCS-MPC scheme cannot be easily enhanced. As seen in Fig. 5.14, due to the existence of the control delay, the one-step ahead compensation of state variable is necessary for the digital realization. In this case, the system information $\boldsymbol{x}(k+1)$ will be taken as the starting point for the prediction stage. Correspondingly, both the output information used in the cost function and the optimized control law will be compensated by one-step forward.

5.5 Proposed Multi-rate CCS-MPC Design

The MRFCS-MPC type has been proposed, where the ratio of switching frequency to sampling frequency can be enhanced. However, due to the inherent searching process of FCS-MPC, i.e., the enumeration approach, the computational burden exponentially increases as the dimension of the lifting switching sequence increase, which implies the simultaneous solving of all elements in the high-dimension switching sequence is quite difficult. Therefore, the suboptimal method is adopted, where each element in the high-dimension switching sequence is solved one by one. To address this issue, the MRCCS-MPC is developed such that the lifting sequence can be solved simultaneously according to the differentiation of the cost function. Besides, the more general prediction problem, i.e., the long predictive horizon modeling can be addressed in the proposed MRCCS-MPC, which is challenging for the MRFCS-MPC type. Due to the utilization of the modulator, it is also more convenient to decide the number of control periods within each S/I period.

5.5.1 Lifting Model With Long Prediction Horizon

The lifting state vector, which contains the state variable information at all control instants within the predictive horizon N_p, is expressed as

$$\underline{\boldsymbol{x}}(k+1\,|k\,)=\left\{\begin{array}{l}\left[\begin{array}{l}\boldsymbol{x}(1T_c\,|k\,)\\ \boldsymbol{x}(2T_c\,|k\,)\\ \vdots\\ \boldsymbol{x}(NT_c\,|k\,)\end{array}\right],\left[\begin{array}{l}\boldsymbol{x}(1T_c\,|k+1\,)\\ \boldsymbol{x}(2T_c\,|k+1\,)\\ \vdots\\ \boldsymbol{x}(NT_c\,|k+1\,)\end{array}\right],\cdots\\ ,\left[\begin{array}{l}\boldsymbol{x}(1T_c\,|k+N_p-1)\\ \boldsymbol{x}(2T_c\,|k+N_p-1)\\ \vdots\\ \boldsymbol{x}(NT_c\,|k+N_p-1)\end{array}\right]\end{array}\right\}^{\mathrm{T}} \tag{5.41}$$

Therefore, the lifting output vector $\underline{\mathbf{Y}}(k+1\,|k\,)$ over the predictive horizon N_p can be written in the compact matrix form as

$$\underline{\mathbf{Y}}(k+1\,|k\,)=\underline{\boldsymbol{\Phi}_s}\boldsymbol{x}(k)+\underline{\boldsymbol{\Gamma}_s}\underline{\mathbf{U}}(k)+\underline{\boldsymbol{\Xi}_s} \tag{5.42}$$

where $\underline{\mathbf{U}}(k)$ is the lifting control sequence over the predictive horizon. The lifting vector $\underline{\mathbf{Y}}(k+1\,|k\,)$,$\underline{\mathbf{U}}(k)$ and the matrix $\underline{\boldsymbol{\Phi}_s}$, $\underline{\boldsymbol{\Gamma}_s}$, $\underline{\boldsymbol{\Xi}_s}$ are shown in the

following, respectively,

$$\underline{\mathbf{Y}}(k+1\,|k\,) = \left\{ \begin{array}{l} \left[\begin{array}{l} \boldsymbol{y}(1T_c\,|k\,) \\ \boldsymbol{y}(2T_c\,|k\,) \\ \vdots \\ \boldsymbol{y}(NT_c\,|k\,) \end{array} \right], \left[\begin{array}{l} \boldsymbol{y}(1T_c\,|k+1\,) \\ \boldsymbol{y}(2T_c\,|k+1\,) \\ \vdots \\ \boldsymbol{y}(NT_c\,|k+1\,) \end{array} \right], \\ \cdots \left[\begin{array}{l} \boldsymbol{y}(1T_c\,|k+N_p-1) \\ \boldsymbol{y}(2T_c\,|k+N_p-1) \\ \vdots \\ \boldsymbol{y}(NT_c\,|k+N_p-1) \end{array} \right] \end{array} \right\}^{\mathrm{T}} \tag{5.43}$$

$$\underline{\mathbf{U}}(k) = \left\{ \begin{array}{l} \left[\begin{array}{l} \boldsymbol{u}(0T_c\,|k\,) \\ \boldsymbol{u}(1T_c\,|k\,) \\ \vdots \\ \boldsymbol{u}((N-1)T_c\,|k\,) \end{array} \right], \left[\begin{array}{l} \boldsymbol{u}(0T_c\,|k+1\,) \\ \boldsymbol{u}(1T_c\,|k+1\,) \\ \vdots \\ \boldsymbol{u}((N-1)T_c\,|k+1\,) \end{array} \right], \\ \cdots \left[\begin{array}{l} \boldsymbol{u}(0T_c\,|k+N_p-1) \\ \boldsymbol{u}(1T_c\,|k+N_p-1) \\ \vdots \\ \boldsymbol{u}((N-1)T_c\,|k+N_p-1) \end{array} \right] \end{array} \right\}^{\mathrm{T}} \tag{5.44}$$

$$\underline{\boldsymbol{\Phi}_s} = \left[\begin{array}{llll|llll|l} \mathbf{CA}_c & \mathbf{CA}_c{}^2 & \ldots & \mathbf{CA}_c{}^N & \mathbf{CA}_c{}^{N+1} & \mathbf{CA}_c{}^{N+2} & \ldots & \mathbf{CA}_c{}^{2N} & \ldots \\ \mathbf{CA}_c{}^{(N_p-1)N+1} & \mathbf{CA}_c{}^{(N_p-1)N+2} & \ldots & \mathbf{CA}_c{}^{N_pN} & & & & & \end{array} \right]^{\mathrm{T}} \tag{5.45}$$

$$\underline{\boldsymbol{\Gamma}_s} = \left[\begin{array}{cccc} \mathbf{CB}_c & & & \\ \mathbf{CA}_c\mathbf{B}_c & \mathbf{B}_c & & \\ \vdots & & \ddots & \\ \mathbf{CA}_c{}^{N-1}\mathbf{B}_c & \mathbf{CA}_c{}^{N-2}\mathbf{B}_c & \ldots & \mathbf{B}_c \\ \hline \mathbf{CA}_c{}^{N}\mathbf{B}_c & \mathbf{CA}_c{}^{N-1}\mathbf{B}_c & \ldots & \mathbf{CA}_c\mathbf{B}_c \;\; \mathbf{CB}_c \\ \mathbf{CA}_c{}^{N+1}\mathbf{B}_c & \mathbf{CA}_c{}^{N}\mathbf{B}_c & \ldots & \mathbf{CA}_c\mathbf{B}_c \;\; \mathbf{CB}_c \\ \vdots & \ddots & & \\ \mathbf{CA}_c{}^{2N-1}\mathbf{B}_c & \mathbf{CA}_c{}^{2N-2}\mathbf{B}_c & \ldots & \mathbf{CA}_c\mathbf{B}_c \; \mathbf{CB}_c \\ \hline \vdots & \ddots & & \\ \mathbf{CA}_c{}^{(N_p-1)N}\mathbf{B}_c & \mathbf{CA}_c{}^{(N_p-1)N-1}\mathbf{B}_c & \ldots & \mathbf{CA}_c\mathbf{B}_c \;\; \mathbf{CB}_c \\ \mathbf{CA}_c{}^{(N_p-1)N+1}\mathbf{B}_c & \mathbf{CA}_c{}^{(N_p-1)N}\mathbf{B}_c & \ldots & \mathbf{CA}_c\mathbf{B}_c \;\; \mathbf{CB}_c \\ \vdots & \ddots & & \\ \mathbf{CA}_c{}^{N_pN-1}\mathbf{B}_c & \mathbf{CA}_c{}^{N_pN-2}\mathbf{B}_c & \ldots & \mathbf{CA}_c\mathbf{B}_c \; \mathbf{CB}_c \end{array} \right] \tag{5.46}$$

$$\underline{\boldsymbol{\Xi}_s} = \begin{bmatrix} \mathbf{C}\mathbf{E}_c & \mathbf{C}\mathbf{A}_c\mathbf{E}_c + \mathbf{C}\mathbf{E}_c & \cdots & \sum_{i=0}^{N-1} \mathbf{C}\mathbf{A}_c{}^i\mathbf{E}_c | \\ \sum_{i=0}^{N} \mathbf{C}\mathbf{A}_c{}^i\mathbf{E}_c & \sum_{i=0}^{N+1} \mathbf{C}\mathbf{A}_c{}^i\mathbf{E}_c & \cdots & \sum_{i=0}^{2N-1} \mathbf{C}\mathbf{A}_c{}^i\mathbf{E}_c | \\ \cdots & \sum_{i=0}^{(N_p-1)N} \mathbf{C}\mathbf{A}_c{}^i\mathbf{E}_c & \sum_{i=0}^{(N_p-1)N+1} \mathbf{C}\mathbf{A}_c{}^i\mathbf{E}_c & \cdots \sum_{i=0}^{N_pN-1} \mathbf{C}\mathbf{A}_c{}^i\mathbf{E}_c \end{bmatrix}^{\mathrm{T}} \tag{5.47}$$

The information of the output variable at each control instant can be obtained according to the lifting modeling (5.42). All of the prediction outputs are calculated in terms of the current state variable information $\boldsymbol{x}(k)$ and the future lifting control input $\underline{\mathbf{U}}(k)$, which needs to be solved according to the optimization of the system behavior.

5.5.2 Optimized Lifting Control Law

Different from the SRCCS-MPC scheme, the proposed MRCCS-MPC scheme steers all of the outputs in the lifting vector $\underline{\mathbf{Y}}(k+1\,|k\,)$ to track the corresponding reference. In this case, the cost function of the MRCCS-MPC problem is expressed as

$$J_{MR} = \Delta\underline{\mathbf{Y}}(k+1\,|k\,)^{\mathrm{T}}\underline{\boldsymbol{\Theta}}\Delta\underline{\mathbf{Y}}(k+1\,|k\,)+\underline{\mathbf{U}}(k)^{\mathrm{T}}\underline{\boldsymbol{\Upsilon}}\underline{\mathbf{U}}(k) \tag{5.48}$$

where $\Delta\underline{\mathbf{Y}}(k+1\,|k\,) = \underline{\mathbf{Y}}(k+1\,|k\,) - \underline{\mathbf{Y}}^*(k+1\,|k\,)$ is the lifting tracking error vector. $\underline{\mathbf{Y}}^*(k+1\,|k\,)$ is the lifting reference vector within the predictive horizon, i.e.,

$$\underline{\mathbf{Y}^*}(k+1\,|k\,) = \left\{ \begin{bmatrix} \boldsymbol{y}^*(1T_c\,|k\,) \\ \boldsymbol{y}^*(2T_c\,|k\,) \\ \vdots \\ \boldsymbol{y}^*(NT_c\,|k\,) \end{bmatrix}, \begin{bmatrix} \boldsymbol{y}^*(1T_c\,|k+1\,) \\ \boldsymbol{y}^*(2T_c\,|k+1\,) \\ \vdots \\ \boldsymbol{y}^*(NT_c\,|k+1\,) \end{bmatrix}, \cdots \begin{bmatrix} \boldsymbol{y}^*(1T_c\,|k+N_p-1) \\ \boldsymbol{y}^*(2T_c\,|k+N_p-1) \\ \vdots \\ \boldsymbol{y}^*(NT_c\,|k+N_p-1) \end{bmatrix} \right\}^{\mathrm{T}} \tag{5.49}$$

$\underline{\boldsymbol{\Theta}}$ and $\underline{\boldsymbol{\Upsilon}}$ are the corresponding lifting weighting factor matrix, which are composed of diagonal elements $\mathbf{Q}$ and $\mathbf{R}$ respectively in the total number of $N_p \times N$.

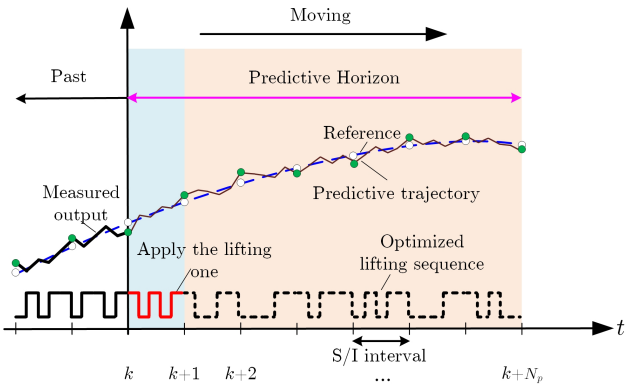

Figure 5.15: The principle of the proposed MRCCS-MPC scheme.

Similarly, substituting (5.42) into (5.48) and taking the derivative of J_{MR} with respect to $\underline{\mathbf{U}}(k)$ equals zero, the optimized lifting control vector within the predictive horizon N_p can be derived as

$$\underline{\mathbf{U}}(k) = (\underline{\boldsymbol{\Gamma}}_s{}^{\mathrm{T}}\underline{\boldsymbol{\Theta}}\underline{\boldsymbol{\Gamma}}_s + \underline{\boldsymbol{\Upsilon}})^{-1}\underline{\boldsymbol{\Gamma}}_s{}^{T}\underline{\boldsymbol{\Theta}}\,[\underline{\mathbf{Y}}^* - \underline{\boldsymbol{\Phi}}_s\boldsymbol{x}(k) - \underline{\boldsymbol{\Xi}}_s] \tag{5.50}$$

With the extended receding horizon policy, the first N element of $\underline{\mathbf{U}}(k)$ will be applied during the current S/I interval. Therefore, the final expression of the lifting control law of the proposed MRCCS-MPC is

$$\underline{\boldsymbol{u}}(k) = \boldsymbol{\Psi}(\underline{\boldsymbol{\Gamma}}_s{}^{\mathrm{T}}\underline{\boldsymbol{\Theta}}\underline{\boldsymbol{\Gamma}}_s + \underline{\boldsymbol{\Upsilon}})^{-1}\underline{\boldsymbol{\Gamma}}_s{}^{T}\underline{\boldsymbol{\Theta}}\,[\underline{\mathbf{Y}}^* - \underline{\boldsymbol{\Phi}}_s x(k) - \underline{\boldsymbol{\Xi}}_s] \tag{5.51}$$

where the matrix $\boldsymbol{\Psi} = \begin{bmatrix} 1\,0\ldots0\ldots0 \\ 0\,1\ldots0\ldots0 \\ \vdots \quad \ddots \\ 0\ldots0\,1\ldots0 \end{bmatrix}$ with $N\times N_pN$ dimension.

Fig. 5.15 shows the physical-level principle of the proposed MRCCS-MPC scheme during the kth S/I interval. Compared to Fig. 5.13, the same predictive horizon with length N_p still serves as a moving window. The difference is the future output information at all control instants which are calculated based on the kth step state variable and the lifting control sequence. As a result, the first N element in (5.50), i.e. the control law (5.51) is applied to the next S/I interval. Since the control input updates multiple times within each S/I interval, the output variable will show reduced ripples with the improved switching frequency.

5.5.3 Stability Analysis

The stability of the proposed MR-MPC scheme can be investigated by finding the eigenvalues of the system matrix in the closed-loop model. Based on (5.2) and the control law (5.51), the closed-loop system model can be expressed as

$$\begin{aligned}
\boldsymbol{x}(k+1) &= \mathbf{A}_s\boldsymbol{x}(k) + \left[\mathbf{A}_c{}^{N-1}\mathbf{B}_c \quad \mathbf{A}_c{}^{N-2}\mathbf{B}_c \ldots \quad \mathbf{B}_c\right]\underline{\boldsymbol{u}}(k) + \mathbf{E}_s \\
&= \left\{ \begin{array}{l} \mathbf{A}_s - \left[\mathbf{A}_c{}^{N-1}\mathbf{B}_c \quad \mathbf{A}_c{}^{N-2}\mathbf{B}_c \ldots \quad \mathbf{B}_c\right] \\ \cdot\boldsymbol{\Psi}(\underline{\boldsymbol{\Gamma}}_s{}^{\mathrm{T}}\underline{\boldsymbol{\Theta}\boldsymbol{\Gamma}}_s + \underline{\boldsymbol{\Upsilon}})^{-1}\underline{\boldsymbol{\Gamma}}_s{}^{\mathrm{T}}\underline{\boldsymbol{\Theta}\boldsymbol{\Phi}}_s \end{array} \right\}\boldsymbol{x}(k) \\
&+ \left[\mathbf{A}_c{}^{N-1}\mathbf{B}_c \quad \mathbf{A}_c{}^{N-2}\mathbf{B}_c \ldots \quad \mathbf{B}_c\right] \\
&\cdot\boldsymbol{\Psi}(\underline{\boldsymbol{\Gamma}}_s{}^{\mathrm{T}}\underline{\boldsymbol{\Theta}\boldsymbol{\Gamma}}_s + \underline{\boldsymbol{\Upsilon}})^{-1}\underline{\boldsymbol{\Gamma}}_s{}^{\mathrm{T}}\underline{\boldsymbol{\Theta}}\left[\underline{\mathbf{Y}}^* - \underline{\boldsymbol{\Xi}}_s\right] + \mathbf{E}_s
\end{aligned} \tag{5.52}$$

The closed-loop stability can be guaranteed if the eigenvalues of $\mathbf{A}_s - \left[\mathbf{A}_c{}^{N-1}\mathbf{B}_c\ \mathbf{A}_c{}^{N-2}\mathbf{B}_c \ldots \mathbf{B}_c\right]\boldsymbol{\Psi}(\underline{\boldsymbol{\Gamma}}_s{}^{\mathrm{T}}\underline{\boldsymbol{\Theta}\boldsymbol{\Gamma}}_s + \underline{\boldsymbol{\Upsilon}})^{-1}\underline{\boldsymbol{\Gamma}}_s{}^{\mathrm{T}}\underline{\boldsymbol{\Theta}\boldsymbol{\Phi}}_s$ are all within the unit circle on the discrete z-domain. The suitable design of the weighting factors $\mathbf{Q}$ and $\mathbf{R}$ can move the closed-loop poles and achieve the desired dynamic performance.

5.5.4 Digital Realization

The implementation process of the proposed MRCCS-MPC scheme in the digital processor is shown in Fig. 5.16. During each S/I interval, the modulated reference will update multiple times based on the solution of the lifting control law. The frequency of the triangle carrier is increased to be the same as the control frequency. The interrupt frequency is maintained the same as the SRCCS-MPC scheme. Therefore, a high switching frequency can be achieved while a low S/I frequency is adopted. The relatively long S/I interval allows the easy execution of the computational tasks and the demand of the WBG device-based power converter can also be met.

The one S/I interval delay compensation is still necessary for the proposed MR-MPC scheme. Thus, instead of the state variable $\boldsymbol{x}(k)$, the predictive vector $\boldsymbol{x}(k+1)$ will be used, i.e.

$$\boldsymbol{x}(k+1) = \mathbf{A}_s\boldsymbol{x}(k) + \left[\mathbf{A}_c{}^{N-1}\mathbf{B}_c\ \mathbf{A}_c{}^{N-2}\mathbf{B}_c \ldots \mathbf{B}_c\right]\underline{\boldsymbol{u}}(k) + \mathbf{E}_s \tag{5.53}$$

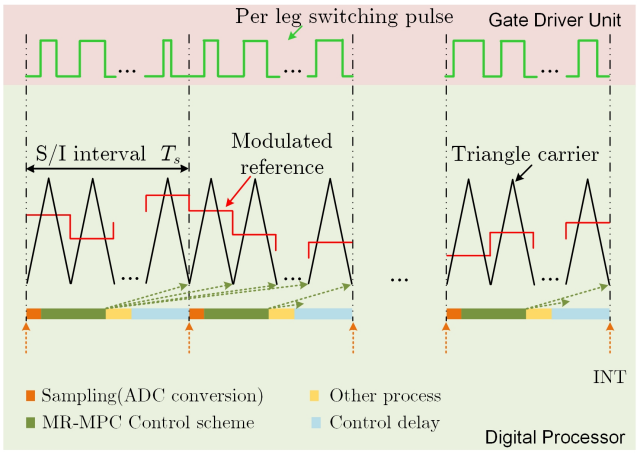

Figure 5.16: The digital realization of the proposed MRCCS-MPC scheme.

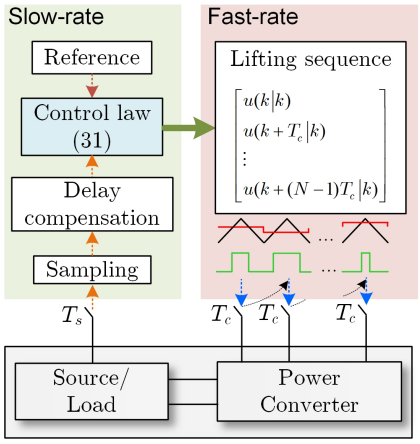

Figure 5.17: The control diagram of the proposed MR-MPC scheme.

In this case, the predictive state variable in both the cost function (5.48) and the control law (5.51) will move one-step forward. The control diagram of the proposed MR-MPC scheme for the high switching frequency power converter is shown in Fig. 5.17.

5.5.5 Experimental Results and Evaluation

The proposed MRCCS-MPC scheme is verified on a two-level voltage source inverter-fed surface-mounted PMSM drive system. The dynamic modeling of the PMSM in the $\alpha\beta$ reference frame is written as

$$\begin{aligned} \frac{di_{s\alpha}}{dt} &= -\frac{R_s}{L_s} i_{s\alpha} + \frac{1}{L_s} u_{inv\alpha} + \frac{\omega_e \psi_f}{L_s} \sin\theta_e \\ \frac{di_{s\beta}}{dt} &= -\frac{R_s}{L_s} i_{s\beta} + \frac{1}{L_s} u_{inv\beta} - \frac{\omega_e \psi_f}{L_s} \cos\theta_e \end{aligned} \tag{5.54}$$

where the state variable $\boldsymbol{x} = [i_{s\alpha}, i_{s\beta}]^{\mathrm{T}}$ includes the $\alpha\beta$-axes stator current and the control input $\boldsymbol{u} = [u_{inv\alpha}, u_{inv\beta}]^{\mathrm{T}}$ includes the $\alpha\beta$-axes modulated voltage generated by VSI. R_s and L_s are the stator resistance and inductance of the PMSM. ω_e is the synchronous angular velocity and θ_e is the rotor position angle. φ_f represents the permanent flux linkage. Based on the S/I interval T_s and the control interval T_c, the discrete matrix can be obtained as

$$\mathbf{A}_s = \begin{bmatrix} 1-\frac{R_s T_s}{L_s} & 0 \\ 0 & 1-\frac{R_s T_s}{L_s} \end{bmatrix},\ \mathbf{B}_s = \begin{bmatrix} \frac{T_s}{L_s} & 0 \\ 0 & \frac{T_s}{L_s} \end{bmatrix},\ \mathbf{E}_s = \begin{bmatrix} \frac{\omega_e \psi_f T_s}{L_s}\sin\theta_e \\ -\frac{\omega_e \psi_f T_s}{L_s}\cos\theta_e \end{bmatrix}$$

$$\mathbf{A}_c = \begin{bmatrix} 1-\frac{R_s T_c}{L_s} & 0 \\ 0 & 1-\frac{R_s T_c}{L_s} \end{bmatrix},\ \mathbf{B}_c = \begin{bmatrix} \frac{T_c}{L_s} & 0 \\ 0 & \frac{T_c}{L_s} \end{bmatrix},\ \mathbf{E}_c = \begin{bmatrix} \frac{\omega_e \psi_f T_c}{L_s}\sin\theta_e \\ -\frac{\omega_e \psi_f T_c}{L_s}\cos\theta_e \end{bmatrix}$$

The output variable $\boldsymbol{y}$ is the same as the state variable $\boldsymbol{x}$ and the output matrix $\mathbf{C}$ equals the 2×2 dimension identity matrix. To reduce the effect that comes from the parameter mismatch and the slow-varying disturbance, the Luenberger observer is utilized to estimate the lumped disturbance item online. To prove that the proposed scheme can effectively enhance the switching frequency, the S/I frequency of the SRCCS-MPC scheme is set as 5kHz and the resulted switching frequency is also 5kHz. As a comparison, the MRCCS-MPC scheme with two cases, i.e. N=4 and N=8 are realized, which implies that the switching frequency can reach 20kHz and 40kHz respectively while only 5kHz S/I frequency is still adopted. For simplicity, the predictive horizon N_p is set as one for both SRCCS-MPC and MRCCS-MPC schemes. Besides, the weighting matrix $\mathbf{R}$ is excluded and thus the matrix $\mathbf{Q}$ can be set as the identity matrix. For the SRCCS-MPC scheme, the cost function (5.35) evaluates the predictive stator current at the next S/I instant. On the other hand, the cost function (5.48) in the MRCCS-MPC contains all of the predictive output information at each control instant within the next S/I interval. All of the MPC schemes use the outer speed PI loop with the same parameters, which generates the q-axis current reference. The d-axis current reference is set as zero for the maximum torque-current-ratio operation. The dq-axes current references are transformed to the $\alpha\beta$-axes. The SPWM block generates the control law for SRCCS-MPC and MRCCS-MPC schemes respectively.

Fig. 5.18 shows the SiC device-based experimental prototype with the

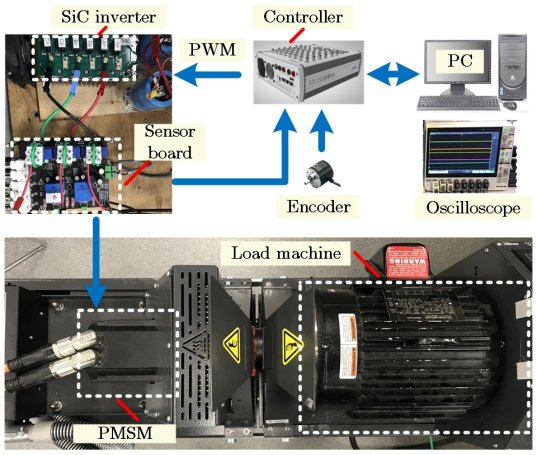

Figure 5.18: The SiC MOSFET-based inverter-fed PMSM drive system.

MicroLabBox 1202 controller and the parameters of the PMSM are given in Table 5.3. The MPC algorithm and the interrupt tasks are programmed and realized on the QorlQ P5020 processors. On the other hand, the function of the interface, i.e., the ADC and PWM pulse emission are realized on the programmable FPGA (Xilinx Kintex-7 XC7K325T). The inverter is configurated by the discrete SiC power MOSFET (C3M0065100K). The sampling rate of the oscilloscope is set as 1.25MHz.

Table 5.3: Experimental parameters of the PMSM drive system

Parameters	Value
DC-link voltage	240V
DC-link capacitance	2000μF
Rated power	1.1kW
Rated stator frequency	100Hz
Number of pole pairs	5
Rotor flux	0.15Wb
Stator resistance	0.5Ω
Stator inductance	3.1mH

Fig. 5.19 shows the steady-state rotor speed, electromagnetic torque, and stator current performance of the PMSM drive. The motor operates at 1000r/min rotor speed and 5N·m load torque. The SR-MPC scheme with only 5kHz S/I frequency is shown in Fig. 5.19(a). It can be observed that obvious ripples exist in the stator current because of the low switching frequency 5kHz,

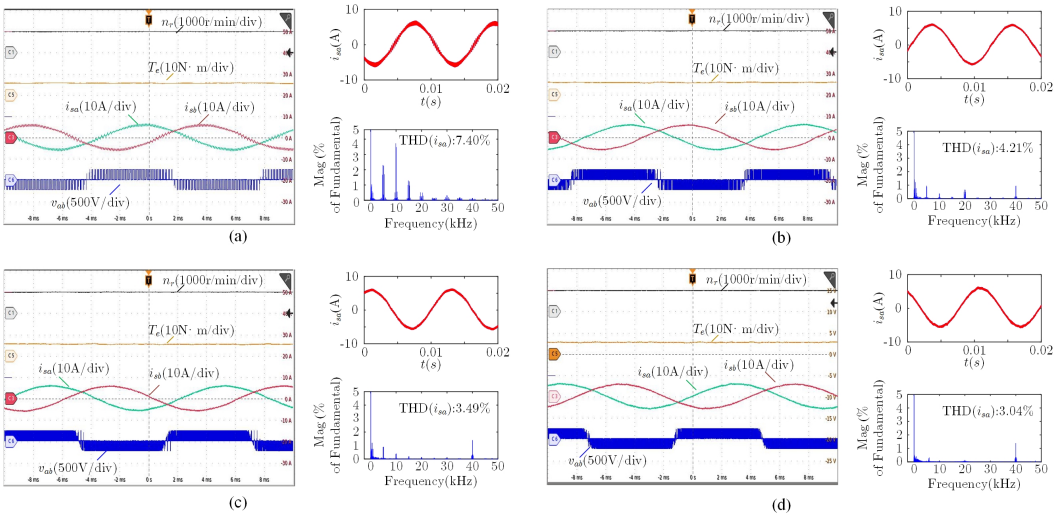

Figure 5.19: Experimental results of the motor speed (1000r/min), electromagnetic torque (5N·m), stator current, and line-to-line voltage inverter output V_{ab} (a) SRCCS-MPC (5kHz S/I frequency and switching frequency). (b) N=4 case MRCCS-MPC (5kHz S/I frequency and 20kHz switching frequency). (c) N=8 case MRCCS-MPC (5kHz S/I frequency and 40kHz switching frequency). (d) SRCCS-MPC (40kHz S/I frequency and switching frequency).

and the THD is 7.40%. The sparse line-to-line voltage pulse also reflects the low switching frequency. The performance of the MRCCS-MPC (N=4 case) is shown in Fig. 5.19(b), the switching ripples of the stator current are effectively reduced compared to Fig. 5.19(a) and the THD has been reduced to 4.21%. The reason is that the switching frequency is enhanced to 20kHz. Also, the voltage pulse becomes denser. Furthermore, Fig. 5.19(c) gives the waveform of the MRCCS-MPC (N=8 case), where the switching frequency reaches 40kHz. As expected, the switching ripples of stator current are continuously reduced and 3.49% THD is obtained, which is beneficial to the improvement of motor efficiency and noise reduction. To show the effectiveness of the improved switching frequency, the SRCCS-MPC scheme with directly enhanced 40kHz S/I frequency is presented in Fig. 5.19(d) as the benchmark for comparison. It can be seen that the MRCCS-MPC (N=8) case in Fig. 5.19(c) shows comparable performance with that in Fig. 5.19(d), which proves the strength of the proposed strategy in terms of the switching frequency improvement.

Fig. 5.20 shows the dynamic response of PMSM with two tests. The left one shows the load torque changing from 0N·m to 5N·m and the other

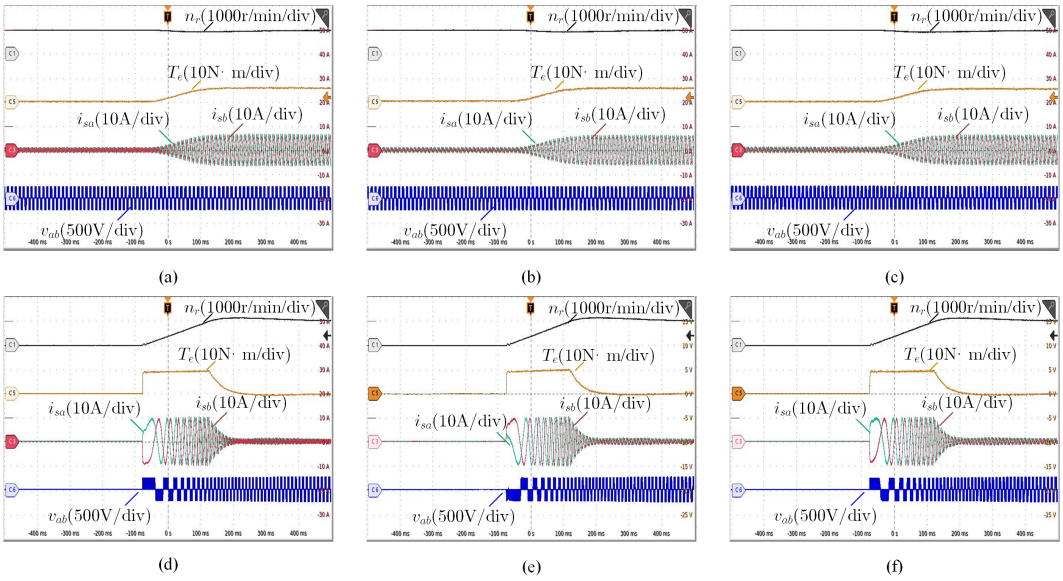

Figure 5.20: Dynamic response of PMSM with load torque change and start-up process. (a) SRCCS-MPC (5kHz S/I frequency and load torque change). (b) N=4 case MRCCS-MPC (load torque change). (c) N=8 case MR-MPC (load torque change). (d) SRCCS-MPC (5kHz S/I frequency and start-up process). (e) N=4 case MRCCS-MPC (start-up process). (f) N=8 case MRCCS-MPC (start-up process).

is PMSM speeding up from standstill state to 1000r/min rotor speed. From the experimental waveform, it can be seen that all of the MPC schemes show similar performance and the proposed multi-rate technique has no negative effect on the dynamic response.

Fig. 5.21 shows the execution time of each control scheme measured by the dSPACE Profiler. The available computational period for SRCCS-MPC (5kHz), MRCCS-MPC (N=4), and MRCCS-MPC (N=8) are all 200μs. As can be seen, these three schemes need 18.68μs, 21.52μs, and 28.76μs to finish the interrupt tasks respectively. As a comparison, the computation time of the classical PI-based control scheme is 15.19μs. The interrupt tasks of the MPC scheme include measurement sampling of stator currents, speeds, data filtering, and processing, input solving algorithm and outer speed loop, protection module, modulator, and pulse emission, etc. Although the MRCCS-MPC (N=8) costs the additional 10μs within each S/I interval, the percent of the interrupt occupancy 12.88% is still tiny, and abundant computational resource remains. When the S/I frequency of SRCCS-MPC is enhanced to 40kHz, the 25μs computational period implies 73.12% of interrupt has been used, which might be

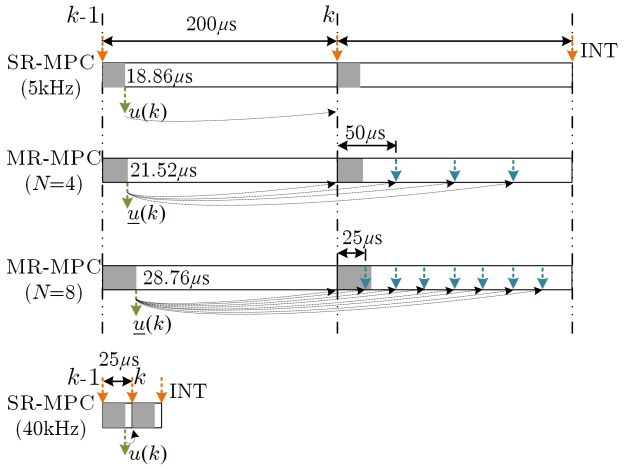

Figure 5.21: The computational time comparison of the MPC interrupt task.

overload for a more complex power converter case and more functions requirement. Besides, the proposed MRCCS-MPC can be potentially operated with a switching frequency higher than 40kHz which is difficult for the SRCCS-MPC. The proposed MRCCS-MPC effectively enhances the switching frequency with a quite long S/I interval maintained, which solves the computational burden issue of the high S/I frequency in the SRCCS-MPC scheme.

The proposed MRCCS-MPC scheme can enhance the switching frequency of power converter by increasing the number of N, i.e., the switching-to-S/I-frequency ratio. Since the predictive process within each control interval is executed in an open-loop manner, the cumulative prediction error caused by parameter mismatch will be increase as N increase. In the PMSM drive system, the value of stator resistance, inductance, and permanent flux are the key parameters that will affect the prediction accuracy. In this work, the permanent flux is estimated into the lumped disturbance by the observer. Therefore, the system performance and stability under the resistance and inductance mismatch situation are investigated. For the SRCCS-MPC and proposed MRCCS-MPC (N=8), Fig. 5.22 and Fig. 5.23 show the steady-state performance of these two controllers when the ±40% value variation of the resistance and inductance occur respectively. It can be seen that the system is always stable without obvious differences from the regular case. The proposed MRCCS-MPC also shows similar strong robustness to both the resistance and

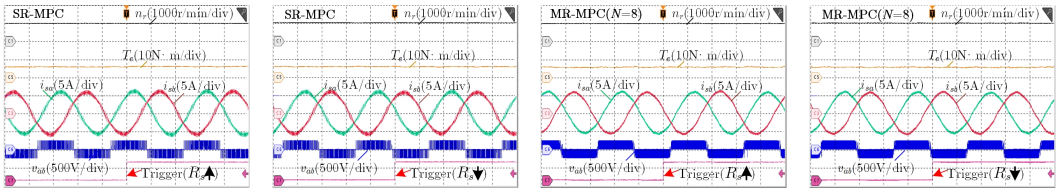

Figure 5.22: Experimental test of the PMSM with stator resistance mismatch (motor speed 1000r/min, electromagnetic torque 5N·m) (a) SR-MPC with 140% resistance used value. (b) SR-MPC with 60% resistance value. (c) N=8 case MR-MPC with 140% resistance value. (d) N=8 case MR-MPC with 60% resistance value.

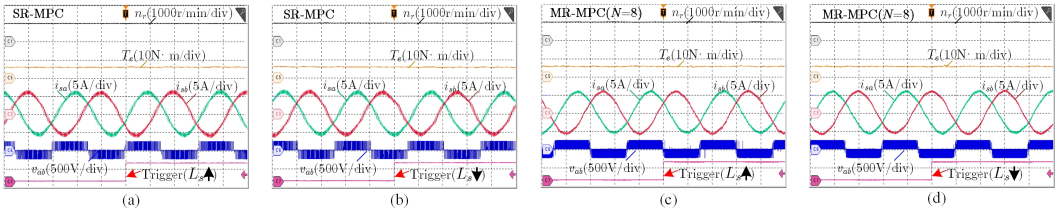

Figure 5.23: Experimental test of the PMSM with stator inductance mismatch (motor speed 1000r/min, electromagnetic torque 5N·m) (a) SR-MPC with 140% inductance value. (b) SR-MPC with 60% inductance value. (c) N=8 case MR-MPC with 140% inductance value. (d) N=8 case MR-MPC with 60% inductance value.

inductance as the typical SRCCS-MPC scheme.

The closed-loop poles of the system in the discrete domain can be drawn according to (5.52). Fig. 5.24 shows the repeated closed-loop poles using SRCCS-MPC and MRCCS-MPC (N=8) scheme when the ±40% value variation of the resistance and inductance occur respectively. With accurate system parameters, the closed-loop poles of both the SRCCS-MPC and MRCCS-MPC are placed at the origin, which endows the MPC scheme with the fast dynamic response property. On the other hand, the closed-loop poles will be moved away from the origin with the mismatch parameters used. It can be seen that the system stability can be guaranteed with all closed-loop poles lain within the unit circle on the z-plane. The mismatch of inductance has more effect on the system performance than that of resistance. The proposed MRCCS-MPC shows strong robustness to the parameter mismatch and the system stability can be checked with the closed-loop poles.

Theoretically, the value of N can be infinite. The larger the value of N, the higher the switching frequency and the better system performance. However, the value of N is restricted by several factors in digital realization. The first

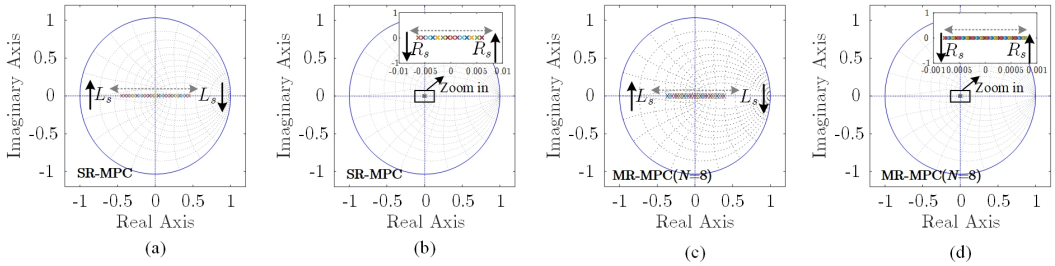

Figure 5.24: The root loci of the closed-loop model with 0% to ±40% stator resistance and inductance mismatch. (a) SR-MPC with 0% to ±40% stator inductance mismatch. (b) SR-MPC with 0% to ±40% resistance mismatch. (c) MR-MPC(N=8) with 0% to ±40% stator inductance mismatch. (d) MR-MPC(N=8) with 0% to ±40% resistance mismatch.

one is the computational capability of the digital processor. With larger N adopted, more computational power is required to solve the optimized lifting input sequence. Secondly, the parameter mismatch will affect the prediction accuracy and the cumulative error becomes larger in the lifting model. Therefore, to enhance the system robustness and make the increase of N more efficient, existing methods dealing with parameters can be built into the proposed MRCCS-MPC scheme, such as the disturbance observer [129], adaptive reference tracking [130], the increment modeling [131] and the feedback self-correction [132]. In practical application, it is recommended to reasonably utilize the computing resources. To further increase the switching frequency, the selection of N can be determined based on a higher S/I frequency, such as 10kHz. Therefore, the proposed MRCCS-MPC provides a flexible parameter combination for the power converter.

5.6 Summary

The application of the MPC scheme for the emerging WBG device-based power converter is always a challenge, where the high switching frequency demand requires a short interrupt interval and may cause the concern of computational overload. Particularly, the low switching frequency is another common challenge of the typical FCS-MPC framework due to the limitations of sampling rates. Therefore, this chapter contributes to a improved form of typical FCS-MPC, which can solve this drawback effectively. The proposed MRFCS-

MPC maintains the advantage of typical FCS-MPC, which can handle complex and nonlinear control objectives. The fast rate control signals are applied within each sampling interval, and the recursive solving process is adopted with a good tradeoff between the computational burden and optimized system performance. From the case study, it has been verified that the proposed MRFCS-MPC can significantly improve system performance, which suits the power converter with high switching frequency operation. The MRFCS-MPC still reserve enough computational margin in the digital controller, which can be assigned to other process design for multi-functional requirements in power converters application. Therefore, the proposed MRFCS-MPC shows great flexibility and scalability.

On the other hand, the multi-rate control input update technique is designed into the CCS-MPC framework, i.e, the MRCCS-MPC, which can effectively enhance the power converter switching frequency, and only a low interrupt frequency is needed in the DSPs. In this case, the quite long interrupt period allows the easy realization of the control algorithm and remains an abundant computational margin. The general formulation of the long-horizon prediction and the receding horizon-based control law is derived. The proposed MRCCS-MPC has been verified on a two-level SiC MOSFET inverter-fed PMSM drive system and it can also be applied to the grid-connected occasion and multi-level converter case. The MRCCS-MPC also shows advantages over the MRFCS-MPC type in terms of the more efficient and optimal solving process for the lifting control input.

The proposed MR-MPC stands for a general formulation of MPC, which not only facilitates the high switching frequency operation in the DSPs but also contributes to the theoretical development of the MPC applied to power converters. Although the two-level VSC is taken as the case study in this chapter, this new tool can be universally applied to other converter topologies with high switching frequency demand.

Chapter 6

Conclusions and Future plans

MPC has been an attractive solution to power converters and industrial drives with provided benefits including the intuitive concept, fast dynamic response, multivariable control capability, nonlinear objective handling ability, etc. This thesis thus uses the MPC to address the dominant control challenges that remain unsolved in industrial drives and show new contributions compared to the existing solutions. Specifically, the industrial MV CSCs and low-power VSCs-fed motor drive applications are focused and the objective includes the improvement of the power quality for the grid-side application, guaranteed stability for the motor-side application with output LC filter, the system optimization in the BTB converter structure, including the CM resonance mitigation in the transformerless CSCs application and the dc-link capacitor RMS current reduction in the VSCs-fed drive system, and finally the computational facilitation of the high switching frequency operation for the WBG power converters.

6.1 Conclusion and Thesis Contribution

The conclusion and the contribution of this thesis can be summarized into two categories based on the MV CSCs and low-power VSCs applications.

1) **Developing FCS-MPC for MV CSCs-fed drive application with improved resonance damping, good harmonic rejection ability, enhanced robustness, and CM resonance mitigation and VSCs-fed drives with reduced dc-link capacitor current**.

In chapter 2, the FCS-MPC is designed for the transformerless CSCs-fed drive system. Different from the conventional virtual-impedance-based active damping principle, the FCS-MPC directly regulated the inductor current and capacitor voltage through the cost function to mitigate the second-order resonance at the grid-connected CSR and CSI-fed motor side. Thus, lower control complexity and computational burden can be achieved through the proposed method. Besides, the low-order harmonic can be rejected by including the selective harmonic feedback into the cost function, and the sinusoidal current can be maintained under distorted grid conditions. To enhance the robustness of FCS-MPC applied to CSR, the disturbance observer is designed to estimate the unknown disturbance and capacitor voltage reference. The long prediction horizon FCS-MPC with only grid current feedback benefit is also revealed. On the other hand, the CMV effect on the transformerless CSC system and the CM resonance in both the high-speed region and low-speed region has been analyzed. The CSI-side cost function with switchable items, i.e, the peak-to-peak magnitude of CMV or the third-order harmonic component of CMV is developed to solve the CM resonance. The reduced CM current contributes to a lower size CM choke. In chapter 3, the FCS-MPC is proposed to reduce the capacitor RMS current in the BTB VSCs-fed VSD system, which can extend the designed capacitor lifespan or reduce the dc-link size with improved power density. The synchronous carriers-based SVPWM scheme cannot eliminate the carrier sideband component and it cannot suit all of the operation points of the motor. In the proposed FCS-MPC, the direct switching pulse generation without using the carrier gives a distinctive capacitor current spectrum and the possible current pulse cancellation between the VSR and VSI sides can be conveniently designed through the cost function. The simulated and experimental results highlight the effectiveness and benefits of the proposed method in terms of 20%-35% capacitor RMS current reduction compared to the typical synchronous carrier-based PWM scheme.

2) **Developing hybrid MPC for high-order VSCs-fed drive system with faster dynamic response, simplified tuning procedure and satisfactory resonance damping.**

In chapter 4, for the grid-connected VSCs application with LCL filter, the CCS-MPC is designed because of the benefits including the constant and convenient configuration of the switching frequency. The guaranteed system stability can be achieved with explicit weighting factors design. The proposed CCS-MPC not only keeps a good injected grid current quality but also shows a significantly faster dynamic response than the conventional capacitor-current-based active damping scheme. On the other hand, for the LC filtered VSCs-fed VSD application, the FCS-MPC is designed to realize the speed command tracking while suppressing the filter resonance simultaneously. The trajectory of state variables is intuitively revealed in the time domain. The experimental results prove that the proposed FCS-MPC scheme can achieve a motor-friendly waveform and overcome the resonance problem effectively. The robustness of the controller to parameter variations of the filter is also verified.

3) **Developing MPC incorporated with the multi-rate technique for the high switching frequency power converter with the reduced computational difficulty.**

Although it is desirable to exploit the benefits provided by SiC and GaN devices, the expected high switching frequency in power converters is always a great challenge for the controller design. The reason is that the sampling/interrupt interval is too short for digital signal processors to accomplish heavy interrupt tasks. In chapter 5, the MR-MPC is developed to ease such a computational issue brought by the high switching frequency operation for the WBG switching device. The multi-rate technique enables the S/I trigger and switching device transition to be performed at different rates. Compared to the typical MPC schemes, the main feature of the proposed MR-MPC is that the high-dimension control sequence is solved and applied within each S/I interval. As a result, the high switching frequency objective can be easily achieved with a low S/I frequency configuration (long available period for computation), which can significantly relieve the execution of the heavy interrupt tasks in DSPs. The multi-rate technique has been applied to both the typical FCS-MPC and the CCS-MPC framework in combination with their respective characteristics, and the lifting modeling process and distinctive solving

procedure for the control input have been developed.

6.2 Future Work

The future works are suggested to focus on the following topics.

1) **Analyzing explicit stability for the FCS-MPC.**

Unlike the conventional PWM-based control, the FCS-MPC does not give an explicit formulation of the control input, which makes characterizing the resulting closed-loop performance a nontrivial task. However, the stability issue is indispensable in power converter applications. A study using the Lyapunov stability concepts is carried out to design the cost function that satisfies the requirement for the state variable tracking error as well as the guaranteed stability [133]. Another approach is to convert the Lyapunov function as a constraint in the FCS-MPC, which filters the discrete control input resulting in instability in advance [134]. Despite these improvements, the stability of FCS-MPC still needs to be further explored, especially with more control objectives involved in the cost function.

2) **Developing efficient tuning tools for the weighting factor selection.**

The cost function endows MPC with great flexibility to deal with multiple control objectives, where the weighting factors are adopted to connect those items with different physical nature. However, how to design the weighting factors to achieve optimal balance is not trivial, especially with the increased number of control objectives. Currently, the simulation-based trial-and-error approach is commonly used, which shows limited performance and is time-consuming. A genetic algorithm is proposed to speed up the weighting factor tuning process but more time-consuming simulated work is required [135]. With the development of artificial intelligence (AI), the artificial neural network (ANN) shows a promising ability to optimize the weighting factor [136]. However, how to obtain sufficient data to train the network is required to be considered first. Nevertheless, these more efficient tools give new insight into the automatic design of the weighting factor, which can be considered a

potential solution in future tuning work.

3) **Optimizing the computational burden for the MPC with long prediction horizon.**

The longer prediction horizon-based FCS-MPC brings improvements for power converter applications [15]. Especially, for the high-order system, the long predictive horizon improves the current quality and reduces the harmonic distortion [137]. To facilitate the realization of FCS-MPC with a long prediction horizon length, advanced branch and bound searching processes, such as the sphere decoding method have been applied [98]. Despite this, it is still a far distance to apply the sphere decoding method in general DSPs. Further optimization of the sphere decoding method is still required and more efficient searching algorithms are also welcome to be developed and can be applied to the power converters. In the future, it is desired to discover more about the benefits of applying long prediction horizon FCS-MPC to power converters while developing the corresponding algorithm for practical digital realization.

4) **Developing efficient solving procedures for MPC problems with constraints.**

The CCS-MPC scheme enables an easier realization of the long horizon prediction and the constant switching frequency. However, the optimized control law derived is the typical kind of unconstrainted solution. In practical power converter applications, the constraints are usually imposed on the state variables and control inputs, particularly subjects to the transient operation or large-signal disturbance. With regard to multiple constraints, the CCS-MPC scheme is required to solve the quadratic programming (QP) problem online [119]. In this case, the computational burden will significantly increase, which is difficult to be realized in the DSPs. Therefore, an efficient solving algorithm is worthy to be developed in the future for the constrained case to improve the reliability of MPC.

5) **Model-free structure-based predictive control design with enhanced robustness.**

Most existing MPC schemes for power converters or motor drives are highly dependent on well-known system parameters. Also, with a more large-scale

power system as the control object, the modeling process becomes extremely complex. To this end, data-driven or AI-based predictive control might be a good future research topic [138]–[140]. Instead of focusing on the explicit modeling process, the prediction can be based on machine learning algorithms such as neural networks or support vector machines. In this case, more complex and nonlinear systems, which may be difficult to model using traditional techniques, can be handled by AI-based black box. Besides, it also has the potential to adapt to changing operating conditions and to learn from experience, improving its performance over time.

References

[1] J. D. van Wyk and F. C. Lee, "On a future for power electronics," *IEEE Journal of Emerging and Selected Topics in Power Electronics*, vol. 1, no. 2, pp. 59–72, 2013.

[2] J. G. Kassakian and T. M. Jahns, "Evolving and emerging applications of power electronics in systems," *IEEE Journal of Emerging and Selected Topics in Power Electronics*, vol. 1, no. 2, pp. 47–58, 2013.

[3] R. W. Erickson and D. Maksimovic, *Fundamentals of power electronics*. Springer Science & Business Media, 2007.

[4] F. Blaabjerg, Z. Chen, and S. Kjaer, "Power electronics as efficient interface in dispersed power generation systems," *IEEE Transactions on Power Electronics*, vol. 19, no. 5, pp. 1184–1194, 2004.

[5] X. Wang, F. Blaabjerg, and W. Wu, "Modeling and analysis of harmonic stability in an ac power-electronics-based power system," *IEEE Transactions on Power Electronics*, vol. 29, no. 12, pp. 6421–6432, 2014.

[6] F. Blaabjerg, R. Teodorescu, M. Liserre, and A. Timbus, "Overview of control and grid synchronization for distributed power generation systems," *IEEE Transactions on Industrial Electronics*, vol. 53, no. 5, pp. 1398–1409, 2006.

[7] B. K. Bose, "Power electronics and motor drives recent progress and perspective," *IEEE Transactions on Industrial Electronics*, vol. 56, no. 2, pp. 581–588, 2009.

[8] W. Lee, S. Li, D. Han, B. Sarlioglu, T. A. Minav, and M. Pietola, "A review of integrated motor drive and wide-bandgap power electronics for high-performance electro-hydrostatic actuators," *IEEE Transactions on Transportation Electrification*, vol. 4, no. 3, pp. 684–693, 2018.

[9] W. Cai and F. Yi, "An integrated multiport power converter with small capacitance requirement for switched reluctance motor drive," *IEEE Transactions on Power Electronics*, vol. 31, no. 4, pp. 3016–3026, 2016.

[10] C. Jacobina, M. de Rossiter Correa, E. da Silva, and A. Lima, "Induction motor drive system for low-power applications," *IEEE Transactions on Industry Applications*, vol. 35, no. 1, pp. 52–61, 1999.

[11] H. Wang, M. Liserre, and F. Blaabjerg, "Toward reliable power electronics: Challenges, design tools, and opportunities," *IEEE Industrial Electronics Magazine*, vol. 7, no. 2, pp. 17–26, 2013.

[12] J. Harikumaran, G. Buticchi, G. Migliazza, *et al.*, "Failure modes and reliability oriented system design for aerospace power electronic converters," *IEEE Open Journal of the Industrial Electronics Society*, vol. 2, pp. 53–64, 2021.

[13] L. de Lillo, L. Empringham, P. W. Wheeler, *et al.*, "Multiphase power converter drive for fault-tolerant machine development in aerospace applications," *IEEE Transactions on Industrial Electronics*, vol. 57, no. 2, pp. 575–583, 2010.

[14] S. Vazquez, J. Rodriguez, M. Rivera, L. G. Franquelo, and M. Norambuena, "Model predictive control for power converters and drives: Advances and trends," *IEEE Transactions on Industrial Electronics*, vol. 64, no. 2, pp. 935–947, 2017.

[15] T. Geyer, *Model predictive control of high power converters and industrial drives*. John Wiley & Sons, 2016.

[16] J. Rodriguez and P. Cortes, *Predictive control of power converters and electrical drives*. John Wiley & Sons, 2012.

[17] I. Takahashi and Y. Ohmori, "High-performance direct torque control of an induction motor," *IEEE Transactions on Industry Applications*, vol. 25, no. 2, pp. 257–264, 1989.

[18] T. Noguchi, H. Tomiki, S. Kondo, and I. Takahashi, "Direct power control of pwm converter without power-source voltage sensors," *IEEE Transactions on Industry Applications*, vol. 34, no. 3, pp. 473–479, 1998.

[19] M. Malinowski, M. Kazmierkowski, and A. Trzynadlowski, "A comparative study of control techniques for pwm rectifiers in ac adjustable speed drives," *IEEE Transactions on Power Electronics*, vol. 18, no. 6, pp. 1390–1396, 2003.

[20] G. Singh, K. Nam, and S. Lim, "A simple indirect field-oriented control scheme for multiphase induction machine," *IEEE Transactions on Industrial Electronics*, vol. 52, no. 4, pp. 1177–1184, 2005.

[21] D. Casadei, F. Profumo, G. Serra, and A. Tani, "Foc and dtc: Two viable schemes for induction motors torque control," *IEEE Transactions on Power Electronics*, vol. 17, no. 5, pp. 779–787, 2002.

[22] T. Dragičević, S. Vazquez, and P. Wheeler, "Advanced control methods for power converters in dg systems and microgrids," *IEEE Transactions on Industrial Electronics*, vol. 68, no. 7, pp. 5847–5862, 2021.

[23] C. E. Garcia, D. M. Prett, and M. Morari, "Model predictive control: Theory and practice—a survey," *Automatica*, vol. 25, no. 3, pp. 335–348, 1989.

[24] S. Kouro, P. Cortes, R. Vargas, U. Ammann, and J. Rodriguez, "Model predictive control—a simple and powerful method to control power converters," *IEEE Transactions on Industrial Electronics*, vol. 56, no. 6, pp. 1826–1838, 2009.

[25] P. Karamanakos and T. Geyer, "Guidelines for the design of finite control set model predictive controllers," *IEEE Transactions on Power Electronics*, vol. 35, no. 7, pp. 7434–7450, 2020.

[26] M. Intelligence, *Industrial motors market-growth, trends, COVID-19 impact, and forecasts (2022-2027)*. 2021.

[27] B. Wu and M. Narimani, *High-power converters and AC drives*. John Wiley & Sons, 2017.

[28] H. Abu-Rub, S. Bayhan, S. Moinoddin, M. Malinowski, and J. Guzinski, "Medium-voltage drives: Challenges and existing technology," *IEEE Power Electronics Magazine*, vol. 3, no. 2, pp. 29–41, 2016.

[29] M. P. Kazmierkowski, L. G. Franquelo, J. Rodriguez, M. A. Perez, and J. I. Leon, "High-performance motor drives," *IEEE Industrial Electronics Magazine*, vol. 5, no. 3, pp. 6–26, 2011.

[30] A. Emadi, Y. J. Lee, and K. Rajashekara, "Power electronics and motor drives in electric, hybrid electric, and plug-in hybrid electric vehicles," *IEEE Transactions on Industrial Electronics*, vol. 55, no. 6, pp. 2237–2245, 2008.

[31] N. Mohan, T. M. Undeland, and W. P. Robbins, *Power electronics: converters, applications, and design*. John wiley & sons, 2003.

[32] E. P. Wiechmann, P. Aqueveque, R. Burgos, and J. Rodriguez, "On the efficiency of voltage source and current source inverters for high-power drives," *IEEE Transactions on Industrial Electronics*, vol. 55, no. 4, pp. 1771–1782, 2008.

[33] W. Liang, J. Wang, P. C.-K. Luk, W. Fang, and W. Fei, "Analytical modeling of current harmonic components in pmsm drive with voltage-source inverter by svpwm technique," *IEEE Transactions on Energy Conversion*, vol. 29, no. 3, pp. 673–680, 2014.

[34] X. del Toro Garcia, A. Arias, M. G. Jayne, and P. A. Witting, "Direct torque control of induction motors utilizing three-level voltage source inverters," *IEEE Transactions on Industrial Electronics*, vol. 55, no. 2, pp. 956–958, 2008.

[35] S. Yin, K. J. Tseng, R. Simanjorang, Y. Liu, and J. Pou, "A 50-kw high-frequency and high-efficiency sic voltage source inverter for more electric aircraft," *IEEE Transactions on Industrial Electronics*, vol. 64, no. 11, pp. 9124–9134, 2017.

[36] N. Abdel-Rahim and J. Quaicoe, "Analysis and design of a multiple feedback loop control strategy for single-phase voltage-source ups inverters," *IEEE Transactions on Power Electronics*, vol. 11, no. 4, pp. 532–541, 1996.

[37] J. Rodriguez, J.-S. Lai, and F. Z. Peng, "Multilevel inverters: A survey of topologies, controls, and applications," *IEEE Transactions on Industrial Electronics*, vol. 49, no. 4, pp. 724–738, 2002.

[38] B. Wu, J. Pontt, J. Rodriguez, S. Bernet, and S. Kouro, "Current-source converter and cycloconverter topologies for industrial medium-voltage drives," *IEEE Transactions on Industrial Electronics*, vol. 55, no. 7, pp. 2786–2797, 2008.

[39] J. Esch, "High-power wind energy conversion systems: State-of-the-art and emerging technologies," *Proceedings of the IEEE*, vol. 103, no. 5, pp. 736–739, 2015.

[40] R. E. Torres-Olguin, A. Garces, M. Molinas, and T. Undeland, "Integration of offshore wind farm using a hybrid hvdc transmission composed by the pwm current-source converter and line-commutated converter," *IEEE Transactions on Energy Conversion*, vol. 28, no. 1, pp. 125–134, 2013.

[41] J. Millán, P. Godignon, X. Perpiñà, A. Pérez-Tomás, and J. Rebollo, "A survey of wide bandgap power semiconductor devices," *IEEE Transactions on Power Electronics*, vol. 29, no. 5, pp. 2155–2163, 2014.

[42] K. Shenai, "Future prospects of widebandgap (wbg) semiconductor power switching devices," *IEEE Transactions on Electron Devices*, vol. 62, no. 2, pp. 248–257, 2015.

[43] A. K. Morya, M. C. Gardner, B. Anvari, *et al.*, "Wide bandgap devices in ac electric drives: Opportunities and challenges," *IEEE Transactions on Transportation Electrification*, vol. 5, no. 1, pp. 3–20, 2019.

[44] Y. W. Li, "Control and resonance damping of voltage-source and current-source converters with *LC* filters," *IEEE Transactions on Industrial Electronics*, vol. 56, no. 5, pp. 1511–1521, 2009.

[45] J. Wiseman and B. Wu, "Active damping control of a high-power pwm current-source rectifier for line-current thd reduction," *IEEE Transactions on Industrial Electronics*, vol. 52, no. 3, pp. 758–764, 2005.

[46] F. Liu, B. Wu, N. R. Zargari, and M. Pande, "An active damping method using inductor-current feedback control for high-power pwm current-source rectifier," *IEEE Transactions on Power Electronics*, vol. 26, no. 9, pp. 2580–2587, 2011.

[47] Z. Bai, H. Ma, D. Xu, B. Wu, Y. Fang, and Y. Yao, "Resonance damping and harmonic suppression for grid-connected current-source converter," *IEEE Transactions on Industrial Electronics*, vol. 61, no. 7, pp. 3146–3154, 2014.

[48] H.-J. Lee, S. Jung, and S.-K. Sul, "A current controller design for current source inverter-fed ac machine drive system," *IEEE Transactions on Power Electronics*, vol. 28, no. 3, pp. 1366–1381, 2013.

[49] H. Zhou, Y. W. Li, N. R. Zargari, Z. Cheng, R. Ni, and Y. Zhang, "Selective harmonic compensation (shc) pwm for grid-interfacing high-power converters," *IEEE Transactions on Power Electronics*, vol. 29, no. 3, pp. 1118–1127, 2014.

[50] N. Zhu, D. Xu, B. Wu, N. R. Zargari, M. Kazerani, and F. Liu, "Common-mode voltage reduction methods for current-source converters in medium-voltage drives," *IEEE Transactions on Power Electronics*, vol. 28, no. 2, pp. 995–1006, 2013.

[51] J. Shang and Y. W. Li, "A space-vector modulation method for common-mode voltage reduction in current-source converters," *IEEE Transactions on Power Electronics*, vol. 29, no. 1, pp. 374–385, 2014.

[52] B. Wu, S. Rizzo, N. Zargari, and Y. Xiao, "An integrated dc link choke for elimination of motor common-mode voltage in medium voltage drives," in *Conference Record of the 2001 IEEE Industry Applications Conference. 36th IAS Annual Meeting (Cat. No.01CH37248)*, vol. 3, 2001, 2022–2027 vol.3.

[53] Y. Lian, Y. Zhang, Y. Wei Li, N. R. Zargari, and Z. Cheng, "Common-mode resonance suppression in transformerless pwm current-source drive," *IEEE Transactions on Power Electronics*, vol. 31, no. 8, pp. 5721–5731, 2016.

[54] H. Wang and F. Blaabjerg, "Reliability of capacitors for dc-link applications in power electronic converters—an overview," *IEEE Transactions on Industry Applications*, vol. 50, no. 5, pp. 3569–3578, 2014.

[55] H. Wen, W. Xiao, X. Wen, and P. Armstrong, "Analysis and evaluation of dc-link capacitors for high-power-density electric vehicle drive systems," *IEEE Transactions on Vehicular Technology*, vol. 61, no. 7, pp. 2950–2964, 2012.

[56] J. Dannehl, M. Liserre, and F. W. Fuchs, "Filter-based active damping of voltage source converters with LCL filter," *IEEE Transactions on Industrial Electronics*, vol. 58, no. 8, pp. 3623–3633, 2011.

[57] A. Reznik, M. G. Simões, A. Al-Durra, and S. M. Muyeen, "LCL Filter design and performance analysis for grid-interconnected systems," *IEEE Transactions on Industry Applications*, vol. 50, no. 2, pp. 1225–1232, 2014.

[58] M. Liserre, F. Blaabjerg, and S. Hansen, "Design and control of an lcl-filter-based three-phase active rectifier," *IEEE Transactions on Industry Applications*, vol. 41, no. 5, pp. 1281–1291, 2005.

[59] T. Habetler, R. Naik, and T. Nondahl, "Design and implementation of an inverter output lc filter used for dv/dt reduction," *IEEE Transactions on Power Electronics*, vol. 17, no. 3, pp. 327–331, 2002.

[60] V. Dzhankhotov and J. Pyrhönen, "Passive *LC* filter design considerations for motor applications," *IEEE Transactions on Industrial Electronics*, vol. 60, no. 10, pp. 4253–4259, 2013.

[61] P. Mishra and R. Maheshwari, "Design, analysis, and impacts of sinusoidal lc filter on pulsewidth modulated inverter fed-induction motor drive," *IEEE Transactions on Industrial Electronics*, vol. 67, no. 4, pp. 2678–2688, 2020.

[62] X. Yuan, I. Laird, and S. Walder, "Opportunities, challenges, and potential solutions in the application of fast-switching sic power devices and converters," *IEEE Transactions on Power Electronics*, vol. 36, no. 4, pp. 3925–3945, 2021.

[63] I. Jlassi, J. O. Estima, S. Khojet El Khil, N. Mrabet Bellaaj, and A. J. Marques Cardoso, "Multiple open-circuit faults diagnosis in back-to-back converters of pmsg drives for wind turbine systems," *IEEE Transactions on Power Electronics*, vol. 30, no. 5, pp. 2689–2702, 2015.

[64] J.-Z. Zhang, T. Sun, F. Wang, J. Rodríguez, and R. Kennel, "A computationally efficient quasi-centralized dmpc for back-to-back converter pmsg wind turbine systems without dc-link tracking errors," *IEEE Transactions on Industrial Electronics*, vol. 63, no. 10, pp. 6160–6171, 2016.

[65] R. Razi, B. Asaei, and M. R. Nikzad, "A new battery charger for plug-in hybrid electric vehicle application using back to back converter in a utility connected micro-grid," in *2017 8th Power Electronics, Drive Systems & Technologies Conference (PEDSTC)*, 2017, pp. 13–18.

[66] Z. Qin, H. Wang, F. Blaabjerg, and P. C. Loh, "Investigation into the control methods to reduce the dc-link capacitor ripple current in a back-to-back converter," in *2014 IEEE Energy Conversion Congress and Exposition (ECCE)*, 2014, pp. 203–210.

[67] D. Holmes and B. McGrath, "Opportunities for harmonic cancellation with carrier-based pwm for a two-level and multilevel cascaded inverters," *IEEE Transactions on Industry Applications*, vol. 37, no. 2, pp. 574–582, 2001.

[68] C. Bao, X. Ruan, X. Wang, W. Li, D. Pan, and K. Weng, "Step-by-step controller design for lcl-type grid-connected inverter with capacitor–current-feedback active-damping," *IEEE Transactions on Power Electronics*, vol. 29, no. 3, pp. 1239–1253, 2014.

[69] X. Wang, C. Bao, X. Ruan, W. Li, and D. Pan, "Design considerations of digitally controlled lcl-filtered inverter with capacitor- current-feedback active damping," *IEEE Journal of Emerging and Selected Topics in Power Electronics*, vol. 2, no. 4, pp. 972–984, 2014.

[70] D. Pan, X. Ruan, C. Bao, W. Li, and X. Wang, "Capacitor-current-feedback active damping with reduced computation delay for improving robustness of lcl-type grid-connected inverter," *IEEE Transactions on Power Electronics*, vol. 29, no. 7, pp. 3414–3427, 2014.

[71] Y. Tang, P. C. Loh, P. Wang, F. H. Choo, and F. Gao, "Exploring inherent damping characteristic of lcl-filters for three-phase grid-connected voltage source inverters," *IEEE Transactions on Power Electronics*, vol. 27, no. 3, pp. 1433–1443, 2012.

[72] M. Xue, Y. Zhang, Y. Kang, Y. Yi, S. Li, and F. Liu, "Full feedforward of grid voltage for discrete state feedback controlled grid-connected inverter with lcl filter," *IEEE Transactions on Power Electronics*, vol. 27, no. 10, pp. 4234–4247, 2012.

[73] W. Li, X. Ruan, D. Pan, and X. Wang, "Full-feedforward schemes of grid voltages for a three-phase LCL-type grid-connected inverter," *IEEE Transactions on Industrial Electronics*, vol. 60, no. 6, pp. 2237–2250, 2013.

[74] Y. Zhang and C. Qu, "Model predictive direct power control of pwm rectifiers under unbalanced network conditions," *IEEE Transactions on Industrial Electronics*, vol. 62, no. 7, pp. 4011–4022, 2015.

[75] T. Zhao, J. Wang, A. Q. Huang, and A. Agarwal, "Comparisons of sic mosfet and si igbt based motor drive systems," in *2007 IEEE Industry Applications Annual Meeting*, 2007, pp. 331–335.

[76] D. Zhang, J. He, and D. Pan, "A megawatt-scale medium-voltage high-efficiency high power density "sic+si" hybrid three-level anpc inverter for aircraft hybrid-electric propulsion systems," *IEEE Transactions on Industry Applications*, vol. 55, no. 6, pp. 5971–5980, 2019.

[77] J. Steinke, "Use of an lc filter to achieve a motor-friendly performance of the pwm voltage source inverter," *IEEE Transactions on Energy Conversion*, vol. 14, no. 3, pp. 649–654, 1999.

[78] M. F. Rahman, P. Niknejad, and M. R. Barzegaran, "Comparing the performance of si igbt and sic mosfet switches in modular multilevel converters for medium voltage pmsm speed control," in *2018 IEEE Texas Power and Energy Conference (TPEC)*, 2018, pp. 1–6.

[79] K. Kumar, "Efficiency improvement of three phase traction inverter through gan devices for pmsm," in *2016 IEEE International Conference on Power Electronics, Drives and Energy Systems (PEDES)*, 2016, pp. 1–6.

[80] M. S. Diab and X. Yuan, "A quasi-three-level pwm scheme to combat motor overvoltage in sic-based single-phase drives," *IEEE Transactions on Power Electronics*, vol. 35, no. 12, pp. 12 639–12 645, 2020.

[81] A. von Jouanne and P. Enjeti, "Design considerations for an inverter output filter to mitigate the effects of long motor leads in asd applications," *IEEE Transactions on Industry Applications*, vol. 33, no. 5, pp. 1138–1145, 1997.

[82] B. Liu, R. Ren, Z. Zhang, F. Wang, and D. Costinett, "A sampling scheme for three-phase high switching frequency and speed converter," in *2018 IEEE Applied Power Electronics Conference and Exposition (APEC)*, 2018, pp. 3031–3035.

[83] W. Tu, G. Luo, Z. Chen, C. Liu, and L. Cui, "Fpga implementation of predictive cascaded speed and current control of pmsm drives with two-time-scale optimization," *IEEE Transactions on Industrial Informatics*, vol. 15, no. 9, pp. 5276–5288, 2019.

[84] C. Xue, L. Ding, Y. Li, and N. R. Zargari, "Improved model predictive control for high-power current-source rectifiers under normal and distorted grid conditions," *IEEE Transactions on Power Electronics*, vol. 35, no. 5, pp. 4588–4601, 2020.

[85] N. Panten, N. Hoffmann, and F. W. Fuchs, "Finite control set model predictive current control for grid-connected voltage-source converters with lcl filters: A study based on different state feedbacks," *IEEE Transactions on Power Electronics*, vol. 31, no. 7, pp. 5189–5200, 2016.

[86] S. Nalakath, Y. Sun, M. Preindl, and A. Emadi, "Optimization-based position sensorless finite control set model predictive control for ipmsms," *IEEE Transactions on Power Electronics*, vol. 33, no. 10, pp. 8672–8682, 2018.

[87] P. Cortes, J. Rodriguez, C. Silva, and A. Flores, "Delay compensation in model predictive current control of a three-phase inverter," *IEEE Transactions on Industrial Electronics*, vol. 59, no. 2, pp. 1323–1325, 2012.

[88] P. Correa and J. Rodriguez, "A predictive control scheme for current source rectifiers," *2008 13th International Power Electronics and Motion Control Conference*, pp. 699–702, 2008.

[89] H. Gao, B. Wu, D. Xu, and N. R. Zargari, "A model predictive power factor control scheme with active damping function for current source rectifiers," *IEEE Transactions on Power Electronics*, vol. 33, no. 3, pp. 2655–2667, 2018.

[90] A. Nabae and T. Tanaka, "A new definition of instantaneous active-reactive current and power based on instantaneous space vectors on polar coordinates in three-phase circuits," *IEEE Transactions on Power Delivery*, vol. 11, no. 3, pp. 1238–1243, 1996.

[91] P. Cortes, G. Ortiz, J. I. Yuz, J. Rodriguez, S. Vazquez, and L. G. Franquelo, "Model predictive control of an inverter with output *LC* filter for ups applications," *IEEE Transactions on Industrial Electronics*, vol. 56, no. 6, pp. 1875–1883, 2009.

[92] Y. Zhang and H. Yang, "Two-vector-based model predictive torque control without weighting factors for induction motor drives," *IEEE Transactions on Power Electronics*, vol. 31, no. 2, pp. 1381–1390, 2016.

[93] F. Lin, *Robust control design: an optimal control approach*. John Wiley & Sons, 2007.

[94] E. Jacobsen and R. Lyons, "The sliding dft," *IEEE Signal Processing Magazine*, vol. 20, no. 2, pp. 74–80, 2003.

[95] H. A. Young, M. A. Perez, and J. Rodriguez, "Analysis of finite-control-set model predictive current control with model parameter mismatch in a three-phase inverter," *IEEE Transactions on Industrial Electronics*, vol. 63, no. 5, pp. 3100–3107, 2016.

[96] C. K. Chui, G. Chen, *et al.*, *Kalman filtering*. Springer, 2017.

[97] F. M. Callier and C. A. Desoer, *Linear system theory*. Springer Science & Business Media, 2012.

[98] T. Geyer and D. E. Quevedo, "Multistep finite control set model predictive control for power electronics," *IEEE Transactions on Power Electronics*, vol. 29, no. 12, pp. 6836–6846, 2014.

[99] H. Gao, B. Wu, D. Xu, M. Pande, and R. P. Aguilera, "Common-mode-voltage-reduced model-predictive control scheme for current-source-converter-fed induction motor drives," *IEEE Transactions on Power Electronics*, vol. 32, no. 6, pp. 4891–4904, 2017.

[100] D. G. Holmes and T. A. Lipo, *Pulse width modulation for power converters: principles and practice*. John Wiley & Sons, 2003, vol. 18.

[101] S.-M. Yang and C.-H. Lee, "A deadbeat current controller for field oriented induction motor drives," *IEEE Transactions on Power Electronics*, vol. 17, no. 5, pp. 772–778, 2002.

[102] G. Wang, M. Valla, and J. Solsona, "Position sensorless permanent magnet synchronous machine drives—a review," *IEEE Transactions on Industrial Electronics*, vol. 67, no. 7, pp. 5830–5842, 2020.

[103] J. Rodriguez, M. P. Kazmierkowski, J. R. Espinoza, *et al.*, "State of the art of finite control set model predictive control in power electronics," *IEEE Transactions on Industrial Informatics*, vol. 9, no. 2, pp. 1003–1016, 2013.

[104] S. S. Hakami, L. Halabi, and K.-B. Lee, "Dual-carrier-based pwm method for dc-link capacitor lifetime extension in three-level hybrid anpc inverters," *IEEE Transactions on Industrial Electronics*, pp. 1–1, 2022.

[105] X. Lyu, Y. Li, and D. Cao, "Dc-link rms current reduction by increasing paralleled three-phase inverter module number for segmented traction drive," *IEEE Journal of Emerging and Selected Topics in Power Electronics*, vol. 5, no. 1, pp. 171–181, 2017.

[106] A. Tcai, H.-U. Shin, and K.-B. Lee, "Dc-link capacitor-current ripple reduction in dpwm-based back-to-back converters," *IEEE Transactions on Industrial Electronics*, vol. 65, no. 3, pp. 1897–1907, 2018.

[107] L. González, G. Garcerá, E Figueres, and R González, "Effects of the pwm carrier signals synchronization on the dc-link current in back-to-back converters," *Applied Energy*, vol. 87, no. 8, pp. 2491–2499, 2010.

[108] L. Shen, S. Bozhko, G. Asher, C. Patel, and P. Wheeler, "Active dc-link capacitor harmonic current reduction in two-level back-to-back converter," *IEEE Transactions on Power Electronics*, vol. 31, no. 10, pp. 6947–6954, 2016.

[109] L. Shen, S. Bozhko, C. I. Hill, and P. Wheeler, "Dc-link capacitor second carrier band switching harmonic current reduction in two-level back-to-back converters," *IEEE Transactions on Power Electronics*, vol. 33, no. 4, pp. 3567–3574, 2018.

[110] A. Albertsen, "Electrolytic capacitor lifetime estimation," *JIANGHAI Eur. GmbH*, pp. 1–13, 2010.

[111] L. Tarisciotti, P. Zanchetta, A. Watson, J. C. Clare, M. Degano, and S. Bifaretti, "Modulated model predictive control for a three-phase active rectifier," *IEEE Transactions on Industry Applications*, vol. 51, no. 2, pp. 1610–1620, 2015.

[112] Y. Zhang, Y. Peng, and H. Yang, "Performance improvement of two-vectors-based model predictive control of pwm rectifier," *IEEE Transactions on Power Electronics*, vol. 31, no. 8, pp. 6016–6030, 2016.

[113] C. Zheng, T. Dragičević, B. Majmunović, and F. Blaabjerg, "Constrained modulated model-predictive control of an lc-filtered voltage-source converter," *IEEE Transactions on Power Electronics*, vol. 35, no. 2, pp. 1967–1977, 2020.

[114] C. Zheng, T. Dragičević, and F. Blaabjerg, "Current-sensorless finite-set model predictive control for lc-filtered voltage source inverters," *IEEE Transactions on Power Electronics*, vol. 35, no. 1, pp. 1086–1095, 2020.

[115] P. Falkowski and A. Sikorski, "Finite control set model predictive control for grid-connected ac–dc converters with lcl filter," *IEEE Transactions on Industrial Electronics*, vol. 65, no. 4, pp. 2844–2852, 2018.

[116] J. He, Y. W. Li, and M. S. Munir, "A flexible harmonic control approach through voltage-controlled dg–grid interfacing converters," *IEEE Transactions on Industrial Electronics*, vol. 59, no. 1, pp. 444–455, 2012.

[117] Z. Li, Y. Li, P. Wang, H. Zhu, C. Liu, and W. Xu, "Control of three-phase boost-type pwm rectifier in stationary frame under unbalanced input voltage," *IEEE Transactions on Power Electronics*, vol. 25, no. 10, pp. 2521–2530, 2010.

[118] J. Dannehl, F. W. Fuchs, S. Hansen, and P. B. Thøgersen, "Investigation of active damping approaches for pi-based current control of grid-connected pulse width modulation converters with lcl filters," *IEEE Transactions on Industry Applications*, vol. 46, no. 4, pp. 1509–1517, 2010.

[119] L. Wang, *Model predictive control system design and implementation using MATLAB®*. Springer Science & Business Media, 2009.

[120] J. D. Barros and J. F. Silva, "Optimal predictive control of three-phase npc multilevel converter for power quality applications," *IEEE Transactions on Industrial Electronics*, vol. 55, no. 10, pp. 3670–3681, 2008.

[121] D. Zhou, C. Jiang, Z. Quan, and Y. R. Li, "Vector shifted model predictive power control of three-level neutral-point-clamped rectifiers," *IEEE Transactions on Industrial Electronics*, vol. 67, no. 9, pp. 7157–7166, 2020.

[122] K. Ogata, *Discrete-time control systems*. Prentice-Hall, Inc., 1995.

[123] K. Hatua, A. K. Jain, D. Banerjee, and V. T. Ranganathan, "Active damping of output *LC* filter resonance for vector-controlled vsi-fed ac motor drives," *IEEE Transactions on Industrial Electronics*, vol. 59, no. 1, pp. 334–342, 2012.

[124] T. Chen and B. A. Francis, *Optimal sampled-data control systems*. Springer Science & Business Media, 2012.

[125] H. Tian, Y. W. Li, and Q. Zhao, "Multirate harmonic compensation control for low switching frequency converters: Scheme, modeling, and analysis," *IEEE Transactions on Power Electronics*, vol. 35, no. 4, pp. 4143–4156, 2020.

[126] Y. Zhang, D. Xu, J. Liu, S. Gao, and W. Xu, "Performance improvement of model-predictive current control of permanent magnet synchronous motor drives," *IEEE Transactions on Industry Applications*, vol. 53, no. 4, pp. 3683–3695, 2017.

[127] S. G. Petkar, K. Eshwar, and V. K. Thippiripati, "A modified model predictive current control of permanent magnet synchronous motor drive," *IEEE Transactions on Industrial Electronics*, vol. 68, no. 2, pp. 1025–1034, 2021.

[128] X. Zhang, L. Zhang, and Y. Zhang, "Model predictive current control for pmsm drives with parameter robustness improvement," *IEEE Transactions on Power Electronics*, vol. 34, no. 2, pp. 1645–1657, 2019.

[129] S.-K. Kim, D.-K. Choi, K.-B. Lee, and Y. I. Lee, "Offset-free model predictive control for the power control of three-phase ac/dc converters," *IEEE Transactions on Industrial Electronics*, vol. 62, no. 11, pp. 7114–7126, 2015.

[130] Y. Yang, S.-C. Tan, and S. Y. R. Hui, "Adaptive reference model predictive control with improved performance for voltage-source inverters," *IEEE Transactions on Control Systems Technology*, vol. 26, no. 2, pp. 724–731, 2018.

[131] M. Yang, X. Lang, J. Long, and D. Xu, "Flux immunity robust predictive current control with incremental model and extended state observer for pmsm drive," *IEEE Transactions on Power Electronics*, vol. 32, no. 12, pp. 9267–9279, 2017.

[132] Y. Wang, C. Wang, W. Zeng, and F. Bai, "Multifactorial prediction errors analysis and a feedback self-correction on model predictive control for the three-phase inverter," *IEEE Transactions on Industrial Electronics*, vol. 66, no. 5, pp. 3647–3654, 2019.

[133] R. P. Aguilera and D. E. Quevedo, "Predictive control of power converters: Designs with guaranteed performance," *IEEE Transactions on Industrial Informatics*, vol. 11, no. 1, pp. 53–63, 2015.

[134] H. T. Nguyen and J.-W. Jung, "Finite control set model predictive control to guarantee stability and robustness for surface-mounted pm synchronous motors," *IEEE Transactions on Industrial Electronics*, vol. 65, no. 11, pp. 8510–8519, 2018.

[135] P. Zanchetta, "Heuristic multi-objective optimization for cost function weights selection in finite states model predictive control," in *2011 Workshop on Predictive Control of Electrical Drives and Power Electronics*, 2011, pp. 70–75.

[136] T. Dragičević and M. Novak, "Weighting factor design in model predictive control of power electronic converters: An artificial neural network approach," *IEEE Transactions on Industrial Electronics*, vol. 66, no. 11, pp. 8870–8880, 2019.

[137] T. Geyer, P. Karamanakos, and R. Kennel, "On the benefit of long-horizon direct model predictive control for drives with lc filters," in *2014 IEEE Energy Conversion Congress and Exposition (ECCE)*, 2014, pp. 3520–3527.

[138] S. Lucia, D. Navarro, B. Karg, H. Sarnago, and s. Lucía, "Deep learning-based model predictive control for resonant power converters," *IEEE Transactions on Industrial Informatics*, vol. 17, no. 1, pp. 409–420, 2021.

[139] X. Liu, L. Qiu, J. Rodríguez, *et al.*, "Data-driven neural predictors-based robust mpc for power converters," *IEEE Transactions on Power Electronics*, vol. 37, no. 10, pp. 11 650–11 661, 2022.

[140] D. Wang, Z. J. Shen, X. Yin, *et al.*, "Model predictive control using artificial neural network for power converters," *IEEE Transactions on Industrial Electronics*, vol. 69, no. 4, pp. 3689–3699, 2022.